Investigation of effects of performance recovery procedures for polymer electrolyte membrane fuel cells (PEMFCs)

Von der Fakultät Energie-, Verfahrens- und Biotechnik der Universität Stuttgart
zur Erlangung der Würde eines Doktors der
Ingenieurwissenschaften (Dr.-Ing.) genehmigte Abhandlung

Vorgelegt von

M. Eng. **Qian Zhang**
aus Shanxi, VR China

Hauptberichter: Prof. Dr. rer. nat. K. Andreas Friedrich
Mitberichter: Prof. Dr. Andrea Casalegno
Prüfungsvorsitzender: Prof. Dr. rer. nat. habil. André Thess

Tag der mündlichen Prüfung: 28.02.2024

Institut für Gebäudeenergetik, Thermotechnik und Energiespeicherung
der Universität Stuttgart
2024

It doesn't matter how beautiful your theory is, it doesn't matter how smart you are. If it doesn't agree with experiment, it's wrong.

Richard P. Feynman

Acknowledgments

First, I would like to express my gratitude to Prof. Dr. K. Andreas Friedrich for allowing me to pursue Ph.D. research in the Department of Electrochemical Energy Technology from the Institute of Engineering Thermodynamics at the German Aerospace Center (DLR) in Stuttgart. I appreciate his kind and continuous support over the past several years, including helping me with my funding application, drafting my research proposal, discussing the results, providing suggestions with writing and publications, and guiding the research focus.

Additionally, I am incredibly grateful to my co-supervisors, Dr. Pawel Gazdzicki and Dr. Mathias Schulze, for their unwavering support. They are always willing to help with their valuable expertise and enormous patience whenever I have problems with my research.

I also wish to express my gratitude to my DLR colleagues, especially Dr. Krishan Talukdar, Dr. Mitzel Jens, Dr. Wang Li, Pia Aßmann, Dr. Indro Biswas, Qingying Zhao, Dr. Daniel Garcia, Dr. Norbert Wagner, Dr. Corinna Harms for their support in a scientific aspect. I am very grateful to Siegfried Graf for the daily technical support with troubleshooting the testbench and fuel cell hardware. I am grateful to Ina Plock for the SEM measurements, who supplied high-quality SEM pictures.

Thanks should also go to my parents, Yali Qiao and Tianliang Zhang, who impacted and inspired me. Although we could not see each other in person often, they always tried to help and cheer me up with words and video chats, especially in my difficult moments. Their belief in me has kept my spirits and motivation high during this process. This endeavor would not have been possible without their emotional support.

Moreover, I would like to thank my boyfriend, Robert Schober, who has made countless sacrifices to help me get to this point. He gave me valuable advice on manuscript writing and dealing with stress. I'd like to thank you for all the unconditional support during the process.

Last but not least, I would like to thank CSC (China Scholarship Council) for supporting and funding my Ph.D. for four years at the DLR in Germany.

Declaration

I certify that the dissertation entitled “Investigation of effects of performance recovery procedures for polymer electrolyte membrane fuel cells (PEMFCs)” is entirely my own work. Passages and ideas from other sources have been clearly marked.

Erklärung

Ich versichere, dass ich die vorliegende Dissertation mit dem Titel “Investigation of effects of performance recovery procedures for polymer electrolyte membrane fuel cells (PEMFCs)” selbständig verfasst und keine anderen als die angegebenen Quellen und Hilfsmittel benutzt habe. Passagen und Gedanken aus fremden Quellen sind als solche kenntlich gemacht.

Abstract

Polymer electrolyte membrane fuel cells (PEMFCs) are promising energy converters to realize the transition to a carbon-free society, especially for mobile and stationary applications. The two main barriers hindering widespread commercialization are limited durability and high cost. Throughout the lifetime of PEMFCs, their components undergo different operating conditions, which result in both mechanical and chemical degradation. To ensure acceptable longevity of the PEMFCs, it becomes necessary to mitigate these degradation effects. However, it is important to note that some of the performance losses are reversible and can be regained through specific recovery procedures. This cumulative doctoral thesis consists of three original research articles and two experiments as a further discussion part. The focus of this work is: i) establishing a methodology to evaluate the recovery efficiency of a recovery procedure, ii) understanding the recovery mechanism of different recovery procedures, iii) comparing the recovery efficiency of different recovery procedures, and iv) tailoring specific recovery mechanisms to improve recovery efficiency of a recovery procedure. The three original research articles and two experiments included in this cumulative doctoral thesis lead to the following main findings:

In Article I, a methodology was proposed for evaluating and comparing the efficiencies of different recovery procedures. The methodology utilizes logged voltage data from load cycling tests, polarization curves, and electrochemical impedance spectroscopy (EIS) data to quantify reversible losses versus current density. Determining the efficiency of a recovery procedure using either logged voltage data from load cycling tests or polarization curves lead to a similar result. The proposed methodology analyzed parameters that provide information on recovered performance losses as well as non-recovered losses, enabling the quantification and comparison of the studied recovery procedures.

Articles I and II followed the proposed methodology to investigate the recovery efficiency of three recovery protocols (DOE-based, JRC-based, and overnight rest protocols. Among the three protocols, the JRC protocol was found to recover the highest performance losses at current density from 0 to 1.5 $A \cdot cm^{-2}$, while the DOE protocol recovered the least. The JRC protocol recovered kinetic losses by reducing Pt oxides and changing the ionomer structure through a reduction in the cathode potential and fuel cell temperature, respectively. However, the DOE protocol led to a relatively low recovery of losses in the kinetic region of the polarization curves. Therefore, the JRC recovery protocol was selected as a reference for

the durability tests in the subsequent work to evaluate other recovery procedures.

Article III aimed to evaluate and investigate the mechanism of performance recovery due to temperature reduction using two durability tests. The first durability test involved operando temperature reduction, where the load cycling was not interrupted for recovery. The second durability test involved non-operando temperature reduction, where the load cycling was stopped. The measurements indicate that reducing the temperature from 80 °C to 45 °C results in a performance recovery of 60 - 70 % in a shorter time than the JRC recovery protocol. It is interesting to note that the absolute recovered voltage is directly proportional to the total amount of liquid water produced.

The DOE recovery protocol, with a total duration of only 29 minutes, has the advantage of being shorter compared to the JRC recovery protocol and the overnight rest. However, the DOE recovery protocol was found to reduce charge transfer resistance much less than the other two recovery procedures. To improve the recovery efficiency of fuel cell performance degradation, two steps in the original DOE recovery protocol are modified. Specifically, a fuel cell cooling-down step is introduced to replace the air soak step, and the duration of the hydrogen soak step is extended. The durability test results indicate that the modified DOE protocol exhibits an enhanced recovery efficiency compared to the original DOE protocol due to a more significant reduction in charge transfer resistance.

Articles II and III have demonstrated that water condensation induced by temperature reduction can positively impact the recovery of reversible performance losses. To comprehend the mechanism underlying the recovery procedures involving temperature reduction, the change in oxygen transport resistance in the cathode is examined in the second part of the further discussion. A durability test is conducted to evaluate the recovery efficiency of the temperature reduction from 80 °C to 30 °C. Exposure to liquid water through water condensation contributes to the regeneration and redistribution of the ionomer structure in the cathode, enhancing the hydrophilicity of the ionomer. This process occurs at a slow rate but eventually reaches a quasi-equilibrium state. Consequently, the ionic transfer and ohmic resistance in the catalyst layer are reduced.

Eventually, this work lays a solid foundation for further investigating the recovery mechanism of reversible performance degradation of PEMFCs and makes an essential contribution by developing efficient recovery procedures.

Zusammenfassung

Polymer-Elektrolytmembran-Brennstoffzellen sind vielversprechende Energiewandler, die den Übergang zu einer nachhaltigen Energieversorgung erleichtern, insbesondere für mobile und stationäre Anwendungen. Zwei wesentliche Hindernisse, die eine weitreichende Kommerzialisierung behindern, sind die begrenzte Haltbarkeit und die hohen Kosten. Die PEMFCs sind während ihres Lebenszyklus verschiedenen Betriebsbedingungen ausgesetzt. Die Betriebsbedingungen sind sowohl von mechanischem als auch von chemischem Stress geprägt. Um eine akzeptable Langlebigkeit der PEMFCs zu garantieren, ist es notwendig, diese Degradationseffekte zu vermindern. Es ist wichtig festzuhalten, dass einige der Leistungsverluste reversibel sind und durch spezielle Erholungsverfahren wiederhergestellt werden können. Diese kumulative Doktorarbeit besteht aus drei Original-Forschungsartikeln sowie zwei Studien als weiteren Diskussionsteil. Ziel dieser Arbeit ist es, i) eine Methodik zur Bewertung der Regenerationseffizienz eines Regenerationsverfahrens zu etablieren, ii) den Regenerationsmechanismus verschiedener Prozeduren zu verstehen, iii) die Regenerationseffizienz verschiedener Prozeduren zu vergleichen und iv) spezifische Regenerationsmechanismen anzupassen, um die Regenerationseffizienz einer Prozedur zu verbessern. Die wichtigsten Ergebnisse, welche in den drei Artikeln und im weiteren Diskussionsteil enthalten sind, werden nachstehend zusammengefasst:

Artikel I schlägt eine Methodik zur Bewertung und Vergleich der Effizienz verschiedener Regenerationsverfahren vor. Die vorgeschlagene Methodik quantifiziert reversible Verluste als Funktion der Stromdichte auf der Grundlage von protokollierten Lastwechseltests, Polarisationskurven und elektrochemischer Impedanzspektroskopie (EIS). Es wird gezeigt, dass die Verwendung von protokollierten Lastwechseltests und die Verwendung von Polarisationskurven zur Bestimmung der Effizienz eines Regenerationsverfahrens zu einem ähnlichen Ergebnis führen. Die vorgeschlagene Methodik analysiert Parameter, welche Informationen über wiederhergestellte Leistungsverluste sowie nicht wiederhergestellte Leistungsverluste liefern und ermöglicht somit die Quantifizierung und Vergleichbarkeit der untersuchten Regenerationsverfahren.

Artikeln I und II folgten der vorgeschlagenen Methodik und untersuchten die Regenerationseffizienz von drei Regenerationsprotokollen (DOE-basiert, JRC-basiert und Übernacht-Regenerationsprotokoll). Unter den drei untersuchten Protokollen hatte das JRC-Protokoll die höchste Wiederherstellung der Leistungsverluste bei Stromdichten von 0 bis

1,5 $A \cdot cm^{-2}$, während das DOE-Protokoll die niedrigste Rückgewinnung aufwies. Das JRC-Protokoll stellt die kinetischen Verluste durch Reduzierung von Pt-Oxiden und Strukturänderung des Ionomers durch Verringerung des Kathodenpotentials und der Brennstoffzellentemperatur wieder her. Das DOE-Protokoll hingegen führt zu einer vergleichsweisen geringen Wiederherstellung von Verlusten im kinetischen Bereich der Polarisationskurven. Daher wird das JRC-Regenerationsprotokoll als Referenz in den nachfolgenden Haltbarkeitstests verwendet, um andere Regenerationsverfahren zu bewerten.

Artikel III zielt darauf ab, mit zwei Haltbarkeitstests den Mechanismus der Leistungsregeneration aufgrund von Temperaturreduktion zu bewerten und zu untersuchen. Der erste Haltbarkeitstest umfasste operando-Temperaturreduktionen, d. h. die Lastzyklen wurden während der Regeneration nicht unterbrochen. Der zweite Haltbarkeitstest hingegen wurde mit nicht-operando-Temperaturreduktionen (Lastzyklen wurden gestoppt) durchgeführt. Die Ergebnisse zeigen, dass eine Temperaturreduktion von 80 °C auf 45 °C eine Leistungsregeneration von 60 bis 70 % in kürzerer Zeit im Vergleich zum JRC-Regenerationsprotokoll ermöglicht. Interessanterweise ist die absolut wiederhergestellte Spannung direkt proportional zur Gesamtmenge an produziertem flüssigem Wasser.

Das DOE-Regenerationsprotokoll hat mit insgesamt nur 29 Minuten den Vorteil einer kürzeren Dauer im Vergleich zum JRC-Regenerationsprotokoll und der Übernacht-Abschaltung. Wie in Artikel II berichtet wurde, reduziert das DOE-Regenerationsprotokoll den Ladungstransferwiderstand deutlich weniger als die anderen beiden Regenerationsverfahren. Um die Effizienz der Wiederherstellung der Leistungsdegradation der Brennstoffzelle zu verbessern, werden zwei Schritte im ursprünglichen DOE-Regenerationsprotokoll modifiziert. Ein Schritt zum Abkühlen der Brennstoffzelle ersetzt den Luftspülungsschritt, und die Dauer des Wasserstoffspülungsschritts wird verlängert. Die Ergebnisse der Haltbarkeitstests zeigen eine verbesserte Effizienz der Regeneration im Vergleich zum ursprünglichen DOE-Protokoll aufgrund einer stärkeren Reduzierung des Ladungstransferwiderstands.

In Artikel II und III wurde festgestellt, dass sich Wasser-Kondensation aufgrund der Temperatursenkung durch den Kühlschritt der Brennstoffzelle positiv auf die Wiederherstellung reversibler Leistungsverluste auswirkt. Um den Mechanismus der

Regenerationsverfahren mit Temperatursenkung zu verstehen, wurde im zweiten Teil der weiteren Diskussion die Veränderung des Sauerstofftransportwiderstands in der Kathode untersucht. Die Regenerationseffizienz der Temperatursenkung von 80 °C auf 30 °C wurde mit einem Haltbarkeitstest bewertet. Die Exposition gegenüber flüssigem Wasser durch Wasser Kondensation trägt zur Regeneration und Umverteilung der Ionomerstruktur in der Kathode bei und verbessert die Hydrophilie des Ionomers. Dieser Prozess verläuft langsam, erreicht jedoch schließlich einen Gleichgewichtszustand. Infolgedessen wird der ohmsche Widerstand in der Katalysatorschicht reduziert, weil der Ionentransport verbessert wird.

Letztendlich legt diese Arbeit eine solide Grundlage für weitere Untersuchungen des Regenerationsmechanismus reversibler Leistungsverschlechterungen von PEMFCs und leistet einen wesentlichen Beitrag durch die Entwicklung effizienter Regenerationsverfahren.

Contents

List of Tables

List of Figures

List of Abbreviations

Abbreviation	Description
AFC	Alkaline fuel cell
AST	Accelerated stress test
BP	Bipolar plate
CCM	Catalyst coated layer
CL	Catalyst layer
COP26	Conference of the Parties
CPE	Constant phase element
CV	Cyclic voltammetry
DLR	German Aerospace Center
DOE	U.S. Department of Energy
ECSA	Electrochemical active surface area
EIS	Electrochemical impedance spectroscopy
EU	European Union
FC-DLC	Fuel Cell Dynamic Load Cycle
FRA	Frequency response analyzer
GDL	Gas diffusion layer
GDP	Gross domestic product
GHG	Greenhouse gas
HDV	Heavy-duty vehicle
HOR	Hydrogen oxidation reaction
ICE	Internal combustion engine
JRC	Joint Research Center of the European Commission

LDV	Light-duty vehicle
MCFC	Molten carbonate fuel cell
MEA	Membrane electrode assembly
MMT	Million metric ton
MPL	Microporous layer
OCV	Open circuit voltage
ORR	Oxygen reduction reaction
PAFC	Phosphoric acid fuel cell
PEEK	Polyetheretherketon
PEM	Polymer electrolyte membrane
PEMFC	Polymer electrolyte membrane fuel cell
PEN	Polyethylene naphthalate
PFSA	Perfluoro sulfonic acid
PLC	Programmable logic controller
PTFE	Polytetrafluoroethylene
SEM	Scanning electron microscope
SMR	Steam methane reforming
SOFC	Solid oxide fuel cell

List of Symbols

Symbol	Description	Unit
A	Effective surface area	cm^2
E	Theoretical potential	V
E_{OCV}	Open circuit voltage	V
F	Faraday constant	$C \cdot mol^{-1}$
ΔG	Gibbs free energy	$kJ \cdot mol^{-1}$
ΔH	Higher heating value	$kJ \cdot mol^{-1}$
n	Number of electrons in the reaction	
η	Theoretical efficiency	%
$\eta_{Activation}$	Activation voltage loss	V
η_{Last}	Relative recovery related to the cell performance degradation of the previous operation	%
$\eta_{Mass\ transport}$	Mass transport voltage loss	V
η_{Ohmic}	Ohmic voltage loss	V
i	Current density	$A \cdot cm^{-2}$
L	Inductance	H
P	Pressure	kPa
R	Ideal gas constant	$J \cdot mol^{-1} \cdot K^{-1}$
$R_{Charge\ transfer}$	Charge transfer resistance	$m\Omega \cdot cm^2$
$R_{Electronic}$	Electron transport resistance	$m\Omega \cdot cm^2$
R_{Ionic}	Ionic impedance	$m\Omega \cdot cm^2$
$R_{Mass\ transfer}$	Mass transfer resistance	$m\Omega \cdot cm^2$
R_{NP}	Pressure-independent oxygen transfer resistance	$S \cdot m^{-1}$

R_{Ohmic}	Ohmic resistance	$m\Omega \cdot cm^2$
R_P	Pressure-dependent oxygen transfer resistance	$S \cdot m^{-1}$
R_{Total}	Total oxygen transfer resistance	$S \cdot m^{-1}$
t	Time	s
T	Temperature	K

List of Scientific Peer-Reviewed Publications

This is a cumulative thesis, which is based on three scientific articles listed below.

Article I: Quantification of effects of performance recovery procedures for polymer electrolyte membrane fuel cells

Zhang, Q., Schulze, M., Gazdzicki, P., & Friedrich, K. A.

Journal of Power Sources 512 (2021): 230467

DOI: https://doi.org/10.1016/j.jpowsour.2021.230467

Contribution of Qian Zhang: Conception of the work, execution of experiments, as well as writing, data analysis, and reviewing.

Article II: Comparison of different performance recovery procedures for polymer electrolyte membrane fuel cells

Zhang, Q., Schulze, M., Gazdzicki, P., & Friedrich, K. A.

Applied Energy 302 (2021): 117490

DOI: https://doi.org/10.1016/j.apenergy.2021.117490

Contribution of Qian Zhang: Conception of the work, execution of experiments, as well as writing, data analysis, and reviewing.

Article III: Temperature Reduction as Operando Performance Recovery Procedure for Polymer Electrolyte Membrane Fuel Cells

Zhang, Q., Schulze, M., Gazdzicki, P., & Friedrich, K. A.

Energies 17 (2024): 774

DOI: https://doi.org/10.3390/en17040774

Contribution of Qian Zhang: Conception of the work, execution of experiments, as well as writing, data analysis, and reviewing.

Additional contributions to peer-reviewed publications:

Article IV: The Challenges in Reliable Determination of Degradation Rates and Lifetime in Polymer Electrolyte Membrane Fuel Cells

Zhang, Q., Harms, C., Mitzel, J., Gazdzicki, P., & Friedrich, K. A.

Current Opinion in Electrochemistry 31 (2022): 100863

DOI: 10.1016/j.coelec.2021.100863

Contribution of Qian Zhang: Conceptualization, literature research, writing, and reviewing.

Article V: Review on mechanisms and recovery procedures for reversible performance losses in polymer electrolyte membrane fuel cells

Mitzel, J., Zhang, Q., Gazdzicki, P., & Friedrich, K. A.

Journal of Power Sources 488 (2021): 229375

DOI: https://doi.org/10.1016/j.jpowsour.2020.229375

Contribution of Qian Zhang: Conceptualization, literature research, and writing.

Conference contributions:

Poster presentation: Investigation and Comparison of Different Performance Recovery Procedures for Polymer Electrolyte Membrane Fuel Cells

Zhang, Q., Gazdzicki, P., Schulze, M., & Friedrich, K. A.

71st Annual Meeting of the International Society of Electrochemistry, Belgrade Online (2020)

Contribution of Qian Zhang: Conception of the work, execution of experiments, as well as writing, data analysis, and reviewing.

1 Introduction

1.1 Background

Nowadays, the mitigation of climate change, including global warming, is considered to be the key challenge for all the countries around the globe. As a result of an increase in human activities during the last several decades due to population growth and industrialization, greenhouse gas (GHG) emissions surged dramatically with the combustion of fossil fuels, which contributes to global warming. The effects of global warming are recently clearly visible on many continents, such as the melting of glaciers, rising water levels, greater frequency of extreme weather events, as well as droughts and floods due to disturbances of water-related phenomena [1, 2]. According to the Paris Agreement in 2015, global cooperation to reduce carbon emissions should be built up to keep the warming below 2 °C (pursuing to keep it below 1.5 °C) above pre-industrial levels [3]. In the UN Climate Change Conference of the Parties (COP26) in 2021, to achieve the 1.5 °C target, 153 countries, which covered 90 % of the world gross domestic product (GDP) and 80 % of global GHG emissions, put forward the path to a low-carbon future [4].

The energy sector, which accounts for a quarter of global GHG emissions, is facing major challenges. Efforts are taken to use existing energy more efficiently and at the same time, figure out the transition towards renewable energies to avoid using polluting fossil fuels, such as coal and oil. Hydrogen is a versatile energy carrier and can be used as a feedstock and replacement for fossil fuels in many areas, such as mobility, industries, households, and energy services. Thus, in the last decade, the concept of a hydrogen economy has drawn substantial attention from the public, industry, and governments. Green hydrogen, i.e., hydrogen produced using renewable energies, can be produced by electrolysis of water using green electricity from intermittent and fluctuating renewable energies, such as solar and wind. Green hydrogen can be used as the feedstock for the production of various chemicals and synthetic hydrocarbons and carbon-free energy carriers for mobile power applications via conversion with electrochemical cells (fuel cells). The European Union (EU) estimates that by 2050 up to 24 % of the total energy demand could be met by clean hydrogen to achieve the 1.5 °C target [5]. The U.S. Department of Energy (DOE) released the National Clean Hydrogen Strategy and Roadmap in 2022, where clean hydrogen production in the United States is supposed to be increased from nearly zero in 2022 to 10 million metric

tons (MMT) per year by 2030 and 50 MMT per year by 2050 [6].

Fuel cells are electrochemical energy conversion devices, which convert chemically stored energy in form of H_2 molecules into electricity. Polymer electrolyte membrane fuel cells (PEMFCs) dominate the market by units and capacity among other fuel cells types such as alkaline fuel cells (AFCs), phosphoric acid fuel cells (PAFCs), solid oxide fuel cells (SOFCs), and molten carbonate fuel cells (MCFCs) [7]. In PEMFCs, the electricity is generated with only exhaust gas of pure water during the oxidation of fuel hydrogen by oxygen from the air. PEMFCs have the advantages of a relatively low operating temperature (60 to 100 °C), fast start-up/shut-down, along with high efficiency and power density, which make the PEMFCs suitable for transportation applications. For heavy-duty vehicles, the European Commission set the 2030 targets for the fuel cell stack to a durability of 30,000 h with a system cost below 100 Euro/kW [8]. For comparison, the current state of the art is defined as 15,000 h durability with a cost of 1,500 Euro/kW. Similarly, the DOE set the interim durability targets for heavy-duty applications at 25,000 h till 2030 and the ultimate targets at 30,000 h and 1,000,000 miles. Numerous projects supporting the commercialization of transportation with PEMFCs are have been conducted [9-11], including the development of infrastructure, fueling components, and hydrogen storage.

Overall, hydrogen technologies are of great interest in context of transition of energy systems to emission-free systems. With ongoing rapid technological developments and the urgency to achieve carbon neutrality before 2050, hydrogen has taken a key priority within many scenarios of the energy transition.

1.2 Thesis structure

This thesis aims to investigate the effects of performance recovery procedures for PEMFCs. After a short introduction in Section 1.1 to the background of hydrogen energy, the research motivation to clarify the importance of understanding the reversible performance degradation and developing effective recovery procedures for PEMFCs is provided in Section 2.

Before the experimental work is discussed in detail, the essential information about PEMFCs, including the description of each component of a single PEMFC, the working mechanism of PEMFCs, and the origin and mechanism of reversible performance degradation of PEMFCs

is introduced in Section 3. In the following Section 4, the experimental approaches and methodology, which are utilized in this work, are summarized. Also, the experimental processes, hardware and software, characterization methods, and investigated recovery procedures are presented.

Three publications (Articles I - III) and the further discussion in Section 5 contribute to the main research findings of this cumulative thesis, as shown in Figure 1.

As a solid foundation for investigating the efficiency of a recovery procedure and understanding the recovery mechanism, a methodology is established to evaluate and compare different recovery procedures for PEMFCs using durability tests. All recovery procedures and durability tests performed in this thesis follow this methodology. The methodology is explained in detail in Article I. Afterward, three available recovery procedures, JRC-based [12], DOE-based [13], and overnight recovery procedures [14, 15], are investigated and compared based on durability tests in Article II. Furthermore, the recovery mechanism of each step of the recovery procedures and the recovery efficiency are discussed according to the results of electrochemical characterization measurements. The recovery mechanisms due to operando recovery procedures based on temperature reduction are investigated in Article III. The effect of operando performance recovery procedures with different temperature reductions and cooling-down durations were evaluated and analyzed.

According to Article I, the DOE-based recovery protocol leads to a relatively low recovery of losses in the kinetic region of the polarization curves. Hence three specific modifications of the DOE-based recovery protocol are adapted in order to increase its recovery efficiency, which is discussed in section 5.1 and goes beyond the findings of Articles I - III.

Section 5.2 provides specific tests to understand the contribution of oxygen transport resistance to performance recovery, serving as additional supplements to the findings of Articles I - III.

Eventually, the efficiency of the investigated recovery procedures and related mechanisms are consolidated. Advantages and drawbacks are identified along with open questions, which are not answered within this thesis.

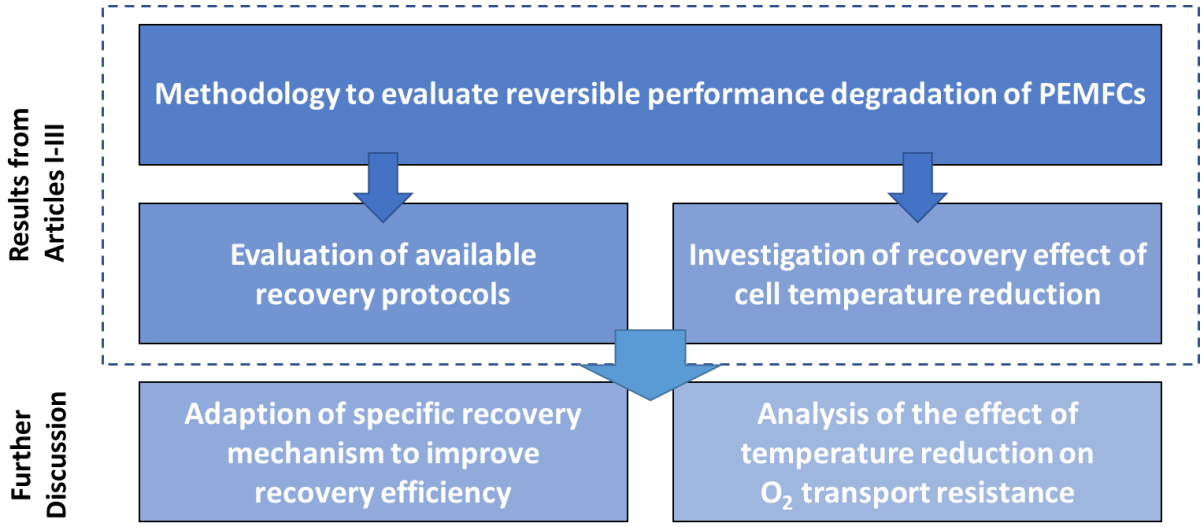

Figure 1: Outline of main topics of the thesis and the link between the results of Articles I - III and further discussion in Section 5.

2 State-of-the-art and motivation

As mentioned in Section 1.1, despite significant technical progress in the last several decades, the main barriers hindering the widespread application and commercialization of PEMFCs are durability limitations, high cost, and lack of hydrogen refueling stations [16].

In order to rival internal combustion engines (ICEs) in transportation uses, the European Commission has established a goal for fuel cell systems to have a projected lifespan of 7,000 h for fuel cell light-duty vehicles (LDVs) and 30,000 h for fuel cell heavy-duty vehicles (HDVs) by the year 2030 [17]. Meanwhile, the DOE set the ultimate durability target for LDVs of 8,000 h with a lower than 10 % loss of performance [13]. However, as of 2017, the current state-of-the-art durability for fuel cell systems in use by LDVs is reported to be 4,000 hours by the EU [17] and 5,000 hours by the DOE as of 2020 [18]. Furthermore, there has been a recent surge in interest in fuel cells for HDVs because they require less investment in refueling infrastructure, particularly for dedicated and predictable routes [19]. The DOE has set interim and ultimate targets for the lifetime durability of HDV systems, with a goal of 25,000 hours by 2030 and 30,000 hours by 2050 with less than 20 % of the performance loss [20]. However, the current state-of-the-art durability for HDV systems averages at 13,236 hours according to the latest report from the DOE [18, 21].

Throughout the lifetime of PEMFCs, their components are exposed to a range of operating conditions such as idling, start-up and shut-down, and transient load changes, which can result in both mechanical and chemical degradation. In order to achieve an acceptable level of longevity, it is necessary to mitigate these degradation effects. However, it is important to note that some of the performance losses can be recovered through specific refresh procedures. This subject is currently drawing more attention since the understanding of reversible performance degradation and using recovery procedures in durability tests can greatly affect the determined degradation rates of PEMFCs. Peng et al. [22] and Wang et al. [23] have put forth techniques for health prognostics and lifespan prediction that account for the impact of reversible performance degradation. These methods have demonstrated the ability to precisely model the performance degradation and lifetime of PEMFCs.

In general, the fuel cell's reversible and irreversible degradation rates depend on the operation conditions and cell configurations. Although there are no universal methods to identify and evaluate the reversible and irreversible performance degradation and the

degradation rate, the Joint Research Center of the European Commission (JRC) provides a scheme with the definition and the terminology, as shown in Figure 2. During a long-term PEMFC operation under a specific current load, a recovery procedure is performed after each operation period, and the change in cell voltage is recorded over time. The reversible performance degradation is expressed as the difference between the cell voltage before and after the recovery procedure, whereas the irreversible performance part is the difference between the cell voltage at the beginning (or at the end) of the previous and following operation periods.

In the literature, the reversible and irreversible performance degradation rates were evaluated with durability tests, and the reversible part was identified as playing a significant role [24, 25]. In a study with a 5-cell stack, the total degradation rate under a constant current load over 1800 h was 60 $\mu V \cdot cell^{-1} \cdot h^{-1}$ [26]. A recovery procedure was performed at different operation times during the durability test, with at least 80 % of total voltage loss being reversible. Wang et al.'s group confirmed that the reversible performance degradation increased along the current density range from 0 to 1.6 $A \cdot cm^{-2}$ [27]. The percentage of the reversible performance degradation also increased from 25 % to 80 % or from 42 % to 86 %, depending on the chosen technique of MEA fabrication. Further, the percentage of the reversible performance degradation was proved to decrease along the operation time due to the accumulation of the irreversible performance degradation. Han et al.'s work showed a recovery rate of 55 % - 65 % of a 3-cell stack after 100 h under a dynamic load cycling operation, while the recovery rate dropped to 5 % from 40 % after 300 h at the current density range from 0 to 1.4 $A \cdot cm^{-2}$ [28]. Besides, the evaluated reversible performance degradation rate also depends on the applied specific recovery procedure. Seven recovery procedures were compared in a durability test, and the evaluated reversible performance degradation differed from -20 % to 68 % at the current density of 0.8 $A \cdot cm^{-2}$ [29].

Understanding the recovery mechanism and developing suitable recovery procedures for PEMFCs aim to prolong the durability of the PEMFCs by eliminating the reversible performance degradation during their lifetime. The main scientific gaps and challenges are as follows:

(i) Establishment of a harmonized methodology for the evaluation of recovery effects

Although the JRC provided a simple scheme to present the reversible and irreversible performance degradation as mentioned above, there is still no universal methodology to

evaluate and compare the efficiency of recovery procedures. In the literature, different methods are utilized by authors to quantify the rate of performance degradation and recovery effects. Accordingly, there are different ways to interpret the recovery procedures and different focuses for the explanations of the recovery mechanism. Therefore, it is necessary to establish a harmonized methodology to evaluate the recovery efficiency of the recovery procedures for PEMFCs.

(ii) Detailed understanding of the recovery mechanism

Although the recovery mechanism has been studied extensively in the literature, especially the recovery mechanism due to different contaminants in the gas feed, the mechanism of several recovery effects is still unclear, such as the recovery effect resulting from the shut-down step. Besides, during the lifetime of PEMFCs, various sources of reversible performance degradation are involved, making it complicated to distinguish and understand all the recovery effects and mechanisms upon a specific recovery procedure. Usually, a recovery procedure contains several steps, such as the recovery procedures provided by JRC and DOE. However, there is still a lack of explanation of all involved mechanisms and a comparison of the efficiency of different recovery procedures.

(iii) Tailoring of recovery procedures according to specific mechanisms to improve the recovery efficiency

DOE set the specific technical target to define a recovery procedure that recovers more than 95 % of the reversible performance degradation of PEMFCs within 30 s [13]. To achieve an efficient recovery of performance degradation, recovery procedures should be proposed, investigated, and optimized according to different applications of PEMFCs with consideration to specific operation conditions. Depending on the reasons for reversible performance degradation, the recovery procedure can be adjusted, and the recovery efficiency can be further improved based on an understanding of the specific recovery mechanism. Furthermore, during the optimization of a recovery procedure, more considerations should be given to i) if an extra power supply is needed, ii) if the duration of the recovery procedure is acceptable, and iii) if extra space is necessary, e.g., a bypass, which constrains the possibilities of the development.

The most frequently discussed types of reversible performance degradation in the literature will be explained in Section 3.2. However, two kinds of reversible performance degradation

are still under discussion due to the unclear mechanism or the difficulty of recovering.

Part of the performance degradation resulting from ionomer structure changes in the electrodes and membrane can be recovered by increasing the humidity of the electrodes. Jomori et al. and Du et al. [30, 31] recovered the performance degradation due to long-term dry operation with an increased gas relative humidity upon low fuel cell voltage for several hours. The reversible ionomer structure changes are attributed to the adsorption/desorption of ionomer sulfonate groups on the catalyst surface. However, more work needs to be executed on the mechanism of the nano-scale ionomer structure changes.

The corrosion of the carbon support of electrodes is often recognized as irreversible mechanical damage resulting in the dissolution and detachment of catalyst in the cathode and, thereby, fuel cell performance degradation. The carbon oxidation occurs at high electrode potential under local fuel starvation and start-up/shut-down conditions, where the cathode potential can reach above 1 V due to the presence of hydrogen/air fronts [32]. However, the initial reactions in the carbon oxidation process, from the formation of hydroxyl groups to the carbonyl groups as oxidation products, are reported to be reversible by low potential (0.4 V) and reductive atmosphere with the presence of Pt catalyst [33, 34]. Nevertheless, no effective recovery procedure was developed in the literature to recover the performance degradation due to carbon corrosion.

In summary, Table 1 presents the main reversible performance degradation mechanism and corresponding recovery procedures in the literature, which is adapted from the work of Mitzel et al. [35]. However, most of the contributions focused on investigating the mechanism of reversible performance degradation. In recent years, the development of practical recovery procedures has drawn increasing attention.

Comprehending the mechanism behind both reversible and irreversible degradation in performance is a crucial requirement for designing effective methods to restore the longevity of PEMFCs. Only with effective recovery procedures can the reversible performance degradation of PEMFCs be identified and separated from the irreversible part. Furthermore, as a crucial part of the operation strategies of PEMFCs, effective recovery procedures help with prognostics and health management and prevent the deterioration of the fuel cell performance.

Although understanding reversible performance degradation and developing efficient

recovery procedures are essential, due to their high complexity, there is still a lack of contribution in this field. This work aims to shed more light on this topic. The main reasons for the reversible and irreversible performance degradation during the PEMFCs' operation will be clarified in detail in the next section.

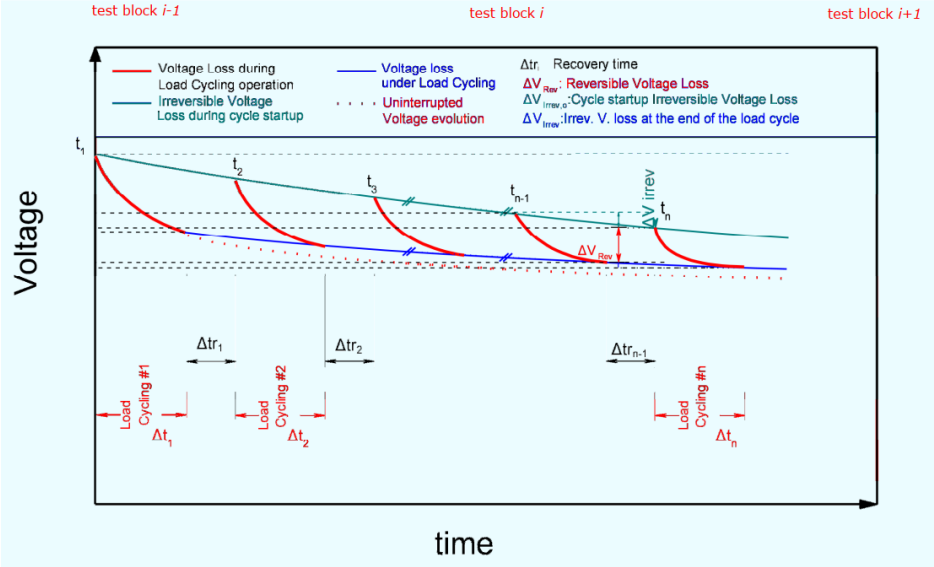

Figure 2: Definition of the reversible and irreversible performance degradation from the Joint Research Center of the European Commission (JRC) [12].

Table 1: Type of the reversible performance degradation, corresponding recovery methods, and mechanism. Adapted from [35].

Reversible degradation type	**Recovery methods**	**Recovery mechanism**
Pt oxidation	1. Low cathode potential (<0.63 V) 2. Decrease cathode potential by feeding H_2	$Pt\text{-}O + H_2 \rightarrow Pt\text{-}OH \rightarrow Pt\text{-}O + Pt + H_2O$ $Pt\text{-}O + H^+ + e^- \rightarrow Pt + H_2O$ [36]
Sulfur poisoning by H_2S, SO_2, COS	Potential cycling in H_2/N_2 atmosphere between 0.1 and 1.1 V, flushing with oversaturated gas flow	$Pt\text{-}S_{ads} + H_2O \rightarrow Pt\text{-}SO_4^{2-}{}_{ads} + H^+ + e^-$ [34] $Pt\text{-}SO_4^{2-}{}_{ads} \rightarrow Pt + SO_4^{2-}$ [37]
Nitrogen oxides poisoning	Applying an electrode potential above 0.9 V, flushing with oversaturated gas flow	$Pt\text{-}NO_x + H_2O \rightarrow Pt + NO_3^- + H^+ + e^-$ [38]
CO poisoning	1. Air bleeding 2. Applying the anode potential at high potential (about 0.3 V)	$O_2 + 2Pt \leftrightarrow Pt\text{-}O_2 + Pt \rightarrow 2(Pt\text{-}O)$ $CO + Pt \leftrightarrow CO\text{-}Pt$ $CO\text{-}Pt + Pt\text{-}O \rightarrow 2Pt + CO_2$ [39] $Pt\text{-}CO_{ads} + H_2O \rightarrow Pt + CO_2 + H^+ + e^-$ [40]
Water management	1. Gas purging with dry gas 2. Cell shut-down and restart	Water removal from the cathode catalyst layer and GDL [41]
Changes in ionomer/membrane structure	Increasing the humidity of the electrodes upon low potential (<0.2 V)	$Pt\text{-}RSO_3^-{}_{ads} \rightarrow Pt + RSO_3^-$ [31]
Carbon support degradation	Low potential and reductive atmosphere	$R_2C{=}O + H^+ + e^- \rightarrow R_2CH + H_2O$ [42]

3 Fundamentals

In Section 3.1, the fundamental information for the PEMFCs is introduced briefly, including the essential components of the PEMFCs and the various types of voltage losses. In Section 3.2, the different sources of reversible performance degradation of the PEMFCs are described. Section 3.3 summarizes the scientific gap.

3.1 Polymer electrolyte membrane fuel cell principle

The PEMFC is a device to convert chemically stored energy into electricity through electrochemical reactions. In general, according to the required power output, multiple single cells can be combined into fuel cell stacks. Figure 3 a) depicts the key layout of the single polymer electrolyte membrane (PEM) fuel cell and the mechanism of the electrochemical reactions [43]. The membrane electrode assembly (MEA), as the heart of a PEMFC, has an electrode-membrane-electrode structure. Figure 3 b) is a cross-sectional scanning electron microscope (SEM) image of a MEA used in Article II. The membrane, as the electrolyte, separates the hydrogen and gas in the anode and cathode compartments and conducts only protons. Currently, perfluoro sulfonic acid (PFSA) is the most commonly used membrane material for PEMFCs due to the desirable properties of i) high ionic conductivity, ii) thermally stability throughout the operating temperature range, iii) effective prevention of electron and hydrogen crossover, and iv) mechanically robustness, especially if strengthened with a backbone structure of polytetrafluoroethylene (PTFE, also known as Teflon). The anode and cathode catalyst layers (CLs) are two thin, porous, and electrically conductive electrodes on each side of the membrane; at the same time, these areas are where the hydrogen oxidation reaction (HOR) and oxygen reduction reaction (ORR) take place. The catalyst layers are usually prepared by finely dispersing small catalyst particles (e.g., Pt particles of 4 nm diameter or smaller) with large electrochemical active surface area (ECSA), premixed with ionomer, on the surface of the conductive substrate, typically carbon powders. Assuming equal Pt loading and Pt/C ratios of the CLs, the ECSA and the utilization of Pt play a critical role in reducing the reaction activation barrier and enhancing the fuel cell performance. Since Pt or Pt alloy is still the most popular catalyst for HOR and ORR, the development of CLs is of great importance to reduce fuel cell costs. A gas diffusion layer (GDL) covers each side of the electrode, which is porous to transport both reactant gases and

water, as well as electrically and thermally conductive in through-and in-plane directions. A popular GDL material is carbon fiber-based porous media such as carbon fiber paper or carbon cloth with 5 % to 30 % PTFE loading on the surface to improve the hydrophobic properties and avoid water flooding. Furthermore, the state-of-art GDL is often covered by a microporous layer (MPL) on the surface to enhance the electrical conductivity and enable uniform distribution of the gases on the CLs [44]. The two outmost components in Figure 3 a) are flow fields (also called gas flow channels) which are always integrated into the bipolar plates (BPs). Through the flow fields, the reactant gases are injected and distributed;

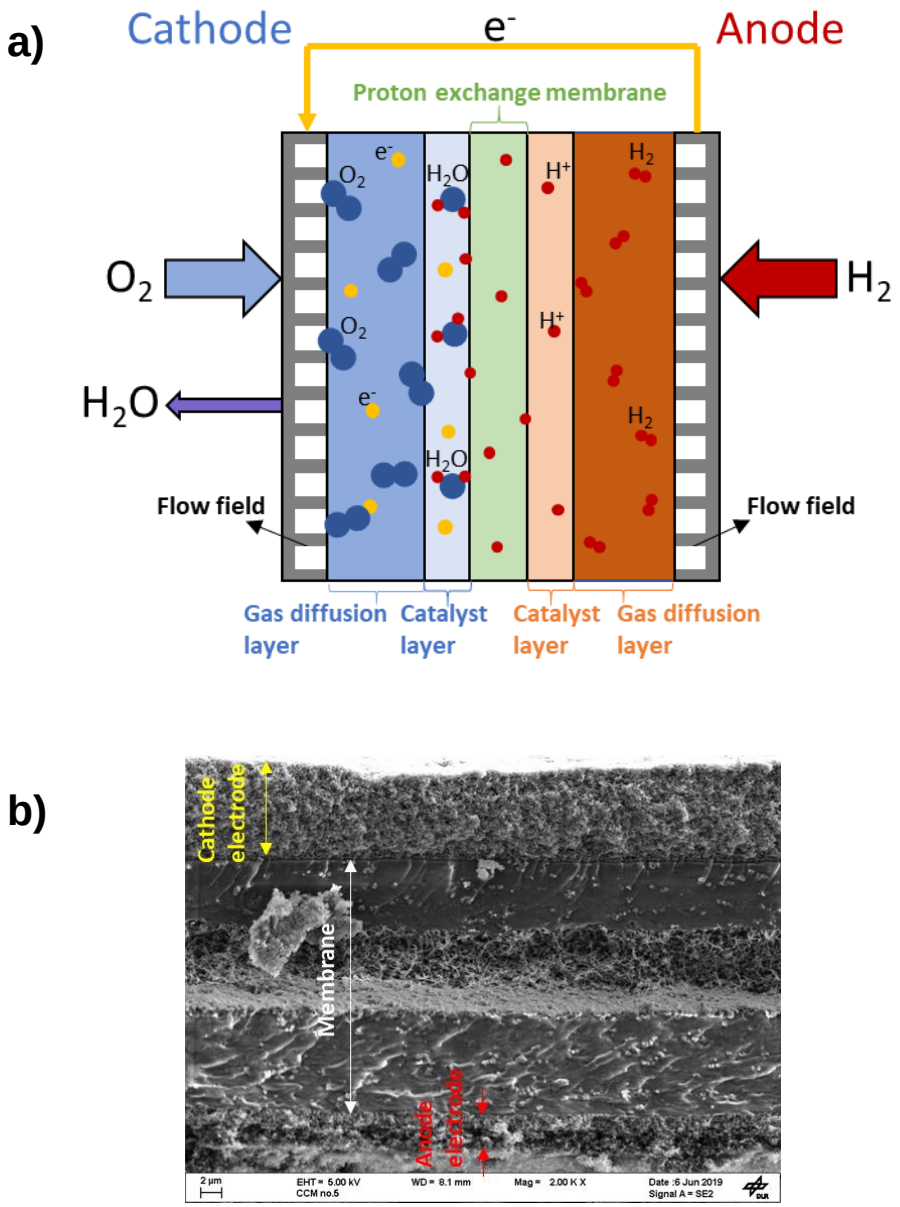

Figure 3: a) Layout of the single PEMFC and the mechanism of the electrochemical reaction. b) Cross-sectional SEM of a CCM. Adapted from Article II.

likewise, the byproduct water is collected and removed. The BPs are generally made of metal or graphite to provide heat and electron conductivity. Several flow field types and designs have been developed, such as parallel, serpentine, and pin-type flow field, with various configurations such as single channel, multiple channels, and cyclic-single channel. The selection of the flow field type influences the water and heat management schemes in the PEMFCs, which is crucial for the fuel cell performance. In a fuel cell system, there are many components to support the function of the PEMFCs, including air and hydrogen supply systems, water and thermal management systems, and so on [45].

Figure 3 a) also shows the process of the electrochemical reaction in a PEMFC. As reactant gases, hydrogen, and air (or oxygen) flow into the cathode and anode flow fields, respectively. Then the gases reach the top of the electrodes through GDLs by diffusion. The protons and electrons are produced at the anode electrode according to Eq. (3.1.1)

$$H_2 \rightarrow 2H^+ + 2e^-. \tag{3.1.1}$$

The electrons are forced to flow through an external circuit from the anode to the cathode, where the current is generated for applications. Meanwhile, the protons are transported through the proton exchange membrane to the three-phase boundary (consisting of the electrolyte, the reactant gas, and the electrocatalyst) in the cathode, where the oxygen is reduced to water according to Eq. (3.1.2)

$$O_2 + 4H^+ + 4e^- \rightarrow 2H_2O. \tag{3.1.2}$$

The total reaction of the PEMFC is shown as Eq. (3.1.3)

$$2H_2 + O_2 \rightarrow 2H_2O. \tag{3.1.3}$$

The only exhaust product is pure water in the cathode which is then expelled out of the cell through the cathode gas outlet.

The theoretical potential of a PEMFC, E, can be calculated by Eq. (3.1.4)

$$E = \frac{-\Delta G}{nF}, \tag{3.1.4}$$

where n = 2 is the number of electrons in the reaction Eq. (3.1.3) and F = 96485 C·mol^{-1} is the Faraday constant. The Gibbs free energy, ΔG, of the above-mentioned reaction is the theoretical amount of electrical energy by a PEMFC, which equals -237 kJ·mol^{-1} under

standard-state conditions for liquid water product [46].

Thus, the theoretical potential of the PEMFC is 1.23 V at 25 °C and standard operating conditions, which is also called as standard thermodynamic potential. As the orange line shows in Figure 4, the theoretical open circuit voltage (OCV) is 1.23 V, while the actual OCV (E_{OCV}) is about 1 V due to i) reactants crossover [47], ii) mixed cathode potential caused by reactions of the catalyst with oxygen [48], and iii) possible impurity oxidation [49]. The theoretical efficiency, η, as well as the maximum efficiency of a fuel cell, when all the Gibbs free energy is converted into electrical energy, can be calculated by the ratio between the Gibbs free energy and hydrogen higher heating value, ΔH = 286 kJ·mol^{-1}, according to Eq. (3.1.5) [50]

$$\eta = \frac{\Delta G}{\Delta H} = \frac{237}{286} = 83\%. \tag{3.1.5}$$

Generally, polarization is the potential difference between the electrode surface potential and the equilibrium value. The performance of a fuel cell device can be described with its voltage-current characteristics, as so-called polarization curves or i-V curves. The black curve in Figure 4 shows the actual polarization curve of a PEMFC over the current density, which shifts away from the OCV because of the three typical and unavoidable voltage losses i) activation losses, $\eta_{Activation}$, ii) ohmic losses, η_{Ohmic}, and iii) mass transport losses, $\eta_{Mass\ transport}$. The fuel cell voltage, U, can be described with the Eq. (3.1.6)

$$U = E_{OCV} - \eta_{Activation} - \eta_{Mass\ transport} - \eta_{Ohmic}, \tag{3.1.6}$$

or with the Eq. (3.1.7)

$$U = E_{OCV} - \eta_{Activation} - \eta_{Mass\ transport} - iR_{Ohmic}, \tag{3.1.7}$$

where i is the current density and the η_{ohmic} is the ohmic resistance of the fuel cell [51].

The activation losses resulting from reaction kinetics, $\eta_{activation}$, dominate the voltage losses in the low current density range of the polarization curve and can be affected by several factors: i) intrinsic electrochemical activity and surface area of the catalyst, ii) contamination in the gas flows, and iii) operation conditions such as flow rates and temperature. The ohmic losses resulting from ionic and electronic transportation, η_{ohmic}, greatly influence the fuel cell voltage at the middle current density range of the polarization curve, which mainly consists of contact resistance between the fuel cell subcomponents and

the proton resistance of the membrane. The mass transport losses, $\eta_{mass\ transport}$, also called concentration losses, inhibit the fuel cell performance at the high current density range of the polarization curve, which are determined by the gas- and liquid-phase transport of the reactants and products [52].

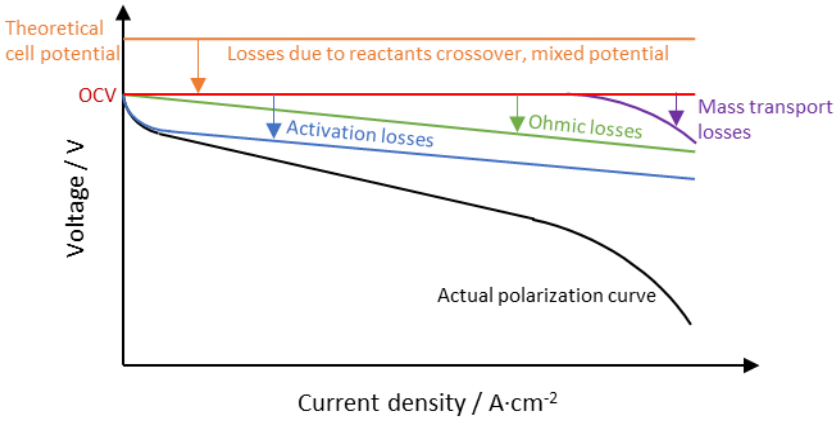

Figure 4: Various voltage losses and the actual polarization curve of a PEMFC.

3.2 Reversible performance degradation of the PEMFCs and the mechanisms

The performance, durability, and reliability of a PEMFC or stack are determined by both internal and external factors. Typical internal factors essentially involve the material selection of the fuel cell components, MEA parameters design, flow field design, assembly of the fuel cell or stack, and the manufacturing process. External factors mainly include operation conditions, contaminants from the gas flow and system, as well as operation strategies.

Generally, the operating conditions in a PEMFC are usually heterogeneous, resulting in a dynamic and heterogeneous response of the PEMFC performance along the flow channels. Especially for automotive applications, the wide range of operating conditions can enhance the diversity and complexity of the performance degradation phenomena. Many researchers reported a voltage degradation rate of a PEMFC stack in the range of 1 – 10 $\mu V \cdot h^{-1}$ with long-term durability tests [53]. Besides, many studies also observed much higher voltage degradation rates due to harsh operating conditions such as start-up/shut-down conditions,

cold start conditions, open-circuit/idling conditions, and dynamic changing load conditions [54, 55].

For the long-term operation of PEMFCs, various degradation mechanisms have been identified and investigated during the past several decades in the literature: i) water flooding in the cathode and anode due to changes in water management [56], ii) reactant crossover due to membrane degradation and thinning [57], iii) catalyst particle agglomeration, dissolution and carbon corrosion in the cathode electrode [58], iv) contamination of the electrodes/catalysts [59], and v) corrosion and mechanical degradation of the GDLs, bipolar plates, flow fields, and gaskets [60, 61]. Part of the performance degradation during the long-term operation is irreversible, which results from various types of mechanical damage to the fuel cell components, such as carbon corrosion of the cathode catalyst layer after frequent start-up/shut-down operation [62]. Meanwhile, part of the performance degradation is reversible (or called as recoverable) and can be recovered by specific procedures, which is sometimes even higher than irreversible performance degradation [63, 64]. Besides, irreversible performance degradation can be accelerated and deteriorate if reversible performance degradation is not timely and effectively removed [28]. Recently, the investigation of reversible performance degradation and the development of effective recovery procedures have gained increasing attention from the community and the first review paper was published by our group [35].

The following Sections 3.2.1 – 3.2.6 outline the mechanisms of commonly mentioned types of reversible performance degradation, as well as the corresponding recovery procedures:

3.2.1 Reversible performance degradation due to Pt oxidation

During their lifetime, the PEMFCs undergo voltage changes typically between 0.65 V and OCV. However, Pt in the cathode catalyst layer oxides at electrode potential above 0.7 V. Therefore, several oxide species, which cover the surface of the catalyst surface i) $Pt\text{-}O$, ii) $Pt\text{-}O_2$, iii) $Pt\text{-}OH$, and iv) $Pt\text{-}OOH$, block the active site of the Pt, and the ORR rate is decreased. With water as an oxygen source, the formation of the Pt oxides follows Eq. (3.2.1) and Eq. (3.2.2) [65]:

$$Pt + H_2O \leftrightarrow Pt\text{-}OH + H^+ + e^-, \tag{3.2.1}$$

$$Pt\text{-}OH \leftrightarrow Pt\text{-}O + H^+ + e^-. \quad (3.2.2)$$

With oxygen in the cathode as an oxygen source, the formation of the Pt oxides follows Eq. (3.2.3). Eq. (3.2.4), and Eq. (3.2.5) [66]:

$$Pt + O_2 \rightarrow Pt\text{-}O_2, \quad (3.2.3)$$

$$Pt\text{-}O_2 + H^+ + e^- \rightarrow Pt\text{-}OOH, \quad (3.2.4)$$

$$Pt\text{-}OOH + Pt \rightarrow Pt\text{-}OH + Pt\text{-}O. \quad (3.2.5)$$

However, the Pt oxides can be reduced to Pt under specific electrode potential. So, the performance degradation caused by Pt oxides on the catalyst surface is mainly reversible. Therefore, the specific amount and composition of the oxidation layer covered on the Pt surface depend on the humidity, temperature, pressure, and electrode potential of the fuel cell. In general, an electrode potential below 0.4 V is required to reduce the Pt oxides in the cathode catalyst layer and achieve full recovery of the reversible performance degradation of the fuel cell [67].

Commonly, three methods for recovery procedures in the literature have been proven to reduce the Pt oxides in the cathode catalyst layer effectively: i) applying a low voltage pulse (0.2 V) or cyclic voltammetry (0 to 0.1 V) to the cell in an H_2/N_2 atmosphere [68], ii) operating the cell at low voltage conditions, such as 0.2 or 0.3 V [69], and iii) stopping the cathode gas flow while purging the anode with H_2 to promote H_2 permeation to the cathode [70]. On the other hand, the efficiency of each recovery procedure, which is defined by the ratio of the Pt oxides in the catalyst layer that can be successfully removed, is influenced by the composition and structure of the Pt oxides and the specific design of the recovery procedure such as the applied voltage load and duration. For example, the Pt oxides are mainly reduced by chemical reactions when the majority of the Pt catalyst surface is covered by Pt oxides. Afterward, Pt oxides are mainly reduced by electrochemical reactions when enough active sites on the catalyst surface are available [67]. Theoretically, the complete reduction of Pt oxide species is supposed to finish in the range of several seconds. However, in the experiments with PEMFCs, it could take from several seconds to hours to achieve a full recovery of performance degradation due to the complexity of Pt oxidation conditions.

3.2.2 Reversible performance degradation due to sulfur compounds

Sulfur compounds are widely recognized as one of the common contaminants during the operation of PEMFCs. The sulfur compounds, including H_2S, SO_2, COS, sulfonate, and sulfate ions, can strongly absorb on the Pt surface in the catalyst layer and block the active Pt surface area for reaction (so-called catalyst poisoning), resulting in decreased ORR kinetics and fuel cell performance degradation. However, the performance degradation caused by sulfur compounds is mostly reversible and several recovery procedures have been discussed in the literature [38, 71].

During the lifetime of PEMFCs, sulfur compounds may come from different sources. Steam methane reforming (SMR) from natural gas and biomass is a common source for hydrogen production, which inevitably introduces several types of contaminants into the hydrogen gas, such as H_2S. In the cathode, the sulfur-containing airborne contaminants, SO_x, H_2S, and COS, are combustion products of fossil fuels due to automotive exhaust and industrial processes. Besides, sulfonate anions can also result from ionomer and membrane degradation, especially when the PEMFCs undergo the long-term operation of idling and OCV conditions.

Respectively, the SO_x, H_2S, and COS adhere firmly to the Pt surface and dissociate under the formation of $Pt\text{-}S$ as the poisoning species either by chemical decomposition as Eq. (3.2.6) [72]

$$Pt + H_2S \rightarrow Pt\text{-}SH_2 \rightarrow Pt\text{-}S + H_2, \tag{3.2.6}$$

by electrochemical oxidation as Eq. (3.2.7) [73]

$$Pt + H_2S \rightarrow Pt\text{-}S + 2H^+ + 2e^-, \tag{3.2.7}$$

by electrochemical reduction as Eq. (3.2.8) and (3.2.9) [74]

$$Pt + SO_2 + 2H^+ + 2e^- \rightarrow Pt\text{-}SO + H_2O, \tag{3.2.8}$$

$$Pt\text{-}SO + 2H^+ + 2e^- \rightarrow Pt\text{-}S + H_2O, \tag{3.2.9}$$

or by chemisorption as Eq. (3.2.10) and Eq. (3.2.11) [75]

$$Pt + COS \rightarrow Pt\text{-}COS, \tag{3.2.10}$$

$$Pt\text{-}COS + Pt \rightarrow Pt\text{-}S + Pt\text{-}CO. \tag{3.2.11}$$

The recovery of performance degradation due to the H_2S, SO_2, and COS contaminants requires both the oxidation of Pt-S to sulfonate and the removal of the sulfate ions out of the catalyst layer. For an efficient Pt-S oxidation, an electrode potential above 0.9 V is necessary [76]. In the literature, a full Pt-S oxidation can be achieved by cyclic voltammetry between 0.1 and 1.1 V with hydrogen purging in the anode and nitrogen in the cathode. Furthermore, instead of potential cycling with a scan rate, the recovery can be accelerated by applying potential pulses on the electrode between 0.2 and 1.5 V [77]. Afterward, the sulfonate and sulfate ions adsorb on the Pt surface due to the coulombic interactions with the electrode. The complete desorption of sulfonate and sulfate ions can be achieved by applying an electrode potential under 0.17 V [37]. Then, under fully humidified conditions or condensation operations like the shut-down, the sulfonate and sulfate ions can be fully flushed out of the PEMFCs.

3.2.3 Reversible performance degradation due to nitrogen oxides

Similar to SO_x, nitrogen oxides, NO_x (mainly NO and NO_2) are common pollutants in the air resulting from the combustion of fossil fuels. The presence of NO_x causes a strong catalyst poisoning effect due to chemical adsorption on the Pt surface, which leads to the blockage of the ORR reaction and the performance degradation of PEMFCs. The NO_x species can be fully oxidized to nitrate ions by either applying an electrode potential above 0.9 V or purging the electrode with neat air in the cathode [78, 79]. Afterward, the resulting water-soluble nitrate ions can be flushed out of the cell by an oversaturated air flow or a condensation operation like shut-down.

3.2.4 Reversible performance degradation due to carbon compounds

Even low concentrations of CO in the hydrogen can greatly influence the fuel cell performance due to the strong adsorption effect of CO on the Pt catalyst surface. In addition, the CO_2 in the air can permeate from the cathode to the anode, especially in PEMFCs with very thin membranes, and result in catalyst poisoning by CO in the anode according to the Eq. (3.2.12) and Eq. (3.2.13) [80]

$$2Pt + H_2 \rightarrow 2Pt\text{-}H_{ads}, \tag{3.2.12}$$

$$2Pt\text{-}H_{ads} + CO_2 \rightarrow H_2O + Pt\text{-}CO_{ads}. \quad (3.2.13)$$

The removal of CO contaminants from the anode electrode can be achieved with the chemical oxidation of CO to CO_2 with a small amount of oxygen in the anode [81]. With air bleeding, which means keeping air purging in the cathode and closing the hydrogen feed and outlet in the anode, the oxygen permeation rate from the cathode to the anode can be accelerated. Thus, the performance degradation due to CO poisoning in the anode can be recovered in the range of several minutes [82]. Besides, applying the anode potential at a high potential (about 0.3 V) can facilitate the CO electrochemical oxidation to CO_2 [83].

3.2.5 Reversible performance degradation due to water management

Appropriate water management plays an important role in the long-term performance of PEMFCs. Water is necessary for the hydration of the membrane and the ORR reaction in the three-phase interface in the cathode. On the one hand, only with enough wettability can the membrane transport protons from the anode to the cathode with low resistance [84]. On the other hand, water is also a reaction product during dynamic operation conditions and needs to be transported and removed properly. Numerous studies have disclosed the water flooding effect, that excess water can accumulate in the porous electrode and the catalyst surface, which then blocks the access for the ORR reactants [85]. Similarly, excess water also tends to occupy the pathway of the gas transportation in the GDL and flow channels, resulting in a reversible performance degradation of PEMFCs. To recover the performance degradation due to water flooding and to remove the excess water from the fuel cells, the following methods are frequently used in the literature i) cathode gas purging with dry air or nitrogen [86], ii) increasing the cathode gas flow [87], and iii) shut-down and restart of the fuel cell [88]. As for recovery procedures against membrane dehydration, it is identified to be effective to increase the gas humidity in the cathode or operate the fuel cell under high current conditions [89]. This can also be accomplished by lowering cell temperature which will increase relative humidity and may even lead to water condensation.

4 Research approaches and methodology

In this section, the research approaches and experimental methodology are displayed. Especially, all the test protocols and recovery procedures used in this work are described.

4.1 Test hardware

The test hardware, consisting of the testbenches, MEAs, and single cells in Articles I - III, and Section 5.1 were the same in order to evaluate and investigate the effect of different recovery procedures. Different hardware was selected on purpose to enable the reliable measurement of oxygen transport resistance in the cathode in Section 5.2. An explanation for the choice of hardware will be given in detail in Section 5.2.

4.1.1 MEA

To evaluate the effect of accelerated stress test (AST) and recovery procedures, all the MEAs used in this work were manufactured by IRD Fuel Cells A/S [90] following the DLR's specifications. Table 2 presents a summary of the specifications of all the MEAs used in this work. Each of the MEAs consists of a 27.5 μm thick Nafion™ XL membrane sandwiched by

Table 2: Specifications of the MEAs used in this work.

MEA specifications	In Articles I - III and Section 5.1	In Section 5.2
Membrane	Nafion™ XL	Nafion™ XL
Pt/C ratio / wt%	50:50	40:60
Anode Pt loading / mg·cm^{-2}	0.05	0.05
Cathode Pt loading / mg·cm^{-2}	0.25	0.1
GDL	SIGRACET® 29 BC, SGL Carbon SE	Toray Carbon Paper 060
Active area / cm^2	5x5	3x4

an anode and a cathode catalyst layer. More information about the stability and durability of the perfluorosulfonic acid (PFSA) membrane with mechanical reinforcement and chemical stabilizers can be found in the literature [91].

The catalyst layers of the anode and cathode of the MEAs used in Articles I - III and Section 5.1 contain a Pt/C ratio of 50 wt % with a Pt loading of 0.05 and 0.25 mg·cm^{-2}, respectively. The active area is 5 × 5 cm^2 which is consistent with the configuration of the flow field of the house-developed single cell, as shown in Figure 5 1 a). Each side of the catalyst layer is covered with a gas diffusion layer of SIGRACET® 29 BC from SGL Carbon SE. An image of the cross-sectional SEM of a catalyst coated layer (CCM) used in Article III was presented in Figure 2 b).

The catalyst layers of the anode and cathode of the MEAs used in Section 5.2 contain a Pt/C ratio of 40 wt % with a Pt loading of 0.05 and 0.1 mg·cm^{-2}, respectively. The active area of the CCM is 3 × 4 cm^2 to fit the Baltic qCf 12 High Amp single cell [92], see Figure 5 b). The untreated Toray Carbon Paper 060 is used as the diffusion media on top of each side of the MEA. The Baltic qCf 12 High Amp single cell and Toray Carbon Paper 060 enable the reliable measurement of oxygen transport resistance in the cathode in Section 5.2. Further explanation about the choice of the test material and hardware will be provided in Section 5.2.

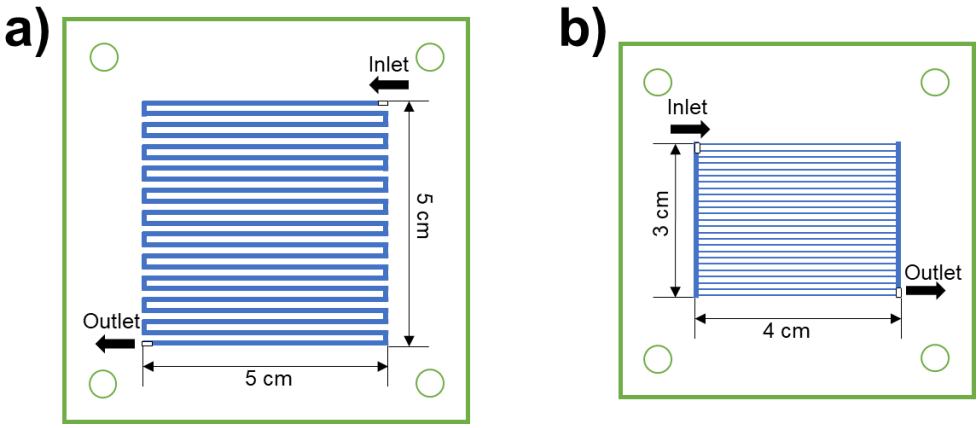

Figure 5: The schemes of the single cells used in a) Articles I - III and Section 5.1, and b) in Section 5.2.

4.1.2 Single cells

In Articles I - III and Section 5.1 the single cell was designed and developed by DLR in-house with the active area of 5 × 5 cm^2 and one-channel-serpentine flow fields as shown in Figure

5 a). The plane of the flow field was oriented parallel to the direction of gravity and arranged in co-flow configuration. The gas channels were oriented parallel to gravity direction while gas inlets and outlets were at the top and bottom of the cell. Ice Cube Sealing from Freundenberg FST GmbH [93] with 350 µm of thickness was used for both sides of the flow fields.

In Section 5.2, the commercial Baltic qCf 12 High Amp single cell was used with straight channels and an active area of 3 × 4 cm^2 as shown in Figure 5 b). The cell plates were arranged parallel to the gravity direction and the flow channels were vertical to the gravity direction. The flow configuration was counter-flow. The anode inlet and the cathode outlet were at the top of the cell. The cell was designed for high current density operation and homogeneous temperature distribution over the flow field. Figure 6 shows the assembly of the Baltic qCf 12 High Amp single cell in detail. Polyethylene naphthalate (PEN) films with a thickness of 25 µm were used as sub-gaskets for both sides of the MEA. There are four positioning holes at the edge of each PEN-film to fit with the adjustment pins. Polyetheretherketon (PEEK) films were inserted between the flow fields and PEN-films to fill the gap. Besides, two sealing rings were placed around the flow fields.

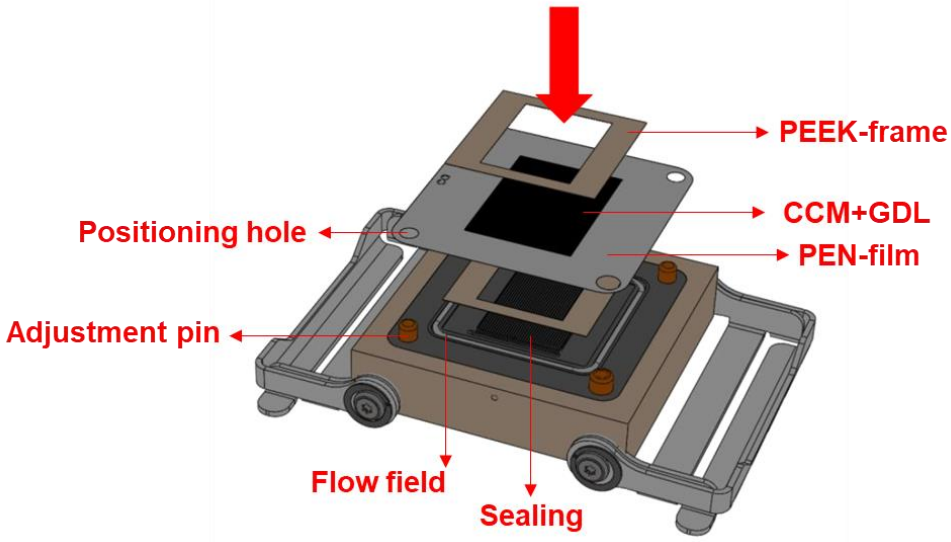

Figure 6: Assembly of the Baltic qCf 12 High Amp single cell.

4.1.3 Testbenches

Two testbenches developed in-house by DLR were used in this dissertation, including the control software. The flow diagrams of the two testbenches are shown in Figure 7. With both testbenches, a variety of operating parameters can be adjusted and recorded manually or automatically by scripts through programmable logic controllers (PLCs), such as cell temperature, anode, and cathode gas flow, humidity of the reactants, as well as outlet pressures. The testbench used for Articles I - III, and Section 5.1 was equipped with a commercial electronic load with a maximum current of 60 A. The reactants in the anode and cathode were humidified by external water-filled humidifiers (bubblers). In Section 5.2, the testbench contained an electronic load with a maximum current of 160 A to adapt to the high current density operation of the Baltic qCf 12 High Amp single cell. The hydrogen and air were humidified by two steam vaporizers, which enabled a faster control of the gas humidity than that with bubblers. Besides, in both the anode and cathode sides, there were two flow controllers with different ranges of gas flow. In the cathode side, one gas flow controller was connected to the nitrogen gas feed. Thus, the testbench in Section 5.2 enabled the adjustment of the oxygen concentration in the cathode by mixing the nitrogen and the air, which is essential for the limiting current measurement.

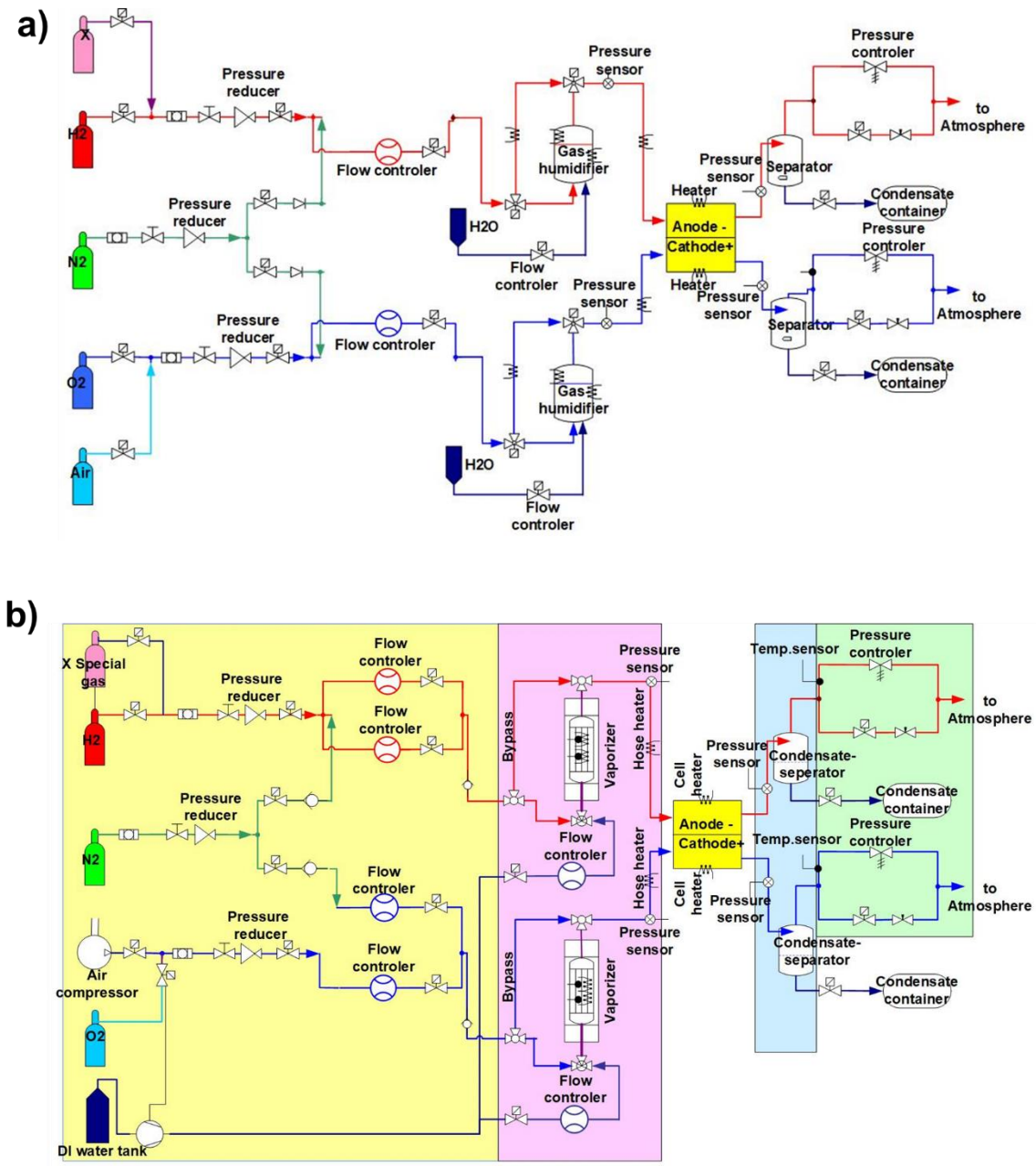

Figure 7: The flow diagrams of the testbenches used in a) Articles I - III and Section 5.1, b) in Section 5.2.

4.2 Test protocols

In this dissertation, 5 different durability tests were performed to evaluate and investigate the mechanisms and the efficiencies of the performance degradation recovery procedures for PEMFCs.

The first durability test was performed to i) establish the methodology to evaluate the recovery effect of different recovery procedures, as described in Article I, and ii) compare the efficiency of three available recovery procedures and understand their recovery mechanisms, as described in Article II.

Article III aims to investigate the recovery mechanism and efficiency of the cell cooling down, including two durability tests with operando and non-operando recovery procedures of temperature reduction, respectively.

Section 5.1 comprised one durability test interrupted with original and modified DOE recovery protocols. Thereby, the recovery efficiency of the DOE recovery protocol after specific optimization was quantitatively analyzed, which was proposed according to the recovery mechanism discussed in Articles II and III.

To further understand the recovery mechanism in Article III, a durability test is performed in Section 5.2 with the focus on the oxygen transfer resistance change in the cathode catalyst layer due to the recovery procedure of temperature reduction.

The Fuel Cell Dynamic Load Cycle (FC-DLC) protocol [12] was performed in all the above-mentioned durability tests as an AST to simulate fuel cell operation for automotive applications. As shown in Figure 8, the maximum current density of the FC-DLC is defined as

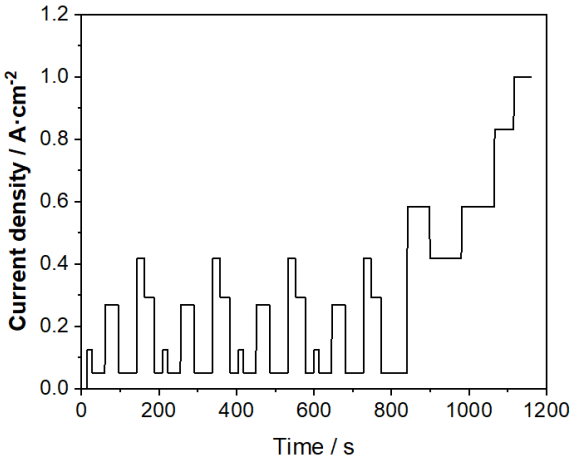

Figure 8: Fuel cell dynamic load cycle (FC-DLC) used in this dissertation.

the current density yielding 0.65 V, which is 1 A·cm^{-2}. The operation parameters during the FC-DLCs are listed in Table 3. To measure the oxygen transport resistance in the cathode of the fuel cell, the material and single cell hardware in Section 5.2 was different from those in the other durability tests. Thus, the operation parameters set in the durability test in Section 5.2 were different from those in Articles I - III, and Section 5.1.

At the very beginning of each experiment, the fresh MEA was conditioned according to the conditioning steps from EU Harmonized Test Protocols [12] to reach a stable performance. The flow rates of hydrogen and air were adjusted corresponding to the current density of 2 A·cm^{-2}. Other operating parameters during the MEA conditioning process follow the values in Table 3, including the cell temperature, gas humidity, hydrogen and air stoichiometry, and outlet pressures. The conditioning procedure consisted of voltage cycling between 2 min hold at 0.8 V and 4 min at 0.4 V. The fuel cell performance was considered stable when the current density variation at 0.4 V was lower than +/- 0.04 A·cm^{-2}.

Table 3: Operating parameters of the fuel cell during the FC-DLCs in durability tests of the Articles I - III, Section 5.1 and Section 5.2.

Operating parameters	**In Articles I - III and Section 5.1**	**In Section 5.2**
Cell temperature / °C	80	80
Anode humidity / %	100	0
Cathode humidity / %	100	100
Hydrogen flow rate / L·min^{-1}	0.263	2
Air flow rate / L·min^{-1}	0.83	5.98
Hydrogen stoichiometry	1.5	8
Air stoichiometry	2	10
Anode outlet absolute pressure / kPa	250	105
Cathode outlet absolute pressure / kPa	230	105

Afterward, several test blocks were performed and repeated in each of the durability tests. In Figure 9, the different test blocks used in the five durability tests are presented, respectively. As Figure 9 a) shows, each test block in Articles I and II consisted of i) fuel cell characterization, ii) accelerated stress test, iii) fuel cell characterization, and iv) recovery procedure. In Article I, a methodology was proposed for the evaluation and comparison of the efficiency of different recovery procedures, while the Article II compared three recovery procedures (two protocols adapted by JRC and DOE, and a simple recovery procedure with overnight shut-down). The JRC recovery protocol was proved to provide higher recovery effectiveness than DOE and overnight shut-down, especially at the current density range from 0 to 1.5 $A \cdot cm^{-2}$, which was then used as a reference recovery procedure in Article III, sections 5.1 and 5.2.

As shown in Figure 9 c), the durability tests in Article III and Section 5.1 followed the process in Figure 9 a) with an additional fuel cell characterization step and the JRC recovery protocol at the end of each test block. In Article III, one durability test was performed for the study of operando recovery procedures, which followed the process in Figure 9 b) including the steps i) fuel cell characterization, ii) accelerated stress test, iii) recovery procedure, iv) short period of FC-DLCs, and v) JRC recovery protocol. The durability test in Section 5.2 followed the process in Figure 9 d), which is the same as Figure 9 c) with additional 10 FC-DLCs before the JRC recovery protocol.

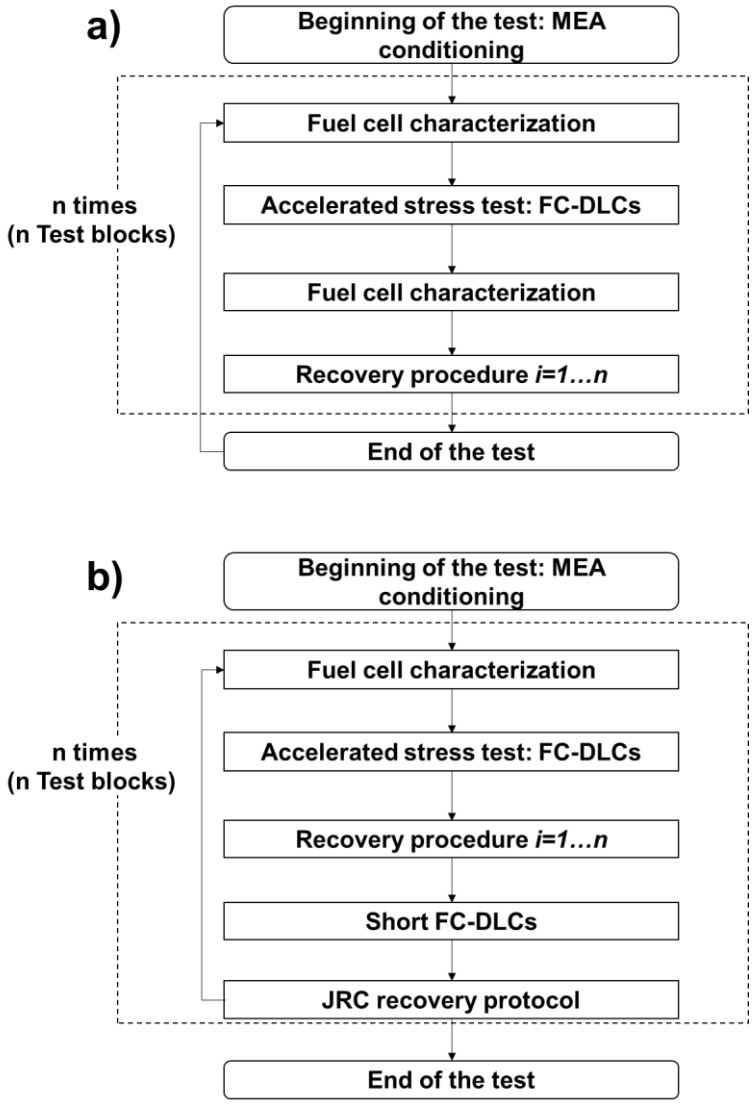
a)
Beginning of the test: MEA conditioning
Fuel cell characterization
Accelerated stress test: FC-DLCs
Fuel cell characterization
Recovery procedure i=1…n
End of the test
n times
(n Test blocks)
b)
Beginning of the test: MEA conditioning
Fuel cell characterization
Accelerated stress test: FC-DLCs
Recovery procedure i=1…n
Short FC-DLCs
JRC recovery protocol
End of the test
n times
(n Test blocks)

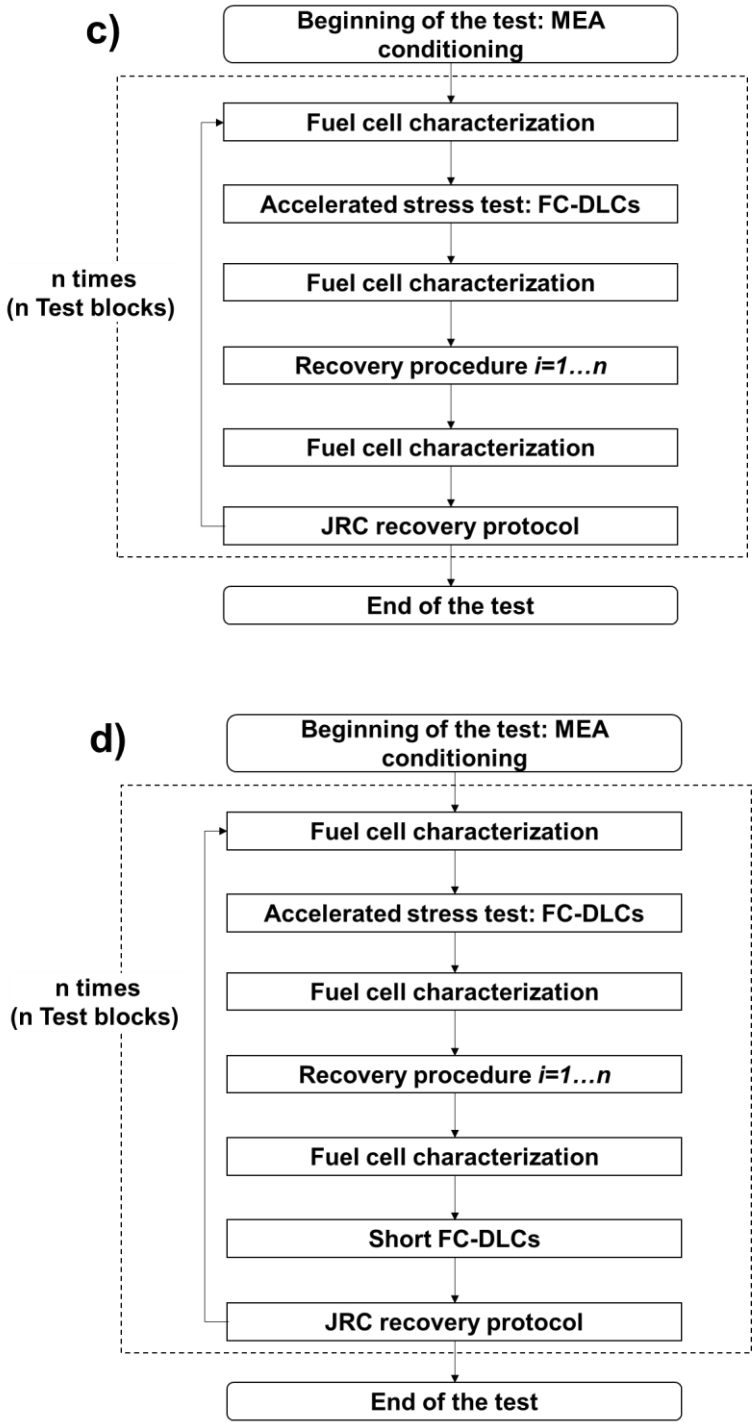

Figure 9: The processes of the durability tests for the study of recovery procedures used in a) Articles I and II, b) Article III, c) Article III and Section 5.1, and d) Section 5.2.

4.3 Characterization methods

4.3.1 Polarization curves measurement

In this dissertation, polarization curves were measured with an electronic load in galvanostatic mode to evaluate the fuel cell performance in terms of cell voltage against

current density. The operation parameters, such as cell temperature, stoichiometry, the humidity of reactants, and gas pressures of the anode and cathode during the polarization curves measurement were the same as during the load cycling as shown in Table 3. The dwell time of each set point and stabilization criteria for the data acquisition time followed the recommendation by the EU Harmonized Test Protocols for MEA Testing [12]. The error bar corresponded to the standard deviation from the average of the last 30 s of the dwell time of each tested current density. Figure S1 in the supporting information shows typical logged data during the polarization curves measurement.

4.3.2 Data analysis with FC-DLC data

This work also calculated fuel cell performance based on the online recorded data of FC-DLCs to collect the operando information in a durability test. The FC-DLC protocol covered nine current densities from 0 to 1 $A \cdot cm^{-2}$. At each current density, the average voltage of the first or last three FC-DLCs of the AST step and its standard deviation were calculated as Figure S2 in the supporting information. The efficiency of the recovery procedure was also evaluated with the cell voltage changes upon the nine current density values based on the FC-DLC data. In Article I, the data calculated with polarization curves and online FC-DLC data were compared in detail and showed little difference from each other. The advantages and disadvantages of the data analysis with FC-DLC data were also discussed in Article I.

4.3.3 Electrochemical impedance spectroscopy (EIS) measurement

EIS has proven to be a powerful analytical diagnostic tool for the analysis of electrochemical systems. The application of EIS in PEMFCs allows the modeling of the fuel cell system with a selected equivalent circuit and, consequently, to identify individual contributions to the total impedance [94]. A common setup of EIS measurement consists of a frequency response analyzer (FRA) and a potentiostat or a load bank. The FRA has two terminals for current or voltage generation and two terminals for accepting voltage or current responses [51]. Two modes (controlling the current or the voltage perturbation to the measured fuel cell) are available to obtain the impedance spectra. The frequency range of the interrupted sine wave of sweeping can be adjusted before the measurement. The impedance spectrum can be presented in Nyquist, Bode, impedance-frequency plots and so on.

In this work, the EIS measurement was carried out in the galvanostatic mode applying a small current perturbation (5 %) to the fuel cell and recording the potential response. The operation parameters during the EIS measurements followed those listed in Table 3 according to the specific measured current. The modular electrochemical workstation Zennium X and electronic load PP241 from ZAHNER-Elektrik GmbH & CoKG were used, which enabled a test frequency range from 100 mHz to 10 kHz with a excitation amplitude of +/- 5% of the applied current. The Thales XT software package, including Zahner Analysis software, enabled data acquisition and evaluation.

(i) Evaluation of EIS data recorded in hydrogen/air atmosphere

EIS data are commonly fitted to an equivalent electric circuit model for a deeper analysis. An equivalent electric circuit can be comprised of resistances, inductances, capacitances, and some electrochemical elements such as constant phase elements. The equivalent electric circuit produces the same responses as the measured fuel cell when applying the perturbation signal. Each circuit component comes from a physical process in the fuel cell and matches largely the impedance behavior of the fuel cell component.

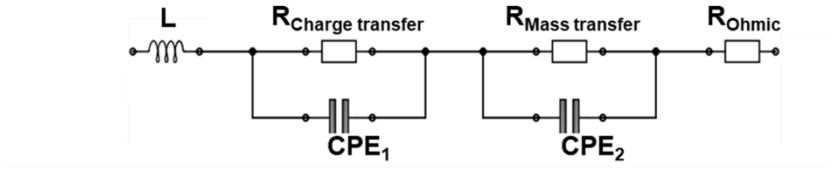

Figure 10: Equivalent circuit model used to fit EIS data in this work.

The equivalent circuit, as shown in Figure 10, was selected to evaluate the EIS measurements, which consists of four components in series: i) a resistor R_{Ohmic} which describes the ohmic resistance, ii) the charge transfer circuit consisting of $R_{Charge\ transfer}$ in parallel with CPE_1 (constant phase element) representing the charge transfer resistance of the cathode catalyst layer, iii) the mass transfer resistance circuit consisting of $R_{Mass\ transfer}$ in parallel with a constant phase element CPE_2 and iv) an inductance element L. The model was selected due to its simplicity and capability to determine the main mechanism necessary to assess the recovery procedures. A deeper discussion about this model can be found in Articles I and II.

(ii) Evaluation of EIS data recorded in hydrogen/nitrogen atmosphere

Impedance measurement under a hydrogen/nitrogen (anode/cathode) atmosphere has

been widely used to extract the ionic resistance of an electrode. Figure 11 a) presents the finite transmission-line equivalent circuit describing the impedance behavior of a porous electrode, including the electron ($R_{Electronic}$) and ionic transport (R_{Ionic}) resistance and the electrolyte resistance of the electrode [51, 95]. Based on this model, the ionic impedance can be extracted because i) the electron transport resistance ($R_{Electronic}$) is negligible due to the much higher conductivity of carbon particles compared to ionic transport resistance (R_{Ionic}), ii) the electrolyte resistance can be subtracted from the intercept of the plot along the real axis [95]. Figure 11 b) is an example of the result of the ionic impedance measurement. At the high-frequency range of the Nyquist plot, a Warbung-like response is observed. After the subtraction of the ohmic resistance (R_{Ohmic}) of the fuel cell, the high-frequency intercept with the real axis corresponds to $R_{Ionic}/3$ [95, 96].

In Section 5.2, for characterizing the ionic impedance (R_{Ionic}) of the cathode catalyst layer, potentiostatic EIS was measured with the above-mentioned EIS device and software. The hydrogen and nitrogen were fed in anode and cathode, respectively, with a flow rate of 0.5 L·min^{-1}, while other operation parameters were constant with those in Table 3. Ionic impedance was recorded at a potential of 0.45 V vs. anode with 10 mV perturbation through the frequency from 0.5 to 100 kHz.

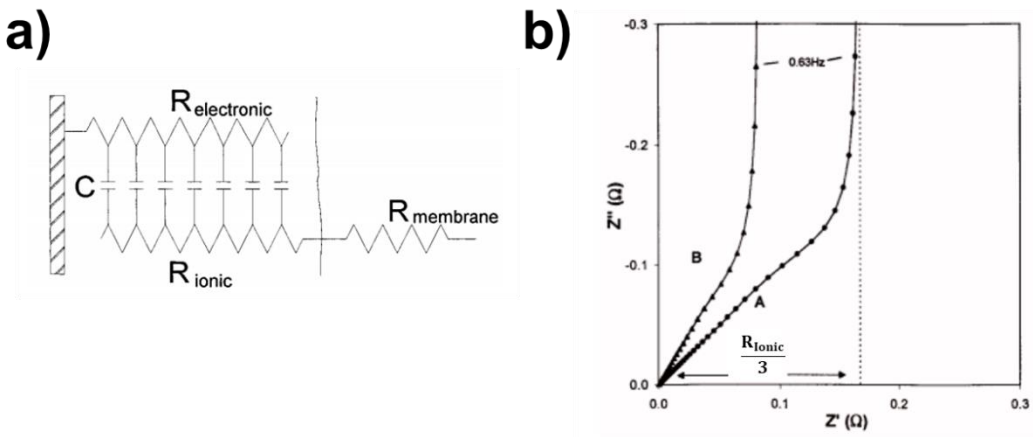

Figure 11: a) Finite transmission-line equivalent circuit describing the impedance behavior of a PEMFC electrode. b) A scheme of the Nyquist impedance plot to evaluate the ionic resistance. Both figures are adapted from [95] with permission to republish.

4.3.4 Limiting current measurement

As the literature reported, using limiting current measurements, oxygen transfer resistance in the cathode can be calculated and different contributions of components can be further distinguished [97, 98]. Figure 12 a) shows an example of the measured limiting current with diluted air under different total pressures in the cathode. The cell current keeps constant at the cell voltage lower than 0.2 V, indicating that all the oxygen is consumed and the oxygen concentration at the outlet is zero. The total oxygen transfer resistance in the cathode is defined as the oxygen concentration difference between the cathode inlet and outlet, divided by the average normal molar flux of oxygen [98]. The molar flux of oxygen can be calculated by the current density and Faraday constant, F. To minimize the deviation, in Section 5.2, a commercial Baltic qCf 12 High Amp single cell was utilized to satisfy the main assumptions of the limiting current technique such as i) straight reactant channels, ii) isothermal and isobaric operation, iii) constant cell voltage along the cell length [99]. Besides, high gas stoichiometry and small active area ensure that no large pressure gradients across the cell were created. Figure 12 b) is a scheme to show the methodology of the calculation of the total oxygen transfer resistance in the cathode (R_{Total}) [97]. b is the slope of the measured limiting current density versus the oxygen partial pressure. The total oxygen transfer resistance in the cathode (R_{Total}) at different total cathode outlet pressure can be calculated using Eq. 4.3.1

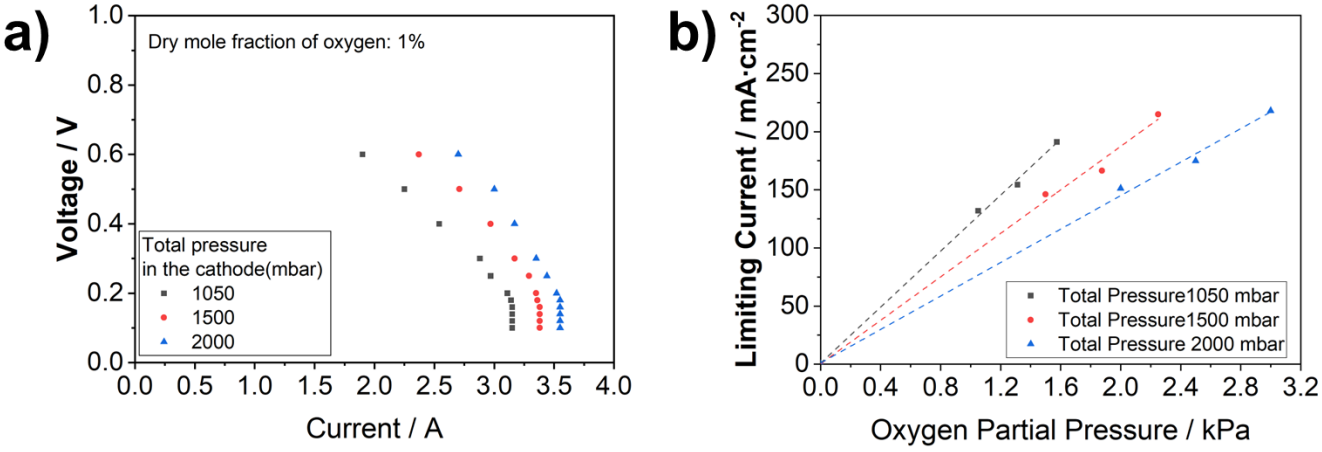

Figure 12: a) An example of the limiting current of a fuel cell with dry mole fraction of oxygen of 1 %. b) A scheme to show the measured limiting current density versus oxygen partial pressure under different cathode total pressure. Both figures are adapted from Section 5.2.

$$R_{Total} = \frac{4F}{bRT} \tag{4.3.1}$$

with the ideal gas constant R = 8.3143 J·mol^{-1}·K^{-1}, T being the thermodynamic temperature of the cell, and the Faraday constant F = 96485 C·mol^{-1} [100].

In Section 5.2, the anode was fed with the hydrogen of 2 L·min^{-1}, while the cathode was fed with a mixture of air and nitrogen of 6 L·min^{-1}. The cathode oxygen concentrations were 1 %, 1.25 %, and 1.5 %. At each oxygen concentration, the limiting current was quantified when the cell current was kept constant by decreasing the applied voltage from 0.4 V to 0.1 V. The limiting current was recorded at total pressure in the cathode of 110, 140, and 170 kPa, respectively.

4.3.5 Scanning electron microscopy (SEM)

With a focused beam of electrons, scanning electron microscopy (SEM) produces surface images providing information about the surface topography and composition. In this work, scanning electron microscopy was utilized to analyze the material structure of the cross-sectional images of the MEA samples. A piece of 1 × 1 cm^2 sample was cut off from the examined MEA and fully immersed into liquid nitrogen for 10 s. Then the MEA was taken out of the liquid nitrogen and held with two tweezers from the left and right sides. Applying slight pressure on the two sides of the MEA with tweezers, the MEA was broken into two pieces from the middle due to cryo-fracture. The GDLs on both sides were carefully peeled off and the broken cross-section of the CCM was fixed upwards to the sample holder and analyzed using ZEISS Ultra Plus SEM equipment. To get high-resolution images with clear morphology information, the operating conditions of the SEM were adjusted and optimized, such as the positions of the CCM and detector. In this work, an electron beam of 5.0 kV was used, and the magnification of the images was 2000x. An example of the cross-sectional SEM image is given in Figure 3 b).

4.4 Recovery procedures

In this work, several recovery procedures were conducted in the durability tests mentioned in Section 4.2, and their efficiencies and mechanisms were investigated.

In Articles I and II, JRC-based recovery protocol, DOE-based recovery protocol, and overnight rest procedure were performed, investigated, and compared. It is concluded that the JRC recovery protocol provides high recovery effect in the entire studied current density range (0 to 1.9 $A \cdot cm^{-2}$), while the DOE recovery protocol shows only high recovery effect in the high current density range (above 1.5 $A \cdot cm^{-2}$). Thus, the JRC recovery protocol was taken as a reference during the durability tests in Article III, Section 5.1, and Section 5.2 to evaluate other recovery procedures. Based on the findings about the recovery mechanism in Articles I and II, Section 5.1 proposed recommendations to modify the DOE recovery protocol to improve the recovery efficiency. Besides, from Article II, it was concluded that with temperature reduction, which is also included in the JRC recovery protocol, part of the performance degradation of fuel cells can be recovered without interrupting fuel cell operation. Thus, in Article III, operando and non-operando recovery procedures with temperature reduction were studied to figure out the specific recovery mechanism. Section 5.2 provides the investigation of the recovery effect of temperature reduction in relation to the oxygen transfer resistance in the cathode.

4.4.1 JRC-based recovery protocol

As shown in Table 4, the JRC-based recovery protocol consists of 5 steps and has a total duration of 10 h 25 min including a restart procedure. When the load is switched off, the air flow and cathode outlet are closed. The hydrogen flow on the anode side is maintained until the cell voltage drops below 0.1 V due to hydrogen cross over to the cathode side which leads to a drop of cathode potential aiming on the reduction of Pt oxide, which took about 25 min. Then both the anode and cathode were purged by dry nitrogen for 30 min, followed by dry air purging for another 30min. Afterward, the gas supply of both the anode and cathode is switched off while the cell gas outlet valves are kept closed. For the subsequent 8 h, the cell heating is shut down, and the cell cools down to the environment temperature. By the restart of the cell, the anode and cathode are purged by humidified nitrogen for 30 min while the cell is heated to 80 °C. Subsequently, hydrogen/air operation is started applying nominal conditions.

Table 4: Details of the JRC-based recovery protocol referred in this work.

	Step	Cathode	Anode	Duration
1	H_2 soak	Shut off	1.5 L·min^{-1} H_2 until U < 0.1V	25 min
2	N_2 purge	1.5 L·min^{-1} dry N_2		30 min
3	Air purge	1.5 L·min^{-1} dry air		30 min
4	Shut-down	Stop gas supply; Stop heating the cell; Release pressure; Keep cell outlets closed		8 h
5	Restart	1.5 L·min^{-1} dry N_2; start heating the cell		30 min

4.4.2 DOE-based recovery protocol

The four-step procedure of the DOE-based recovery protocol, which takes 29 min, is listed in Table 5. The four steps are 1) purging the anode and cathode with dry nitrogen for 2 min, 2) purging the cathode with air while the hydrogen feed in the anode is shut off, 3) purging the anode and cathode with dry nitrogen for 2 min again, and 4) purging the anode with hydrogen while the air flow in the cathode is shut off.

Table 5: Details of the DOE-based recovery protocol referred in Articles I and II, and Section 5.1.

	Step	Cathode	Anode	Duration
1	N_2 purge	4 L·min^{-1} dry N_2	2 L·min^{-1} dry N_2	2 min
2	Air soak	Air 4 L·min^{-1}	Shut off	15 min
3	N_2 purge	4 L·min^{-1} dry N_2	2 L·min^{-1} dry N_2	2 min
4	H_2 soak	Shut off	2 L·min^{-1} H_2	10 min

4.4.3 Overnight rest recovery procedure

The steps of the overnight rest recovery procedure are listed in Table 6. After the disconnection of the load, the gas supply and heating of the fuel cell are shut down letting the cell cool down to ambient temperature. The outlet pressure of the cathode and anode is set to ambient pressure and the cell's anode and cathode outlets are kept closed. This process takes around 8 h.

Table 6: Details of the overnight recovery protocol referred in Articles I and II.

	Step	Cathode and anode	Duration
1	Shut-down	Stop gas supply; Stop heating the cell; Release pressure; Keep cell outlet closed	8 h
2	Restart	1.5 L·min^{-1} dry N_2; start heating the cell	0.5 h

4.4.4 Operando recovery procedures using temperature reduction

During the application of operando recovery procedures, the operation of the fuel cell is not affected. For example, the AST operation continues upon the operando recovery procedures using temperature reduction in Article III. Only the heating of the fuel cell is switched off, while other operation parameters are unchanged. The cell cools down automatically once the heating is disconnected. On the other hand, the process of cell cooling down can be accelerated by an extra fan. After the cell temperature drops to the targeted value, the cell is reheated to 80 °C as the nominal operation temperature.

4.4.5 Non-operando recovery procedures with temperature reduction

Unlike the above-mentioned operando recovery procedure, upon the application of non-operando recovery procedure with temperature reduction, the load is disconnected from the fuel cell. Then the heating of the cell is switched off until the targeted cell temperature is reached. During the cooling down, other operation parameters such as gas flow and pressure are kept constant. In other words, OCV is applied to the cell during the non-operando recovery procedure with temperature reduction. Similar to the operando recovery procedure, the duration of the cell cooling-down can be shortened by an extra fan. The cell is reheated to the nominal operation temperature once the cell temperature drops to the targeted value.

4.4.6 Modified DOE recovery protocol

As shown in Table 7, based on the DOE recovery protocol two steps are modified as mentioned above. Step 2 is replaced by a cooling down step, which means the cell is cooled down to 45 °C and then reheated to 80 °C. Step 2 takes about 30 min in this work. Besides, the duration of step 4 is not limited to 10 min, but it lasts until the cell voltage drops below 0.1 V plus an additional 10 min; this takes about 35 min in total. Overall, the modified DOE recovery protocol takes around 70 min, while the duration of the original DOE recovery protocol was around 30 min.

Table 7: Details of the modified DOE recovery protocol referred in Section 5.1.

	Step	Cathode	Anode	Duration
1	N_2 purge	4 L·min^{-1} dry N_2	2 L·min^{-1} dry N_2	2 min
2	Cool down	Shut off, cell cooling down to 45 °C and reheat		30 min
3	N_2 purge	4 L·min^{-1} dry N_2	2 L·min^{-1} dry N_2	2 min
4	H_2 soak	Shut off	2 L·min^{-1} H_2	Till the voltage < 0.1 V, wait for 10 min (About 35 min)

5 Discussion - Increasing recovery efficiency and understanding mass transport issues

This section provides two additional studies, which build on the observations and results in Articles I - III. Based on the DOE recovery protocol, Section 5.1 proposes adaptations in order to increase the recovery efficiency by reducing the charge transfer resistance of the fuel cell. Section 5.2 provides in-depth analyses of the role of oxygen transfer resistance in the cathode catalyst layer in the recovery procedures investigated in Article III.

5.1 Tailoring of specific recovery mechanisms to improve the efficiency of the DOE recovery protocol

In Article II, the DOE recovery protocol was identified to have a lower recovery efficiency at low and middle current density range (< 1.5 $A \cdot cm^{-2}$) compared to the JRC recovery protocol and overnight rest due to the limited impact of charge transfer resistance. Hence, two steps of the original DOE recovery protocol are modified in this section to improve the recovery efficiency.

5.1.1 Description of the experiment

The steps of the original and the proposed modified DOE recovery protocols are displayed in Section 4.4 in Table 5 and Table 7, respectively. The proposed modifications based on the findings from Articles II and III are:

(i) It is concluded that the air soak step of the DOE recovery protocol, which is supposed to reduce CO poisoning on the anode side, is not necessary if hydrogen with 5N purity is used. Therefore, this step was removed, which has the benefit of shortening the duration of the recovery procedure.

(ii) According to Article III, the presence of liquid water in the cathode catalyst layer positively affects performance recovery. A cell cooling-down step, i.e., reducing the cell temperature from the nominal operation temperature of 80 °C to 45 °C and reheating to 80 °C, is recommended as an efficient recovery procedure. The performance losses can be recovered by reducing the charge and mass transfer

resistance of the fuel cell due to the regeneration/redistribution of the ionomer structure in the cathode. This step missing in the original DOE recovery protocol, is added in the modified version. Its duration is 30 min.

(iii) The duration of the hydrogen soak step in the original DOE takes 10 min. According to Article II, this duration was insufficient to reduce the cathode potential to a targeted value < 0.1 V in order to eliminate the Pt oxides in the catalyst surface. Thus, the fixed duration of 10 min is replaced by flexible time, which is needed until the cell voltage drops below 0.1 V plus an additional 10 min hold. This modification is adapted from the JRC recovery protocol and aims to ensure the thorough removal of Pt oxides on the surface of the cathode catalyst. For the experimental setup used in this work, this step takes about 35 min.

To compare and investigate the efficiency of the original and modified DOE recovery protocols, a durability test consisting of five operation periods using the FC-DLC protocol was performed. The operation parameters of the durability test are provided in Section 4.2 and Table 3. Four test blocks interrupted by recovery protocols were performed following the scheme in Figure 9 c). Before and after each recovery, the fuel cell performance was characterized by a polarization curves measurement and EIS. The JRC recovery protocol at the end of each test block was taken as a reference.

5.1.2 Results and discussion

Figure 13 shows the cell voltages at different current density levels recorded during the durability test with FC-DLC protocol (see Figure 8) interrupted by different recovery procedures. The original DOE recovery protocol was applied as Recovery 1 and 3 in the first and third test blocks, while the modified DOE recovery protocol was used as Recovery 2 and 4 in the second and fourth test blocks. The vertical red dashed lines label the starting point of the applied recovery procedures, while the black dashed lines label the JRC recovery protocol. Within each test block, the cell voltage decreases during operation and increases after recovery. Figure 14 shows the polarization curves measured at the current density range of 0 to 1.7 A·cm^{-2} at the beginning of each test block, before and after each recovery protocol. The data from the polarization curves are used to evaluate the efficiency of the original and modified DOE recovery protocols.

Figure 15 a) shows a simple scheme used to evaluate the recovery efficiency of a recovery procedure, including different definitions. $U_{i=n}^{Begin}$ and $U_{i=n}^{End}$ are the fuel cell voltages at the beginning and end of the n^{th} AST operation with FC-DLCs. The following investigated recovery procedure then recovers the fuel cell performance, and the cell voltage is $U'^{End}_{i=n}$. This methodology was defined in detail in Article I and utilized in Articles II, III, and Section 5 to quantify and compare the efficiency of different recovery procedures. The most important definitions are the absolute recovered voltage loss, $\Delta U_{i=n}^{rec}$, which is defined as the

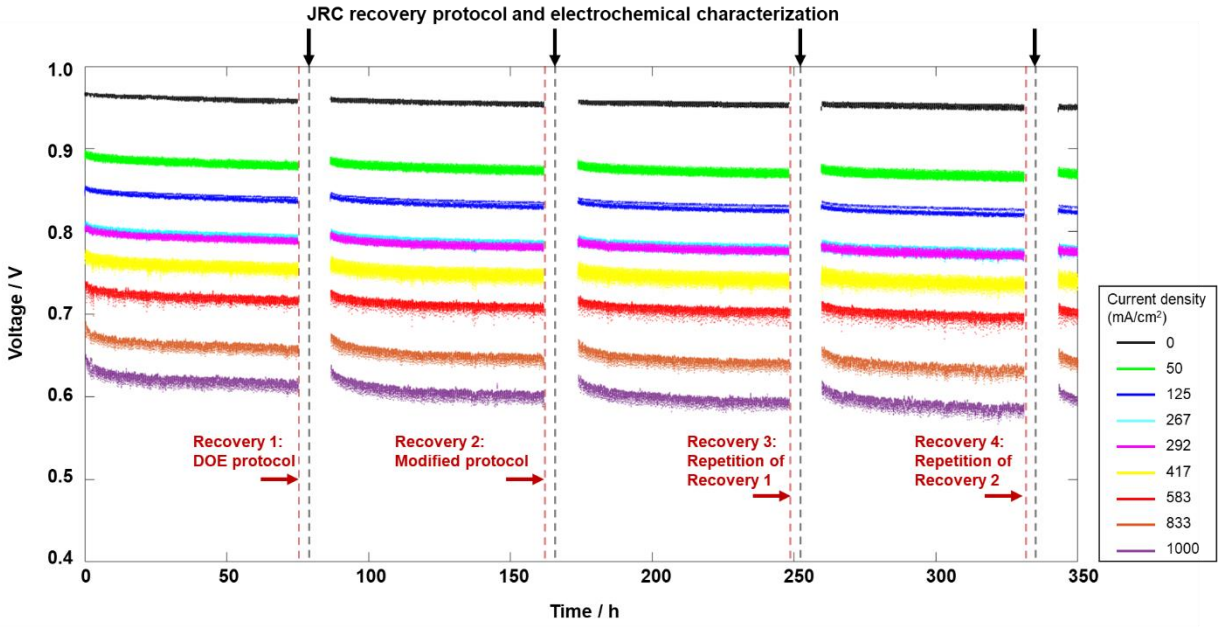

Figure 13: Cell voltage recorded during the durability test for the investigation of original DOE and modified recovery protocols.

voltage difference before and after the n^{th} applied recovery procedure according to Eq. (5.1.1),

$$\Delta U_{i=n}^{rec} = U'^{End}_{i=n} - U_{i=n}^{End}, \tag{5.1.1}$$

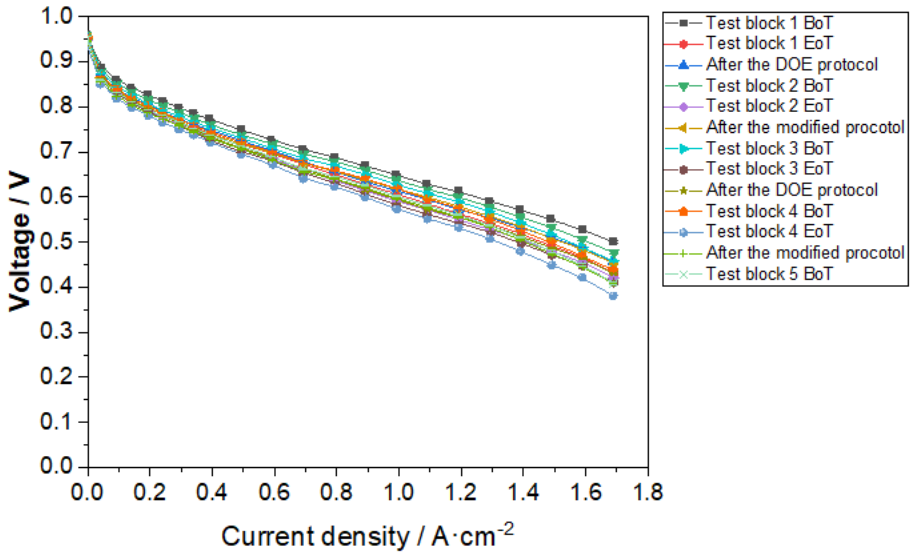

Figure 14: Polarization curves measured during the durability test with original and modified DOE recovery protocols.

and the total reversible performance loss, $\Delta U_{i=n}^{rev}$, assumed to be fully recovered by the JRC recovery protocol, is defined according to Eq. (5.1.2) as the difference in the fuel cell voltage at the end of the n^{th} AST operation, $U_{i=n}^{End}$, and the fuel cell voltage at the beginning of the next test block, $U_{i=n+1}^{Begin}$,

$$\Delta U_{i=n}^{rev} = U_{i=n+1}^{Begin} - U_{i=n}^{End}. \tag{5.1.2}$$

Figure 15 b) shows the absolute recovered voltage loss versus the current density in the range of 0 to 1.7 A·cm^{-2} for both the original DOE protocol (Recovery 1 and 3) and the modified DOE recovery protocol (Recovery 2 and 4). Both protocols are highly reproducible, as demonstrated by the overlap of data of Recovery 1 and 2, and Recovery 2 and 4 within the error bars. According to Figure 15 b), the absolute recovered voltage losses increase with increasing current density from 0 to 1.7 A·cm^{-2}. The recovered voltage loss due to the DOE recovery protocol is lower than 10 mV till the current density of 1.0 A·cm^{-2} and then increases gradually to 25 mV at 1.7 A·cm^{-2}. The same trend is reported in Article II. On the

other hand, the recovered voltage loss due to the modified DOE recovery protocol increases significantly from 0.5 A·cm^{-2} and reaches around 30 mV at 1.0 A·cm^{-2}. At the current densities from 1.0 to 1.7 A·cm^{-2}, the recovered voltage remains in the range of around 30 mV. Figure 15 c) shows relative performance recovery (related to the effect of the subsequent JRC protocol). The relative recovery of each recovery procedure is congruent with the repeated one in the analyzed current density range (0 to 1.7 A·cm^{-2}). The original DOE protocol recovers 20 - 40 % of reversible performance losses in the current density range of 0 to 1.3 A·cm^{-2}. At 1.3 to 1.7 A·cm^{-2}, the recovery efficiency increases to around 60 %. On the other hand, the modified DOE recovery protocol recovers 30 - 50 % of the reversible performance losses at the current density from 0 to 0.5 A·cm^{-2}. Then, the recovery efficiency increases significantly to around 75 % at 1.0 A·cm^{-2} and then exhibits minor changes up to 1.7 A·cm^{-2}. From Figure 15 b) and c), it is concluded that the recovery efficiency of the DOE protocol is significantly enhanced after the modification, especially at the current density between 0.7 and 1.5 A·cm^{-2}. The increased relative recovery efficiency due to the modifications compared to the original DOE protocol is 20 % to 50 % (depending on the specific current density).

To address the recovery mechanism of the modified DOE recovery protocol, EIS measurements at the current density of 1.2 A·cm^{-2} were performed at the beginning and end of each test block, and after the investigated recovery procedure. The hardware and software used for the EIS measurement and the operation parameters of the fuel cell during the measurement were introduced in Section 4.3.3. The recorded data are shown in Figure 16 as Nyquist plots according to the four test blocks. The measured data are then fitted with the equivalent electric circuit described in detail in Section 4.3.3 and presented in Figure 10. The fitting results of the measured EIS data including errors from the Thales XT software are presented in Table S1 in the supporting information. Figure 17 displays the recovered ohmic, charge transfer, and mass transfer resistance of the fuel cell of each test block due to the recovery procedures, following the methodology introduced in Figure 2 in Article I. The black columns stand for the reduction of resistance caused by the investigated recovery procedure, while the red patterned columns correspond to the change caused by subsequent JRC recovery protocol. In general, similar to Figure 6 of Article II and Figure 8 of Article III,

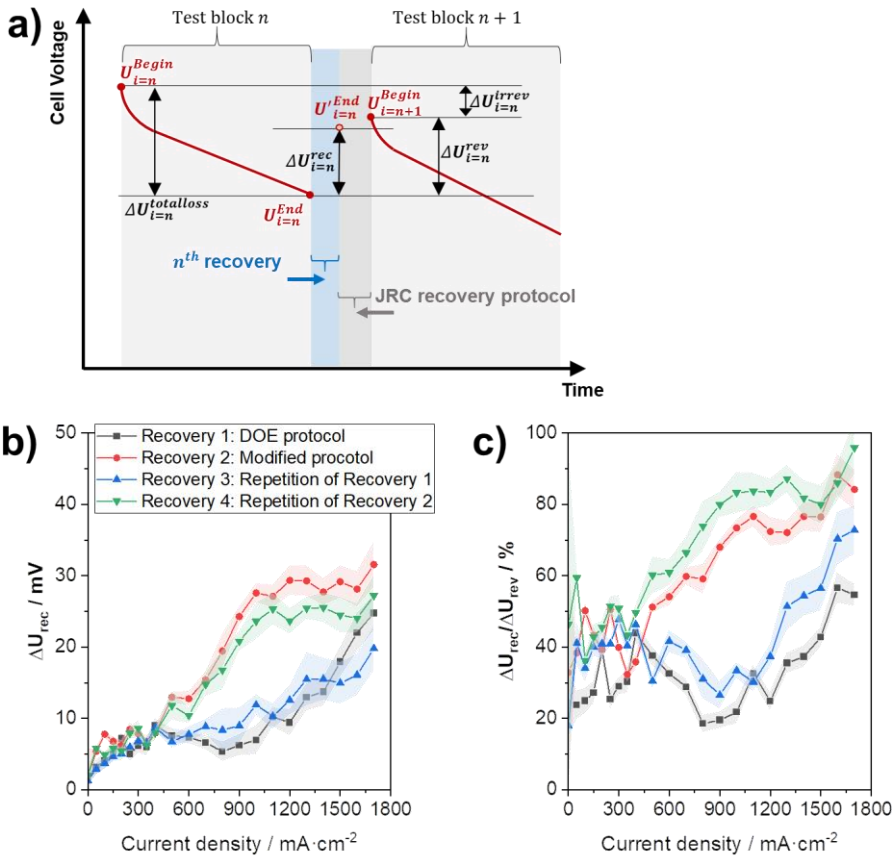

Figure 15: a) Definitions for the evaluation of the recovery efficiency of a recovery procedure. b) Recovered voltage versus current density calculated according to Eq (5.1.1). c) Relative recovery according to Eq. (5.1.1) and Eq. (5.1.2).

all three recovery procedures in this experiment mainly affect the charge transfer and mass transfer resistance other than the ohmic resistance. The modified DOE recovery protocols (Recovery 2 and 4) lead to around 60 % of the reduction of charge transfer resistance of the one caused by the following JRC recovery protocols. However, the original DOE recovery protocols (Recovery 1 and 3) reduce about 30% of the charge transfer resistance, which is reduced by the JRC recovery protocols. On the other hand, considering the error bars, the modified DOE recovery protocols (Recovery 2 and 4) recover 83 % of the mass transfer resistance that the JRC recovery protocols reduce. The original DOE recovery protocols reduce 80 % of the mass transfer resistance related to the reduction due to JRC recovery protocols. Thus, the modified DOE recovery protocols only show a slight effect by further reducing the mass transfer resistance compared to the original DOE recovery protocols. This observation was also mentioned in Article II, that the DOE recovery protocol showed high recovery efficiency at a high current density range due to the prominent reduction effect of mass transfer resistance. In Figure 15 c), at the current density of 1.2 $A \cdot cm^{-2}$, the recovery relative to the JRC recovery protocol of the modified DOE recovery protocol is about 35 % higher than that of the original DOE recovery protocol. It can be concluded that the improved recovery efficiency results from the contribution of the reduced charge transfer resistance due to the modifications as described in Section 5.1.1. Both modifications, prolonging the hydrogen step and the introduction of a cell cooling-down step, contribute to the reduction of charge transfer resistance of the fuel cell. According to Article III, the absolute recovered fuel cell voltage resulting from the cell cooling-down step is positively correlated with the amount of liquid water in the cathode, especially at the current density of 0 to 1 $A \cdot cm^{-2}$. This is consistent with the observation in Figure 15 b) that the difference of the absolute recovered performance losses due to the original and modified DOE recovery protocols increases upon the current density from 0.4 to 1.2 $A \cdot cm^{-2}$. At the current density range lower than 0.4 $A \cdot cm^{-2}$, the absolute recovered performance losses are relatively low (around 40 %), along with a higher error taking the error bar into account. This is consistent with the Figure 3 c) in Article III, that at current density lower than 1 $A \cdot cm^{-2}$, the recovery relative to the JRC recovery protocol of the 35-min operando temperature reduction from 80 to 45 °C is about 40 %, while the recovery of the 95-min operando temperature reduction from 80 to 45 °C is about 70 %. Upon exposure to liquid water, the regeneration/redistribution of the PFSA ionomer in the electrode has been observed to occur at a low rate, eventually reaching a quasi-equilibrium between the chemical and mechanical energies [101, 102]. The time

constant of the process depends on factors such as water uptake, morphology, temperature, and relative humidity and can vary dramatically from days to months [103, 104].

To summarize, the modified DOE recovery protocol significantly enhances the recovery efficiency, particularly at current densities between 0.7 and 1.5 $A \cdot cm^{-2}$, thanks to the reduction in charge transfer resistance. The primary reason for this improvement is similar to what was observed in Article III, which is the rearrangement or reorganization of the PFSA ionomer in the cathode caused by water condensation during the temperature reduction step.

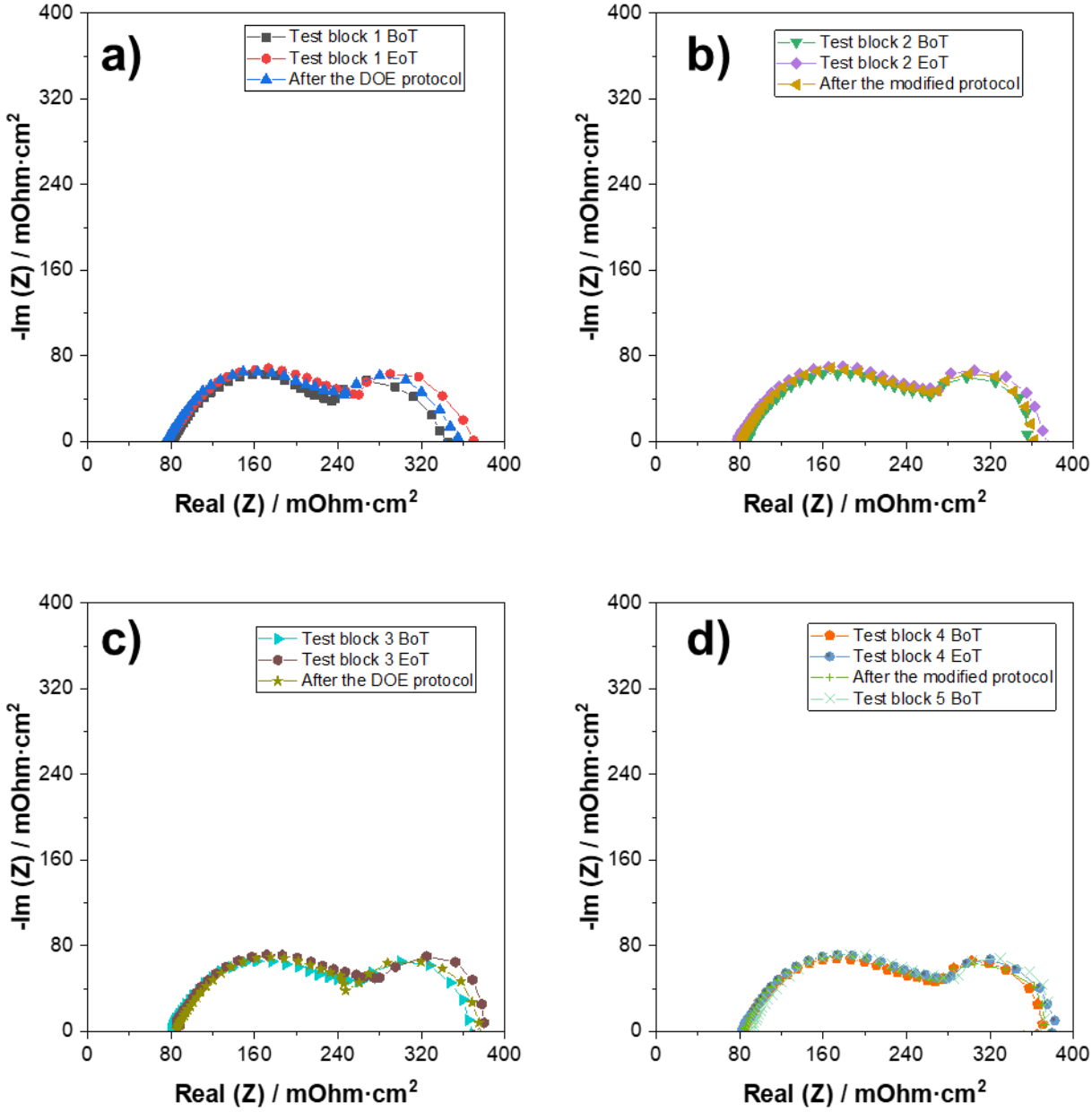

Figure 16: The EIS measured at 1.2 A·cm^{-2} at the beginning and end of each test block, as well as after the recovery procedure.

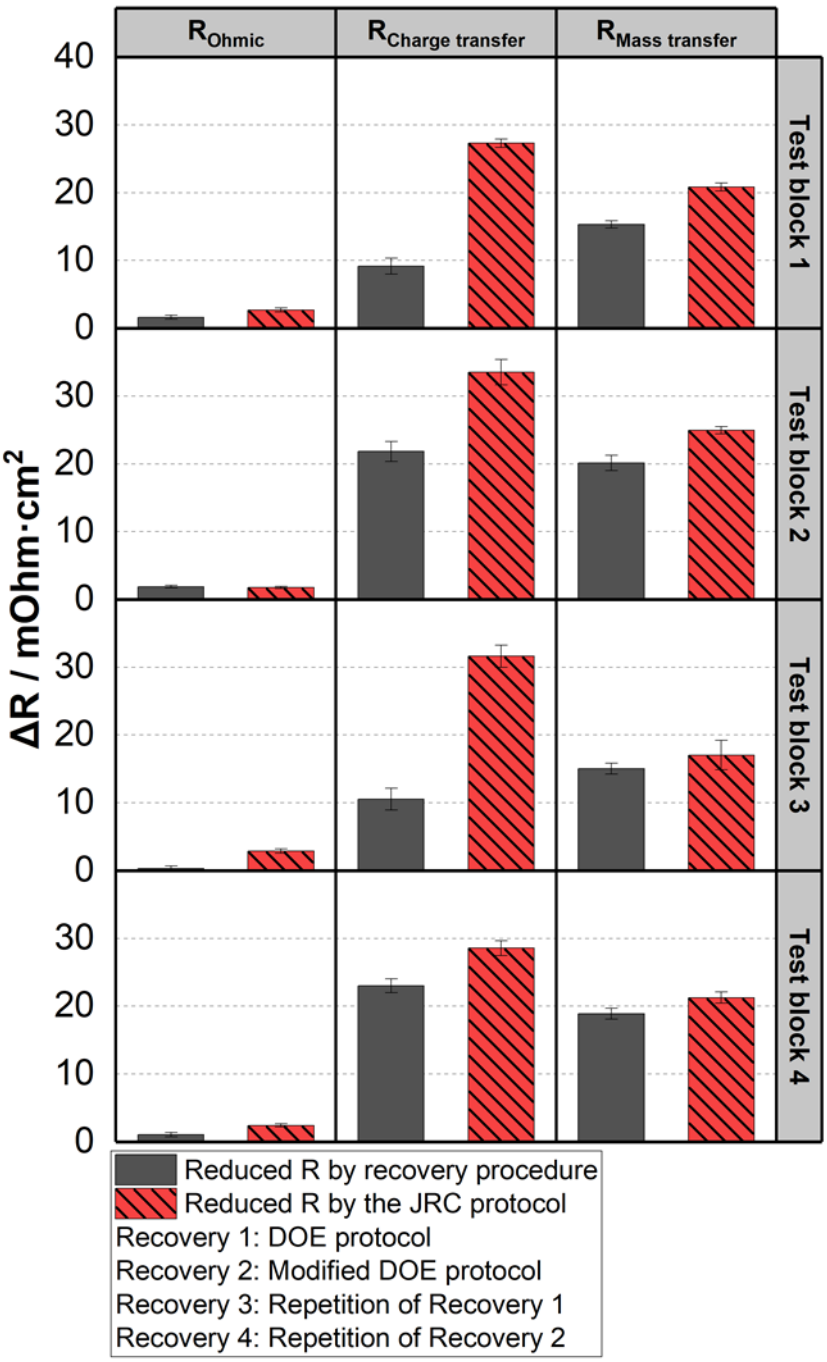

Figure 17: Reduction of ohmic resistance, charge transfer resistance, and mass transfer resistance due to each performed recovery procedure (corresponding test and the following JRC recovery protocol).

To bring the conclusions of Article I, II, III, and 5.1 into an overall context, the relative recovery related to the cell voltage change of the previous AST operation of several recovery procedures are calculated. As shown in Figure 15 a), the cell voltage change of the previous AST operation is defined as Eq. (5.1.3)

$$\Delta U_{totalloss} = U_{i=n}^{Begin} - U_{i=n}^{End}. \quad (5.1.3)$$

This factor of relative recovery related to the cell performance degradation of the previous operation was named as η_{Last} in Articles I and II. In Figure 18, the relative recovery of the DOE recovery protocols from Article II and Section 5.1, the modified DOE protocol, and the operando recovery procedures with temperature reduction of 80 °C to 45 °C from Article III (95 min and accelerated to 35 min) are calculated and presented. Interestingly, the DOE recovery protocols in Article I and Section 5.1 show similar recovery efficiency in the current density range from 0 to 1.7 A·cm^{-2}, although the DOE recovery protocol was performed in the second test block in Article II and the first test block in Section 5.1. It indicates that the recovery procedure performed in the first test block in Article II, JRC recovery protocol, almost completely recovered the reversible performance degradation. It also proves the reliability of using the JRC recovery protocol as a reference to recover all the reversible performance degradation in Article III and Section 5.

Nevertheless, the relative recovery of the operando recovery procedure with a temperature reduction from 80 °C to 45 °C, which had a similar duration as in the modified DOE recovery protocol, kept constant at around 30 % at the current density range from 0 to 1.0 A·cm^{-2}. This recovery efficiency is also higher than that due to the original DOE recovery protocol in the investigated current density range. This indicates that only the 35-min operando recovery procedure with a temperature reduction from 80 °C to 45 °C leads to higher recovery efficiency than the 29-min DOE recovery protocol. For the applied FC-DLC operation, the operando recovery procedure with a temperature reduction is easier to implement and also achieves higher recovery efficiency at the current density range from 0 to 1.0 A·cm^{-2}. If the temperature reduction step took 95 min, as performed in Article III, the relative recovery related to the previous AST operation is enhanced by over 10 % due to the increased amount of liquid water in the cathode. It is found in the Article III that absolute recovered cell voltage increased linearly with the amount of liquid amount water formed in the cathode during the operando recovery procedure, especially at the current density range

from 0 to 1.0 A·cm^{-2}. Thus, it can also be concluded that the recovery efficiency of the modified DOE recovery protocol can be further improved by increasing the amount of liquid water in the cathode.

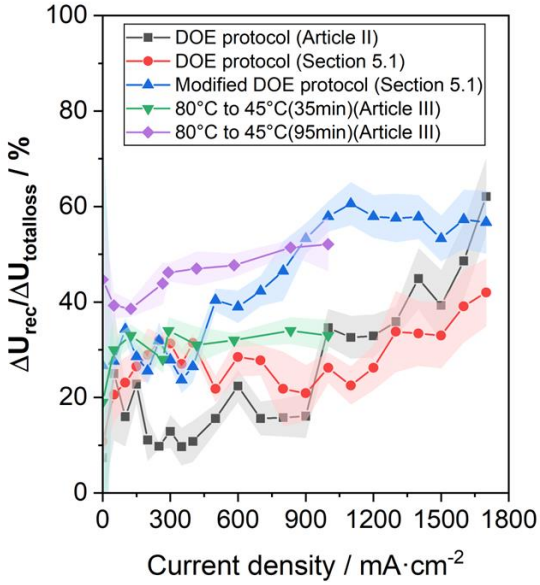

Figure 18: The relative recovery related to the cell voltage change of the previous AST operation of the DOE recovery protocols in Article I, II, and Section 5.1, modified DOE protocol, operando procedures with temperature reduction of 80 °C to 45 °C in Article III (95 min and accelerated to 35 min).

5.1.3 Conclusions

Two steps in the original DOE recovery protocol are modified to improve the recovery efficiency of the fuel cell performance degradation. The results of the durability test indicate an enhanced recovery efficiency compared to the original DOE protocol at the current density between 0.7 and 1.5 $A \cdot cm^{-2}$. Especially at the current density over 1.0 $A \cdot cm^{-2}$, around 75 % of the reversible performance losses are recovered by the modified DOE protocol. The modified DOE recovery protocol reduces 60 % of the reduced charge transfer resistance due to the JRC recovery protocol.

However, the modified DOE recovery protocol can be further improved to increase the recovery efficiency, especially at low and middle current density ranges, as follows:

(i) According to the conclusions in Article III, to improve the recovery efficiency, the cell cooling-down process can be prolonged to increase the amount of liquid water in the cathode catalyst layer. The cell cooling-down step in this modified DOE recovery protocol can be prolonged to 95 min as performed in the operando Recovery 1 and 3 in Article III, which means that the fuel cell's heating system is shut off and the cell just cools down without an extra cooling fan.

(ii) To reduce the Pt oxides on the cathode catalyst layer, the hydrogen soak step should be further prolonged or replaced by a step to purge the cathode with hydrogen. However, strong bond Pt oxides have a considerable impact on the decrease of ORR activity, which is crucial for the full recovery of reversible performance losses. As described in the literature, the duration of the exposure of the cathode catalyst to the low potential can vary from several minutes to hours to achieve a full recovery, depending on the oxide composition [105]. To figure out the composition of the oxide species on the cathode catalyst surface and the kinetics for the reduction of the oxide layers, further experiments should be performed with methods such as low potential and cyclic voltammetry (CV).

On the other hand, the original DOE recovery protocol has a short duration of 29 min compared to the 69-min modified protocol, which makes it more favorable for applications with frequent short stops. Furthermore, the modified DOE recovery protocol recovers over 50 % of reversible performance degradation in the current density range over 0.5 $A \cdot cm^{-2}$, which is the most relevant current density range for transport applications. For stationary

applications, on the other hand, typically a current density below 0.5 $A \cdot cm^{-2}$ is applied, so the modified DOE recovery protocol may be of less interest for these kinds of applications.

5.2 Investigation of oxygen transport resistance change caused by the recovery procedure based on temperature reduction

Articles II and III found that water condensation caused by cell temperature reduction positively affects the recovery of reversible performance losses. Especially in Article III, it is figured out that the amount of the liquid water (i.e., integration of the liquid water flow at the cathode outlet during the cell cooling-down step) in the cathode is positively correlated with the absolute recovered performance loss. The recovery effect can be attributed to the reduction of the charge transfer and mass transfer resistance in the cathode due to the regeneration/redistribution of the ionomer structure.

It is commonly acknowledged that the oxygen transfer resistance in the cathode can lead to severe performance losses, especially at a low Pt loading (lower than 0.25 $mg \cdot cm^{-2}$) and at high power density [106, 107]. As reported in the literature, it is still unclear where part of the oxygen transfer resistance originates from, which significantly reduces the partial pressure of oxygen at the Pt surface and hinders the ORR in the cathode [100, 108]. Thus, it is interesting to investigate the change of oxygen transport resistance in the cathode due to the recovery procedure involving temperature reduction, which has been identified as an effective recovery procedure in previous studies.

5.2.1 Description of the experiment

Details of the conducted durability test are described in Section 4.2 in Figure 9 d). It includes two test blocks after the MEA conditioning step. Each test block began with a polarization curve measurement, limiting current test, and proton conductivity test for the characterization of the fuel cell, followed by an AST process of 76-h FC-DLCs. Then the cell temperature was reduced from 80 °C to 30 °C as a recovery procedure according to Article III. Before and after the recovery procedure, the limiting current test and proton conductivity test were performed. Afterward, the voltage responses of 10 FC-DLCs were recorded. At the end of the test block, the JRC recovery protocol was applied to recover reversible performance losses (see Table 4 and Article II). The hardware used for this experiment, including the MEA, single cell, and testbench, is presented in Section 4.1. The operation parameters of the fuel cell during the AST, the recovery procedure, and the characterization measurements are described in Section 4.2. The operation parameters of the used electrochemical characterization methods, including the polarization curve measurement, limiting current test, and proton conductivity test, are summarized in Section 4.3.

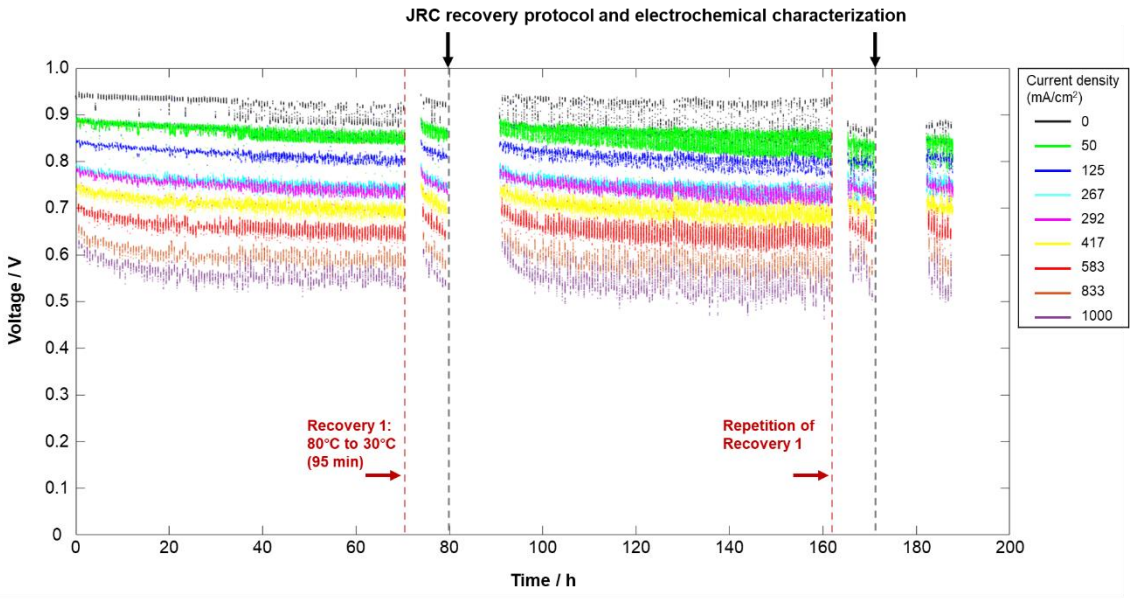

Figure 19: Cell voltages recorded during the durability test for the investigation of oxygen transfer resistance change caused by temperature reduction (80 °C to 30 °C).

5.2.2 Results and discussion

The cell voltage recorded during the experiment is shown in Figure 19. The red and black vertical lines indicate the implementation of the recovery procedures. The methodology of the quantitative evaluation follows the scheme of Figure 15 a), which is consistent with the methodology described in Section 5.1 and Articles I - III. Figure 20 a) and b) display the absolute recovered cell voltage and the relative recovery due to temperature reduction from 80 °C to 30 °C related to the JRC recovery protocol calculated according to Eq. (5.1.1) and Eq. (5.1.2) in Section 5.1. Figure 20 c) shows the total performance loss during each AST

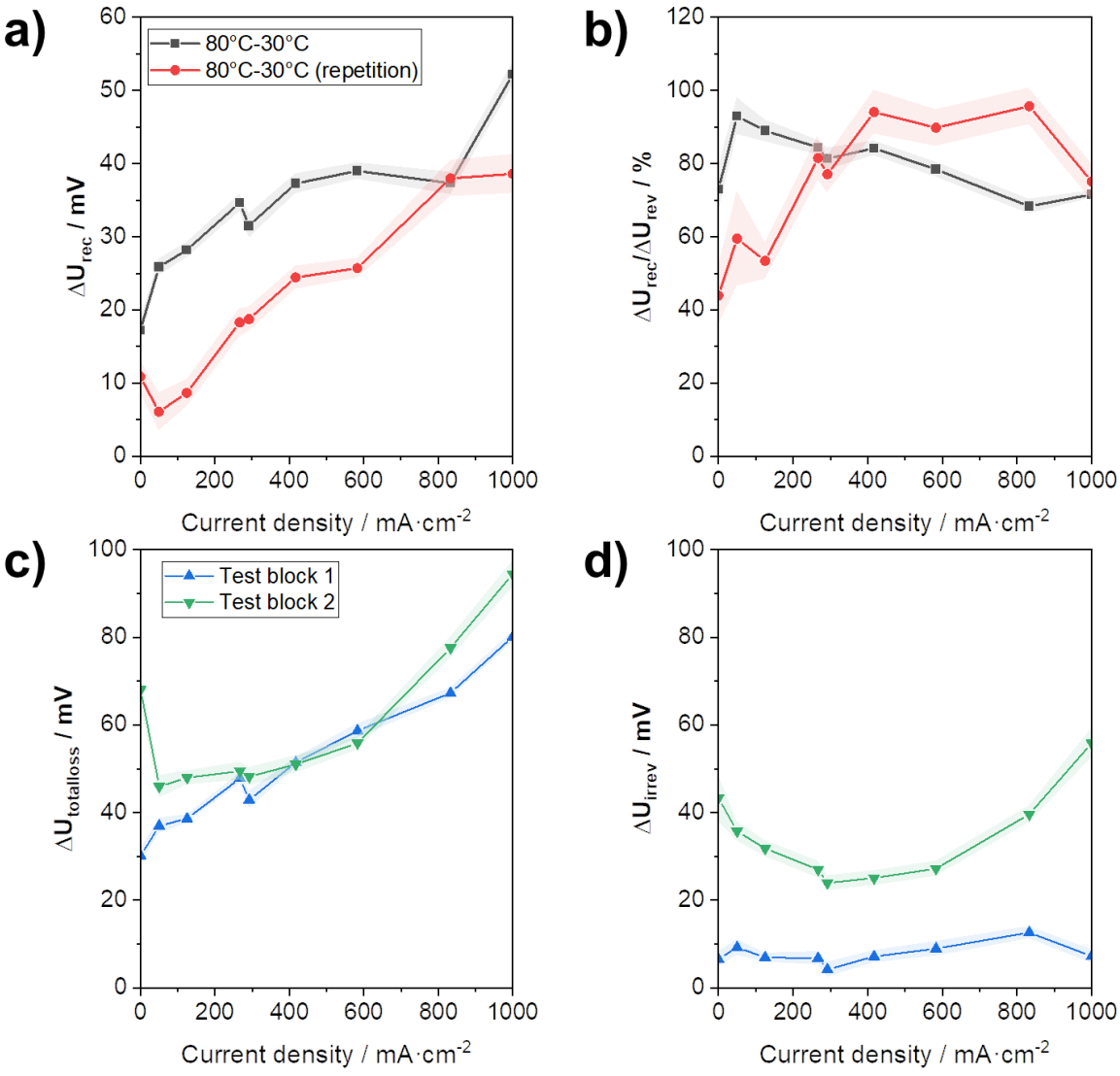

Figure 20: a) Absolute recovered voltage loss versus current density calculated according to Eq. (5.1.1). b) Relative recovery of the investigated recovery procedure related to JRC recovery protocol according to Eq. (5.1.1) and Eq. (5.1.2). c) Total voltage loss during the two test blocks according to Eq. (5.1.3). d) Irreversible voltage losses during the two test blocks according to Eq. (5.2.1). The shadow area is the error bar resulted from the standard deviation from the average of the last 30 s of the dwell time of each tested current density.

operation according to Eq. (5.1.3). Figure 20 d) presents the irreversible performance losses during the two test blocks according to Eq. (5.2.1)

$$\Delta U_{i=n}^{irrev} = U_{i=n}^{Begin} - U_{i=n+1}^{Begin}, \tag{5.2.1}$$

while the $U_{i=n}^{Begin}$ stands for the fuel cell voltage at the beginning of the n^{th} test block.

In Figure 20 c), the high reproducibility of the two test blocks is demonstrated. However, the irreversible performance loss during the second AST operation is much higher than during the first AST, as shown in Figure 20 d). The irreversible performance loss in the first test block is around 5 to 10 mV, while that in the second test block is from 20 to 55 mV. Moreover, the absolute recovered cell voltage in the first test block is about 10 mV higher in the investigated current density range than in the second test block, as shown in Figure 20 a). Therefore, the recovery procedure in the two test blocks shows similar relative recovery related to the JRC recovery protocol of 70 % to 95 %, especially at a current density between 0.292 and 1 A·cm^{-2}, as shown in Figure 20 b). Besides, the temperature reduction from 80 °C to 30 °C was also performed and evaluated in Article III as a non-operando recovery procedure. The relative recovery efficiency related to the JRC recovery protocol in this durability test is consistent with the results in Figure 6 v) in Article III, regardless of the different sets of fuel cell hardware.

The ionic impedance was measured at the beginning, and end of each test block, before and after each recovery procedure, as the Nyquist plot displayed in Figure 21 a). The ohmic and ionic resistance, as R_{Ohmic} and R_{Ionic}, are extracted from the Figure 21 a) with the method described in Section 4.3.3 and presented in Figure 21 b) over the durability test. In both test blocks, the ohmic resistance of the fuel cell increases after the AST operation and then decreases dramatically after the recovery procedure of temperature reduction from 80 °C to 30 °C, which can be attributed to the water condensation in the cathode. However, the ohmic

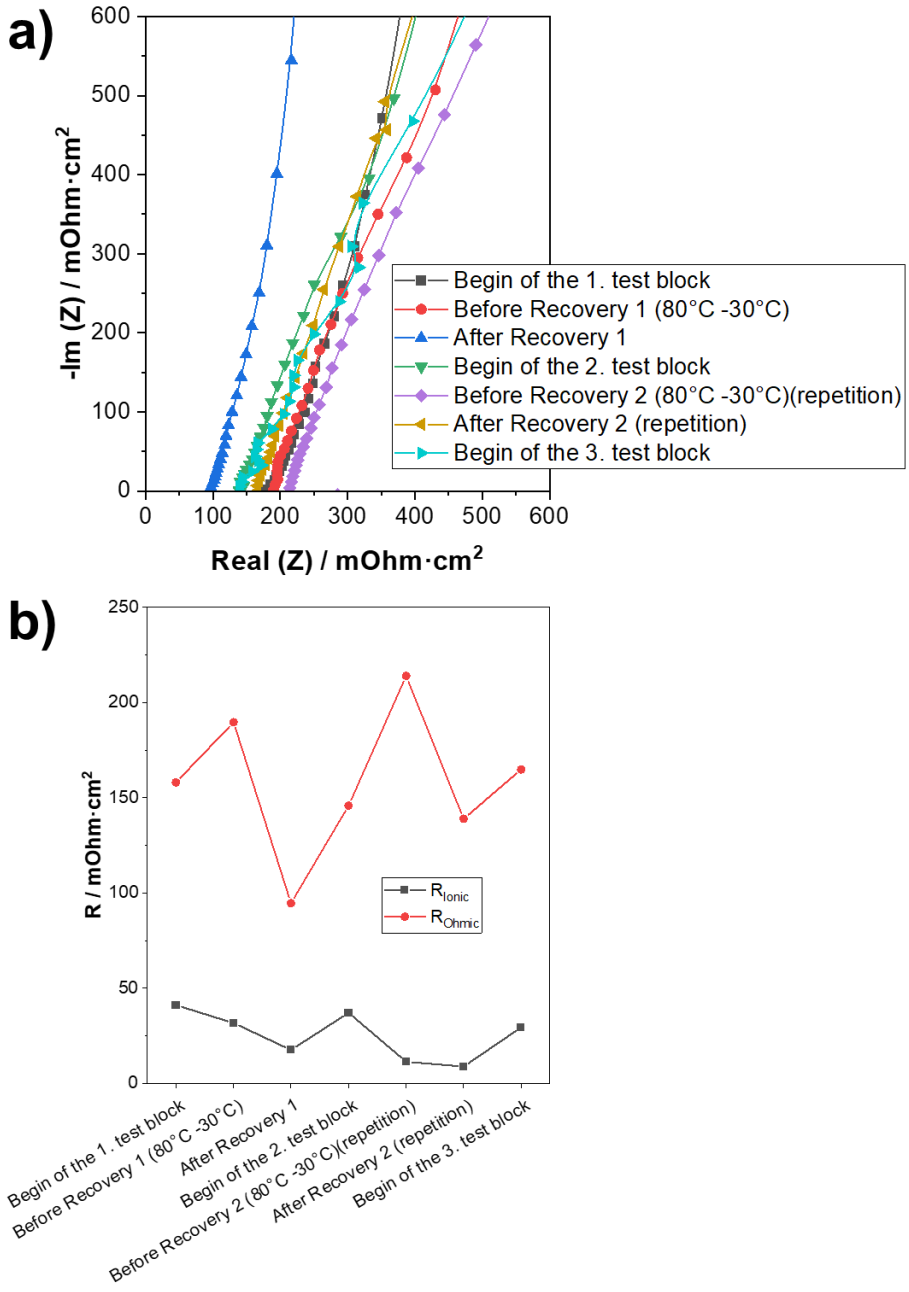

Figure 21: Nyquist impedance spectra of the ionic impedance measurement, and b) ionic and ohmic resistance of the fuel cell at the beginning of each test block, before and after each recovery protocol during the durability test.

resistance increases again after the JRC recovery protocol at the beginning of each test block, which is likely related to the membrane dehydration caused by the 90-min dry gas purge in both the anode and cathode and 8-hour cooling-down step at the end of the JRC protocol. Besides, the ohmic resistance of the fuel cell during the durability test is in the range of 100 to 200 mΩ·cm^2, while the ionic resistance is lower than 50 mΩ·cm^2. It is interesting to note that the ionic resistance decreases not only after the AST operation but also after the recovery procedure of temperature reduction. On the other hand, the JRC recovery protocol leads to an increase of the ionic resistance in the cathode during both test blocks, as shown in Figure 21 b).

The introduction and analysis of the limiting current measurement are provided in Section 4.3.4. The limiting current density of the fuel cell upon different oxygen partial pressure was measured to investigate the oxygen transfer resistance in the cathode (R_{Total}) at the beginning of each test block, before and after each recovery procedure. Figure S3 in the supporting information shows the recorded data of each limiting current measurement. In each panel of Figure 22, the limiting current density is recorded at total pressure of 110, 140, and 170 kPa in the cathode at oxygen volume concentrations of 1 %, 1.25 %, and 1.5 %, respectively. The dashed line indicates the linear fitting results of the limiting current densities according to the method described in Section 4.3.4 for each total pressure in the cathode. In all the panels, each R-Square of the fitting line is higher than 0.98, which confirms a low deviation and high reliability of the limiting current measurement results. The slope of the linear fitted results in each panel of Figure 22 can be used to calculate the total oxygen transfer resistance (R_{Total}) in the cathode according to Eq. (4.3.1). Afterword, Figure 23 shows the total oxygen transfer resistance (R_{Total}) as a function of total pressure in the cathode for 110, 140, and 170 kPa at the beginning of each test block, before and after each recovery procedure during the durability test.

The total oxygen transfer resistance in the cathode can be divided into pressure-dependent oxygen transfer resistance (R_P) and pressure-independent oxygen transfer resistance (R_{NP}) [109, 110]. The pressure-dependent resistance (R_P) is dominated by intermolecular diffusion through large pores with a diameter over 100 nm, such as oxygen transportation through the GDL in the cathode [111]. On the other hand, the pressure-independent resistance (R_{NP}) mainly generates from i) Knudsen diffusion of oxygen through the small pores with a diameter lower than 100 nm, such as MPL and CL [99, 112], and ii) oxygen

transportation through the liquid water or/and ionomer film covered on the catalyst surface in the cathode [113, 114]. Thus, the total oxygen transfer resistance (R_{Total}) in the cathode can be described by Eq. (5.2.2) [110, 115]

$$R_{total} = R_P + R_{NP}. \tag{5.2.2}$$

In the literature, many researchers have demonstrated the complexity of distinguishing the contribution of pressure-independent oxygen transfer resistance (R_{NP}) from MPL and CL [116, 117]. Thus, in this work, the Toray Carbon Paper 060 without hydrophobic treatment is used as diffusion media to ensure that the pressure-dependent oxygen transfer resistance is due to GDL and the pressure-independent oxygen transfer resistance results from CL in the cathode. Thereby, the dashed lines in Figure 23 show the linear correlation of the calculated total oxygen transfer resistance (R_{Total}) in the cathode upon the total pressure. Each linear fit shows an R-Square over 0.99, indicating a strong linear correlation of the total oxygen transfer resistance in the cathode (R_{Total}) over the total pressure in the cathode. According to the Eq. (5.2.2), the pressure-dependent and pressure-independent oxygen transfer resistance (R_P and R_{NP}) at a specific total pressure in the cathode can be quantified with the fitted slope and intercept of each dashed line in Figure 23. The slope and intercept of the linear fitting results are displayed in Table S2 in the supporting information.

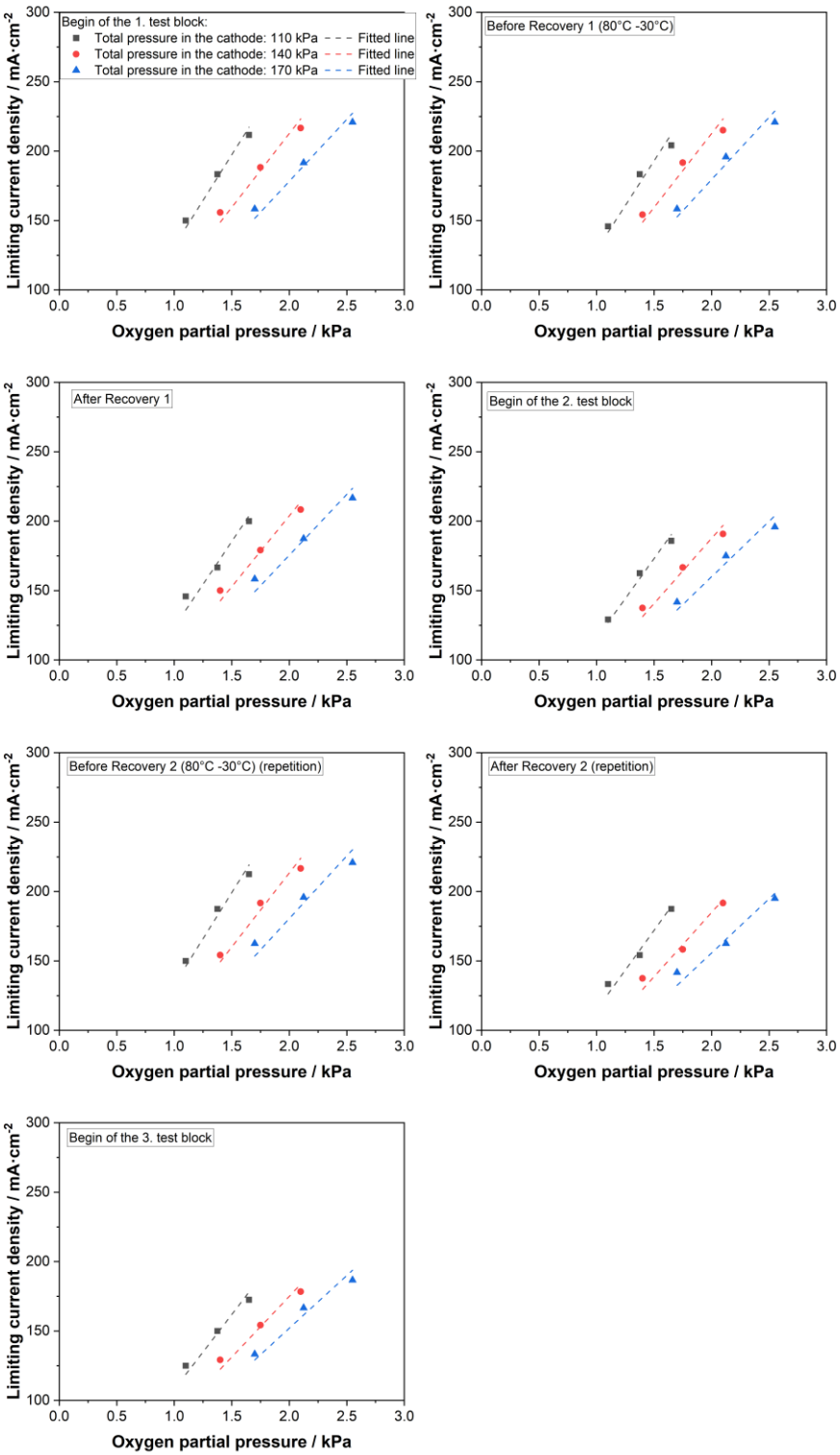

Figure 22: Limiting current density versus oxygen partial pressure with total pressure in the cathode of 110, 140 and 170 kPa at the beginning of each test block, before and after each recovery protocol during the durability test. Dash lines are linear fitted results.

To investigate the changes of the oxygen transfer resistance during the whole durability test, results at three chosen total cathode pressures (105, 170, and 230 kPa) are calculated based on the linear fitting in Figure 23 for further discussion. Thereby, the pressure-dependent and pressure-independent oxygen transfer resistance (R_P and R_{NP}) at the beginning of each test block, before and after each recovery procedure during the durability test, is presented in Figure 24. The pressure-dependent oxygen transfer resistance (R_P) at each total pressure in the cathode does not change dramatically during the whole durability test, implying that the molecular diffusion coefficient through the GDL does not change significantly and as expected, no critical physical degradation occurs with the GDL. The pressure-independent oxygen transfer resistance (R_{NP}) is constant at different total pressures in the cathode. Besides, the total oxygen transfer resistance (R_{Total}) and pressure-dependent oxygen transfer resistance (R_P) increase with increasing total pressures in the cathode. The recovery procedure of temperature reduction from 80 °C to 30 °C leads to increases in the pressure-independent resistance (R_{NP}) of 8 and 17 s·m^{-1} in the two test blocks at the total cathode pressure of 230 kPa, respectively. However, after the JRC recovery protocol, the pressure-independent resistance R_{NP} decreases 15 and 7 s·m^{-1} in the two test blocks, respectively. Taking the results in Figure 21 into account, it can be concluded that the temperature reduction from 80 °C to 30 °C leads to reduced ionic transfer resistance and increased pressure-independent oxygen transfer resistance (R_{NP}) in the cathode. However, the ohmic resistance of the fuel cell is also reduced. Thus, from Figure 21 and Figure 24, it is

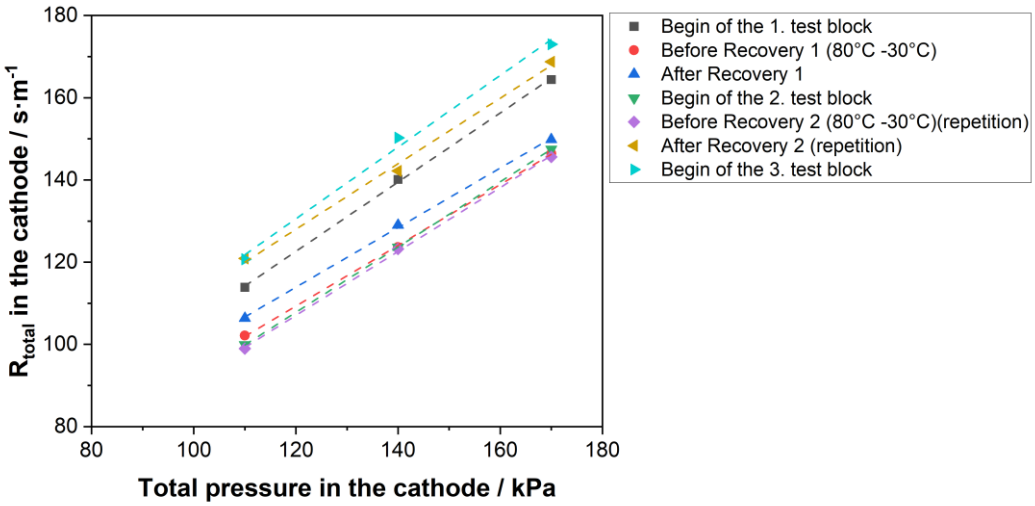

Figure 23: Total oxygen transfer resistance as a function of total pressure in the cathode of 110, 140 and 170 kPa at the beginning of each test block, before and after each recovery protocol during the durability test. Dash lines are linear fitted results.

concluded that during the recovery procedure of temperature reduction from 80 °C to 30 °C, the cathode catalyst layer and the membrane are rehydrated due to the water condensation. According to Figure 24, the recovery procedures of temperature reduction and JRC recovery protocol influence the oxygen transfer resistance in the catalyst layer; however, they do not significantly change the total oxygen transfer resistance in the cathode during the whole durability test. According to Article III, the JRC recovery protocol reduces higher mass transfer resistance in the cathode than the recovery procedures with temperature reduction. Thus, it can be concluded that the JRC recovery protocol reduces more water transfer resistance than the recovery procedures with temperature reduction. Thus, the significantly reduced water transfer resistance is the main reason for the higher recovery efficiency of the JRC recovery protocol at the high current density range (over 1.2 $A \cdot cm^{-2}$), which is observed in Section 3.2 in Article III. In a nutshell, the recovery mechanism of the recovery procedures with temperature reduction and JRC recovery protocol is summarized in Table 8, showing the changes in the ohmic, charge transfer, and mass transfer resistances.

It is widely acknowledged that the ion- and solvent-transport capabilities of PFSA ionomers are governed by their morphology, which, however, highly depend on the hydration of the hydrophilic ionic groups [118, 119]. The ionic and mass transfer resistance reduces with increased humidity due to a varying ionomer morphology, which is minimized when the PFSA ionomer is immersed into water [120, 121]. It has been observed that the fraction of conductive and hydrophilic area of PFSA ionomer increases due to a regeneration/redistribution effect along with increased humidity [122, 123]. In particular, there is a change in water content and morphology depending on the phase of water (vapor or liquid), which further influences the ionic and water conductivity in the ionomer and between the membrane/electrode interface [124, 125]. Therefore, it is observed in Section 5.2 and Article III, the temperature reduction step (in both operando recovery procedures and JRC recovery protocol) results in reduced charge transfer resistance in the cathode catalyst layer and, accordingly, a recovery effect on the performance degradation. However, as mentioned in Section 5.1.2, it can take a long time, from days to weeks, to complete the regeneration/redistribution of the ionomer and reach a quasi-equilibrium state [102, 126]. Thus, in Article III, the duration of the temperature reduction, which refers to the time the ionomer is exposed to liquid water, has a significant impact on the recovery efficiency.

The pressure-independent resistance of the oxygen transfer resistance in the cathode

results from the thin ionomer film (~ 100 nm) in the catalyst substrates [127, 128]. The thickness of this thin film can be altered by both the film/surface and film/substrate interactions, which are also hydration-dependent [129, 130]. In this work, the increase in oxygen transfer resistance after the temperature reduction recovery procedure can be attributed to excess water at the substrate/film interface, leading to a water-enriched surface that blocks the oxygen transfer [131, 132]. Additionally, the solubility of oxygen decreases with increasing water content in the ionomer, which further contributes to a higher R_{NP} at the ionomer/Pt interface in the cathode [133].

Furthermore, both the temperature reduction and JRC recovery protocols result in increased water uptake due to the enhanced hydrophilicity of the ionomer. The pathway for water molecules to move is created within the nanostructure of the ionomer, which needs to accommodate the nanoswelling and growth of water domains [134, 135]. Consequently, the water transfer coefficient increases in the ionomer as the water content increases, until reaching an equilibrium state [136, 137]. In this study, the JRC recovery protocol requires a longer duration compared to the temperature reduction recovery protocol, bringing it closer to the equilibrium state and resulting in a more significant reduction in water transfer resistance.

The ohmic resistance of the fuel cell decreases significantly after the temperature reduction from 80 °C to 30 °C, while it increases after the JRC recovery protocol. In this study, the JRC recovery protocol involves a 60-minute dry gas purging step before the cell cools down, followed by a 30-minute dry gas purging step afterward. This process reduces the total liquid water content in the fuel cell, subsequently decreasing the hydrophilicity of the ionomer [138, 139]. On the other hand, the interfacial conductivity resistance between the membrane/electrode, which is a significant contributor to the ohmic resistance, is highly dependent on humidity and the phase of water [140, 141]. However, the precise nature of the transport mechanism at the membrane/electrode interface is still not fully understood.

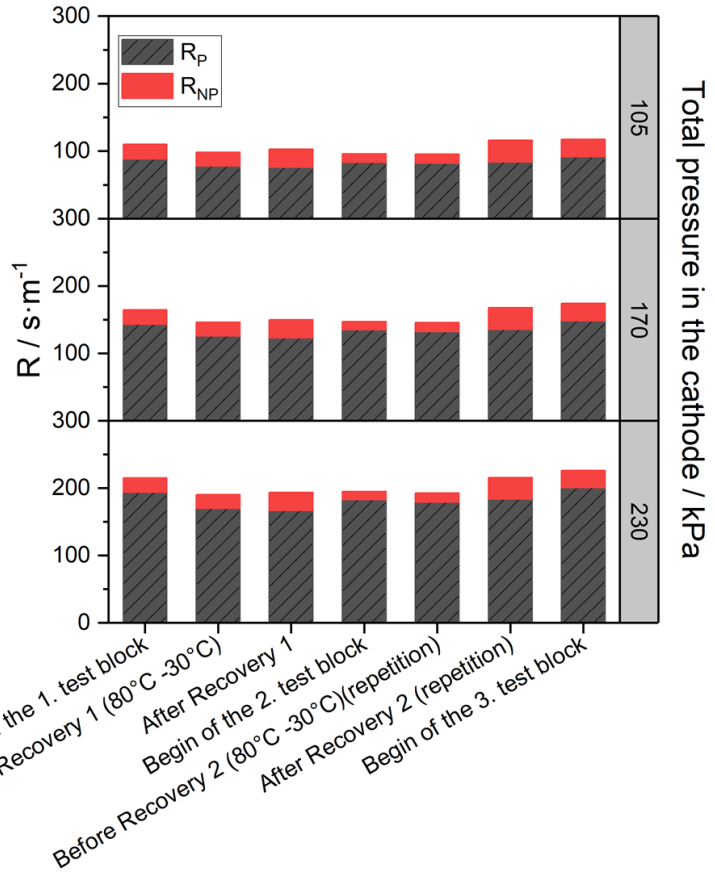

Figure 24: Added up pressure-independent resistance, R_{NP}, and pressure-dependent resistance R_P at total cathode pressure of 105, 170, and 230 kPa at the beginning of each test block, before and after each recovery procedure during the durability test.

Table 8: The recovery mechanism of the recovery procedures with temperature reduction (80 °C to 30 °C) and JRC recovery protocol. The data are the results with total cathode pressure of 230 kPa.

Contribution of the resistance		Temperature reduction	JRC recovery protocol
Ohmic R		Decreases significantly	Increases
Charge transfer R		Reduces significantly	Reduces significantly
Mass transfer R	Total oxygen transfer R	Unchanged	Unchanged
	Oxygen transfer R in the CL	Increases	Decreases
	Water transfer R	Reduces	Reduces significantly

5.2.3 Conclusions

This section performs a durability test composed of two test blocks to investigate the oxygen transfer resistance change due to the recovery procedure of temperature reduction from 80 °C to 30 °C. To separate the two kinds of oxygen transfer resistance originating from the catalyst layer and GDL, untreated Toray Carbon Paper 060 was selected as GDL material. A differential single fuel cell was used with high oxygen and hydrogen stoichiometry (10 and 8) in the cathode and anode, facilitating reliable measurements of the limiting current during the experiment.

Firstly, the recovery efficiency of the temperature reduction was evaluated. Noticeably, the temperature reduction from 80 °C to 30 °C results in similar recovery efficiency related to JRC recovery protocol as in Article III, despite applying different fuel cell hardware, MEA material, and operation parameters.

Afterward, the experimental results of ionic transfer resistance, oxygen transfer resistance in the cathode, and the ohmic resistance of the fuel cell before and after the recovery procedures were analyzed. The recovery procedure of temperature reduction from 80 °C to 30 °C leads to a relative recovery of 70 % - 90 % related to the reversible performance

degradation. Water condensation contributes to the regeneration/redistribution of the ionomer structure in the cathode, improving the hydrophilicity of the ionomer. This, in turn, reduces the ionic transfer and ohmic resistance in the catalyst layer. However, the oxygen transfer resistance in the catalyst layer increases after the temperature reduction recovery procedure due to the presence of excess water at the interface between the catalyst substrate and the ionomer thin film. Nevertheless, the regeneration/redistribution of the ionomer structure occurs at a slow rate, eventually reaching a quasi-equilibrium state. As a result, the ionomer structure is closer to the equilibrium state after the JRC recovery protocol compared to the temperature reduction recovery procedure. This leads to a more significant reduction in water transfer resistance and higher recovery efficiency, particularly in the high current density range (over 1.2 A· cm^{-2}).

6 Conclusions

This cumulative doctoral thesis consists of three peer-reviewed research articles and one further discussion part, which integrate a thorough investigation into the mechanism of the reversible performance degradation of PEMFCs and recovery procedures. The main findings of each contribution are as follows:

The methodology proposed in Article I involved quantifying the reversible losses in relation to the current density, using online logged voltage data from ASTs, polarization curves, and EIS data. The research indicates that using logged voltage data from load cycling tests and polarization curves provide similar results in determining the efficiency of a recovery procedure. However, for a broader current density range, measuring polarization curves is the preferred approach as a necessary experimental characterization method for identifying cell performance losses. If there is a need for more information on the underlying recovery mechanisms, EIS analysis using a simple equivalent circuit can be used. The parameters analyzed provide information on both the recovered performance losses and non-recovered losses, enabling the identification of the advantages and disadvantages of the studied recovery procedures.

Article II compares the recovery efficiency and mechanism of three common recovery protocols (DOE-based, JRC-based, and overnight rest protocols). The results indicated that the DOE protocol has higher recovery efficiency (over 50 %) in the current density range above 1.5 $A \cdot cm^{-2}$ than at lower current densities. The JRC protocol and overnight rest have almost the same relative recovery in the low current density range (0 to 1 $A \cdot cm^{-2}$) from 50 % to 100 % while the DOE protocol shows the lowest achieved recovery efficiency from 0 % to 30 %. All three recovery protocols reduce a similar amount of mass transfer resistance of the PEMFCs while the DOE protocol reduced much less charge transfer resistance than the other two protocols. The study concludes that the choice of a recovery protocol should take into account three factors: i) the operational profiles, ii) the complexity of the devices, and iii) the targeted lifetime. For PEMFC applications in portable communication devices such as mobile phones and portable computers, only the overnight rest protocol can practically be performed due to limited space. However, for PEMFC applications with very short stops that occur more frequently than long stops, the DOE-based procedure is preferable due to its short duration of only 29 minutes. For PEMFC applications that have longer and regular stops, the JRC or overnight rest protocol may be preferred, although they require more time

(both over 8 hours), as they result in much higher recovery efficiency than the DOE protocol.

Article III aims to evaluate and explore the performance recovery mechanism resulting from temperature reduction during the fuel cell operation. The study shows that operando temperature reduction during load cycling results in 60 % - 70 % of the relative recovery achieved by the JRC protocol but at a much shorter duration (1.5 h versus 10.5 h). The amount of liquid water formed in the cathode during the operando recovery procedure has a positive linear correlation with the absolute recovered voltage, especially at a current density range lower than 1 $A \cdot cm^{-2}$. The reason for the performance recovery is the reduction of charge transfer and mass transfer resistance due to the reorganization/rearrangement of the ionomer caused by water condensation. The temperature reduction recovery approach is more suitable for use in transport applications than common recovery procedures, such as the JRC protocol, because it is less time-consuming and easier to perform, requiring no additional equipment like a nitrogen gas supply. As a result, the temperature reduction method can be easily executed during operation, making it a more practical solution for transport applications.

In the first part of the further discussion, two steps of the original DOE recovery protocol are modified to enhance the recovery efficiency. The results of the durability test show an improved recovery efficiency compared to the original DOE protocol, particularly at current densities between 0.7 and 1.5 $A \cdot cm^{-2}$. The modified DOE protocol recovers approximately 75 % of reversible performance losses at current densities over 1.0 $A \cdot cm^{-2}$. Additionally, the modified DOE recovery protocol reduces the changed charge transfer resistance caused by the JRC recovery protocol by 60 %. Although the modified DOE recovery protocol has a longer duration of 69 min compared to the original 29-min protocol, it is still favorable for applications with frequent short stops. Moreover, the modified DOE recovery protocol can recover over 50 % of reversible performance degradation in the current density range over 0.5 $A \cdot cm^{-2}$, which is the most relevant current density range for transport applications.

In the second part of the discussion, the effect of temperature reduction from 80 °C to 30 °C on oxygen transfer resistance during the recovery procedure is investigated. This temperature reduction led to a relative recovery of 70 % to 90 % in terms of reversible performance degradation. Water condensation plays a significant role in the regeneration /redistribution of the ionomer structure in the cathode, resulting in improved water uptake. This, in turn, reduces both the ionic transfer and ohmic resistance within the catalyst layer.

However, the temperature reduction recovery procedure leads to an increase in the oxygen transfer resistance in the catalyst layer due to the accumulation of excess water at the interface between the catalyst substrate and the thin ionomer film. Besides, the regeneration/redistribution of the ionomer structure occurs gradually, eventually reaching a quasi-equilibrium state. As a result, the change in the fuel cell impedance during the recovery procedures also shows a time-dependent characteristic.

7 Outlook

The objective of this research is to enhance comprehension of reversible performance deterioration and the development of efficient recovery procedures for PEMFCs. Achieving these goals is crucial for ensuring reliable assessment of fuel cell performance and extending their lifetime. However, investigating the recovery mechanisms is complicated due to the intricate nature of reversible fuel cell performance degradations. Therefore, the following factors should be considered for future studies.

(i) Several factors associated with PEMFC applications, such as operation parameters, fuel cell materials, flow field design, gas contaminants, and fuel cell dimensions, affect the extent of reversible and irreversible performance degradation.

(ii) The recovery mechanism for a given recovery procedure can differ across the investigated current density range and should be analyzed separately.

(iii) In certain cases, a recovery method's efficiency may result from multiple recovery mechanisms, requiring further exploration to distinguish their individual contributions.

(iv) The regeneration/redistribution of the ionomer structure in the cathode contributes to the recovery mechanism. However, nanoscale investigations are necessary for further identification.

Article II and Section 5.1 highlight the importance of considering the limitations of a PEMFC system while designing recovery procedures. The following concerns must be taken into account:

(i) The system constraints, such as available gases and external devices, must be considered while developing recovery procedures for PEMFC systems.

(ii) Different recovery procedures must be selected based on their suitability for specific PEMFC applications. For instance, operando recovery procedures are more suitable for transport applications where shut-down events are frequent.

(iii) Recovery procedures can be combined with shut-down strategies of PEMFC systems, as the shut-down step involves a cell cooling-down procedure and can result in recovery of performance degradation.

(iv) The recovery efficiency of a recovery procedure may vary over time due to

irreversible performance degradation accumulation during the PEMFC system's lifetime.

(v) Practical recovery procedures typically comprise several steps because of the reversible performance degradation's complexity. Thus, different steps can be combined to achieve a high recovery efficiency.

(vi) Ideally, recovery procedures should be adjusted based on the fuel cells' health diagnostics, which entail assessing the type and quantity of performance degradation during operation.

Eventually, there is still a significant amount of work that must be undertaken to comprehend recovery mechanisms and develop recovery procedures both in the laboratory and industry.

8 Scientific articles

8.1 Article I

Quantification of effects of performance recovery procedures for polymer electrolyte membrane fuel cells

Zhang, Q., Schulze, M., Gazdzicki, P., & Friedrich, K. A.

Journal of Power Sources 512 (2021): 230467

DOI: https://doi.org/10.1016/j.jpowsour.2021.230467

Contribution of Qian Zhang: Conception of the work, execution of experiments, as well as writing, data analysis, and reviewing.

Journal of Power Sources 512 (2021) 230467

Contents lists available at ScienceDirect

Journal of Power Sources

journal homepage: www.elsevier.com/locate/jpowsour

Quantification of effects of performance recovery procedures for polymer electrolyte membrane fuel cells

Qian Zhang [a,b,*], Mathias Schulze [a], Pawel Gazdzicki [a], K. Andreas Friedrich [a,b]

[a] German Aerospace Center (DLR), Institute of Engineering Thermodynamics, Pfaffenwaldring 38-40, 70569, Stuttgart, Germany
[b] University of Stuttgart, Institute for Building Energetics, Thermal Engineering and Energy Storage (IGTE), Pfaffenwaldring 31, 70569, Stuttgart, Germany

HIGHLIGHTS

- Methodology for quantification of reversible voltage losses versus current density.
- Reversible losses using logged voltage data and polarization curves leads to similar results.
- Analysis of effect of electrochemical measurements on the evolution of recovery.
- Analyzed parameters demonstrate recovered performance losses as well as non-recovered losses.

ARTICLE INFO

Keywords:
Polymer electrolyte membrane fuel cells
Reversible degradation
Irreversible degradation
Recovery procedure
Durability evaluation

ABSTRACT

To distinguish and mitigate the reversible and irreversible performance degradation of polymer electrolyte membrane fuel cells (PEMFCs), the evaluation and investigation of recovery procedures are of great importance. In this work, a methodology for quantification of recovery of reversible voltage losses is presented taken a durability test containing well-defined operation periods interrupted by two recovery procedures as an example. Each recovery procedure is characterized by polarization curves and electrochemical impedance spectroscopy (EIS). To evaluate the influence of the two used recovery procedures on the fuel cell performance, four factors are considered: (i) absolute recovered voltage, (ii) absolute non-recovered voltage, (iii) relative recovery related to previous operation period, and (iv) relative recovery related to the beginning of the test. The results show that voltage recovery quantified using polarization curves and voltage data logged during load cycling lead to the same result. Hence, to briefly assess the efficiency of a recovery procedure in a (narrow) current density range covered by the used load cycling profile, in-depth electrochemical characterization is not required. Moreover, EIS data were used to determine the main mechanisms leading to recovery. By this means, weaknesses of specific recovery procedures can be identified in order to propose specific improvements.

1. Introduction

Polymer electrolyte membrane fuel cells (PEMFCs) are commonly envisioned to be a promising energy conversion device for power systems due to the high efficiency and low emission. To be competitive to internal combustion engines (ICEs) in transport applications, for the year 2030 the European Commission sets a targeted lifetime of fuel cell system of 7000 h and 30000 h for fuel cell light-duty and heavy-duty vehicles, respectively [1]. To achieve the targeted longevity, performance losses need to be mitigated. During the lifetime of the PEMFCs, the components undergo various operating conditions resulting in both mechanical and chemical degradation [2]. However, part of these performance losses is recoverable and can be assigned to various phenomena such as (i) catalyst surface oxidation [3,4], (ii) contamination of catalyst surface [5,6], (iii) ionomer and membrane degradation [7,8] and (iv) water management phenomena [9,10], and (v) other possible reasons like catalyst support degradation [11,12]. We have recently discussed the phenomena in a review paper [13]. The reversible performance degradation can be recovered by specific procedures while the irreversible losses can only be avoided by operation strategy and material improvement. The understanding of the recovery mechanism and the development of recovery procedures are still under discussion [14,15]. Moreover, reversible degradation also potentially accelerates irreversible degradation which is another motivation why it is important to

* Corresponding author. German Aerospace Center (DLR), Institute of Engineering Thermodynamics, Pfaffenwaldring 38-40, 70569, Stuttgart, Germany.
E-mail address: qian.zhang@dlr.de (Q. Zhang).

https://doi.org/10.1016/j.jpowsour.2021.230467
Received 19 June 2021; Received in revised form 12 August 2021; Accepted 30 August 2021
Available online 17 September 2021

regularly recover reversible losses during the PEMFC lifetime.

Thus, it is important to investigate and quantify the reversible and irreversible performance losses in order to develop suitable recovery procedures and assess their efficiency. Many studies investigate the effects of specific recovery procedures by applying electrochemical measurements before and after the recovery procedures [16–18]. However, it is necessary to consider the impact of characterization methods used to determine recovery on the recovery itself. For instance, when cyclic voltammetry (CV) measurements are carried out to evaluate the electrochemical surface area (ECSA) of catalyst particles before and after the recovery procedure [4,7,8,10,19,20], one needs to take into account that such measurement can already recover (depending on the applied electrode potentials) catalyst poisoning due to CO or sulfur-containing airborne contaminants or H_2S in the hydrogen feed [21–23]. Besides, the performance losses resulting from the formation of platinum oxides (PtO_x) on the cathode catalyst surface can be removed by low cathode potential (0.2 or 0.3 V) [3,24,25]. For instance, limiting current measurements which lead to low cathode potentials used to evaluate the change of total mass transport resistance [8,26], can unintentionally improve the kinetics of the fuel cell. Similarly, low cathode potential can also be achieved during the measurement of proton conduction resistance using electrochemical impedance spectroscopy (EIS) tests in H_2/N_2. Despite both the Joint Research Center (JRC) of the European Commission and the Department of Energy of the USA (DOE) propose specific recovery procedures [27,28], a uniform method to quantify the recovery effect is not established.

Therefore, a methodology for the evaluation and comparison of the efficiencies of recovery procedures is proposed in this paper. The influence of performance characterization methods is also considered and discussed. In general, this paper aims to contribute to establishing an approach for quantification of reversible performance losses during the lifetime of fuel cells and to contribute to the reliable performance benchmarking of fuel cells.

2. Experimental

2.1. Single cell and test bench

The single cell and fuel cell test bench used in this study are home-developed at the German Aerospace Center (Deutsches Zentrum für Luft-und Raumfahrt e.V., DLR) in Stuttgart. The single cell has triple-channel-serpentine flow fields arranged in co-flow configuration. As sealing, Ice Cube Sealing from Freudenberg FST GmbH was used with 350 μm thickness. The test bench software enables the automatic control of a variety of operating parameters, including a maximum operating current of 60 A to the fuel cell provided by a commercial electronic load. More information about the hardware is available in previous works of our group [29–31].

The 5-layer membrane electrode assembly (MEA) used in this experiment was manufactured by IRD Fuel Cells A/S following DLR's specifications for the purpose of this investigation. It is composed of (i) Nafion™ XL membrane, (ii) Pt/C ratio of 50 wt % in both electrodes with an active area of 5×5 cm^2, (iii) Pt loadings of 0.05 and 0.25 mg cm^{-2} in anode and cathode electrodes, and (iv) the MEA is sandwiched by two pieces of gas diffusion layers (GDLs) of Sigracet® 29BC.

2.2. Test protocols

As shown in the flow chart of Fig. 1, the test used to demonstrate the methodology for quantifying recovery of reversible performance losses consists of the following steps: (i) MEA conditioning at the beginning of the test, (ii) an operation period, and (iii) a recovery procedure. Data containing two operation periods and two recovery procedures were used for this study. Each operation period contains a block of load cycling and electrochemical performance characterization, including polarization curves and EIS measurements before and after the accelerated stress test (AST).

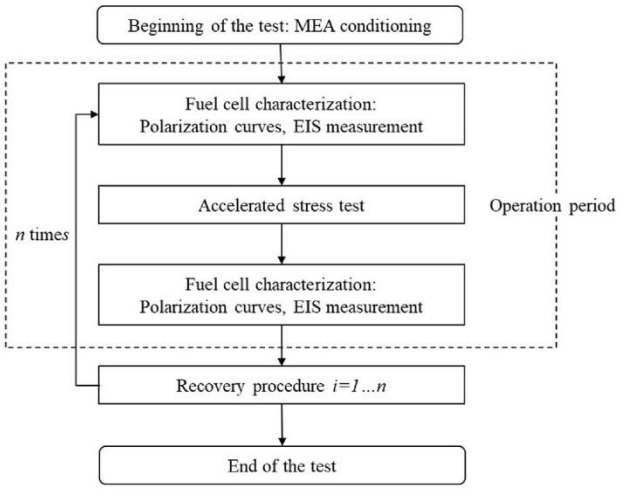

Fig. 1. The process of the durability test for the study of recovery procedures.

2.2.1. Load cycling

In this experiment, the Fuel Cell Dynamic Load Cycle (FC-DLC) protocol [27] was performed continuously for 80 h before applying a recovery procedure. During load cycling the fuel cell was operated with constant H_2 (anode) and air (cathode) flow rates of 0.263 and 0.83 L min^{-1}, respectively, corresponding to H_2 and air stoichiometry of 1.5 and 2 for the current density of 1 A cm^{-2}. The cell temperature was kept at 80 °C. The absolute gas pressures of the anode and cathode outlets were 250 and 230 kPa_{abs} while the relative humidity of both gases was set to 100%.

2.2.2. Performance characterization

Before and after each operation period, the performance of the fuel cell was characterized with polarization curves and EIS measurements. These two characterization measurements are not considered as part of recovery procedures. The polarization curve test followed the recommendation by the EU Harmonized Test Protocols for MEA testing [27]. The current density was increased from 0 to 1.9 A cm^{-2} in steps of 0.05 or 0.1 A cm^{-2} and then decreased to 0 A cm^{-2}. The data were acquired every second and then averaged over the last 30 s of the dwell time. The error bars correspond to the standard deviation from the average. EIS was carried out with the modular electrochemical workstation Zennium X and electronic load PP241 from ZAHNER-Elektrik GmbH & CoKG under three constant current densities of 0.1, 1.0, and 1.4 A cm^{-2}. The EIS data were analyzed with the Thales XT software package.

2.2.3. Recovery procedure

As shown in Fig. 1, a recovery procedure is conducted after each operation period and electrochemical characterization. In this paper, the recovery protocol from JRC [27] and DOE [28], referred to as recovery procedure 1 (Recovery 1) and recovery procedure 2 (Recovery 2), were applied once after the first and second operation period, respectively. The recovery procedure from JRC consists of H_2 soak, N_2 purge, air purge and shut-down steps. On the other hand, the recovery procedure from DOE consists of N_2 purge, air soak, N_2 purge and H_2 soak steps. Since this paper is focusing on methodology, the reproducibility and detailed recovery mechanisms of Recovery 1 and Recovery 2 are not addressed here. Detailed description, duration of each step and possible recovery mechanism of each recovery procedure are reported in our recent publication [32]. Moreover, short descriptions of the recovery procedures are provided in the supporting information as Table S1 and Table S2.

3. Results and discussion

In section 3.1, a methodology to determine recovered voltage losses is introduced. The application of this methodology using (i) voltage data logged during load cycling and (ii) polarization curves is discussed in section 3.2. Eventually, the aim of section 3.3 is to complement the outcomes from section 3.2 using EIS analysis allowing the understanding of the recovery process in more detail.

3.1. Methodology to evaluate recovery procedures

Performance degradation of the fuel cells is successive and accumulative. To eliminate reversible effects, it is targeted by DOE to achieve 95% recovery of reversible degradation in less than 30 s [28]. However, to be able to assess the efficiency of certain recovery procedures, reliable procedures for the evaluation of a performance recovery are required. Moreover, the recovery efficiency depends on the current density. In the literature, approaches how to describe reversible and irreversible degradation are proposed [15,27,28,30]. However, there are no common approaches to describe performance recovery which strongly depends on cell operation history. In other words, when assessing performance recovery, it is mandatory to specify the reference values which is used to quantify voltage recovery values. Therefore, a methodology how to enable a reliable evaluation of the effectiveness of a recovery procedure is discussed in the following.

For the clarification of the definitions used to quantify the impact of the recovery procedures, a scheme of a fuel cell durability test including n recovery procedures is provided in Fig. 2.

The evaluation of performance degradation rate using cell voltage values either from durability tests or from polarization curves is the most practical method. As the red lines shown in Fig. 2, after each operation period numbered $i = 1, 2, \ldots, n$, a recovery procedure is performed. The voltage values $U_{i=n}^{Begin}$ and $U_{i=n}^{End}$ indicate the cell voltages at the beginning and end of the n^{th} operation period, respectively. The grey dash line estimates the voltage change without recovery procedures, which always shows faster performance degradation than that with recovery procedures.

To analyze the efficiency of the n^{th} recovery procedure, the recovered voltage is defined as Eq. (1),

$$\Delta U_{rec} = U_{i=n+1}^{Begin} - U_{i=n}^{End} \tag{1}$$

while the non-recovered voltage corresponds to the Eq. (2),

$$\Delta U_{nonrec} = U_{i=n}^{Begin} - U_{i=n+1}^{Begin} \tag{2}$$

The relative recovery of n^{th} recovery procedure related to the beginning of the previous operation period is defined as Eq. (3),

$$\eta_{Last} = \frac{\Delta U_{rec}}{U_{Last} - \Delta U_{irrev,\ i=n}} = \frac{\Delta U_{rec}}{U_{i=n}^{Begin} - U_{i=n}^{End} - \Delta U_{irrev,\ i=n}} \tag{3}$$

, where $U_{Last} = U_{i=n}^{Begin} - U_{i=n}^{End}$ is the voltage loss during the n^{th} operation period, as shown in Fig. 2. Besides, $\Delta U_{irrev,\ i=n} = U_{irrev,i=n}^{End} - U_{irrev,i=n}^{Begin}$ is the irreversible voltage loss that occurred during the n^{th} operation period indicated by the green dotted line in Fig. 2. Taking the effect of cell operation history into account, the relative recovery of the n^{th} recovery procedure related to the beginning of the test is determined using Eq. (4),

$$\eta_{Past} = \frac{\Delta U_{rec}}{U_{Past} - U_{irrev,i=n}^{End}} = \frac{\Delta U_{rec}}{U_{BoT} - U_{i=n}^{End} - U_{irrev,i=n}^{End}} \tag{4}$$

, where the $U_{irrev,\ i=n}^{End}$ is the absolute irreversible loss values of the fuel cell after n operation periods. $U_{Past} = U_{BoT} - U_{i=n}^{End}$ indicates the voltage loss after n operation periods compared to that at the beginning of the test, as shown in Fig. 2.

Assuming that the $(n-1)^{th}$ recovery procedure does not recover all of the recoverable performance degradation, the recovery efficiency of the subsequent n^{th} recovery procedure, which is assumed to be more efficient, can be overestimated resulting in a negative ΔU_{nonrec} due to recovery of the accumulated reversible losses from both of the $(n-1)^{th}$ and n^{th} operation periods. Then, η_{Last} can reach values higher than 100% according to Eq. (3) while the η_{Past} still remains below 100%. An example of this effect, which highlights the importance of considering both of the values of η_{Past} and η_{Past} is shown in the support information (see Figure S1).

3.2. Evaluation of relative recovery from durability test

The presented methodology is discussed in the following based on FC-DLC data including two different recovery protocols, Recovery procedure 1 (Recovery 1) and Recovery procedure 2 (Recovery 2).

Fig. 3 a) shows the performed durability test consisting of two

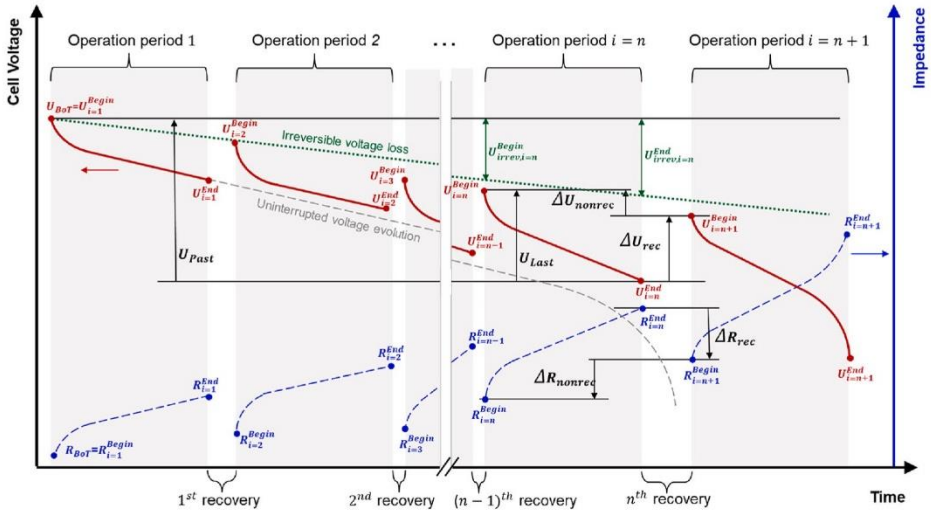

Fig. 2. The scheme of possible cell voltage change (left axis) and cell resistance change (right axis) during a fuel cell durability test consisting of n+1 operation periods interrupted with n recovery procedures.

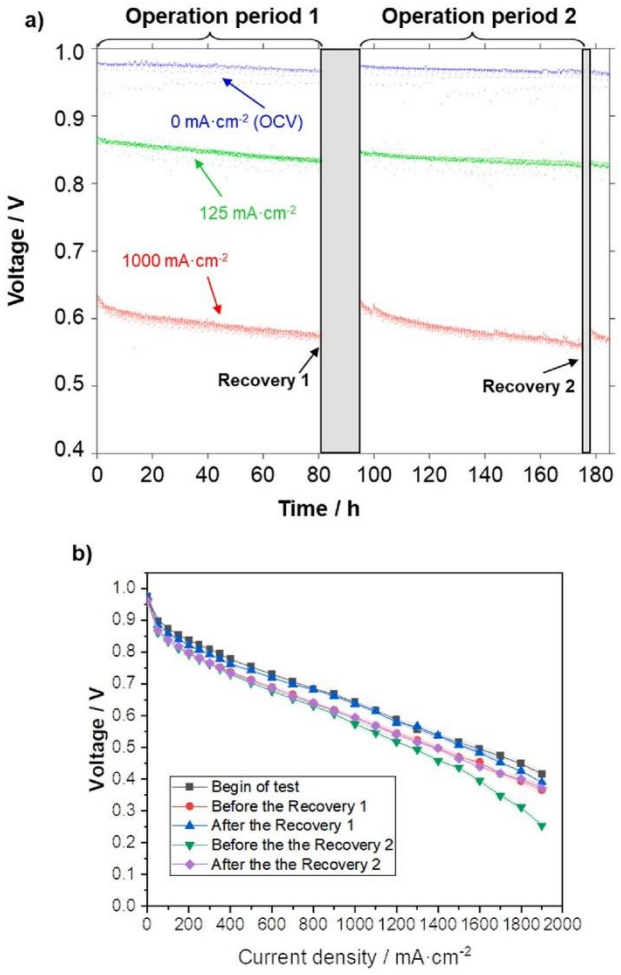

Fig. 3. a) The fuel cell voltage during load cycling using the FC-DLC profile. For clarity of presentation only voltages belonging to the three selected current density levels (indicated in the figure) are shown. b) Polarization curves recorded at the beginning of test, before and after each recovery procedure. The shaded bars correspond to the standard deviation from the average of the last 30 s of the dwell time of each tested current density step.

operation periods using the FC-DLC protocol. While the load cycle contains nine different current density levels, in the figure only three voltage responses at three current density values are selected as an example. Each operation period consists of (i) electrochemical performance characterization, (ii) 82 h continuous operation using FC-DLC, and (iii) the second electrochemical performance characterization. The nine different current density levels of the FC-DLC protocol allow the determination of quasi-polarization curves from the logged voltage data according to the covered current density range from 0 to 1 A cm^{-2}. Moreover, the tests allow clear discrimination between recovered and non-recovered voltage losses after each recovery procedure.

Polarization curves recorded at the beginning of the test, before and after each recovery procedure are provided in Fig. 3 b). The polarization measurements cover a broader current density range than the FC-DLC data, which is an advantage for the evaluation and understanding of the performance degradation of the MEA. EIS was also measured at the beginning of the test, before and after each recovery procedure just following each polarization measurements. EIS spectra at the current density of 0.1, 1.0, and 1.4 A cm^{-2} are presented in Fig. 4a)–c).

In general, the voltage values monitored during the durability test have the advantage of being operando information. On the other hand, polarization curves are performed during the interruption of operation periods and might affect the recovery of reversible losses due to changed operating conditions, such as increased gas flow rate and reduced fuel cell voltage. To analyze the effect of measuring polarization curves on recovery, the methodology from section 3.1 was applied separately to the voltage data monitored during load cycling and to polarization curves. The results are depicted in Fig. 5 for Recovery 1 and Recovery 2. It is noted, that irreversible voltage losses are neglected in the following. Specifically, Fig. 5 a) and e) show the recovered voltage ΔU_{rec} calculated according to Eq. (1) while Fig. 5 b) and d) are the non-recovered cell voltage ΔU_{nonrec} according to Eq. (2). Fig. 5 c), g), d) and h) present recovery relative to the cell voltage change of the previous operation period η_{Last} and that from the beginning of the test η_{Past} according to Eq. (3) and (4), respectively.

In all panels in Fig. 5, the calculated values based on the polarization curves and on load cycling data are consistent. Since the FC-DLC protocol covers current densities up to 1 A cm^{-2}, a comparison at higher current densities is not possible. For the current densities from 0 to 1 A cm^{-2}, the recovered cell voltage ΔU_{rec} due to Recovery 1 and 2 calculated with the polarization curves and FC-DLC data overlapped to a great extent in Fig. 5 a) and e), respectively. Thus, it seems that both of these two recovery procedures are not much influenced by the polarization curves measurements since the recovered cell voltage calculated by load cycling data also contains the impact of the polarization curves measurements. On the other hand, only non-recovered cell voltage ΔU_{nonrec} in Fig. 5 f) determined using load cycling data is slightly lower than the values calculated using polarization curves. Since, polarization curve after recovery is measured before starting load cycling, the lower ΔU_{nonrec} determined by logged cycling data must be attributed to some recovery due to recording the polarization curves. Hence, it is concluded that the Recovery 2 does not recover all the reversible performance losses and at least a part of them are additionally recovered by the polarization curves measurement. Despite that, it can be still summarized that both of these two approaches of recovery evaluation lead to comparable results. However, the approach using polarization curves provides more details due to the broader current density range that can be accessed. For example, η_{Last} and η_{Past} in Fig. 5 g) and h) are higher for Recovery 1 than for Recovery 2 when considering load cycling data. However, using data from polarization curves, it is evident that at the current density above 1.4 A cm^{-2} Recovery 2 outperforms Recovery 1 in the case of η_{Last} and ΔU_{rec}. Besides, Recovery 1 leads to high relative recovery at around 1 A cm^{-2} because (i) the factors η_{Last} and η_{Past} in Fig. 5c) and d) reach almost 100% and (ii) the non-recovered performance loss ΔU_{nonrec} is close to 0 as in Fig. 5 b). A table summarizing the results under the three values of current density is provided in supporting information as Table S3.

The proposed method enables a clear evaluation of relative recovery of a recovery procedure and contributes to the understanding of the mechanism of the recovery, which can be further confirmed with EIS measurements. Besides, different recovery procedures affect the performance at different current density in a different manner [29]. Therefore, it is relevant to evaluate the recovery effect in a wide current density range which can be acquired by polarization curve measurements.

3.3. Analysis of the recovery procedures based on EIS measurements

EIS data are used to support the evaluation of recovery procedures discussed in section 3.2 and to provide insight into the main underlying mechanisms. According to Fig. 2 states at the beginning and end of each operation period are accessible by EIS measurements. Since EIS measurements were performed just after the polarization curves and the three tested current density values were also included in the polarization curves, it can be concluded that the EIS measurements did not lead to additional recovery.

Analogously to the definitions of the voltage values explained in

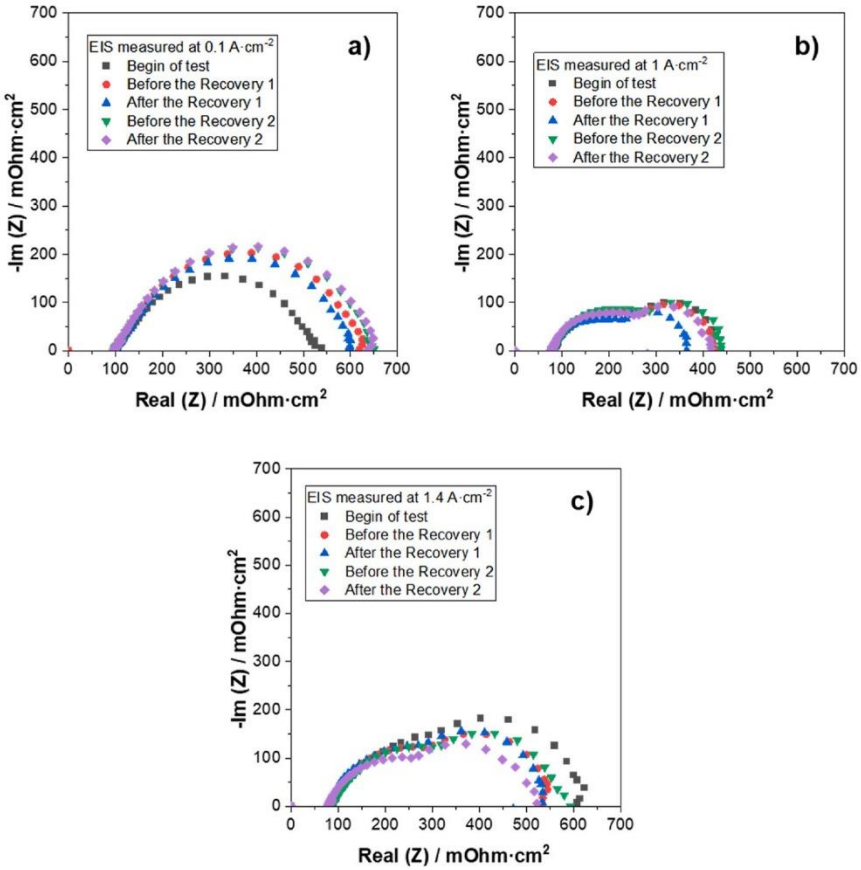

Fig. 4. EIS spectra tested at the beginning of test, before and after each recovery procedure at current density of a) 0.1, b) 1.0 and c) 1.4 A cm^{-2}.

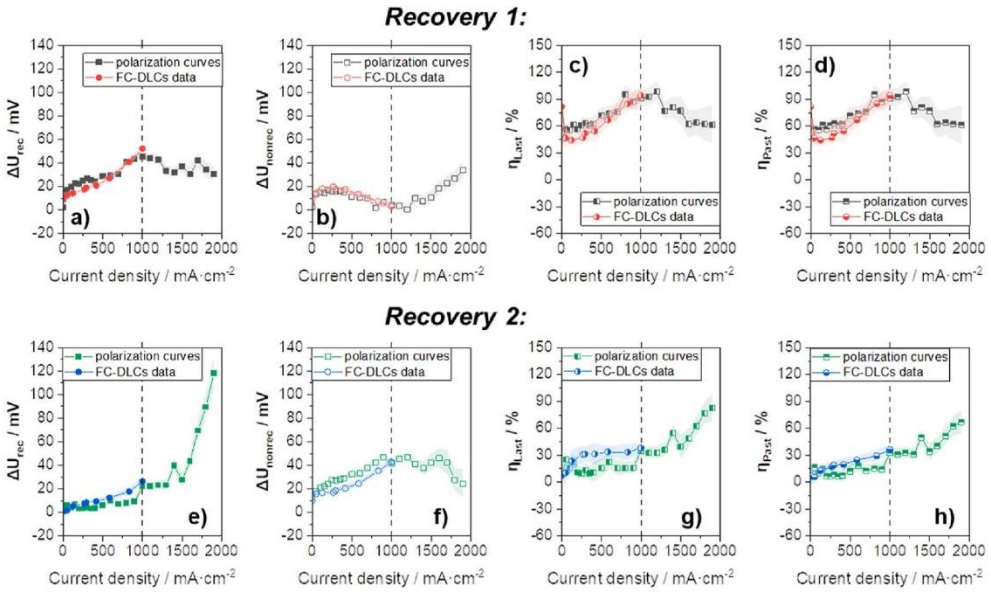

Fig. 5. Evaluation of the relative recovery of the recovery procedure 1 and 2. a) and e): the recovered voltage calculated according to Eq. (1). b) and f): the non-recovered cell voltage according to Eq. (2). c) and g): the relative recovery which relates to the cell voltage change of the previous operation period according to Eq. (3). d) and h): the relative recovery which relates to the cell voltage change from the beginning of the test according to Eq. (4). In each panel, the results are calculated with the voltage data from polarization curves and the FC-DLCs data, respectively. The shaded area of polarization curves corresponds to the standard deviation from the average of the last 30 s of the dwell time of each tested current density step. The shaded area of FC-DLCs data corresponds to the standard deviation from the average of voltage data from the first 3 cycles.

Section 3.1, $R_{i=n}^{Begin}$ and $R_{i=n}^{End}$ stand for the fuel cell resistance at the beginning and end of the n^{th} operation period. The reversible resistance drop due to a recovery procedure is defined as,

$$\Delta R_{rec} = R_{i=n}^{End} - R_{i=n+1}^{Begin} \quad (5)$$

while the non-recovered resistance change is calculated according to,

$$\Delta R_{nonrec} = R_{i=n+1}^{Begin} - R_{i=n}^{Begin}. \quad (6)$$

At high current density, the mass transfer resistance is dominant, while at low current density the charge transfer resistance has the main contribution to total impedance. In this experiment, the EIS data were collected at current density values of 0.1, 1.0, and 1.4 A cm^{-2} as shown in Fig. 3 c) and d) and e). The EIS data was evaluated using the equivalent electric circuit shown in Fig. 6 a). It consists of three elements in series: (i) a resistor R_{Ohmic} describes the ohmic resistance of the MEA including the contact resistance of the fuel cell components, (ii) a mass transfer resistance circuit consisting of $R_{Mass\ transfer}$ in parallel with a constant phase element CPE_1 and (iii) a charge transfer circuit consisting of $R_{Charge\ transfer}$ in parallel with CPE_2 which describes the cathode catalyst layer. The model was selected due to its simplicity and capability to determine the main mechanism necessary to assess the recovery procedures. The equivalent electric circuit in this experiment is selected according to the past empirical studies [33].

The recovered and non-recovered ohmic, charge transfer, and mass transfer resistance due to Recovery 1 and Recovery 2 are calculated according to Eq. (5) and (6) and displayed in Fig. 6b)–e). Thereby, performance recovery, i.e. reduction of resistance, is indicated by a positive ΔR_{rec}; a negative value indicates an increased resistance, i.e. additional performance losses due to detrimental effect. In combination with the observation based on voltage data from durability test and polarization curves in the last section, EIS data allow the distinction effects involved in the recovery process. Evidently, in the case of Recovery 1, the recovered losses, ΔR_{rec}, are due to a uniform reduction of charge transfer resistance in the range 0.1–1.4 A cm^{-2} as well as reduction of mass transport resistance, which dominates at high current density range. Changes in ohmic resistance are not caused by the recovery procedure. From the parameter of non-recovered ohmic ΔR_{nonrec}, it is concluded that non-recovered performance losses (irreversible degradation and/or reversible) are attributed to charge transfer resistance at 0.1 and 1.0 A cm^{-2} as well as to ohmic resistance at 0.1 A cm^{-2}. Mass transfer resistance at 1.0 A cm^{-2} reduced indicating that the performance of the MEA after Recovery 1 is slightly higher than at the beginning of the test which is consistent with the polarization curves shown in Fig. 5 b). In the case of Recovery 2, the dominating effect is the reduction of mass transfer resistance, especially in the high current density range. The reduction of charge transfer resistance is minor and substantially lower than that due to Recovery 1. According to the non-recovered resistance, ΔR_{nonrec}, Recovery 2 exhibits substantial non-recovered charge transfer losses. Hence, the data provide a straightforward way to compare and assess recovery procedures. Further analysis about the mechanism of each recovery procedure can be done in combination with the performed steps of the recovery procedure, which was clarified detailed in our recent published paper [32]. Briefly, it can be concluded that:

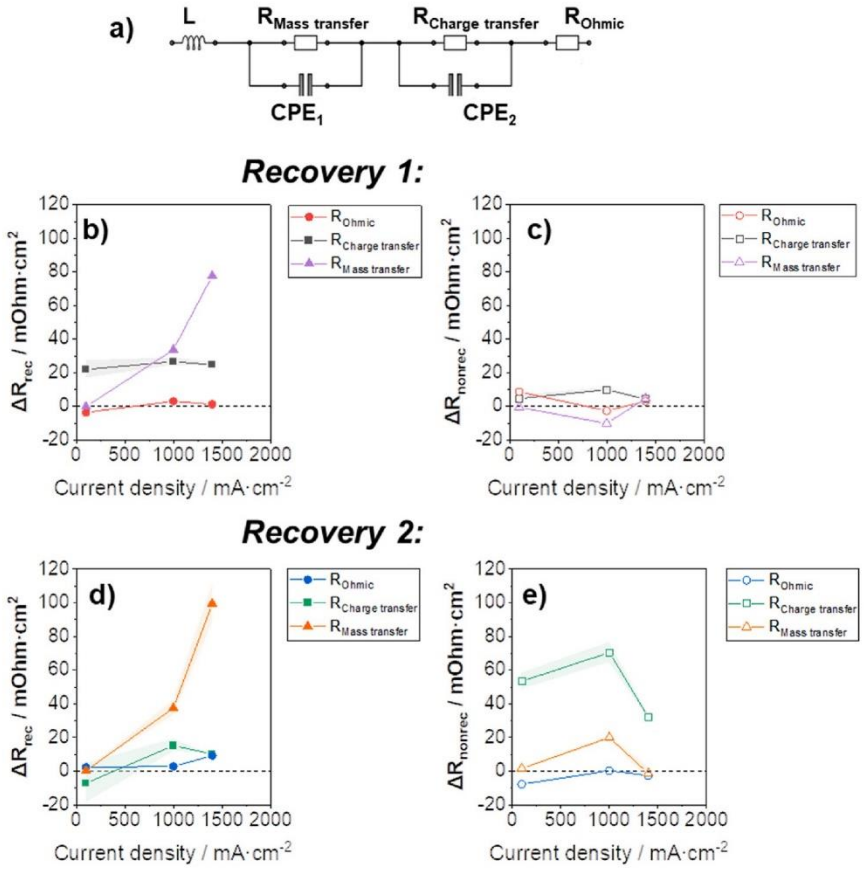

Fig. 6. a) is the used model to fit with the EIS results. b) and d) are the recovered resistance calculated according to Eq. (5) for Recovery 1 and 2. c) and e) show the non-recovered cell resistance according to Eq. (6) for Recovery 1 and 2. Impedance analysis showing the changes of ohmic, charge transfer and mass transfer resistance measured at 0.1, 1.0 and 1.4 A cm^{-2}. The shaded area corresponds to the error of fitting results given by Thales XT software.

(i) Recovery 1 is more efficient than Recovery 2 in the entire current density range. Recovery 1 recovered the kinetic losses by the reduction of Pt oxides on the catalyst surface and structure change of ionomer by reducing the cathode potential and fuel cell temperature;
(ii) The weak point of Recovery 2 is the poor recovery efficiency towards charge transfer resistance resulting from the insufficient time for reduction of Pt oxides and not considering the likely structure change of ionomer occurring at low temperatures;
(iii) Recovery 1 and 2 have relatively high recovery at high current density related to the reduction of mass transfer resistance due to the contribution of gas purging to water removal.

4. Conclusions

In this work, a methodology for the quantification of the impact of recovery procedures to recover reversible performance losses of PEMFC is presented.

The study of recovery procedures, including the understanding of recovery mechanisms, is beneficial to clearly distinguish reversible and irreversible performance degradation at certain operating conditions. The proposed methodology includes quantification of reversible losses versus current density based on logged voltage data from load cycling tests as well as polarization curves and EIS data. It is shown that using logged voltage data from load cycling tests and using polarization curves for the determination of the efficiency of a recovery procedure leads to the same result. Data from load cycling tests are transient responses of the fuel cell while data from polarization curves present steady-state fuel cell performance. The advantage of using logged voltage data from the cycling test is that no interruption of the test for characterization is required and the method is considered operando appropriate. However, only a narrow current density range covered by the load cycling test can be explored. To cover a broader current density range, polarization curves measurement is the favored approach, which was also addressed as a necessary experimental characterization method to identify the cell performance losses in the literature [34]. If details on underlying recovery mechanisms are required, EIS analysis involving a simple equivalent circuit is used. The analyzed parameters give information on recovered performance losses as well as non-recovered losses, therefore, allowing the identification of weak points of the studied recovery procedures.

CRediT authorship contribution statement

Qian Zhang: Conceptualization, Methodology, Software, Validation, Formal analysis, Investigation, Writing – original draft, Writing – review & editing. **Mathias Schulze:** Conceptualization, Methodology, Writing – review & editing, Supervision. **Pawel Gazdzicki:** Conceptualization, Methodology, Writing – review & editing, Supervision. **K. Andreas Friedrich:** Conceptualization, Methodology, Writing – review & editing, Supervision.

Declaration of competing interest

The authors declare that they have no known competing financial interests or personal relationships that could have appeared to influence the work reported in this paper.

Acknowledgments

Qian Zhang gratefully acknowledges financial support from China Scholarship Council. The work is linked to the FCCP project. This FCCP (Fuel Cell Cargo Pedelec) project has received funding from the Interreg North-West Europe under NWE596 in the program Priority Axis2 Low Carbon, specific objective SO4.

Appendix A. Supplementary data

Supplementary data to this article can be found online at https://doi.org/10.1016/j.jpowsour.2021.230467.

References

[1] EERA Joint Programme on Fuel Cells and Hydrogen (JP FCH) and Hydrogen Europe Research. KEY PERFORMANCE INDICATORS (KPIS) for FCH RESEARCH and INNOVATION, 2020 - 2030, 2020.
[2] F.A.D. Bruijn, V.A.T. Dam, G.J.M. Janssen, Fuel Cell. 8 (2008) 3–22.
[3] M. Zago, A. Baricci, A. Bisello, T. Jahnke, H. Yu, R. Maric, P. Zelenay, A. Casalegno, J. Power Sources 455 (2020) 227990.
[4] I. Pivac, F. Barbir, Fuel Cell. 20 (2020) 185–195.
[5] J. Qi, Y. Zhai, J. St-Pierre, J. Power Sources 413 (2019) 86–97.
[6] J. St-Pierre, U. Pasaogullari, T. Cheng, W. Collins, Office of Scientific and Technical Information, OSTI), 2017.
[7] D.A. Langlois, A.S. Lee, N. Macauley, S. Maurya, M.E. Hawley, S.D. Yim, Y.S. Kim, J. Power Sources 396 (2018) 345–354.
[8] F. Du, T.A. Dao, P.V.J. Peitl, A. Bauer, K. Preuss, A.M. Bonastre, J. Sharman, G. Spikes, M. Perchthaler, T.J. Schmidt, J. Electrochem. Soc. 167 (2020) 144513–144527.
[9] J.P. Owejan, T.A. Trabold, J.J. Gagliardo, D.L. Jacobson, R.N. Carter, D.S. Hussey, M. Arif, J. Power Sources 171 (2007) 626–633.
[10] Z. Qi, H. Tang, Q. Guo, B. Du, J. Power Sources 161 (2006) 864–871.
[11] F. Maillard, A. Bonnefont, F. Micoud, Electrochem. Commun. 13 (2011) 1109–1111.
[12] L. Dubau, M. Lopez-Haro, L. Castanheira, J. Durst, M. Chatenet, P. Bayle-Guillemaud, L. Guétaz, N. Caqué, E. Rossinot, F. Maillard, Appl. Catal. B Environ. (2013) 801–808, 142-143.
[13] J. Mitzel, Q. Zhang, P. Gazdzicki, K.A. Friedrich, J. Power Sources 488 (2021) 229375.
[14] M.L. Perry, T. Patterson, C. Reiser, Ecs Transactions 3 (2006) 783.
[15] S. Kundu, M. Fowler, L.C. Simon, R. Abouatallah, J. Power Sources 182 (2008) 254–258.
[16] M. Chen, C. Du, J. Zhang, P. Wang, T. Zhu, J. Power Sources 196 (2011) 620–626.
[17] Prass, Zamel Friedrich, Molecules 24 (2019) 3514.
[18] A. Kabasawa, J. Saito, K. Miyatake, H. Uchida, M. Watanabe, Electrochim. Acta 54 (2009) 2754–2760.
[19] Y.A. Gomez, A. Oyarce, G. Lindbergh, C. Lagergren, J. Electrochem. Soc. 165 (2018) F189–F197.
[20] F. Wang, D. Yang, B. Li, H. Zhang, C. Hao, F. Chang, J. Ma, Int. J. Hydrogen Energy 39 (2014) 14441–14447.
[21] W. Shi, B. Yi, M. Hou, F. Jing, H. Yu, P. Ming, J. Power Sources 164 (2007) 272–277.
[22] R. Mohtadi, W.k. Lee, J.W. Van Zee, J. Power Sources 138 (2004) 216–225.
[23] I.G. Urdampilleta, F.A. Uribe, T. Rockward, E.L. Brosha, B.S. Pivovar, F.H. Garzon, Ecs Transactions 11 (2007) 831–842.
[24] Y. Liu, M. Mathias, J. Zhang, Electrochem. Solid State Lett. 13 (2010) B1–B3.
[25] C.H. Paik, T.D. Jarvi, W.E. O'Grady, Electrochem. Solid State Lett. 7 (2004) A82–A84.
[26] S. Jomori, K. Komatsubara, N. Nonoyama, M. Kato, T. Yoshida, J. Electrochem. Soc. 160 (2013) F1067–F1073.
[27] G. Tsotridis, A. Pilenga, G. De Marco, T. Malkow, JRC Science for Policy Report, 2015, p. 27632.
[28] U.S. DOE, The Fuel Cell Technologies Office Multi-Year Research, Development, and Demonstration Plan, Technical report, US Department of Energy, 2016.
[29] P. Gazdzick, J. Mitzel, D. Garcia Sanchez, M. Schulze, K.A. Friedrich, J. Power Sources 327 (2016) 86–95.
[30] D.G. Sanchez, T. Ruiu, I. Biswas, M. Schulze, S. Helmly, K.A. Friedrich, J. Power Sources 352 (2017) 42–55.
[31] K. Talukdar, P. Gazdzicki, K.A. Friedrich, J. Power Sources 439 (2019).
[32] Q. Zhang, M. Schulze, P. Gazdzicki, K.A. Friedrich, Comparison of different performance recovery procedures for polymer electrolyte membrane fuel cells, Appl. Energy 302 (2021) 117490.
[33] M. Schulze, N. Wagner, T. Kaz, K.A. Friedrich, Electrochim. Acta 52 (2007) 2328–2336.
[34] A. Husar, S. Strahl, J. Riera, Int. J. Hydrogen Energy 37 (2012) 7309–7315.

SUPPORTING INFORMATION FOR

Quantification of Effects of Performance Recovery Procedures for Polymer Electrolyte Membrane Fuel Cells

Qian Zhang[1, 2, *], Mathias Schulze[1], Pawel Gazdzicki[1], K. Andreas Friedrich[1, 2]

[1]: German Aerospace Center (DLR), Institute of Engineering Thermodynamics, Pfaffenwaldring 38-40, 70569 Stuttgart, Germany

[2]: University of Stuttgart, Institute for Building Energetics, Thermal Engineering and Energy Storage (IGTE), Pfaffenwaldring 31, 70569 Stuttgart, Germany

*: qian.zhang@dlr.de, +49 711 6862 8821

1. Recovery procedures

Table S1: Details of the JRC recovery protocol [27] referred as Recovery 1 in the paper

Step		Cathode	Anode	Duration
1	H_2 soak	Shut off	H_2 1.5 L·min^{-1} until U<0.1V	25 min
2	N_2 purge	Dry N_2 1.5 L·min^{-1}		30 min
3	Air purge	Dry Air 1.5 L·min^{-1}		30 min
4	Shut-down	Stop gas supply; Stop heating the cell; Release pressure; Cell outlets open		8 h
5	Restart	N_2 1.5 L·min^{-1}; start heating the cell		30 min

Table S2: Details of the DOE recovery protocol [28] referred as Recovery 2 in the paper.

Step		Cathode	Anode	Duration
1	N_2 purge	Dry N_2 4 L·min^{-1}	Dry N_2 2 L·min^{-1}	2 min
2	Air soak	Air 4 L·min^{-1}	Shut off	15 min
3	N_2 purge	Dry N_2 4 L·min^{-1}	Dry N_2 2 L·min^{-1}	2 min
4	H_2 soak	Shut off	H_2 2 L·min^{-1}	10 min

2. Operation history

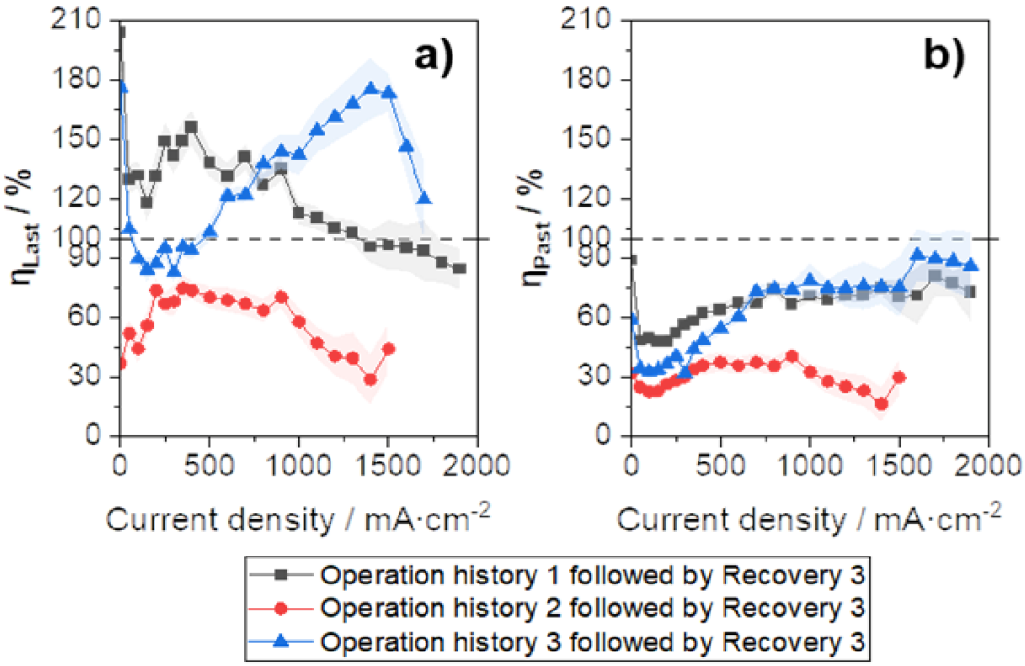

Figure S1: η_{Last} (a) and η_{Past} (b) after three different durability tests with same number of FC-DLC operation, but with different sequence of different recovery procedures (i.e. different operation history). However, all of them had the same recovery procedure (see Ref. 29) as the final recovery protocol.

To further clarify the difference and significance of η_{Last} and η_{Past} which strongly depends on the operation history of a recovery procedure, the Figure S1 is displayed. The three durability tests in Figure S1 have the same number of operation periods and all of them contain the same recovery procedure at the end of test, whereas all the former recovery protocols are different. Apparently, η_{Last} of the Recovery 3 in three durability tests differ from each other significantly at the whole current density range while in two of three durability tests the η_{Past} are largely identical. It can be concluded that the preceding recovery procedures in the first and third durability tests are less efficient than the Recovery 3. Thus, it is necessary to take both of the values of η_{Past} and η_{Past} into consideration especially when several different recovery procedures are involved in a durability test consisted of several operation periods.

3. Quantification of Recovery 1 and Recovery 2

Table S3: Evaluation of Recovery 1 and Recovery 2 at the current density of 0.1, 1.0 and 1.4 A·cm^{-2}. Data are determined from the polarization curves tests shown in Figure 5.

	Current density /A·cm^{-2}	**ΔU_{rec} /mV**	**ΔU_{nonrec} /mV**	**η_{Last} /%**	**η_{Past} /%**
Recovery 1	0.1	19.5±1.8	15.5±1.9	55.7±6.4	55.7±6.4
	1.0	45.5±3.8	4.5±4.0	91±10.4	91±10.4
	1.4	32±4.4	7.5±4.7	81.0±11.5	81.0±11.5
Recovery 2	0.1	4±1.5	21.0±1.8	16.0±8.2	9.9±5.2
	1.0	22±3.4	41.5±3.5	34.6±6	32.4±6
	1.4	39.5±5.1	37.5±5.9	54.9±8.4	49.7±7.5

8.2 Article II

Comparison of different performance recovery procedures for polymer electrolyte membrane fuel cells

Zhang, Q., Schulze, M., Gazdzicki, P., & Friedrich, K. A.

Applied Energy 302 (2021): 117490

DOI: https://doi.org/10.1016/j.apenergy.2021.117490

Contribution of Qian Zhang: Conception of the work, Execution of experiments, as well as Writing, Data analysis, and Reviewing.

Applied Energy 302 (2021) 117490

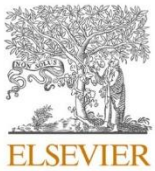

Contents lists available at ScienceDirect

Applied Energy

journal homepage: www.elsevier.com/locate/apenergy

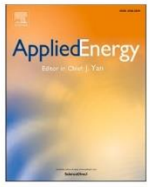

Comparison of different performance recovery procedures for polymer electrolyte membrane fuel cells

Qian Zhang [a,b,*], Mathias Schulze [a], Pawel Gazdzicki [a], K. Andreas Friedrich [a,b]

[a] German Aerospace Center (DLR), Institute of Engineering Thermodynamics, Pfaffenwaldring 38-40, 70569 Stuttgart, Germany
[b] University of Stuttgart, Institute for Building Energetics, Thermal Engineering and Energy Storage (IGTE), Pfaffenwaldring 31, 70569 Stuttgart, Germany

HIGHLIGHTS

- Quantitative analysis and comparison of three different recovery procedures.
- All procedures yield high recovery in mass transfer resistance.
- Short H_2 soak insufficient to recover increase of charge transfer resistance.
- Careful dry gas purge crucial to avoid increase of ohmic resistance.
- Quantification of performance recovery needs to consider operation history.

ARTICLE INFO

Keywords:
Polymer Electrolyte Membrane Fuel Cells
Reversible Degradation
Irreversible Degradation
Recovery Procedure
Durability Evaluation

ABSTRACT

To both extend system lifetime and enable reliable performance benchmarking, recovery procedures are of great importance to distinguish and mitigate the reversible and irreversible performance degradation of polymer electrolyte membrane fuel cells. In this work, three common recovery procedures available in the literature (JRC-based protocol, DOE-based protocol, and overnight rest) being part of a load cycling durability test are characterized by polarization curves and electrochemical impedance spectroscopy. Such direct comparison using same conditions and material has not been published so far. To compare the relative recovery of the three recovery procedures the recovery related to the last operation period, to the beginning of the whole test, and the non-recovered performance loss within each operation period are assessed. Moreover, the mechanisms leading to the various recovery effects are analyzed. Generally, with the contribution of gas purging to water removal, all three recovery procedures reduce greatly mass transfer resistance and recover most of the performance loss in the high current density range. At lower current density, the three procedures differ substantially. In the case of JRC-based protocol, the kinetic losses are recovered by the reduction of Pt oxides and structure change of ionomer by reducing the cathode potential and fuel cell temperature, respectively. The overnight rest results in similar recovery of the performance loss. The DOE-based protocol leads to relatively low recovery of losses in the kinetic region of the polarization curves. Additionally, the effect of the cell operating history is considered.

1. Introduction

Nowadays polymer electrolyte membrane fuel cells (PEMFCs) are commonly considered as promising energy conversion devices due to their high efficiency and zero emission if fed with 'green' hydrogen. However, specific challenges needs to be addressed to achieve the required key performance indicators, such as longevity, power density, and cost [1]. During the PEMFCs' lifetime its components experience various operating conditions such as idling, start-up and shut-down, and transient load changing, which lead to mechanical and chemical degradation. Mitigation of these degradation effects is necessary to achieve acceptable longevity [2,3]. However, part of these performance losses is recoverable by specific refresh procedures [4]. Responsible phenomena for reversible voltage decay are (i) formation of platinum oxides [5,6], (ii) water flooding of the catalyst layers [7,8], (iii) the adsorption of contaminants on the catalyst surface from gas [9] and fuel impurities [10,11], (iv) ionomer structure degradation [12,13] and (v) other possible reasons like contamination of ionomer [14,15]. On the

* Corresponding author at: German Aerospace Center (DLR), Institute of Engineering Thermodynamics, Pfaffenwaldring 38-40, 70569 Stuttgart, Germany.
E-mail address: qian.zhang@dlr.de (Q. Zhang).

https://doi.org/10.1016/j.apenergy.2021.117490
Received 11 February 2021; Received in revised form 20 July 2021; Accepted 27 July 2021
Available online 14 August 2021

other hand, irreversible performance degradation arises from permanent fuel cell material changes like membrane thinning [16,17], catalyst particles dissolution [18] and agglomeration [19], or carbon corrosion [20,21]. Moreover, irreversible material changes also affect reversible performance losses impeding a straight-forward discrimination. Besides, both reversible and irreversible degradation strongly depend on specific operating conditions [22].

Numerous publications address mechanisms leading to reversible performance losses and procedures to recover these losses. According to Kundu et al. [23], a short drop in fuel cell temperature recovers voltage losses due to H_2 cross-over (via pinholes) resulting from increased humidity leading to membrane swelling and temporary sealing of pinholes. Gazdzicki et al. [24] observed a strong recovery of performance losses after a shut-down procedure (fuel cell cooling down for several hours and restart) after continuous dynamic operation periods. The reversible degradation was related to the hydration of ionomer [25] and the correlated alteration of the water balance in the membrane electrode assembly (MEA) [26]. Pivac et al. [27] proposed that the reversible fuel cell performance degradation is due to the accumulated water within the cell and/or formation of platinum oxides (PtO_x) on the cathode catalyst surface. The PtO_x blocks the cathode catalyst surface and inhibits the oxygen reduction reaction (ORR). A corresponding recovery procedure removes PtO_x from the cathode by low cathode potential (0.2 or 0.3 V) caused by hydrogen permeation from anode to cathode [28,29]. In a recent paper by Zago et al. [4], it is concluded that most of the recoverable performance degradation during high voltage operation at 0.85 V with fully humidified oxygen results from the PtO_x formation and is strongly influenced by the oxide composition. The platinum oxide associated with the peak at 0.61 V_{RHE} in CV spectra is found to decrease the specific activity of the cathode catalyst more than oxides associated with peaks at higher potentials. Adsorption of sulfate anions on the cathode catalyst surface due to ionomer degradation leads to a large mass activity reduction and performance drop which is also reversible [9]. After aging an MEA at open circuit voltage, Kongkanand et al. [30,31] applied low cathode potential under condensing conditions and successfully removed the absorbed sulfate anions from the cathode catalyst surface. H_2S and CO_x are common sulfur and carbon contaminants in hydrogen while NO_x [32], SO_x [33], and H_2S [34] are common contaminants in the air. Even a low level of impurities can result in severe performance loss due to the poisoning effect [35,36]. The strong adsorption on the Pt surface blocks the active sites, which can be recovered by desorption methods such as low potential sweeping (<0.3 V) [37,38]. A recent review paper provides a detailed overview of the mechanisms responsible for reversible performance losses and summarizes specific recovery procedures available in the literature [39].

Specific recovery procedures are proposed by the Joint Research Center (JRC) of the European Commission and by the Department of Energy (DOE) of the USA [40,41]. Despite the importance of comparison of different recovery procedures and the papers published in this context, it is difficult to evaluate the recovery effect, since the magnitude of reversible degradation as well as the efficiency of the recovery procedures depends on specific operating conditions and used materials.

To the best of our knowledge, no paper is available so far which focuses on a quantitative comparison of such recovery procedures elucidation recovery mechanisms leading to increased performance. Therefore, in order to provide additional insight into recovery of reversible losses and to provide a clear and direct comparison of the relative recovery of different procedures, in this paper three selected recovery protocols are compared at fixed operating conditions. Moreover, for each recovery procedure, the mechanisms leading to recovery are analyzed. Besides, the effect of the cell operating history is considered as well. The results are of practical use and will allow other researchers to improve recovery procedures when implementing them in their fuel cell durability test plans.

2. Experimental details

2.1. Single cell and test bench

The 5-layer MEA used in this experiment was manufactured by IRD Fuel Cells A/S following DLR's specifications for the purpose of this investigation. Cathode electrode was on purpose selected without any mitigation to see the effect of ASTs and also recovery protocols. It consists of a 27.5 μm thick Nafion^{TM} XL membrane coated by an anode and cathode catalyst layer with Pt/C ratio of 50 wt% and Pt loadings of 0.05 and 0.25 mg·cm^{-2}, respectively. The active area is 5 × 5 cm^2. As gas diffusion layer (GDL) Sigracet® 29BC from SGL Carbon SE was used.

The single cell hardware and fuel cell test bench were designed and developed at the German Aerospace Center (Deutsches Zentrum für Luft- und Raumfahrt e.V., DLR). The test bench is controlled by the in-house developed software with automatic control of a variety of operating parameters, such as temperature, air and hydrogen flow, reactants humidity, and cell outlet pressure. The air and hydrogen were humidified by external water-filled humidifiers (bubblers). A commercial electronic load with maximum current of 60 A connected to the test stand was used to operate the fuel cell. Detailed information about the setup is available in previous works [42,43]. The single cell is made of gold-coated stainless steel, with triple-channel-serpentine flow fields arranged in co-flow configuration. Ice Cube Sealing from Freudenberg FST GmbH was used with 350 μm thickness.

2.2. Test protocols

In this section, the operation protocols, conditions, and the applied characterization methods are outlined.

2.2.1. Conditioning

At the very beginning of the experiment, a leak test was conducted with both of the anodic and cathodic compartments purging with 0.2 L·min^{-1} dry nitrogen and setting anode and cathode pressured to 250 and 230 kPa_{abs}, respectively. The nitrogen flow was shut off after both outlet pressures were stable. The pressure decrease rates for the next 10 min were corresponded to 0.05 and 0.1 kPa·min^{-1} in the anode and cathode, indicating the high tightness of the single cell and test bench and the cell.

Then the MEA was conditioned to reach a stable performance. The cell temperature was kept at 80 °C. The flow rate of H_2 was 0.526 L·min^{-1} corresponding to H_2 stoichiometry of 1.5 for current density of 2 A·cm^{-2}. The flow rate of air was 1.66 L·min^{-1} corresponding to oxygen stoichiometry of 2 for current density of 2 A·cm^{-2}. Humidity of both gases was set to 100 %. The gas pressures of the anode and cathode outlets were 250 and 230 kPa_{abs} (absolute pressure). The procedure constituted of voltage cycling includes 2 min hold at 0.8 V and 4 min hold at 0.4 V until the cell current variations at 0.4 V were lower than +/- 0.04 A·cm^{-2}. In this case, the cycling process took 2 h.

2.2.2. Load cycling

To simulate fuel cell durability for automotive applications, the Fuel Cell Dynamic Load Cycle (FC-DLC) protocol was taken as an accelerated stress test (AST) protocol [40]. The entire durability test consists of four operation periods of 82 h continuous FC-DLC cycling interrupted by three recovery procedures. The maximum current density of the FC-DLC is defined as the current density yielding 0.65 V, which is 1 A·cm^{-2}. At the beginning and the end of the test, before and after each FC-DLC operation period the fuel cell was characterized by means of polarization curves and electrochemical impedance spectroscopy (EIS). During FC-DLC cycling, the fuel cell was operated with constant H_2 (anode) and air (cathode) flow rates of 0.263 and 0.83 L·min^{-1}, respectively, corresponding to H_2 and air stoichiometry of 1.5 and 2 for the current density of 1 A·cm^{-2}. Other operation parameters were the same as in the conditioning procedure.

2.2.3. Performance characterization

To record polarization curves, the flow rate of H_2 at the anode was set according to stoichiometry of 1.5; the air flow at the cathode side was adjusted according to oxygen stoichiometry of 2. However, minimum H_2 and air flows were defined as 0.105 and 0.332 L·min^{-1} corresponding to a minimum current density of 0.4 A·cm^{-2}. The cell temperature, humidity, and gas pressures of the anode and cathode were the same as during the load cycling. The polarization curve test followed the recommendation by the EU Harmonized Test Protocols for MEA Testing [40]. The current density was increased from 0 to 1.9 A·cm^{-2} in steps of 0.05 or 0.1 A·cm^{-2} and then decreased to 0 Acm^{-2}. The dwell time of each setpoint was 30 s from 0 to 0.4 A·cm^{-2} and 120 s from 0.5 to 1 A·cm^{-2} and 300 s from 1.1 to 1.9 A·cm^{-2}. The data were acquired every second and then averaged over the last 30 s of the dwell time. The error bars correspond to the standard deviation from the average.

2.2.4. Impedance spectroscopy

EIS was performed to investigate the impedance change of the fuel cell, including ohmic resistance, charge transfer resistance for the ORR, and mass transfer resistance. In this experiment, EIS was carried out with the modular electrochemical workstation Zennium X and electronic load PP241 from ZAHNER-Elektrik GmbH & CoKG under three constant current densities of 0.1, 1.0, and 1.4 A·cm^{-2} in a frequency range from 100 mHz to 10 kHz with the disturbance amplitude of +/-10% of the applied current. The operation parameters were the same as for polarization curves measurements. For data acquisition and evaluation, the Thales XT software package including Zahner Analysis software was used.

2.2.5. Scanning electron microscopy

To observe the influence of the durability test on MEA structure, scanning electron microscopy (SEM) was utilized to observe the cross-section images of a fresh MEA and the MEA after the durability test. From the center of the MEA, a 1 × 1 cm^2 sample was cut off. Then GDLs were removed and the CCM was fully immersed into liquid nitrogen for 10 s and broke into two pieces by cryo-fracture. Subsequently, the CCM sample was fixed to the sample holder with the broken cross-section upwards for SEM analysis and measured by a ZEISS Ultra Plus SEM equipment. An electron beam of 5.0 kV was used.

2.3. Description of the recovery procedures

In this section, the applied recovery procedures are explained along with measured test bench parameters recorded during recovery. Afterwards, the sequence of the implemented three recovery procedures is addressed.

JRC-based recovery procedure: the individual steps of the JRC recovery procedure [40] are provided in Table 1. The possible recovery mechanisms are provided in the last column based on literature and will be interpreted with experimental results in Section 3.3. The fuel cell operation parameters recorded during the recovery procedure are plotted in Fig. 1 a). As first step, the load is switched off, the air supply and cathode outlet are closed and hydrogen flow on the anode side is maintained. Consequently, H_2 migrates to the cathode side leading to a drop of cathode potential and therefore a reduction of the cell voltage below 0.1 V which took 25 min. Then both sides are purged with dry N_2 for 30 min to remove hydrogen from the cell, followed by dry air purging on both sides for the same period. Upon air purging, the cell voltage is maintained close to zero while both electrode potentials increase to ~ 1 V. For the subsequent 8 h, the gas supply and heating were switched off; the cell gas outlet valves were kept closed. Then the restart of the cell was initiated by purging anode and cathode by humified N_2 for 30 min while increasing the cell temperature to 80 °C. The entire procedure including the restart took 10 h 25 min. Eventually, the cell was again fed with H_2 and air.

DOE-based recovery procedure: As described in Table 2 the DOE protocol [41] consists of 4 subsequent steps. The possible recovery mechanisms are provided in the last column based on literature and will be interpreted with experimental results in Section 3.3. After switching off the electronic load, the anode and cathode compartments were purged with dry N_2 for 2 min. During that step oxygen diffuses to anode leading to the increase of anode potential to ~ 1 V resulting in cell voltage close to 0 V. Then, the gas supply on the anode was stopped and the gas outlet was closed. In parallel the cathode was purged with air for 15 min, followed by dry N_2 purge for 2 min. Then, the cathode outlet was closed while the anode was fed with hydrogen for 10 min. This leads to diffusion of H_2 to cathode. This keeps anode and cathode potentials and the cell voltage close to zero. The recovery took 29 min in total. The operation parameters during this recovery procedure are plotted in Fig. 1 b).

Overnight rest recovery procedure: The overnight rest recovery [24] was conducted following the steps in Table 3. The possible recovery mechanisms are provided in the last column based on literature and will be interpreted with experimental results in Section 3.3. The electrical load was switched off, the gas supplies were stopped and the pressure was released from the cell, the heating was deactivated and the gas outlets of the cell were kept closed. After 8 h, the test bench and fuel cell were restarted analogously to JRC recovery protocol. In contrast to the JRC and DOE protocols, no compulsive purging with N_2 was involved. The operation parameters during the overnight rest recovery procedure and respective cell voltage changes are plotted in Fig. 1 c).

During a durability test, each operation period inevitably results in a certain amount of irreversible performance degradation. Thus, the variation of sequences of the investigated recovery procedures may influence the evaluation and comparison of the relative recovery of different recovery procedures. The JRC-based and overnight recovery procedure intend to recover the reversible performance degradation using similar mechanisms. The DOE-based recovery procedure also involves similar recovery mechanism except the regeneration/hydration of the ionomer in catalyst layer of the cathode. Besides, in view of the steps in each recovery procedure, the duration of DOE-based recovery procedure is much shorter than the other two recovery procedures, which may limit the recovery of the reversible performance degradation.

Table 1
JRC recovery protocol [40] along with recovery mechanisms for each step.

	Step	Cathode	Anode	Duration	Possible recovery mechanism according to literature
1	H_2 soak	Shut off	H_2 1.5 L·min^{-1} until U < 0.1 V	25 min	Pt oxides reduction in cathode CL [4,44] and sulfate anions removal [31,45] due to low cathode potential
2	N_2 purge	Dry N_2 1.5 L·min^{-1}		30 min	Water and H_2 removal due to purging with dry gas [45,46]
3	Air purge	Dry Air 1.5 L·min^{-1}		30 min	Removal of CO contamination in anode due to increase of anode potential [47,48]
4	Shut-down	Stop gas supply; Stop heating the cell; Release pressure; Cell outlets open		8 h	(If step 1 is not sufficient) Pt oxides reduction in cathode CL [4,44] and sulfate anions removal [31,45] due to low cathode potential Regeneration/hydration of the ionomer due to water condensation at low temperature [12,13]
5	Restart	N_2 1.5 L·min^{-1}; start heating the cell		30 min	Water removal to avoid flooding if step 2&3 are not sufficient; hydrate the membrane if over-dry [7,8]

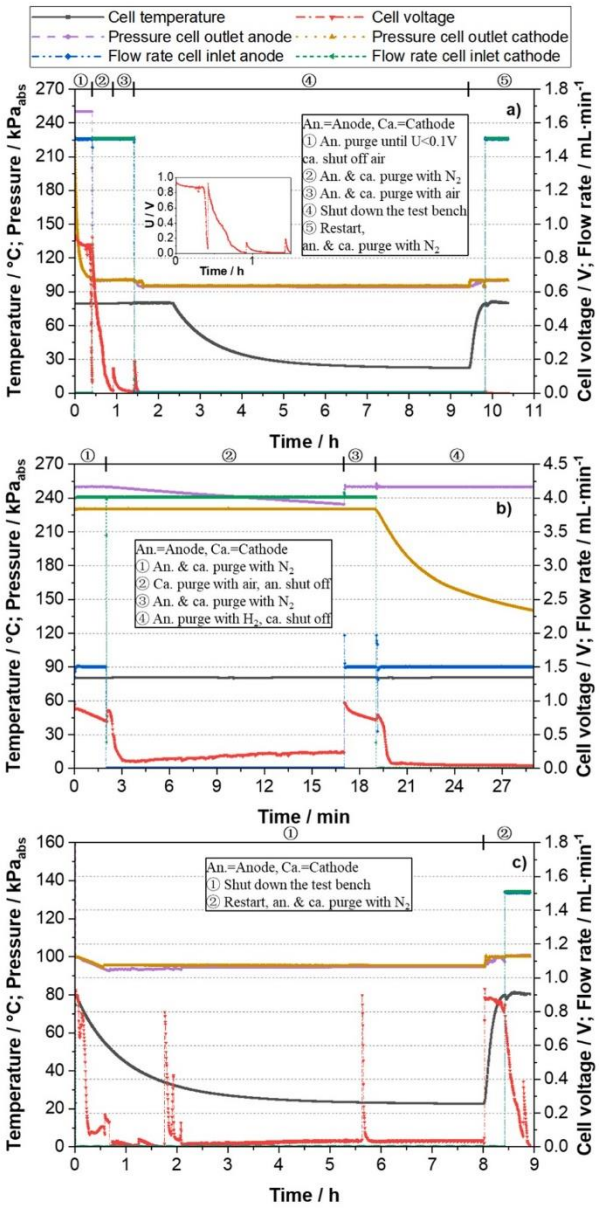

Fig. 1. Testbench parameters during the recovery procedure: a) JRC protocol, b) DOE protocol, c) overnight rest.

Thus, it was assumed before the experiment that the JRC-based and overnight rest recovery procedure would have higher relative recovery than the DOE-based recovery procedure.

Hence, a specific sequence of recovery procedures is chosen in this study starting with JRC, followed by DOE and the overnight rest as the last protocol. This means, the JRC-based recovery procedure as the first performed recovery procedure is supposed to recover most of the reversible performance losses which could leave little influence to the rest of the durability test. Applying overnight rest as the last recovery procedure contributes to investigating the different recovery effectiveness and mechanism of the two recovery procedures, by which the non-recovered reversible performance degradation in the last operation period could be recovered. It is verified in the next section that part of the reversible performance losses after the second operation period is not recovered by the DOE-based recovery procedure, but accumulates until being recovered by the overnight rest recovery procedure.

Table 2
DOE recovery protocol [41] along with recovery mechanisms for each step.

Step		Cathode	Anode	Duration	Possible recovery mechanism according to literature
1	N_2 purge	Dry N_2 4 $L \cdot min^{-1}$	Dry N_2 2 $L \cdot min^{-1}$	2 min	Water, air and H_2 removal by purging with dry inert gas [45,46]
2	Air soak	Air 4 $L \cdot min^{-1}$	Shut off	15 min	CO poisoning elimination in the anode CL due to increase of anode potential after O_2 diffusion [47,48]
3	N_2 purge	Dry N_2 4 $L \cdot min^{-1}$	Dry N_2 2 $L \cdot min^{-1}$	2 min	Water and air removal by purging with dry inert gas [45,46]
4	H_2 soak	Shut off	H_2 2 $L \cdot min^{-1}$	10 min	Pt oxides reduction in cathode CL [4,44] and sulfate anions removal [31,45] due to low cathode potential

Table 3
Overnight rest recovery [7,24] along with recovery mechanisms for each step.

Step	Cathode	Anode	Duration	Possible recovery mechanism according to literature
1	Shut-down	Stop gas supply; Stop heating the cell;Release pressure;	8 h	Pt oxides reduction in cathode CL [4,44] and sulfate anions removal [31,45] due to low cathode potential Removal of CO contamination in anode due to increase of anode potential [47,48] Regeneration/hydration of the ionomer due to water condensation at low temperature [12,13]
2	Restart	N_2 1.5 $L \cdot min^{-1}$; start heating the cell	0.5 h	Water removal to avoid flooding in CL [45,46]

3. Results and discussion

The recovery procedures were analyzed based on a FC-DLC durability test which is presented in Section 3.1. General observation on the impact of recovery procedures on cell voltage using data from polarization curves and procedures on how to quantify impact of recovery are provided in Section 3.2. Quantification of the impact of recovery procedures on kinetic, ohmic, and mass transport regions is provided in Section 3.3 based on EIS measurements. Differences between the recovery procedures and recovery mechanisms are discussed in Section 3.4. Furthermore, irreversible performance degradation and mechanism are analyzed with cross sectional SEM images in Section 3.5. Eventually, the effect of operation history on the quantification of recovery is discussed in Section 3.6.

3.1. Durability test

Fig. 2 shows the performed durability test consisting of four operation periods using the FC-DLC protocol. The durability test contained three recovery procedures as indicated in the figure: the JRC protocol after the first operation period, the DOE protocol after the second operation period, and the overnight rest recovery after the third operation period. The plotted voltage data corresponds to the individual current density values indicated in the figure. Apparently, the voltage values decrease during each operation period. Thereby, the initial

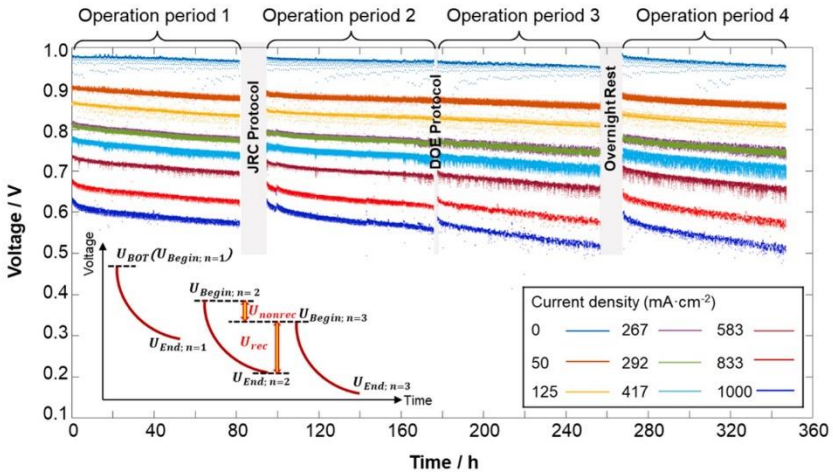

Fig. 2. The fuel cell voltage during the four operation periods of the durability test.

decrease exhibits an exponential shape followed by a slow linear drop afterwards which is clearly visible at 0.8 and 1.0 A·cm^{-2}. Moreover, after each recovery procedure, the voltage values increase to different extent which depends on the current density and specific recovery process. Further information could be concluded from the polarization curves and power density curves recorded at the beginning of test, before and after each recovery procedure and at the end of test, as shown in Fig. 3. At the beginning of the test, the cell voltages at 0.2, 1.0 and 1.6 A·cm^{-2} are 860, 650 and 510 mV, respectively. The voltage and power descent after each operation period does not reach the initial values although recovery procedures are applied. This suggests that there is a significant irreversible degradation effect during the whole durability test. After the four operation periods the cell performance was reduced by 11.6%, 18.5% and 41.2% at the three above-mentioned current densities and the highest power density decreased from 0.81 to 0.55 W·cm^{-2}. The current density values at highest power density shifted towards lower range, from 1.8 A·cm^{-2} at the beginning of the test shifted to 1 A·cm^{-2} after the four operation periods. In terms of the absolute recovered voltages, the DOE protocol showed the lowest values of 3, 22 and 43.5 mV at the current density of 0.2, 1.0 and 1.6 A·cm^{-2}, respectively. The overnight rest leads to the highest recovered voltage with 31.5, 88 and 181.5 mV at the corresponding current densities.

The test allows clear discrimination between recovered voltage losses after each recovery procedure and non-recovered voltage losses and was therefore used to assess the applied recovery procedures.

In the following section, a comparison of the relative recovery of the three recovery procedures is discussed based on data from Fig. 2 and Fig. 3.

3.2. Impact of recovery procedures on cell voltage

The inset of Fig. 2 provides a schematic diagram to show the definitions used to quantify the impact of the recovery procedures. Cell voltages at the beginning and end of an operation period are expressed as $U_{Begin;n=i}$ and $U_{End;n=i}$ where i refers to operation period. For the i^{th} recovery procedure after the i^{th} operation period, the recovered voltage loss is expressed as $U_{rec} = U_{Begin;n=i+1} - U_{End;n=i}$ and the non-recovered voltage loss is named as U_{nonrec}.

With $i = 1\cdots3$, Fig. 4 shows the impact of each recovery procedure on cell voltage determined from polarization curves using the following formulas:

$$\eta_{Last} = \frac{U_{rec}}{U_{Begin;n=i} - U_{End;n=i}}, \tag{1}$$

$$\eta_{Past} = \frac{U_{rec}}{U_{Begin;n=1} - U_{End;n=i}}, \tag{2}$$

$$U_{nonrec} = U_{Begin;n=i} - U_{Begin;n=i+1} \tag{3}$$

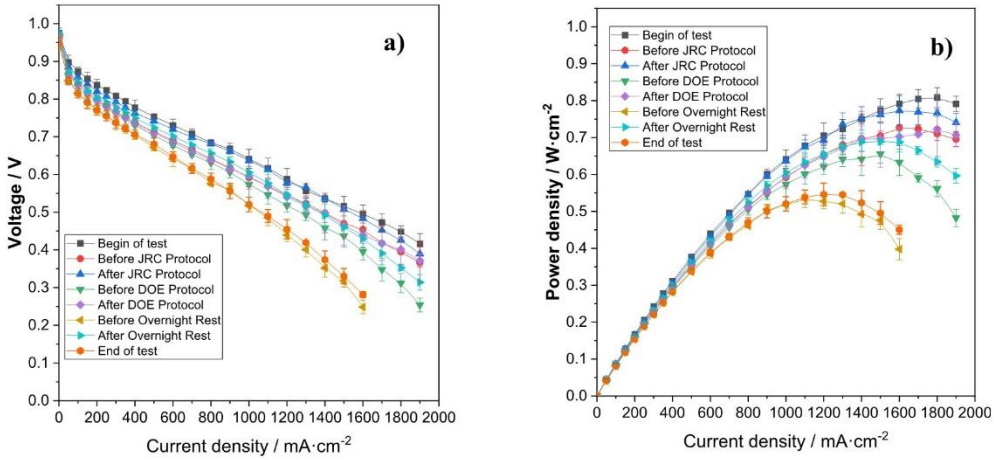

Fig. 3. a) Polarization curves and b) power density curves recorded at the beginning of test, before and after each recovery procedure and end of test.

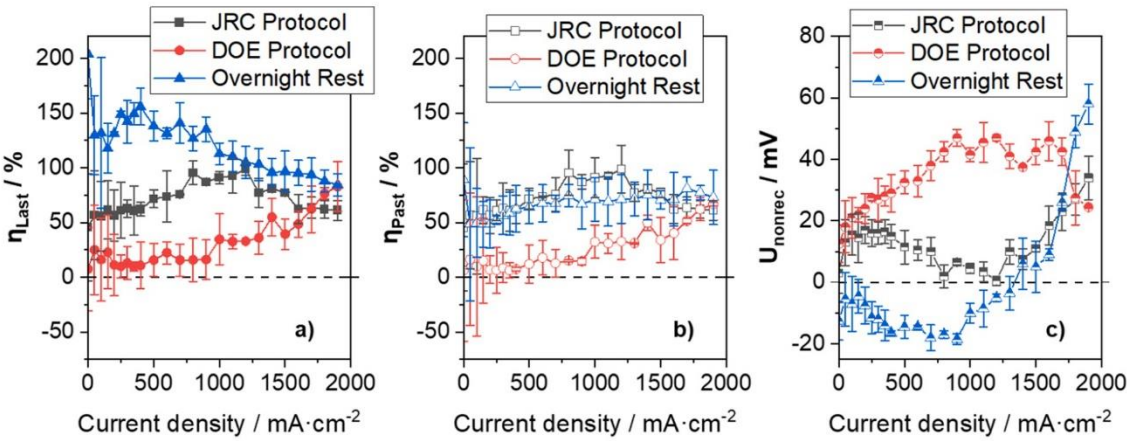

Fig. 4. Evaluation of the relative recovery of the three recovery procedures: JRC protocol, DOE protocol and overnight rest. a) presents relative recovery which relates to the cell voltage change of the previous operation period according to the Eq. (1), while b) relates to that from the beginning of the test according to the Eq. (2). c) shows non-recovered cell voltage as Eq. (3).

η_{Last} corresponds to the relative recovery related to the cell voltage change of the previous operation period while η_{Past} relates to that of beginning of the test. U_{nonrec} corresponds to non-recovered cell voltage. The same parameters can also be obtained from the FC-DLC data in Fig. 2, but only up to 1 A·cm^{-2} which is the maximum current density applied in the cycle. Since both options lead to the same result [49], the option of using voltage data from polarization curves was chosen because it covers a broader current density range up to 1.9 A·cm^{-2} (see Fig. 3) .

According to Fig. 4 a) the relative recovery due to JRC protocol is around 60 % at low current density and increases to 90 % in the range of 1 A·cm^{-2} followed by a slight drop back to 50 – 60 % at 1.9 A·cm^{-2}. For the JRC protocol, η_{Last} and η_{Past} provide the same results since they both refer to the data in the first operation period. η_{Last} and η_{Past} of the subsequent DOE protocol present similar results up to the current density of 1.5 A·cm^{-2}. For current densities > 1.5 A·cm^{-2}, η_{Last} is getting higher than the η_{Past} (16 % higher at 1.9 A·cm^{-2}). η_{Last} is in the range 10 and 30 % for current densities up to 1 A·cm^{-2} followed by a mild rise reaching 80 % at 1.9 A·cm^{-2}. Obviously, the DOE protocol has higher recovery efficiency in the current density range above 1.4 A·cm^{-2} than at lower current densities, despite that there are higher performance losses at higher current densities. The similar values of η_{Last} and η_{Past} of the DOE protocol indicate that after the former recovery procedure (JRC protocol) the reversible voltage losses became largely recovered for current densities up to 1.5 A·cm^{-2}. This agrees with the non-recovered voltage U_{nonrec} in Fig. 4 c) which is relatively low for the JRC protocol in the range from 0 to 1.5 A·cm^{-2}. As shown in Fig. 4 a) and b), the JRC protocol shows higher recovery efficiency η_{Last} and η_{Past} than the DOE protocol up to 1.6 A·cm^{-2}. Besides, in the case of the overnight rest, η_{Last} and η_{Past} exhibit substantial differences. The observation that η_{Past} of the overnight rest protocol increases when increasing the current density from 0 to 1 A·cm^{-2} is consistent with previous studies [24]; however, η_{Last} is higher than 100 % for current densities up to 1.3 A·cm^{-2} and continuously drops down to 80 % at 1.9 A·cm^{-2}. It is explained by the low value of η_{Last} of the previous recovery by the DOE protocol which apparently does not recover all reversible losses. Consequently, η_{Last} of the overnight rest contains recovered voltage losses from the second and third operation periods yielding the accumulation of higher reversible losses than in just one single operation period.

It is interesting to mention that taken the error bars into account, the η_{Past} of the JRC protocol and overnight rest in Fig. 4 b) highly overlap in the entire current density range. Besides, the η_{Last} of the overnight rest, in the current density from 0 to 0.9 A·cm^{-2}, is almost twice that of the JRC protocol while that of DOE protocol is close to 0 %. Hence, the recovery procedures of the JRC protocol and overnight rest are supposed to have almost the same relative recovery in the low current density range while the DOE protocol showed the lowest achieved recovery achieved in the performed experiments. This is also demonstrated by the data in Fig. 4 c) showing non-recovered voltage losses U_{nonrec} of each recovery procedure. For the DOE protocol, the non-recovered voltage U_{nonrec} reached up to 50 mV at around 1 A·cm^{-2}. On the other hand, for the following recovery procedure of overnight rest, the non-recovered voltage is negative at low current densities until 1.3 A·cm^{-2} which means that substantial reversible losses have not been recovered by the preceding recovery step (DOE protocol).

Overall, at current densities above 1.5 A·cm^{-2} for all recovery protocols the differences of the η_{Last} and η_{Past} in Fig. 4 a) and b) are relatively small and insignificant. This indicates that at high current density all three protocols lead to similar relative recovery. However, all recovery protocols showed significant non-recovered voltage losses U_{nonrec} in Fig. 4 c) at the current densities above 1.5 A·cm^{-2} despite the high recovery rate of η_{Last} and η_{Past} in a) and b). With increasing current density, the performance losses values increased significantly, e.g. the voltage losses in the third operation period are 24, 78 and 402 mV at 0.2, 1.0 and 1.8 A·cm^{-2}, respectively. Meantime, over the whole test, the performance losses during each sequence of the operation period increased dramatically due to the accumulated contribution of irreversible performance degradation which is in consistent with previous study [24], e.g. the voltage losses in the three operation periods are 62, 117 and 402 mV at 1.8 A·cm^{-2}. This results in sharp rise in the overnight rest recovery protocol in Fig. 4 c). It demonstrates the importance of comprehensive analysis with all the η_{Last}, η_{Past} and U_{nonrec} considered when comparing different recovery protocols.

3.3. Quantification of impact of recovery procedures based on EIS

At the beginning of test, before and after each recovery procedure, at the end of test EIS measurements are performed at three current density values of 0.1, 1.0, and 1.4 A·cm^{-2} as the solid points displayed in Fig. 5 b)–d), respectively. The measured EIS at current density of 0.1 A·cm^{-2} is a semi-circle as Fig. 5 b) while at current densities of 1.0 and 1.4 A·cm^{-2} the EIS spectra are composed of two semi-circles as shown Fig. 5 c) and d). It is believed that in the current density of 0.1 A·cm^{-2} one electrochemical process dominates in the whole fuel cell impedance while with the increased current density, the significance of the other electrochemical process increases accordingly.

In order to further evaluate the EIS measurements and investigate each recovery procedure, the equivalent circuit as in Fig. 5 a) is utilized,

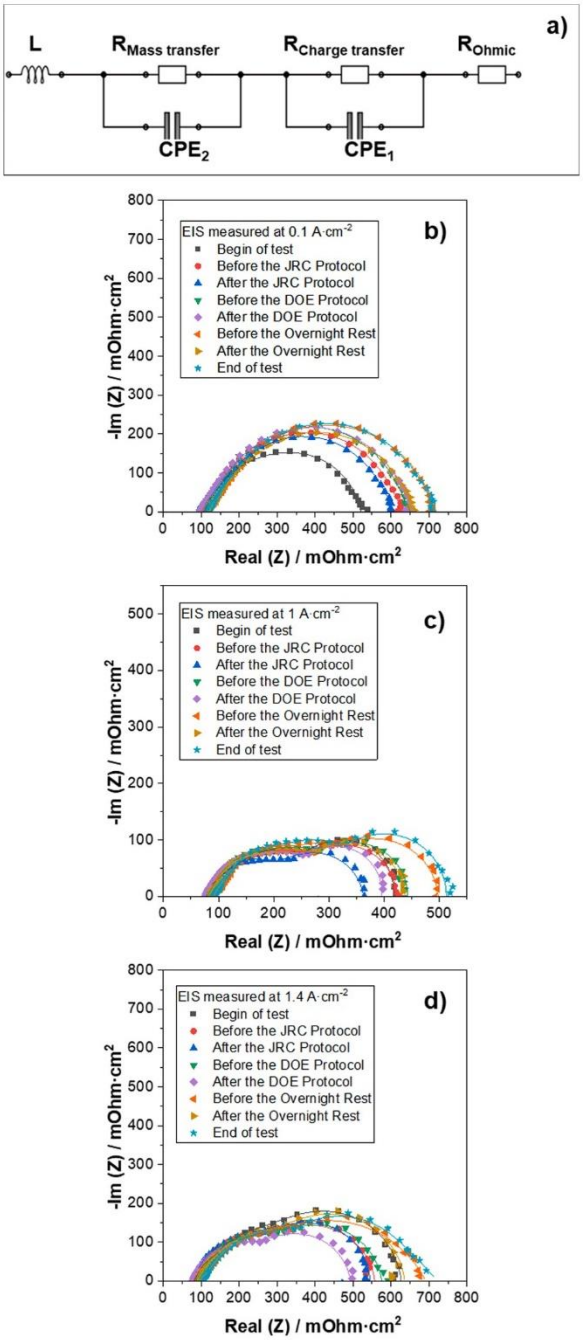

Fig. 5. a) Equivalent circuit model used to fit EIS date. EIS spectra were recorded at the beginning of test, before and after each recovery procedure and at the end of test at current density of b) 0.1 A·cm^{-2}, c) 1.0 A·cm^{-2} and d) 1.4 A·cm^{-2}. The solid points are measured data while the lines are the simulated results after fitting with the model in a).

which consists of four components in series: (i) a resistor R_{Ohmic} which describes the ohmic resistance of the MEA including the contact resistances of the fuel cell components, (ii) the charge transfer circuit consisting of $R_{Chargetransfer}$ in parallel with CPE_1 (constant phase element) which describes the charge transfer resistance of the cathode catalyst layer, (iii) the mass transfer resistance circuit consisting of $R_{Masstransfer}$ in parallel with a constant phase element CPE_2 and (iv) an inductance element L regarding possible interferences due to wires or other sources of disturbance. The solid lines in Fig. 5 b), c) and d) are the fitted results with this model. This model is selected here because: (i) the fitting error is at a relatively low level (in general lower than 3 %), (ii) it is one of the most widely applied equivalent circuits to analyze EIS spectra in the literature, including past work of our group [26,43] and (iii) with the elements in this model, the mechanism of the fuel cell behavior can be observed and understood, which will be clarified in the following.

The bar graphs in Fig. 6 a) - i) show stacked resistances obtained from EIS analysis; i.e. ohmic, charge transfer, and mass transfer resistance. The three bars in each panel represent the resistances (i) at the beginning of the operation period, (ii) at the end of the operation period, and (iii) after the recovery procedure. The comparison of each three bars in a panel allows assessing the resistance accumulated during each operation period and the recovered fraction. At 0.1 A·cm^{-2} reversible performance loss can be mainly ascribed to the increase of charge transfer resistance. At 1.0 A·cm^{-2} the increase of both the charge transfer and mass transport resistance contributes to reversible degradation. Eventually, at 1.4 A·cm^{-2} main effects are clearly due to mass transport resistance with a minor contribution of charge transfer resistance. Generally, the charge transfer resistance decreases with increasing current density, while the mass transfer resistance increases. The effect of current density on ohmic resistance is less obvious. The total resistances at 1 A·cm^{-2} exhibit lower values than those at 0.1 and 1.4 A·cm^{-2}. This observation agrees with literature [22,50]. Under low current density, the amount of product water is low. Especially in the inlets of the fuel cell the electrode and membrane tend to be drier than in the outlets resulting in higher local charge transfer resistance [51,52].

Under high current density such as 1.4 A·cm^{-2}, the accumulated water in the electrode pore structure must be transported away to avoid pore blockage which may cause oxygen starvation [52,53]. Given the similar high recovery efficiency of these three protocols in the high current density range, mass transfer resistance is reduced through water removal by all of these protocols: The DOE protocol contains 4 min dry gas purging with high flow rate, which seems to be sufficient to remove excess water. In cases of the JRC and overnight rest protocols, a 30-min N_2 purging process upon the restart helps with water management. Furthermore, the JRC protocol contains 2 steps of dry gas purging before the shut-down step, which also leads to water removal. Gas purge, including adjustment of the air or H_2 flow [54] or using N_2 [8], is utilized in the literature as a recovery procedure to mitigate flooding in the fuel cell. OCV hold can achieve a similar effect [7,55]. Eventually, a period of dry gas purging is believed to be necessary to achieve a high recovery in high current density range in terms of the reduction of mass transfer resistance. On the other hand, too long gas purging has negative impact on ohmic resistance due to dehydration of the membrane as discussed later in context of Fig. 7.

At 1.0 A·cm^{-2} charge transfer resistance is recovered by JRC and overnight rest protocol to a higher extent than by the DOE protocol. This difference is explained by the short period of H_2 soak step and lack of cell temperature drop in the DOE protocol (see Table 1 - 3). Detailed reasons are interpreted in later discussion. At 0.1 A·cm^{-2} no decrease of total resistance by the DOE protocol is observed. In cases of JRC and overnight rest, certain recovery effect is detectable.

Individual impacts of each recovery procedure on the changes of ohmic, charge transfer, and mass transfer resistance are displayed respectively in Fig. 7 a)–c). Each panel shows resistance changes for the three recovery procedures determined by EIS at three current densities. In each case, the left column is the absolute increased resistance ΔR during the last operation period while the right one is the reduced resistance ΔR_{re} due to the recovery procedure. It is worth to mention that a positive value of ΔR_{re} indicates a recovery of performance loss; a negative value indicates that resistance increased upon the recovery protocol. In that sense, recovery procedures leading to negative ΔR_{re} may have a detrimental effect on cell performance at a given current density. This is the case for the ohmic resistance of the JRC protocol and

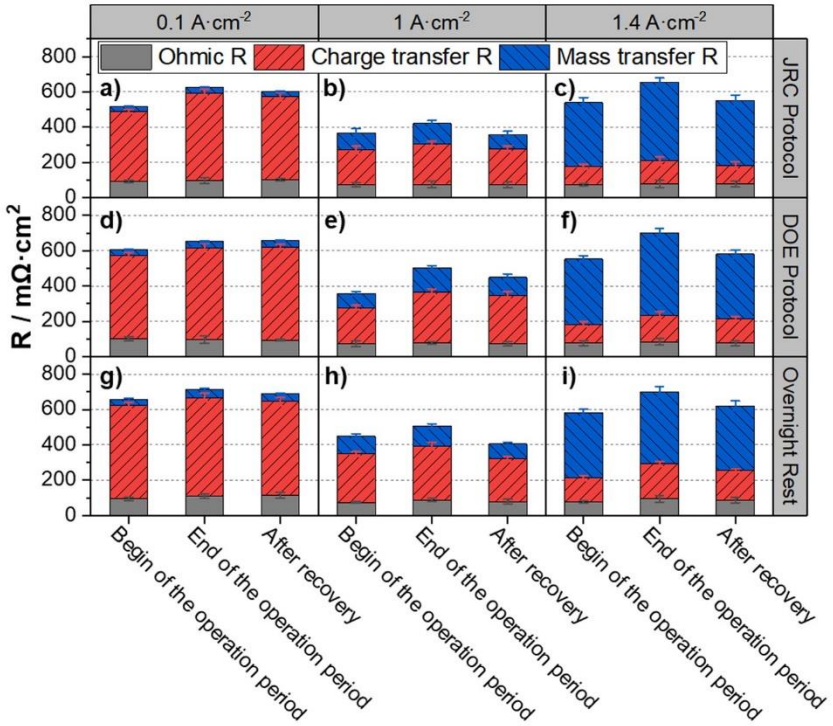

Fig. 6. Impedance analysis showing ohmic, charge transfer and mass transfer resistance at beginning, end of each operation period and after the recovery procedure measured at 0.1, 1.0 and 1.4 A·cm^{-2} for: JRC protocol a)–c), DOE protocol d)–f), overnight rest g)–i).

overnight rest at 0.1 A·cm^{-2} as shown in Fig. 7 a). In other words, only the DOE protocol shows a positive effect on the reduction of ohmic resistance at low current density. Moreover, at 1.4 A·cm^{-2} the highest ohmic resistance recovery value is observed in the case of the DOE protocol, as well. This can be explained by the last step of both the JRC and overnight rest protocols which is a 30 min N_2 purging linked with heating up the fuel cell. Possibly that the membrane is dehydrated temporarily during that step. However, the absolute values of ohmic resistance and its change are small in comparison to the charge and mass transfer resistance. Besides, none of the four steps of the DOE protocol (see Table 2) is reasonable for reducing the ohmic resistance. Hence, the gas purging steps of the JRC and overnight rest protocol are considered as being too extended and lead to a detrimental effect.

According to Fig. 7 b), the DOE protocol leads to a significantly lower reduction of charge transfer resistance compared with JRC and overnight rest protocols. In case of the JRC protocol, the relative recovery is in the range of 50 to 70 %. Remarkably, in the case of the overnight rest ΔR is much lower than ΔR_{re}, indicating that the reduction of charge transfer resistance due to overnight rest overcompensates the accumulated resistance during the last operation period at 1.0 A·cm^{-2}; this is again attributed to the relatively low recovery due to DOE protocol which was applied as the former recovery procedure. With regard to the mass transfer resistance, Fig. 7 c) shows a similar effect for all three recovery protocols at 1.4 A·cm^{-2}. This is consistent with the observation from Fig. 4 showing that voltage recovery of the three recovery protocols is similar at 1.4 A·cm^{-2}.

3.4. Discussion of the mechanism of the recovery procedures

Given the protocols of the recovery procedures shown in Table 1–3, all recovery protocols involve specific steps to reduce the Pt oxides in the catalyst surface of the cathode. Besides, both the JRC and overnight rest protocols include steps to induce liquid water (condensation at low cell temperature) for hydration of the ionomer [13,56]. Both of the two mechanisms are reasonable to reduce the charge transfer resistance of a fuel cell after a durability test.

During fuel cell operation (FC-DLC) the Pt surface becomes partially oxidized resulting in increased charge transfer resistance and performance losses [28,57]. Thereby, the involved reactions for the formation of platinum oxides are mainly considered recoverable [27,58]. For recovery of Pt oxides formation the H_2 permeates from anode to the cathode and lowers the cathode potential to below 0.6 V leading to reduction of platinum surface oxides [59]. As shown in Table 1–3 the specific operations triggering Pt oxide reduction are: (i) H_2 soak step by keeping cathode closed and purging anode with H_2, as in the JRC and DOE protocols, and (ii) stopping anode and cathode gas supplies for several hours allowing for gas diffusion between anode to cathode as in case of the overnight rest protocols. Both operations allow the diffusion of H_2 from anode to cathode and decrease the cathode potential, which are also addressed in literature [58,60]. However, in this experiment, the charge transfer resistance does not decrease significantly after the H_2 soak step in the DOE protocol. The reason can be that the underlying process is generally slow [58,61], which could last several hours and the reaction time strongly depends on the structure and coverage of the formed oxide layers. The H_2 soak step in the DOE protocol lasts 10 min whereas the JRC protocol suggests a duration till the voltage of the cell is lower than 0.1 V, as shown in in the inset of Fig. 1 a). Therefore, the DOE protocol may not provide sufficient time for the H_2 soak process which results in less reduction of charge transfer resistance.

In the shut-down step of the overnight rest protocol, the cell voltage fluctuates temporarily in the range 0 to 0.8 V as shown in Fig. 1 c). There are two significant voltage rises in Fig. 1 c) at about 2 h and 5.7 h indicate a mixed process of the reduction of Pt oxides and redox reaction of H_2O in the cathode. Likely, there is still a certain amount of air diffusing into the cathode compartment over time via the tubes of the fuel cell outlets.

The nanostructure of perfluorosulfonic acids (PFSA) ionomer changes according to operating humidity, temperature, and pressure

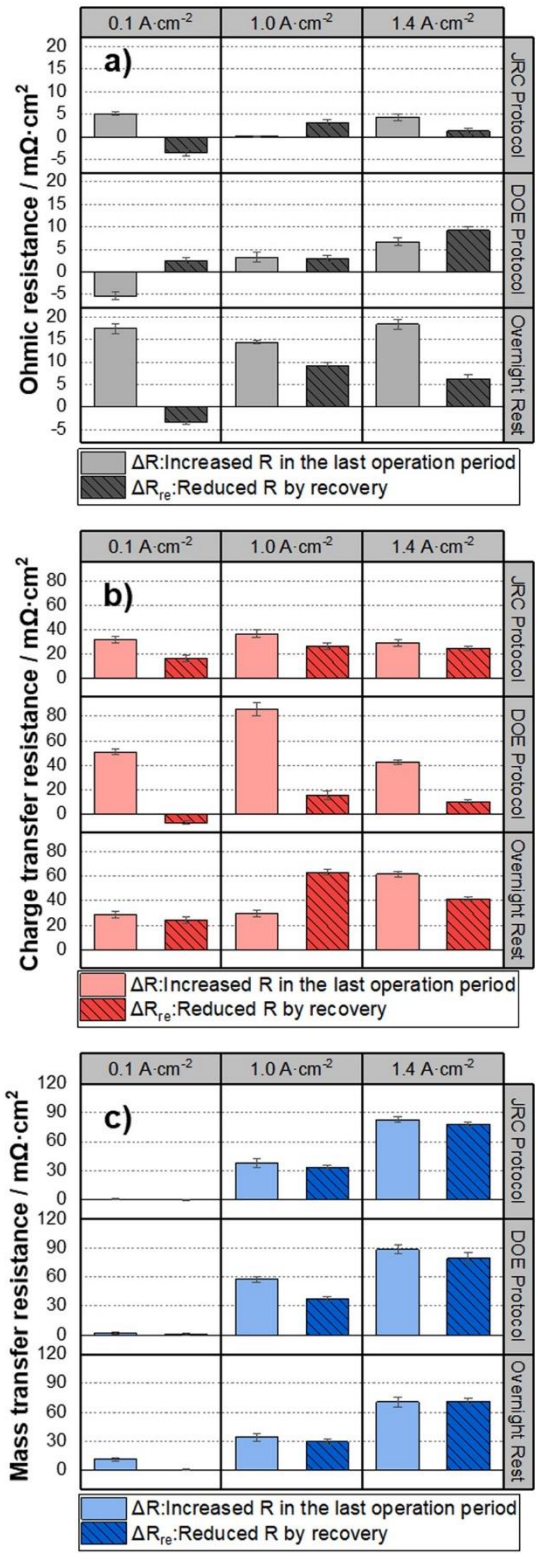

Fig. 7. Changes of ohmic resistance a), charge transfer resistance b) and mass transfer resistance c) due to the previous operation period (light color) and due to subsequent recovery procedure (dark color) measured at the indicated three current densities. In each of a), b) and b), the first row stands for JRC protocol, the second row for DOE protocol and the third row for overnight rest.

[62]. It is reported that the cathode CL degradation results from the strong adsorption of ionomer SO_3^- groups on the catalyst surface which expels the interfacial water. Thus, oxygen transfer resistance in the cathode increases while the proton conductivity decreases [12,63]. The ionomer displacement and redistribution are observed as a loss of total ionomer fraction in the CL over time [64]. Although the nano-scale structure changes of cathode CL upon operation are still under discussion, it is already observed that at least part of the ionomer degradation is recoverable by proper adjustment of relative humidity (RH) including low voltage hold under high RH, or cooling the cell down to room temperature [60,65]. Hence, it is concluded that the presence of liquid water is beneficial for the ionomer redistribution in the cathode CL and facilitates ionomer movement while creating micelles [64]. The shut-down step in JRC and overnight rest procedures involve a reduction of cell temperature from 80 °C to room temperature (about 21 °C) which leads to water condensation in the CL. It is believed that the 1-h dry gas purging in the JRC protocol does not lead to dry-out of the electrodes. Besides, part of the water in membrane may move towards the electrodes, attaches and accumulates in the porous ionomer of the electrodes due to capillary condensation, which also contributes to the regeneration/hydration of ionomer. However, in the DOE protocol, such a step is not included.

As in Table 1 and Table 2, air soak or air purge step in the DOE and JRC protocol is also supposed to improve the kinetics of the fuel cell by means of eliminating the CO poison effect in the anode. In this step, the air is purged to anode directly or air permeates from the cathode to the anode through the membrane and induces the chemical oxidation of adsorbed CO on the anode catalyst. However, in the test performed in this study it is assumed that the presence of CO is not the main reason of the performance degradation during the FC-DLC operation because H_2 of 5 N purity is used. On the other hand, it is reported that even with neat H_2/air, the recovery takes several hours [66,67].

Besides, another two factors in the three protocols contribute to improving the kinetics of the fuel cell. The sulfate anions, as decomposition products of PFSA membranes, tend to adsorb on the catalyst surface which reduces the ORR activity in the cathode. The desorption and removal of the attached sulfate anions can be achieved by lowering the cathode potential along with water condensation [31,68]. In this work this is covered by H_2 soak and reduction of cell temperature. On the other hand, it is reported that the H_2S contaminants in the anode can be oxidized to sulfate ions and flushed away by water condensation by reducing cell temperature and subsequent gas purging process [69]. However, the influence of these two options are considered as minor in this work because (i) the membrane is not dramatically damaged as the OCV keeps stable and according to the cross-sectional SEM images no membrane thinning is observed in Fig. 8, (ii) neat hydrogen is used in the laboratory almost without H_2S.

In general, air pollutants, including nitrogen oxides, sulfur oxides and carbon oxides and other organic chemical species contaminate the fuel cell resulting in performance degradation of the fuel cell. However, this work was carried out using high quality hydrogen and purified air (according to the city air quality monitoring station [70]). Thus, although the performed recovery protocols in this work contains steps to eliminate the influence of contaminants, the reversible performance degradation due to contaminants in this experiment is negligible.

3.5. Discussion of the mechanism of the irreversible performance degradation

As shown in Fig. 8, the cathode catalyst layer is about 20 % thinner after the durability test suggesting significant ionomer structure changes, carbon corrosion, and dissolution of Pt particles which result in irreversible degradation of the fuel cell performance [59]. Similar cathode CL thinning as observed in Fig. 8 was also observed by other groups: For example in a commercial MEA the cathode CL was measured to be reduced from 10 − 11 μm to 8 – 9 μm after the 50 h catalyst ASTs

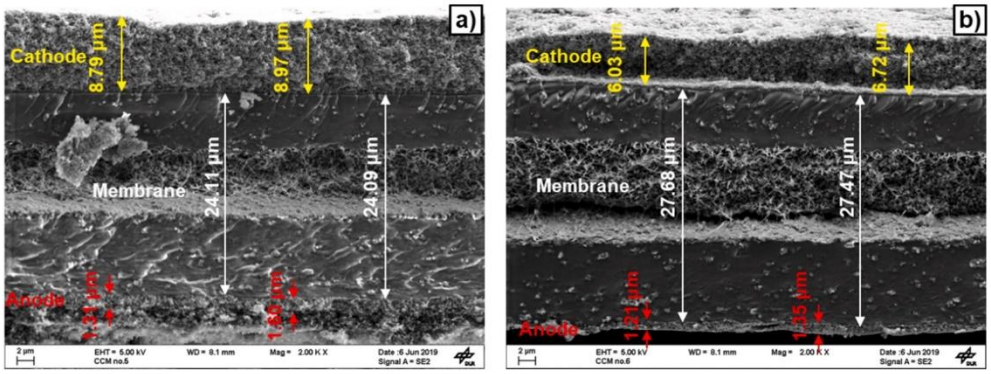

Fig. 8. Cross sectional SEM images of CCMs: a) a fresh CCM, b) the CCM after 328-h operation in FC-DLC conditions, see Fig. 2.

(0.6 – 0.95 V) [71,72]. No cyclic voltammetry (CV) was measured to directly conclude on Pt loss in this test, but in a previous 470 h FC-DLC durability test using MEA with cathode Pt loading of 0.3 and 0.2 mg·cm^{-2} the irreversible degradation rates were measured as 0.2 and 0.3 mV·h^{-1} at 1 A·cm^{-2}; the observed ECSA loss was in the range of 20 – 30 % [25]. In this work, the irreversible degradation rate over the 328 h at 1.0 A·cm^{-2} is calculated as 0.23 mV·h^{-1} with the same method as described in literature. The consistency of experimental data implies that specific cathode CL thinning is connected with irreversible degradation rate and vice versa.

The absolute values of resistance (including ohmic, charge transfer and mass transfer resistance, respectively) at the beginning of the whole durability test and before the 4th operation period at three current densities of 0.1, 1.0 and 1.4 A·cm^{-2} are observed to analyze the mechanism of irreversible performance degradation. The data is displayed in the supporting document as Figure S1. The charge transfer resistance has the most significant increase before and after the whole durability test, 35 %, 24 % and 66 % at the current densities of 0.1, 1.0 and 1.4 A·cm^{-2}. According to the fact of CL thinning and ECSA loss, it is believed that the irreversible performance degradation during the whole durability test with load cycling results from the catalyst agglomeration and the degradation of cathode ionomer. Similar findings were also reported before [73,74].

3.6. Effect of operation history

In many publications [75,76], a recovery procedure was quantified by the relative recovery related to the last operation period, which is called η_{Last} in this paper. However, the voltage at begin of different operation periods strongly depends on the cell operation history. The effect of overnight rest on recovery of cells with different operations histories is shown in in Fig. 9. These three durability tests have the same number of operation periods and all of them take overnight rest as the third recovery procedure, whereas all the former recovery protocols are different (see supplementary information Table S1). For the overnight rest procedure, as shown in Fig. 9 a), the relative recovery related to the last operation period η_{Last} in both the first and third durability tests has values higher than 100 %, while in the second durability test it keeps between 30 and 80 %. The η_{Last} in the first operation history almost decreases constantly over the entire current density range while that in the third operation history keeps increasing until 1.6 A·cm^{-2}. On the other hand, the relative recovery related to the beginning of the whole test, η_{Past}, in the first and the third durability tests are largely identical and even overlap in the range from 0.6 to 1.5 A·cm^{-2} as displayed in Fig. 9 b). From the above-mentioned figures, it can be concluded that the overnight rest procedure in the first and third durability tests are influenced by the corresponding former recovery procedures. In another words, the preceding recovery procedures are less efficient than the

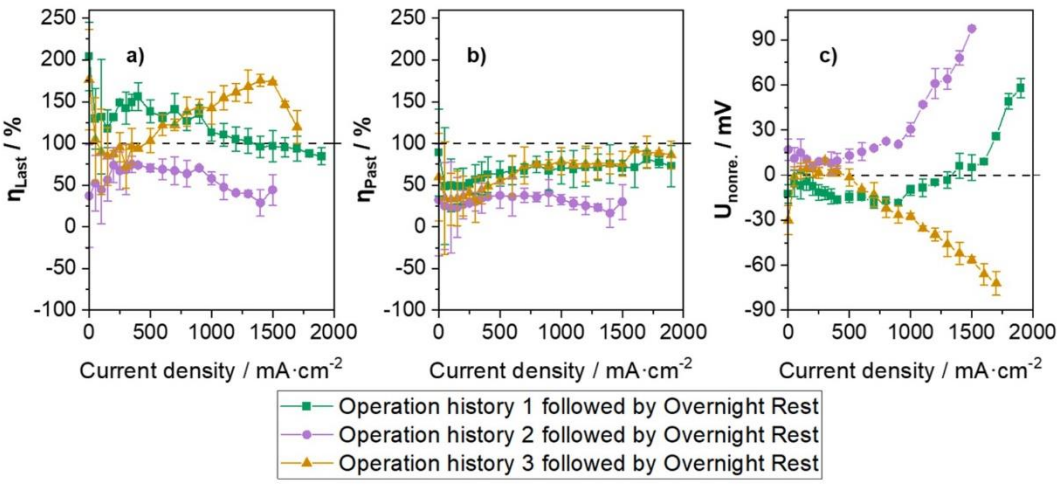

Fig. 9. Three durability tests with same number of operation periods and all of them with overnight rest as the third recovery protocol, whereas all the former recovery procedures are different (see supporting information). a) presents the relative recovery related to the performance loss in the previous operation period according to Eq. (1), while b) shows that related to the performance loss from the beginning of the whole test to just before the recovery procedure according to Eq. (2). c) is the absolute non-recovered performance loss after overnight rest related to the beginning of the preceding operation period according to Eq. (3).

overnight rest. Furthermore, Fig. 9 c) presents that the non-recovered performance losses differ substantially when the operation history is different. In the first durability test (operation history 1), the preceding recovery procedure does not recover all the performance loss only up to 1.4 A·cm^{-2}, while in the third durability test (operation history 3) the preceding recovery is not effective in the whole current density range investigated.

In conclusion, the effect of operation history is significant. Taking η_{Last}, η_{Past} and U_{nonrec} into account provides comprehensive information and helps to determine the effect of operation history in a durability test. For example, η_{Last} exceeding 100 % means that the performance loss due to the former operation period is not sufficiently recovered. As for a specific recovery procedure during a durability test interrupted with several recovery procedures, the η_{Past} is less influenced than η_{Last} by the operation history and should present a similar variation trend even when operation histories are different. Only for the first operation period related to begin of test η_{Last} and η_{Past} are the same. Besides, since the evaluation of relative recovery varies with current density, cell voltages at a wide current density range are recommended to be measured before and after a recovery procedure.

4. Conclusions

In this work the impact of three recovery protocols (DOE-based, JRC-based and overnight rest protocols) on reversible voltage losses are investigated and the mechanisms of each protocol are discussed. The study compares recovery mechanisms of three common recovery protocols based on electrochemical characterization and, additionally, proposes specific improvements of these procedures and assess their applicability for different transport applications. Such direct comparison of the three recovery procedures and recovery effects is novel and of practical use within the scientific community.

Generally, the recovery procedures greatly affect cell performance and reduce reversible performance losses to a large extent and are certainly beneficial for longevity of fuel cells. They can be implemented in transport applications where shut-down events regularly occur without affecting the operation. Among the many applications of PEMFCs, transportation is the most competitive and promising. In transport applications different kinds of shut-downs occur including, e. g. a short stop in the range of minutes without cell temperature drop or significant gas leakages or extended stops with durations from hours to days, where cell temperature is thermalized with the environment and gas diffusion due to small leakages as well as between anode and cathode become relevant. During a very short stop, which occurs naturally more often than a long stop, the DOE-based procedure is certainly the preferred one due to its short duration of 29 min. Moreover, the recovery at high current densities such as > 1.7 A·cm^{-2} are similarly high for all three investigated protocols. For PEMFC applications with long and regular stops, on the other hand, the JRC or overnight rest protocol may be preferred which are more time consuming, but lead to much higher recovery than the DOE protocol at current densities < 1.7 A·cm^{-2}. The utilization of recovery procedures is supposed to improve the durability of stationary PEMFC applications such as stationary power system, uninterrupted power supplies (UPSs), and auxiliary power units (APUs). As for the PEMFC applications for portable communication, such as portable computer and mobile phone, only the overnight rest protocol among the above-discussed protocols can be performed in practice considering the limited space. In short, a recovery protocol should be utilized with the consideration of (i) the operations profiles, (ii) complexity of devices and (iii) target lifetime.

The recovery efficiency of the three protocols on kinetic, ohmic and mas transport losses is assessed in Table 4 which indicates most relevant recovery conditions and mechanisms concluded from our experiments.

Specifically, the JRC protocol not only provides high recovery in the entire current density range, but also includes two protective purging steps to expel the residual H_2 in the fuel cell before the shut-down step to avoid the formation of H_2/air front which causes additional irreversible performance degradation due to carbon corrosion in the cathode CL. The overnight rest protocol lacks purging with inert gas which seems more suitable in terms of implementation in practical application, but has detrimental influence due to carbon corrosion. However, to assess and quantify the negative effect on lifetime, the absolute number of shut-down events containing such recovery procedures needs to be determined and compared with other degradation effects occurring during fuel cell lifetime.

JRC and DOE protocols involve well defined steps to mitigate the influence from specific air or hydrogen contaminants such as CO, H_2S and sulfate anions. These steps triggered by sequential increase and decrease of electrode potentials are needed when the hydrogen fuel or ambient air contain impurities (e.g. from industrial manufacturing processes or exhaust from combustion).

The fuel cell performance in mass transport region is greatly enhanced by all of the three recovery protocols due to purging with dry gas; however, the purging times of the JRC and overnight rest procedure seem too long leading to a detrimental increase of ohmic resistance due to membrane drying. Hence, the duration of this particular step is proposed to be shortened as it is the case for the DOE protocol.

Moreover, to improve the recovery of charge transfer resistance in case of the DOE protocol, the duration of the H_2 soak step is proposed to be prolonged until substantial cell voltage drop close to 0.1 V is

Table 4
Comparison of the recovery assessment, main effective conditions and mechanisms of the three recovery protocols in the respects of recovery of ohmic, charge transfer and mass transfer losses.

		JRC protocol	DOE protocol	Overnight rest
Recovery of ohmic loss	Recovery assessment	low	low	low
	Conditions & mechanisms	Decrease celltemperature → Regeneration/ hydration of the ionomer	none	Decrease cell temperature → Regeneration/hydration of the ionomer
Recovery of charge transfer loss	Recovery assessment	high	low	high
	Conditions & mechanisms	Decrease the cathode potential till < 0.1 V (>25 min) → Reduce Pt oxides in the cathode catalyst surface Decrease cell temperature → Regeneration/ hydration of the ionomer	Decrease the cathode potential (10 min) → Reduce Pt oxides in the cathode catalyst surface	Decrease the cathode potential → Reduce the Pt oxides in the cathode catalyst surface Decrease cell temperature → Regeneration/hydration of the ionomer
Recovery of mass transport loss	Recovery assessment	high	high	high
	Conditions & mechanisms	1-h dry gas purging with 1.5 L·min^{-1} & 30-min gas purging with 1.5 L·min-1 in restart step → Water removal	4-min dry gas purging with cathode 4 L·min^{-1} and anode 2 L·min^{-1} → Water removal	30-min gas purging with 1.5 L·min^{-1} in restart step → Water removal

observed, as it is already established within the JRC protocol to ensure reduction of PtO_x. Furthermore, it is important to include a cell temperature drop in order to induce a wetting of ionomer by condensation.

To make the limitations of the provided study clear and to avoid overinterpretation of the data, it has to be stressed that a specific sequence of the performed recovery procedures was selected within this study. This allows the qualitative assessment of strength and weaknesses of the three procedures as described above. However, the data in Section 3.6 clearly shows that results depend on operation history of the cell and therefore on the sequence of recovery procedures. Consequently, other sequences would likely lead to slightly different results in terms of quantification of the strengths and weaknesses of the studied procedures. Therefore, only qualitative outcomes are provided in Table 4.

CRediT authorship contribution statement

Qian Zhang: Conceptualization, Methodology, Software, Validation, Formal analysis, Investigation, Writing – original draft, Writing – review & editing. **Mathias Schulze:** Conceptualization, Methodology, Writing – review & editing, Supervision. **Pawel Gazdzicki:** Conceptualization, Methodology, Writing – review & editing, Supervision. **K. Andreas Friedrich:** Conceptualization, Methodology, Writing – review & editing, Supervision.

Declaration of Competing Interest

The authors declare that they have no known competing financial interests or personal relationships that could have appeared to influence the work reported in this paper.

Acknowledgments

The work is linked to the FCCP project. This FCCP (Fuel Cell Cargo Pedelec) project has received funding from the Interreg North-West Europe under NWE596 in the program Priority Axis2 Low Carbon, specific objective SO4. Qian Zhang gratefully acknowledges financial support from China Scholarship Council.

Appendix A. Supplementary material

Supplementary data to this article can be found online at https://doi.org/10.1016/j.apenergy.2021.117490.

References

[1] KEY PERFORMANCE INDICATORS (KPIS) FOR FCH RESEARCH AND INNOVATION, 2020 - 2030. HER and EERA Joint Reasearch Programme on Fuel Cells and Hydrogen technologies; 2020.
[2] Ralph TR, Hards GA, Keating JE, Campbell SA, Wilkinson DP, Davis M, et al. Low Cost Electrodes for Proton Exchange Membrane Fuel Cells: Performance in Single Cells and Ballard Stacks. J Electrochem Soc 2019;144:3845–57.
[3] Kim B, Cha D, Kim Y. The effects of air stoichiometry and air excess ratio on the transient response of a PEMFC under load change conditions. Appl Energ. 2015; 138:143–9.
[4] Zago M, Baricci A, Bisello A, Jahnke T, Yu H, Maric R, et al. Experimental analysis of recoverable performance loss induced by platinum oxide formation at the polymer electrolyte membrane fuel cell cathode. J Power Sources 2020;455.
[5] Shrestha BR, Yadav AP, Nishikata A, Tsuru T. Application of channel flow double electrode to the study on platinum dissolution during potential cycling in sulfuric acid solution. Electrochim Acta 2011;56:9714–20.
[6] Topalov AA, Cherevko S, Zeradjanin AR, Meier JC, Katsounaros I, Mayrhofer KJJ. Towards a comprehensive understanding of platinum dissolution in acidic media. Chem Sci 2014;5:631–8.
[7] Qi ZG, Tang H, Guo QH, Du B. Investigation on "saw-tooth" behavior of PEM fuel cell performance during shutdown and restart cycles. J Power Sources 2006;161: 864–71.
[8] Zhai S, Zhou S, Sun PT, Chen FX, Niu JG. Modeling Study of Anode Water Flooding and Gas Purge for PEMFCs. J Fuel Cell Sci Tech. 2012;9.
[9] Nagahara Y, Sugawara S, Shinohara K. The impact of air contaminants on PEMFC performance and durability. J Power Sources 2008;182:422–8.
[10] Zamel N, Li XG. Effect of contaminants on polymer electrolyte membrane fuel cells. Prog Energ Combust. 2011;37:292–329.
[11] Zhai Y, St-Pierre J. Acetonitrile contamination in the cathode of proton exchange membrane fuel cells and cell performance recovery. Appl Energ. 2019;242:239–47.
[12] Jomori S, Komatsubara K, Nonoyama N, Kato M, Yoshida T. An Experimental Study of the Effects of Operational History on Activity Changes in a PEMFC. J Electrochem Soc 2013;160:F1067–73.
[13] Du FM, Dao TA, Peitl PVJ, Bauer A, Preuss K, Bonastre AM, et al. Effects of PEMFC Operational History under Dry/Wet Conditions on Additional Voltage Losses due to Ionomer Migration. J Electrochem Soc 2020;167:144513–27.
[14] Dubau L, Lopez-Haro M, Castanheira L, Durst J, Chatenet M, Bayle-Guillemaud P, et al. Probing the structure, the composition and the ORR activity of Pt3Co/C nanocrystallites during a 3422 h PEMFC ageing test. Appl Catal B-Environ 2013; 142:801–8.
[15] Hongsirikarn K, Goodwin JG, Greenway S, Creager S. Effect of cations (Na+, Ca2+, Fe3+) on the conductivity of a Nafion membrane. J Power Sources 2010;195: 7213–20.
[16] Zhang T, Wang PQ, Chen HC, Pei PC. A review of automotive proton exchange membrane fuel cell degradation under start-stop operating condition. Appl Energ 2018;223:249–62.
[17] Mittal VO, Kunz HR, Fenton JM. Membrane degradation mechanisms in PEMFCs. J Electrochem Soc 2007;154:B652–6.
[18] Kregar A, Kravos A, Katrašnik T. Methodology for Evaluation of Contributions of Ostwald Ripening and Particle Agglomeration to Growth of Catalyst Particles in PEM Fuel Cells. Fuel Cells 2020;20:487–98.
[19] Meier JC, Galeano C, Katsounaros I, Topalov AA, Kostka A, Schuth F, et al. Degradation Mechanisms of Pt/C Fuel Cell Catalysts under Simulated Start-Stop Conditions. Acs Catal 2012;2:832–43.
[20] Riese A, Banham D, Ye SY, Sun XL. Accelerated Stress Testing by Rotating Disk Electrode for Carbon Corrosion in Fuel Cell Catalyst Supports. J Electrochem Soc 2015;162:F783–8.
[21] Young AP, Stumper J, Gyenge E. Characterizing the Structural Degradation in a PEMFC Cathode Catalyst Layer: Carbon Corrosion. J Electrochem Soc 2009;156: B913–22.
[22] Garcia-Sanchez D, Morawietz T, da Rocha PG, Hiesgen R, Gazdzicki P, Friedrich A. Local impact of load cycling on degradation in polymer electrolyte fuel cells. Appl Energ 2020;259:114210.
[23] Kundu S, Fowler M, Simon LC, Abouatallah R. Reversible and irreversible degradation in fuel cells during Open Circuit Voltage durability testing. J Power Sources 2008;182:254–8.
[24] Gazdzick P, Mitzel J, Sanchez DG, Schulze M, Friedrich KA. Evaluation of reversible and irreversible degradation rates of polymer electrolyte membrane fuel cells tested in automotive conditions. J Power Sources 2016;327:86–95.
[25] Gazdzicki P, Mitzel J, Dreizler AM, Schulze M, Friedrich KA. Impact of Platinum Loading on Performance and Degradation of Polymer Electrolyte Fuel Cell Electrodes Studied in a Rainbow Stack. Fuel Cells 2018;18:270–8.
[26] Schulze M, Wagner N, Kaz T, Friedrich KA. Combined electrochemical and surface analysis investigation of degradation processes in polymer electrolyte membrane fuel cells. Electrochim Acta 2007;52:2328–36.
[27] Pivac I, Barbir F. Impact of Shutdown Procedures on Recovery Phenomena of Proton Exchange Membrane Fuel Cells. Fuel Cells 2020;20:185–95.
[28] Rinaldo SG, Lee W, Stumper J, Eikerling M. Mechanistic Principles of Platinum Oxide Formation and Reduction. Electrocatalysis-Us 2014;5:262–72.
[29] Ahluwalia RK, Arisetty S, Wang XP, Wang XH, Subbaraman R, Ball SC, et al. Thermodynamics and Kinetics of Platinum Dissolution from Carbon-Supported Electrocatalysts in Aqueous Media under Potentiostatic and Potentiodynamic Conditions. J Electrochem Soc 2013;160:F447–55.
[30] Kongkanand A, Zhang JX, Liu ZY, Lai YH, Sinha P, Thompson EL, et al. Degradation of PEMFC Observed on NSTF Electrodes. J Electrochem Soc 2014;161: F744–53.
[31] Sugawara S, Maruyama T, Nagahara Y, Kocha SS, Shinohra K, Tsujita K, et al. Performance decay of proton-exchange membrane fuel cells under open circuit conditions induced by membrane decomposition. J Power Sources 2009;187: 324–31.
[32] Izquierdo U, Barrio VL, Cambra JF, Requies J, Guemez MB, Arias PL, et al. Hydrogen production from methane and natural gas steam reforming in conventional and microreactor reaction systems. Int J Hydrogen Energ 2012;37: 7026–33.
[33] Levin DB, Chahine R. Challenges for renewable hydrogen production from biomass. Int J Hydrogen Energ 2010;35:4962–9.
[34] Cheng X, Shi Z, Glass N, Zhang L, Zhang JJ, Song DT, et al. A review of PEM hydrogen fuel cell contamination: Impacts, mechanisms, and mitigation. J Power Sources 2007;165:739–56.
[35] Fu J, Hou M, Du C, Shao ZG, Yi BL. Potential dependence of sulfur dioxide poisoning and oxidation at the cathode of proton exchange membrane fuel cells. J Power Sources 2009;187:32–8.
[36] Garzon FH, Lopes T, Rockward T, Sansinena JM, Kienitz B, Mukundan R, et al. The Impact of Impurities On Long Term PEMFC Performance. ECS Trans 2009;25: 1575–83.
[37] Zhang YL, Chen SG, Wang Y, Ding W, Wu R, Li L, et al. Study of the degradation mechanisms of carbon-supported platinum fuel cells catalyst via different accelerated stress test. J Power Sources 2015;273:62–9.
[38] Urdampilleta IG, Uribe FA, Rockward T, Brosha EL, Pivovar BS, Garzon FH. PEMFC Poisoning with H2S: Dependence on Operating Conditions. ECS Trans 2007;11: 831–42.
[39] Mitzel J, Zhang Q, Gazdzicki P, Friedrich KA. Review on mechanisms and recovery procedures for reversible performance losses in polymer electrolyte membrane fuel cells. J Power Sources 2021;488:229375.

[40] Tsotridis G, Pilenga A, De Marco G, Malkow T. EU harmonised test protocols for PEMFC MEA testing in single cell configuration for automotive applications. JRC Science Policy Rep 2015;27632.
[41] DOE U. The Fuel Cell Technologies Office Multi-Year Research, Development, and Demonstration Plan. Technical report: US Department of Energy; 2016.
[42] Sanchez DG, Ruiu T, Biswas I, Schulze M, Helmly S, Friedrich KA. Local impact of humidification on degradation in polymer electrolyte fuel cells. J Power Sources 2017;352:42–55.
[43] Talukdar K, Gazdzicki P, Friedrich KA. Comparative investigation into the performance and durability of long and short side chain ionomers in Polymer Electrolyte Membrane Fuel Cells. J Power Sources 2019;439.
[44] Choo HS, Chun DK, Lee JH, Shin HS, Lee SK, Park YS, et al. Performance Recovery of Fuel Cell Stack for FCEV. SAE Technical Paper Series 2015.
[45] Inaba M, Yamada H, Umebayashi R, Sugishita M, Tasaka A. Membrane degradation in polymer electrolyte fuel cells under low humidification conditions. Electrochemistry 2007;75:207–12.
[46] Owejan JP, Trabold TA, Gagliardo J, Jacobson DL, Carter RN, Hussey DS, et al. Voltage instability in a simulated fuel cell stack correlated to cathode water accumulation. J Power Sources 2007;171:626–33.
[47] Zhang JX, Datta R. Online monitoring of anode outlet CO concentration in PEM fuel cells. Electrochem Solid St 2003;6:A5–8.
[48] Arena F, Mitzel J, Hempelmann R. Permeability and Diffusivity Measurements on Polymer Electrolyte Membranes. Fuel Cells 2013;13:58–64.
[49] Zhang Q, Schulze M, Gazdzicki P, Friedrich KA. Quantification of Effects of Performance Recovery Procedures for Polymer Electrolyte Membrane Fuel Cells, in preparation.
[50] Mench MM, Wang CY, Ishikawa M. In situ current distribution measurements in polymer electrolyte fuel cells. J Electrochem Soc 2003;150:A1052–9.
[51] Zhang Q, Lin R, Techer L, Cui X. Experimental study of variable operating parameters effects on overall PEMFC performance and spatial performance distribution. Energy 2016;115:550–60.
[52] Sanchez DG, Ruiu T, Friedrich KA, Sanchez-Monreal J, Vera M. Analysis of the Influence of Temperature and Gas Humidity on the Performance Stability of Polymer Electrolyte Membrane Fuel Cells. J Electrochem Soc 2016;163:F150–9.
[53] García-Salaberri P, Sánchez D, Boillat P, Vera M, Friedrich KA. Hydration and dehydration cycles in polymer electrolyte fuel cells operated with wet anode and dry cathode feed: A neutron imaging and modeling study. J Power Sources 2017;359:634–55.
[54] Kimball EE, Benziger JB, Kevrekidis YG. Effects of GDL Structure with an Efficient Approach to the Management of Liquid water in PEM Fuel Cells. Fuel Cells 2010;10:530–44.
[55] Guétaz L, Escribano S, Sicardy O. Study by electron microscopy of proton exchange membrane fuel cell membrane-electrode assembly degradation mechanisms: Influence of local conditions. J Power Sources 2012;212:169–78.
[56] Paul DK, Shim HK, Giorgi JB, Karan K. Thickness Dependence of Thermally Induced Changes in Surface and Bulk Properties of Nafion (R) Nanofilms. J Polym Sci Pol Phys 2016;54:1267–77.
[57] Yang S, Choi S, Kim Y, Yoon J, Im S, Choo H. Improvement of Fuel Cell Durability Performance by Avoiding High Voltage. Int J Auto Tech-Kor 2019;20:1113–21.
[58] Dhanushkodi SR, Tam M, Kundu S, Fowler MW, Pritzker MD. Carbon corrosion fingerprint development and de-convolution of performance loss according to degradation mechanism in PEM fuel cells. J Power Sources 2013;240:114–21.
[59] Dhanushkodi SR, Kundu S, Fowler MW, Pritzker MD. Study of the effect of temperature on Pt dissolution in polymer electrolyte membrane fuel cells via accelerated stress tests. J Power Sources 2014;245:1035–45.
[60] Morawietz T, Handl M, Oldani C, Friedrich KA, Hiesgen R. Quantitative in Situ Analysis of Ionomer Structure in Fuel Cell Catalytic Layers. ACS Appl Mater Interf 2016;8:27044–54.
[61] Owejan JP, Owejan JE, Gu WB. Impact of Platinum Loading and Catalyst Layer Structure on PEMFC Performance. J Electrochem Soc 2013;160:F824–33.
[62] Hanawa H, Kunimatsu K, Watanabe M, Uchida H. In Situ ATR-FTIR Analysis of the Structure of Nafion-Pt/C and Nafion-Pt3Co/C Interfaces in Fuel Cell. J Phys Chem C 2012;116:21401–6.
[63] Orfanidi A, Madkikar P, El-Sayed HA, Harzer GS, Kratky T, Gasteiger HA. The Key to High Performance Low Pt Loaded Electrodes. J Electrochem Soc 2017;164:F418–26.
[64] Morawietz T, Handl M, Oldani C, Gazdzicki P, Hunger J, Wilhelm F, et al. High-Resolution Analysis of Ionomer Loss in Catalytic Layers after Operation. J Electrochem Soc 2018;165:F3139–47.
[65] Yin Y, Li RT, Bai FQ, Zhu WK, Qin YZ, Chang YF, et al. Ionomer migration within PEMFC catalyst layers induced by humidity changes. Electrochem Commun 2019;109:106590.
[66] Bender G, Angelo M, Bethune K, Rocheleau R. Quantitative analysis of the performance impact of low-level carbon monoxide exposure in proton exchange membrane fuel cells. J Power Sources 2013;228:159–69.
[67] Jiménez S, Soler J, Valenzuela RX, Daza L. Assessment of the performance of a PEMFC in the presence of CO. J Power Sources 2005;151:69–73.
[68] Kabasawa A, Saito J, Miyatake K, Uchida H, Watanabe M. Effects of the decomposition products of sulfonated polyimide and Nafion membranes on the degradation and recovery of electrode performance in PEFCs. Electrochim Acta 2009;54:2754–60.
[69] Prass S, Friedrich KA, Zamel N. Tolerance and Recovery of Ultralow-Loaded Platinum Anode Electrodes upon Carbon Monoxide and Hydrogen Sulfide Exposure. Molecules 2019;24:3514.
[70] https://www.stadtklima-stuttgart.de/index.php?klima_messdaten_station_afu.
[71] Borup RL, Weber AZ. FC-PAD: Fuel cell performance and durability consortium. Los Alamos National Lab.(LANL), Los Alamos, NM (United States); 2018.
[72] Borup RL, Kusoglu A, Neyerlin KC, Mukundan R, Ahluwalia RK, Cullen DA, et al. Recent developments in catalyst -related PEM fuel cell durability. Curr Opin Electroche 2020;21:192–200.
[73] Pei P, Chen H. Main factors affecting the lifetime of Proton Exchange Membrane fuel cells in vehicle applications: A review. Appl Energ 2014;125:60–75.
[74] Miller M, Bazylak A. A review of polymer electrolyte membrane fuel cell stack testing. J Power Sources 2011;196:601–13.
[75] Jung JH, Kim SH, Hur SH, Joo SH, Choi WM, Kim J. Polymer electrolyte membrane fuel cell performance degradation by coolant leakage and recovery. J Power Sources 2013;226:320–8.
[76] Kakati BK, Unnikrishnan A, Rajalakshmi N, Jafri RI, Dhathathreyan KS, Kucernak ARJ. Recovery of Polymer Electrolyte Fuel Cell exposed to sulphur dioxide. Int J Hydrogen Energ 2016;41:5598–604.

SUPPORTING INFORMATION FOR

Comparison of Different Performance Recovery Procedures for Polymer Electrolyte Membrane Fuel Cells

Qian Zhang[1, 2, *], Mathias Schulze[1], Pawel Gazdzicki[1], K. Andreas Friedrich[1, 2]

[1]: German Aerospace Center (DLR), Institute of Engineering Thermodynamics, Pfaffenwaldring 38-40, 70569 Stuttgart, Germany

[2]: University of Stuttgart, Institute for Building Energetics, Thermal Engineering and Energy Storage (IGTE), Pfaffenwaldring 31, 70569 Stuttgart, Germany

*: qian.zhang@dlr.de, +49 711 6862 8821

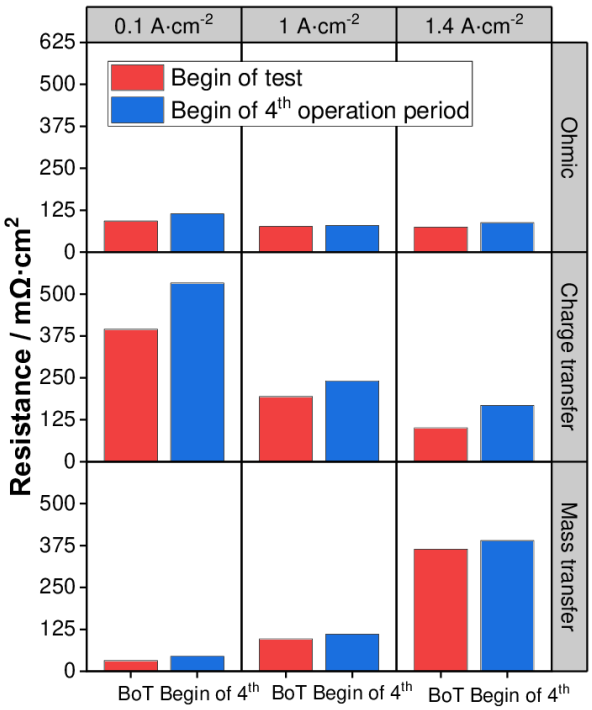

Figure S1: Irreversible degradation. Ohmic, charge transfer and mass transfer resistance at the beginning of the test and before the 4th operation period, measured at the current density of 0.1, 1.0 and 1.4 A·cm-2.

3.6 Effect of operation history

Table S1 The experimental steps of the three durability tests with overnight rest as the third recovery procedure and another two other former recovery procedures

Process of the durability test	**Steps**		
	Operation history 1	**Operation history 2**	**Operation history 3**
Beginning of the test	MEA conditioning		
Operation period 1	Fuel cell characterization		
	82-h FC-DLC drive cycles		
	Fuel cell characterization		
Recovery procedure 1	JRC protocol	Cell cool down to 25℃	60 min, Voltage cycling 0.3V-0.8V
Operation period 2	Fuel cell characterization		
	82-h FC-DLC drive cycles		
	Fuel cell characterization		
Recovery procedure 2	DOE Protocol	Cell cool down to 40℃	30 min, Voltage cycling 0.3V-0.8V
Operation period 3	Fuel cell characterization		
	82-h FC-DLC drive cycles		
	Fuel cell characterization		
Recovery procedure 3	Overnight rest		
Operation period 4	Fuel cell characterization		
	82-h FC-DLC drive cycles		
	Fuel cell characterization		

8.3 Article III

Temperature Reduction as Operando Performance Recovery Procedure for Polymer Electrolyte Membrane Fuel Cells

Zhang, Q., Schulze, M., Gazdzicki, P., & Friedrich, K. A.

Energies 17 (2024): 774

DOI: https://doi.org/10.3390/en17040774

Contribution of Qian Zhang: Conception of the work, execution of experiments, as well as writing, data analysis, and reviewing.

energies

MDPI

Article

Temperature Reduction as Operando Performance Recovery Procedure for Polymer Electrolyte Membrane Fuel Cells

Qian Zhang [1,2], Mathias Schulze [1], Pawel Gazdzicki [1,*] and Kaspar Andreas Friedrich [1,2]

[1] Electrochemical Energy Technology, Institute of Engineering Thermodynamics, German Aerospace Center (DLR), Pfaffenwaldring 38-40, 70569 Stuttgart, Germany; st158059@stud.uni-stuttgart.de (Q.Z.); mathias.schulze@dlr.de (M.S.); andreas.friedrich@dlr.de (K.A.F.)

[2] Institute of Building Energetics, Thermal Engineering and Energy Storage (IGTE), University of Stuttgart, Pfaffenwaldring 31, 70569 Stuttgart, Germany

* Correspondence: pawel.gazdzicki@dlr.de; Tel.: +49-711-6862-8094

Abstract: To efficiently mitigate the reversible performance degradation of polymer electrolyte membrane fuel cells, it is crucial to thoroughly understand recovery effects. In this work, the effect of operando performance recovery by temperature reduction is evaluated. The results reveal that operando reduction in cell temperature from 80 °C to 45 °C yields a performance recovery of 60–70% in the current density range below 1 A cm^{-2} in a shorter time (1.5 h versus 10.5 h), as opposed to a known and more complex non-operando recovery procedure. Notably, the absolute recovered voltage is directly proportional to the total amount of liquid water produced during the temperature reduction. Thus, the recovery effect is likely attributed to a reorganization/rearrangement of the ionomer due to water condensation. Reduction in the charge transfer and mass transfer resistance is observed after the temperature reduction by electrochemical impedance spectroscopy (EIS) measurement. During non-operando temperature reduction (i.e., open circuit voltage (OCV) hold during recovery instead of load cycling) an even higher recovery efficiency of >80% was achieved.

Keywords: durability; irreversible degradation; operando recovery; polymer electrolyte membrane fuel cells; reversible degradation

Citation: Zhang, Q.; Schulze, M.; Gazdzicki, P.; Friedrich, K.A. Temperature Reduction as Operando Performance Recovery Procedure for Polymer Electrolyte Membrane Fuel Cells. *Energies* **2024**, *17*, 774. https://doi.org/10.3390/en17040774

Academic Editors: K. T. Chau, Hongtao Sun, Junfei Liang and Jian Zhu

Received: 15 December 2023
Revised: 21 January 2024
Accepted: 1 February 2024
Published: 6 February 2024

1. Introduction

To achieve carbon neutrality, the development and commercialization of electric vehicles with polymer electrolyte membrane fuel cells (PEMFCs) are gathering increased attention, especially for heavy-duty applications [1,2]. Despite significant technological progress within the last decades, high costs and limited longevity are still regarded as barriers to the widespread application of PEMFCs [3]. For heavy-duty vehicles, the European Commission has established targets for fuel cell stack durability, aiming for 30,000 h and a stack cost below €50/kW by 2030 [4]. For comparison, the current state-of-the-art of 2020 is defined by a durability of 15,000 h with a cost exceeding €100/kW, according to the Strategic Research and Innovation Agenda 2021–2027 of the Clean Hydrogen Joint Undertaking (Clean Hydrogen JU). Similarly, the Department of Energy (DOE) has set interim and ultimate targets for Class 8 Long-Haul Tractor-Trailers, with the fuel cell system expected to have a lifetime of 25,000 h by 2030 and 30,000 h by 2050, along with fuel cell system costs of $80/kW and $60/kW, respectively [5].

Throughout the lifespan of PEMFCs, diverse operational conditions can arise, presenting challenges to both performance and durability. These scenarios include frequent shut-down/start-up, freeze–thaw, idle running, dynamic loading, full power running, and overload running conditions. Each of these conditions imposes unique demands and stresses on the PEMFC system, potentially impacting its overall performance and longevity [6,7]. To achieve the targeted durability, it is essential to mitigate fuel cell performance degradation. Over the lifespan of PEMFCs, various types of performance losses

occur—both reversible and irreversible—depending on the selected operation conditions and materials. A number of publications have proposed mitigation strategies for reversible performance losses, including (i) the elimination of absorbed contaminants of the catalyst [8], (ii) the reduction of catalyst oxides in the cathode [9,10], (iii) the prevention of flooding in the catalyst layer [11], (iv) the rehydration of the membrane [12], and more. An overview of the mechanisms causing reversible performance losses has been published recently [13]. However, accurately quantifying recovery effects is challenging due to several factors: (i) electrochemical characterizations, such as cyclic voltammetry (CV) analyses, can themselves influence the recovery [14], (ii) reversible and irreversible effects are interdependent [13], (iii) the effect of recovery depends on the given operation conditions (e.g., dry versus wet) [15] and the properties of membrane electrode assemblies (MEAs), and (iv) the change in ionomer structure, argued to play a relevant role in the recovery effect, is not fully understood and is challenging to access through operando or in situ characterization methods [16,17].

Empirical studies indicate that shut-down processes, encompassing long stops with a temperature decrease, have a positive impact on performance recovery [18,19]. In this context, water condensation due to temperature reduction is proposed to play a prominent role [20–22]. In the literature [11,23], the recovery of performance losses due to shut-down was observed and ascribed to the removal of water in the catalyst layer and water redistribution in the cell. Steinbach et al. [24] and Prass et al. [25] reported that a shut-down/start-up process, including cooling down the cell to room temperature, leads to the removal of sulfide ions in the anode (effective catalyst poisons) and subsequent performance recovery. Pivac et al. [26] compared the recovery effect of different shut-down procedures involving varying cooling rates. The results showed that an accelerated cell cooling was counterproductive in terms of performance recovery. Kabir et al. [27] proposed a recovery procedure where the cell was cooled down from 80 °C to 40 °C at 0.1 V with air oversaturated with water, leading to the removal of contaminants and catalyst oxides. Additionally, considering changes in oxygen transport resistance during the recovery procedure and drawing on previous relevant research, the authors highlighted the rearrangement of the catalyst atomic structure as an important contribution to the performance recovery. Zhang et al. [28] investigated irreversible chemical degradation of the membrane under open circuit voltage (OCV) conditions. The performance recovery by cooling down from 80 °C to 50 °C and purging with H_2/N_2 for 2 h was mainly attributed to the removal of sulfate anions (generated due to membrane degradation) from both anode and cathode through the analysis of fuel cell effluent water. Similarly, Robb et al. [29] and Shokhen et al. [30] presented a recovery procedure based on an increase in relative humidity (RH) to or above 100%, followed by the application of low cell voltage. This recovery procedure was supposed to release contaminants on the catalyst surface and purge them out of the cell.

A common feature among the aforementioned recovery procedures is that they are non-operando, therefore requiring the interruption of fuel cell operation. This characteristic can be particularly detrimental in cases where long-term continuous operation is essential, such as in the context of ships.

To the best of our knowledge, operando recovery procedures have not been published so far. This work aims to address this gap by investigating and quantifying the mechanism of performance recovery due to operando temperature reduction. Specific tests have been performed at the single-cell level for this purpose. Operando recovery procedures are simpler to implement in real fuel cell (FC) systems compared to complex non-operando procedures. Concerning the recovery, ionomer hydration plays a key role which is likely linked to ionomer rearrangement [16,17]. Additionally, recovery efficiency is assessed and compared to common non-operando recovery procedures. This work outlines conclusions on alternative operation conditions, materials, and scaling-up, while also providing an explanation of the limitations of the presented experiments. Hence, the outcomes contribute to the new body of knowledge by addressing the gap in operando recovery of reversible losses in PEMFCs, with the potential for implementation in future fuel cell systems.

2. Experimental

2.1. Test Hardware

The materials, including the test bench and control software for the durability tests, were developed at the German Aerospace Center (Deutsches Zentrum für Luft- und Raumfahrt e.V., DLR, Stuttgart, Germany), as described in previous publications [31,32]. A variety of operating parameters can be adjusted manually or by scripts, such as cell temperature, gas flow, relative humidity (using bubblers), and outlet pressure.

A single cell with a 5×5 cm^2 active area was utilized, featuring one-channel serpentine flow fields arranged in a co-flow configuration. The gas channels were oriented parallel to the direction of gravity, with gas inlets at the top and outlets at the bottom of the cell. This configuration is reported in the literature to promote stable performance [33].

The 5-layer MEA utilized in this experiment was manufactured by IRD Fuel Cells A/S according to DLR's specifications for the purpose of this investigation. It comprises a 27.5 µm thick Nafion^{TM} XL membrane sandwiched between the anode and cathode catalyst layers, each having a Pt/C ratio of 50 wt % and Pt loadings of 0.05 and 0.25 mg cm^{-2}, respectively. The active area was 5×5 cm^2. As gas diffusion layers (GDLs), Sigracet® 29BC sheets from SGL Carbon SE were employed. Ice Cube Sealings with a thickness of 350 µm from Freudenberg FST GmbH served as a gasket material.

2.2. Operation Conditions and Test Protocols

Prior to each experiment, a leak test was conducted on both the single cell and the test bench. Subsequently, the MEA underwent conditioning to achieve stable performance. A detailed description is provided in a recent work [34].

The load cycling protocol employed for the durability tests was the Fuel Cell Dynamic Load Cycle (FC-DLC), see illustrated in Figure 1a [35]. The maximum current density of the FC-DLC was defined as the current density yielding 0.65 V, corresponding to 1 A cm^{-2}. Throughout FC-DLC operation, constant gas flows of H_2 (0.263 L min^{-1}) and air (0.83 L min^{-1}) were maintained, corresponding to H_2 and oxygen stoichiometry of 1.5 and 2.0 for the current density of 1 A cm^{-2}. The cell operating temperature was set to 80 °C, with relative humidities at the anode and cathode inlets set to 100%. The absolute gas pressures at the anode and cathode outlets were controlled at 250 and 230 kPa, respectively.

Table 1. Performance recovery procedures included in durability tests.

#	Operando	Non-Operando
Recovery 1	80 °C to 45 °C (95 min)	80 °C to 30 °C (95 min)
Recovery 2	80 °C to 60 °C (35 min)	80 °C to 45 °C (95 min)
Recovery 3	Repetition of Recovery 1	80 °C to 60 °C (95 min)
Recovery 4	Repetition of Recovery 2	Repetition of Recovery 1
Recovery 5	80 °C to 60 °C (95 min)	Repetition of Recovery 3
Recovery 6	80 °C to 45 °C (35 min)	-

Two types of durability tests were conducted to investigate the performance recovery effect of (i) operando temperature reduction and (ii) non-operando temperature reduction. The second test allows the implementation of additional electrochemical analyses, such as polarization curves and electrochemical impedance spectroscopy (EIS), which requires the interruption of continuous fuel cell operation. The approaches are shown in Figure 1b,c and described in the following:

- The first durability test comprises 6 test blocks, as indicated in Figure 1b. At the beginning of each test block, a performance characterization was conducted, followed by a 76 h period of load cycling. Subsequently, an operando recovery procedure was implemented; specifically, the cell temperature was reduced to a specific set point and then increased to the nominal operating temperature. After reaching the nominal operating temperature, FC-DLC operation was continued for an additional 3 h

before applying the JRC recovery procedure [35] as a benchmark (see Supplementary Materials for more details). The JRC protocol, proposed by the Joint Research Center (JRC) of the European Commission [35], was chosen for this work based on our previous study [34], assuming 100% recovery. After each test block, it is imperative to implement the JRC protocol to prevent the accumulation of non-recovered reversible losses throughout the experiment [34]. This is crucial to avoid misinterpretation and misevaluation of the effectiveness of the operando recovery procedure.

- The second durability test (Figure 1c) consists of 5 test blocks. After each 76 h load cycling period, the cycling was paused, and performance characterization measurements were conducted before and after each non-operando temperature reduction procedure. Specifically, the cell temperature was reduced once the electrical load was switched off (leading to OCV), while the other operating parameters (gas flow and pressure) were kept constant. To compare the efficiency of the recovery due to temperature reduction with the efficiency of the JRC recovery protocol, at the end of each test block the JRC recovery protocol was performed, followed by an additional performance characterization.

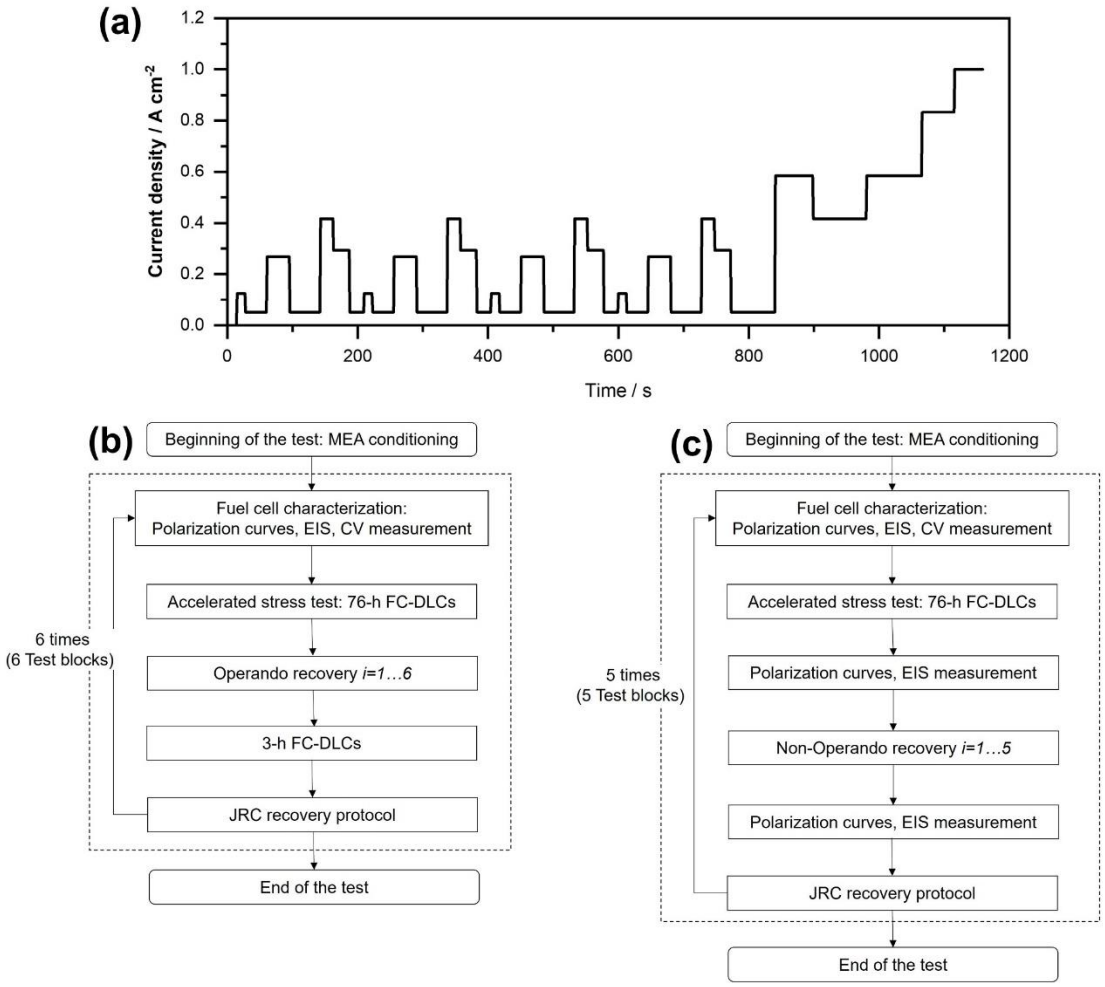

Figure 1. (**a**) Fuel cell dynamic load cycle (FC-DLC) used in this study. Flow charts of the two durability tests carried out to study recovery procedures with (**b**) operando and (**c**) non-operando temperature reduction. The sequence of the applied recovery procedures is provided in Table 1.

2.3. Characterization Methods

Polarization curves were recorded following the EU Harmonized Test Protocols for MEA Testing [34]. The data were acquired every second and then averaged over the last 30 s of the dwell time at each setpoint of the tested current density. The error bars corresponded to the standard deviation from the average. The H_2 and oxygen (in air feed) stoichiometry were set at 1.5 and 2.0, respectively, while cell temperature, humidity, and gas pressures remained consistent with FC-DLC operation, as described above. The minimum H_2 and air flows were maintained at 0.105 and 0.332 L min^{-1}, respectively.

Electrochemical impedance spectroscopy (EIS) testing under a constant current density of 0.8 A cm^{-2} was conducted using the modular electrochemical workstation Zennium X and electronic load PP241 from ZAHNER-Elektrik GmbH & CoKG (Kronach, Germany). The analysis covered a frequency range from 100 mHz to 10 kHz, with a perturbation amplitude of ±5% of the applied current. The EIS data were analyzed with the Thales XT software package (Version 5.3.3). The operation parameters were consistent with the polarization curve measurements.

2.4. Recovery Procedures

The recovery procedures evaluated in the two durability tests are summarized in Table 1 and are labeled as "operando" and "non-operando".

In the case of operando recovery, the cell temperature was reduced from the nominal operating temperature of 80 °C to either 45 °C or 60 °C to observe measurable recovery of performance loss. Although an attempt was made to reduce the temperature to 30 °C, it proved unattainable due to the heat generated during fuel cell operation. After reaching the targeted temperature, the cell was reheated to 80 °C again. The respective durations until reaching the targeted temperature were 95 and 35 min, indicating the time it takes for the fuel cell to naturally reach the target temperature after the heating system is switched off. Subsequently, these two recovery procedures were repeated (labeled as recovery procedures 3 and 4) to test reproducibility. Given that the cell temperature reduction from 80 °C to 45 °C took 60 min longer than to 60 °C, the effect of cooling time was investigated separately (procedures 5 and 6). In the case of procedure 6, the cooling process was accelerated by using a cooling fan, reducing the time required to reach 45 °C from 95 min to 35 min. In the case of recovery procedure 5, the cell temperature reduction from 80 °C to 60 °C was prolonged to 95 min by maintaining the cell at 60 °C for an additional 60 min. The variable selection of recovery procedures 5 and 6 allows for a comparison and analysis of the impact of the cooling time on the recovery effect. The temperature profiles of the different procedures are provided in Figure S1 in the Supplementary Materials.

In the case of non-operando temperature reduction, the fuel cell temperature reduced faster than during operando temperature reduction, as no heat is generated during load shutdown. The cell temperature could also be reduced to 30 °C. For a direct comparison with operando temperature reduction results, Recovery procedures 1, 2, and 3 correspond to cell temperature reductions from 80 °C to 30 °C, 45 °C and 60 °C, respectively. In all cases, the setpoint temperatures were maintained for 95 min under OCV after achieving the target temperature. Recovery procedures 4 and 5 are repetitions of recovery procedures 1 and 3. OCV was applied since other cell voltages may influence several recovery parameters, and OCV represents the natural state without load.

3. Results

In Sections 3.1 and 3.2, the performance recovery effects of operando and non-operando temperature reduction are evaluated. The results of the operando temperature reduction are displayed first. Subsequently, the results of non-operando temperature reduction procedures are discussed, including additional performance characterization measurements carried out before and after each recovery. Eventually, the recovery mechanisms are quantified and discussed.

3.1. Operando Performance Recovery Procedures Based on Temperature Reduction

Cell voltages corresponding to individual current density levels of the FC-DLC cycles performed during the durability test are presented in Figure 2. The vertical red dashed lines indicate the implementation of operando temperature reduction. It is noteworthy that the cell voltage decreased during the temperature reduction and subsequently increased (to a higher value) after returning to nominal operation conditions (refer to Figure S1 in the Supplementary Materials). To prevent the cell voltage from dropping below 500 mV, the lower temperature limit was set to 45 °C.

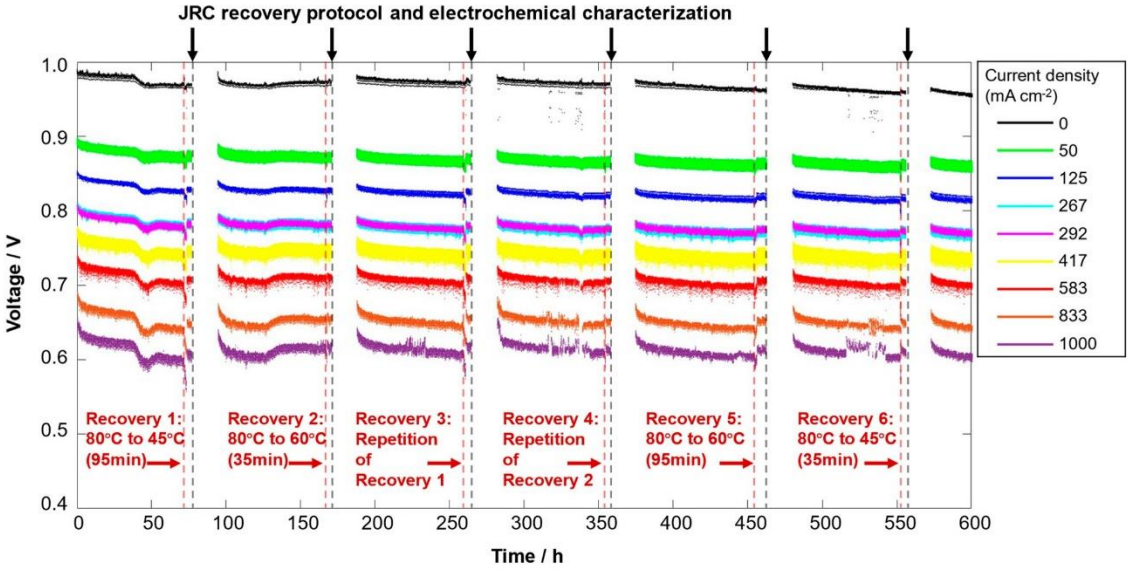

Figure 2. Cell voltage recorded during the durability test (FC-DLC protocol) for the investigation of recovery procedures based on operando temperature reduction. Vertical dashed lines label the starting point of the applied recovery procedures.

In the durability test illustrated in Figure 2, a decrease in cell voltage at each current density is anticipated during the FC-DLC. However, two unexpected voltage fluctuations are observed in the first two test blocks. We attribute these fluctuations to temporary water flooding in the fuel cell channels for the following reasons: (i) the fluctuation is more pronounced at higher current density ranges, where water is more likely to accumulate and block the fuel cell channels, and (ii) the voltage initially decreases and then increases during the FC-DLC, suggesting a temporary water flooding followed by water removal due to increased local gas pressure. Other possible causes of these two fluctuations could be uncertainties in the hardware, such as temporary fluctuations in the gas supply or the electronic load. Importantly, these fluctuations do not recur in subsequent test blocks or in the other durability test depicted in the next section. Despite these fluctuations, the cell voltage decreases after the FC-DLC operation and subsequently increases due to the recovery protocols, which constitute the primary focus of this study.

Figure 3a presents a scheme outlining various definitions used to quantify recovery effects. The solid lines display the cell voltage change during the FC-DLC operation, while the dashed line represents the cell voltage change during the recovery protocols. The voltage values $U_{i=n}^{Begin}$ and $U_{i=n}^{End}$ indicate the cell voltages at the beginning and end of the nth FC-DLC sequence, respectively. $U'^{End}_{i=n}$ corresponds to the voltage after the nth operando recovery procedure. After a subsequent 3 h of FC-DLC and before the next test block, a JRC recovery protocol and performance characterizations are conducted.

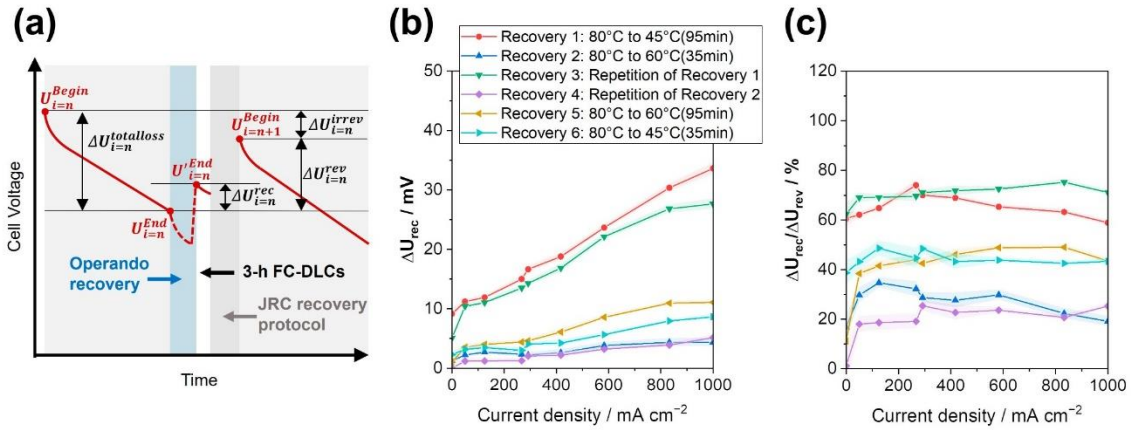

Figure 3. (**a**) Definitions for the evaluation of the relative recovery. (**b**) Recovered voltage versus current density calculated according to Equation (1). (**c**) Relative recovery calculated using Equations (1) and (2).

The voltage recovered due to operando temperature reduction is defined according to Equation (1),

$$\Delta U_{i=n}^{rec} = U'^{End}_{i=n} - U_{i=n}^{End} \quad (1)$$

while the total reversible, recoverable voltage loss is obtained using Equation (2) (i.e., it is assumed that the JRC recovery protocol leads to a full recovery of reversible performance losses),

$$\Delta U_{i=n}^{rev} = U_{i=n+1}^{Begin} - U_{i=n}^{End}. \quad (2)$$

The recovered voltages ΔU^{rec} versus the current density are presented in Figure 3b. It is notable that the recovered reversible voltage losses during the operando procedures are in the range of several mV to 30 mV in each period. The irreversible degradation rates, in contrast, are in the range of 50 µV h^{-1} (see Figure S2 with explanations in the Supplementary Materials). Hence, the reversible performance degradation dominates the overall performance losses.

Apparently, the voltage recovered due to Recovery 1 and Recovery 3 (both 80 °C to 45 °C taking 95 min) as well as Recovery 2 and Recovery 4 (both 80 °C to 60 °C taking 35 min), are similar in the current density range from 0 to 1 A cm^{-2}, indicating reasonable reproducibility. Additionally, in the current density range from 0 to 1 A cm^{-2}, Recovery 1 and 3 (80 °C to 45 °C) lead to a higher recovery compared to Recovery 2 and 4 (80 °C to 60 °C). Moreover, Recovery 5 (80 °C to 60 °C taking 95 min) results in a slightly higher recovery compared to Recovery 2 and 4 (80 °C to 60 °C taking 35 min). Hence, a positive effect of extending the duration of the recovery procedure is concluded, which is consistent with the observation by Pivac et al. [26], who reported a negative effect of rapid cooling on recovery. Figure 3c shows the voltage recovery due to the operando temperature reduction relative to the recovery due to the JRC recovery protocol. The relative recovery efficiencies of the tested procedures are largely constant in the analyzed current density range. When comparing the effect of cooling down to 45 °C and 60 °C, it is evident that a higher recovery effect can be achieved at a lower cell temperature. Specifically, temperature reduction from 80 °C to 60 °C results in less than 30% recovery compared with the JRC protocol, while temperature reduction from 80 °C to 45 °C results in 60–70%. Although the recovery is always lower than for the JRC protocol, the clear advantage is the significantly shorter duration (<2 h vs. 10 h).

However, a longer holding time at the same (low) cell temperature also impacts the recovery and leads to higher recovery efficiencies. Hence, neither the targeted temperature alone nor the holding time is sufficient to describe the efficiency of operando recovery. Interestingly, the recovered voltage is strongly linked with water formation and condensation.

This effect can be described by the amount of liquid water produced in the cell during recovery, $m_{H_2O(liquid)}$, which corresponds to the integration of the liquid water flow at the cathode outlet, $\dot{m}_{H_2O(liquid),outlet}$, according to:

$$m_{H_2O(liquid)} = \int_{recovery} \dot{m}_{H_2O(liquid),outlet}\, dt \tag{3}$$

As an example, the calculated mass flow values for Recovery 1 (80 °C to 45 °C) along with the evolution of cell temperature are shown in Figure 4a. The fluctuations in the signals originate from the load cycling performed during the test, as shown in the FC-DLC protocol in Figure 1a. The liquid water mass flow at the cathode outlet (green data points) is provided by:

$$\dot{m}_{H_2O(liquid),outlet} = \dot{m}_{H_2O(vapor),inlet} + \dot{m}_{H_2O,prod} - \dot{m}_{H_2O(vapor),outlet} \tag{4}$$

with:

1. $\dot{m}_{H_2O(vapor),inlet} + \dot{m}_{H_2O,prod}$, the total water mass flow into the cell (red data points). It consists of the vaporous water mass flow in the inlet air ($\dot{m}_{H_2O(vapor),inlet}$ at 100% RH at 80 °C and a constant flow of 0.83 L min^{-1}), plus product water ($\dot{m}_{H_2O,prod}$) from the electrochemical reaction. It is calculated according to:

$$\dot{m}_{H_2O(vapor),inlet} + \dot{m}_{H_2O,prod} = \frac{\dot{m}_{Air} \cdot M_{H_2O}}{V_{0,mol}} \cdot \left(\frac{P_{air,inlet}}{P_{vapor,\ inlet}} - 1 \right) + \frac{I \cdot M_{H_2O}}{2 \cdot F}, \tag{5}$$

   with $\dot{m}_{Air}$ being the air flow rate of 0.83 L min^{-1}, $P_{air,inlet}$ and $P_{vapor,\ inlet}$ indicating the air pressure and vapor pressure in the cathode inlet, respectively. The constants include $V_{0,mol}$, the molar volume of an ideal gas of 22.414 L mol^{-1}, the Faraday constant, F = 96,485 C·mol^{-1}, and M_{H_2O}, the molar mass of water of 18.015 g mol^{-1}. The current is denoted by I;
2. $\dot{m}_{H_2O(vapor),outlet}$, the maximum output of vaporous water mass flow (blue data points) at the cathode outlet (depending on gas outlet pressure and cell temperature), is calculated using:

$$\dot{m}_{H_2O(vapor),outlet} = \frac{\dot{m}_{Air} \cdot M_{H_2O}}{V_{0,mol}} \cdot \left(\frac{P_{air,outlet}}{P_{vapor,\ outlet}} - 1 \right) \tag{6}$$

   with $P_{air,outlet}$ and $P_{vapor,\ outlet}$ being the air pressure and vapor pressure in the cathode outlet, respectively.

The values of the total amount of liquid water due to the six recovery procedures are provided in Figure 4b. It is noted that the drag of liquid water due to gas flow is not considered, and the integrated data of liquid water do not correspond to the water being present inside the cell, but the amount of liquid water produced during recovery. Apparently, $m_{H_2O(liquid)}$ increases with the duration of the cooling-down period and lower cooling-down temperature.

For the temperature reduction from 80 °C to 45 °C with a duration of 95 min (Recovery 1 and 3) as well as for the temperature reduction from 80 °C to 60 °C with a duration of 35 min (Recovery 2 and Recovery 4), the values $m_{H_2O(liquid)}$ are similar. Specifically, Recovery 1 and 3 exhibit $m_{H_2O(liquid)}$ around 12.9 g, followed by Recovery 5 (80 °C to 60 °C taking 95 min) and Recovery 6 (80 °C to 45 °C taking 35 min), with $m_{H_2O(liquid)}$ equaling 6.8 g and 4.3 g, respectively. On the other hand, cell cooling down from 80 °C to 60 °C (Recovery 2 and 4) leads to $m_{H_2O(liquid)}$ of only 3.4 g.

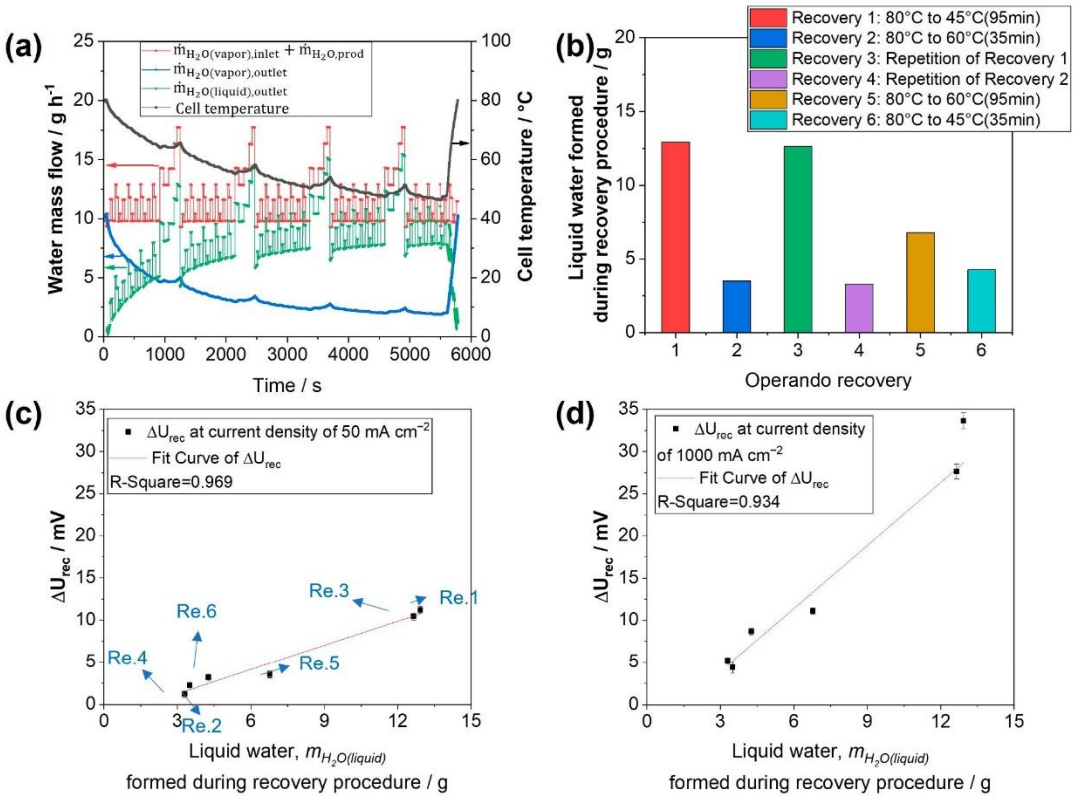

Figure 4. (**a**) Cell temperature (black data) during operando cooling down from 80 °C to 45 °C, along with the calculated value of the total water input in the inlet plus product water, $\dot{m}_{H_2O(vapor),inlet} + \dot{m}_{H_2O,prod}$ (red data), maximum amount of vaporous water, $\dot{m}_{H_2O(vapor),outlet}$, in the cathode outlet considering the pressure drop of the cell (blue data), and the flow of liquid water, $\dot{m}_{H_2O(liquid),outlet}$, in the outlet (green data); (**b**) Total amounts of liquid water, $m_{H_2O(liquid)}$ (integrated signals of $\dot{m}_{H_2O(liquid),outlet}$), during different operando temperature reduction procedures. (**c**,**d**) show the absolute recovered voltage versus the total amount of liquid water formed during the operando recovery (Re. #) at 0.05 A cm^{-2} and 1 A cm^{-2}, respectively. Recovered voltage corresponds to data from Figure 3b.

When comparing the absolute recovered voltage, $\Delta U_{i=n}^{rec}$ and $m_{H_2O(liquid)}$, a strong linear correlation is evident, as shown in Figure 4c,d for current densities of 0.05 and 1 A cm^{-2} (data from Figure 3b). The slope of the fit curves in Figure 4d is higher than that in Figure 4c, indicating that, with the same amount of liquid water, a higher absolute recovered voltage is achieved at a higher current density (1 A cm^{-2}). In the Supplementary Materials (Figure S3), linear correlations between $\Delta U_{i=n}^{rec}$ and $m_{H_2O(liquid)}$ at each evaluated current density from 0 to 1 A cm^{-2} are shown; in Figure S4 the slopes and intercepts of the linear fits are provided. It is noticeable that the slope of the fit curves increases from 0.7 to 2.5 mV g^{-1} with increasing current density from 0.05 to 1 A cm^{-2}. In a previous work [34], rehydration of the membrane and ionomer during temperature reduction was proposed as a major contributing factor to the recovery of performance losses. The trend in Figure 4c,d is particularly interesting, as a direct correlation between recovered voltage and the amount of liquid water has not been reported so far. However, a detailed explanation of specific mechanisms requires additional data.

3.2. Recovery Effect of the Non-Operando Performance Recovery Procedures with Temperature Reduction

Figure 5 shows the voltage recorded during the durability test, consisting of five test blocks using the FC-DLC protocol with non-operando recovery procedures of temperature reduction. The vertical dashed lines indicate the performed recovery procedures, before and after which the fuel cell was characterized with polarization curves and EIS measurements. Before each test block, a JRC recovery protocol and fuel cell performance characterization measurements were conducted, assuming all the reversible performance losses were recovered. The irreversible performance degradation rates (see Figure S5 in the Supplementary Materials) are in the range of 75–125 $\mu V\ h^{-1}$, which is significantly higher compared to the test including operando recovery procedures. The reason is that OCV periods occur during the non-operando recovery procedures. The irreversible effects are not discussed in this paper, but it can be stated that they cannot be justified by electrochemical active surface area (ECSA) loss alone. A similar strong ECSA loss was observed after both tests, with operando recovery (decrease from 478 to 227 $cm^2\ mg^{-1}$) and with non-operando recovery (decrease from 417 to 200 $cm^2\ mg^{-1}$).

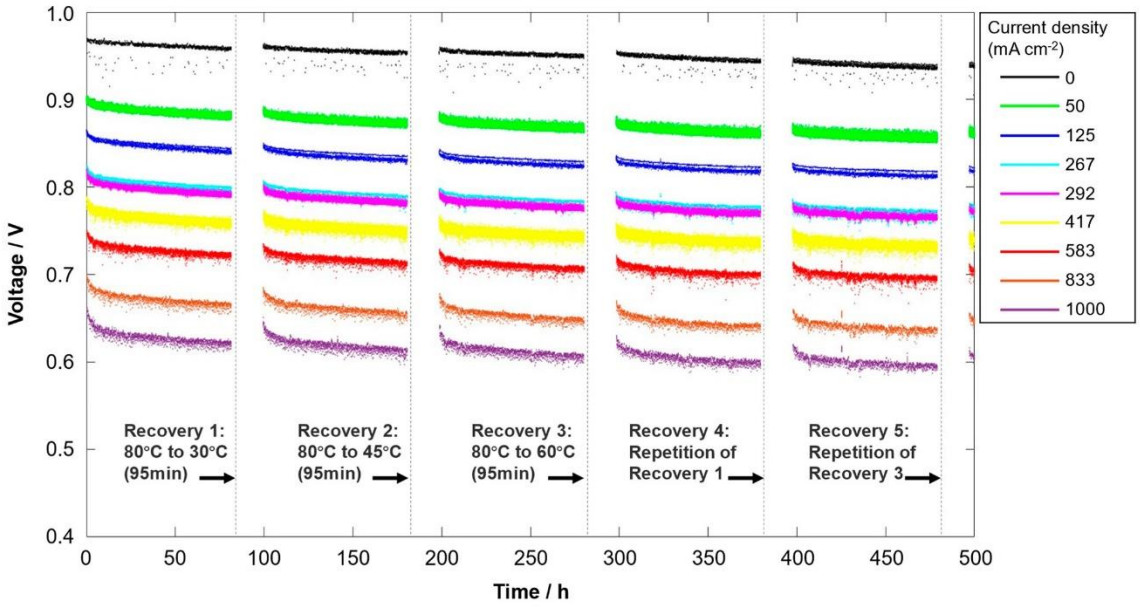

Figure 5. Cell voltage recorded during the durability test (FC-DLC protocol, see Figure 1a) for the investigation of recovery procedures based on non-operando temperature reduction.

In the scheme in Figure 6a, the voltage change between two test blocks is shown. Using Equations (1) and (2), the recovery procedures in this section are evaluated based on the data acquired from polarization curves (see Figure S6 in the Supplementary Materials). Figure 6b shows the absolute recovered voltage losses of the five non-operando temperature reduction procedures in the current density range from 0.0 to 1.5 A cm^{-2} (the current density range is broader than in Section 3.1, because here the polarization curves were measured while in 3.1 only FC-DLC data were available). Notably, temperature reductions from 80 °C to 45 °C and 80 °C to 60 °C were utilized for both operando and non-operando recovery procedures. The absolute recovered voltages due to the temperature reduction from 80 °C to 45 °C and 80 °C to 60 °C using operando (Figure 3b) and non-operando (Figure 6b) recovery procedures show similar trends in the current density range up to 1 A cm^{-2}; in both cases, the recovered voltage increases significantly with increasing current density. The recovered voltages due to the temperature reduction from 80 °C to 30 °C and 45 °C are higher than those from 80 °C to 60 °C and overlap with each other, especially at current densities lower

than 0.9 A cm^{-2}. Interestingly, the recovered voltages due to the temperature reduction from 80 °C to 45 or 30 °C increase over the current density range up to 0.9 A cm^{-2} and then decrease. The relative recovery of non-operando temperature reduction relative to the JRC recovery protocol is shown in Figure 6c. It is clear that a non-operando temperature reduction from 80 °C to 30 °C and 45 °C results in higher than 80% recovery compared to the JRC recovery protocol in a broad current density range of 0.1–1.2 A cm^{-2}. This means that (i) it is sufficient to cool down to 45 °C and further cooling does not lead to a significantly higher recovery, and (ii) the relative recovery of the non-operando temperature reduction is higher than that of operando temperature reduction (60–70%).

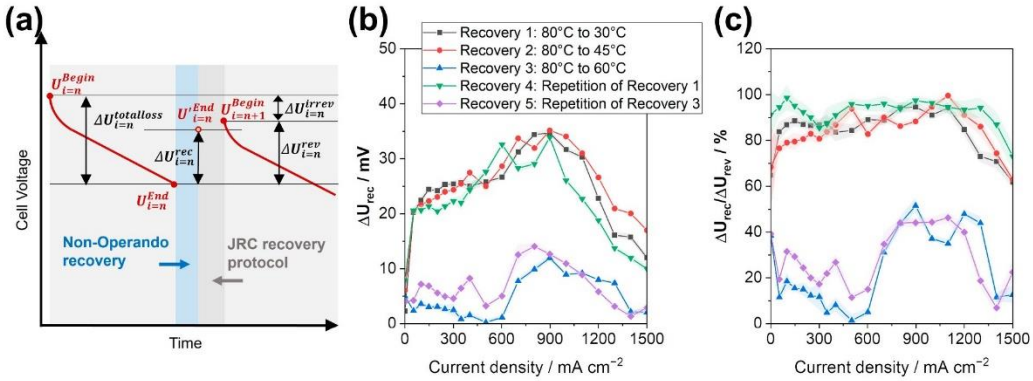

Figure 6. Evaluation of the relative recovery of the five recovery procedures. (**a**) The general scheme of cell voltage changes during a fuel cell durability test with a recovery procedure of non-operando temperature reduction. (**b**) The recovered voltage calculated according to Equation (1). (**c**) The relative recovery which relates to the reversible performance losses, according to Equations (1) and (2).

In Figure 7a, the values of the total amount of liquid water, $m_{H_2O(liquid)}$, due to the five non-operando recovery procedures are provided (evaluated analogously as in Section 3.1). Recovery 1 and 4 (both 80 °C to 30 °C), as well as Recovery 3 and 5 (both 80 °C to 60 °C), have similar values. Cell cooling down from 80 °C to 30 °C, as in Recovery 1 and 4, results in slightly higher $m_{H_2O(liquid)}$, around 13.2 g, than Recovery 2 (80 °C to 45 °C) with 12.34 g, whereas cell cooling down to 60 °C leads to $m_{H_2O(liquid)}$ of 8.51 g and 8.81 g in Recovery 3 and 5. A similar amount of liquid water formed during the non-operando temperature reduction from 80 °C to 30 °C and 45 °C resulted in the aforementioned similar recovery effect in Figure 6. The linear correlation between the absolute recovered voltage (data from Figure 6b) and the formed liquid water, $\Delta U_{i=n}^{rec}$ and $m_{H_2O(liquid)}$, during each non-operando recovery procedure is shown in Figure 7b–d at the current densities of 0.05, 1.0, and 1.5 A cm^{-2}, respectively. In the Supplementary Materials, Figure S7 shows the absolute recovered voltage versus the total amount of liquid water formed during non-operando recovery at all the evaluated current densities from 0 to 1.5 A cm^{-2}. Figure S8 shows the slope and intercept of the linear correlation between the $\Delta U_{i=n}^{rec}$ and $m_{H_2O(liquid)}$ over the current density from 0 to 1.5 A cm^{-2}. Unlike in Figure S4, the slope of the fit curves is much higher and changes between 4 and 6 mV·g^{-1} upon the current density from 0.05 to 1 A cm^{-2}, indicating that during non-operando recovery procedures more performance loss is recovered per amount of liquid water formed. This may be because the electrochemical measurements before and after each recovery procedure also recover part of the performance loss. Similar to Figure 4, the linear correlation is strong at the current density from 0.05 to 1 A cm^{-2}. At current densities above 1 A cm^{-2}, the R-Square of the fitting reduces, indicating a weaker linear correlation. It can be concluded that the linear correlation between the amount of liquid water and recovered voltage is evidently in the low to middle current density range, such as 0.05 to 1 A cm^{-2}. On the other hand,

at a higher current density range, where mass transport effects play a dominant role, the recovered voltage is less directly influenced by the amount of liquid water.

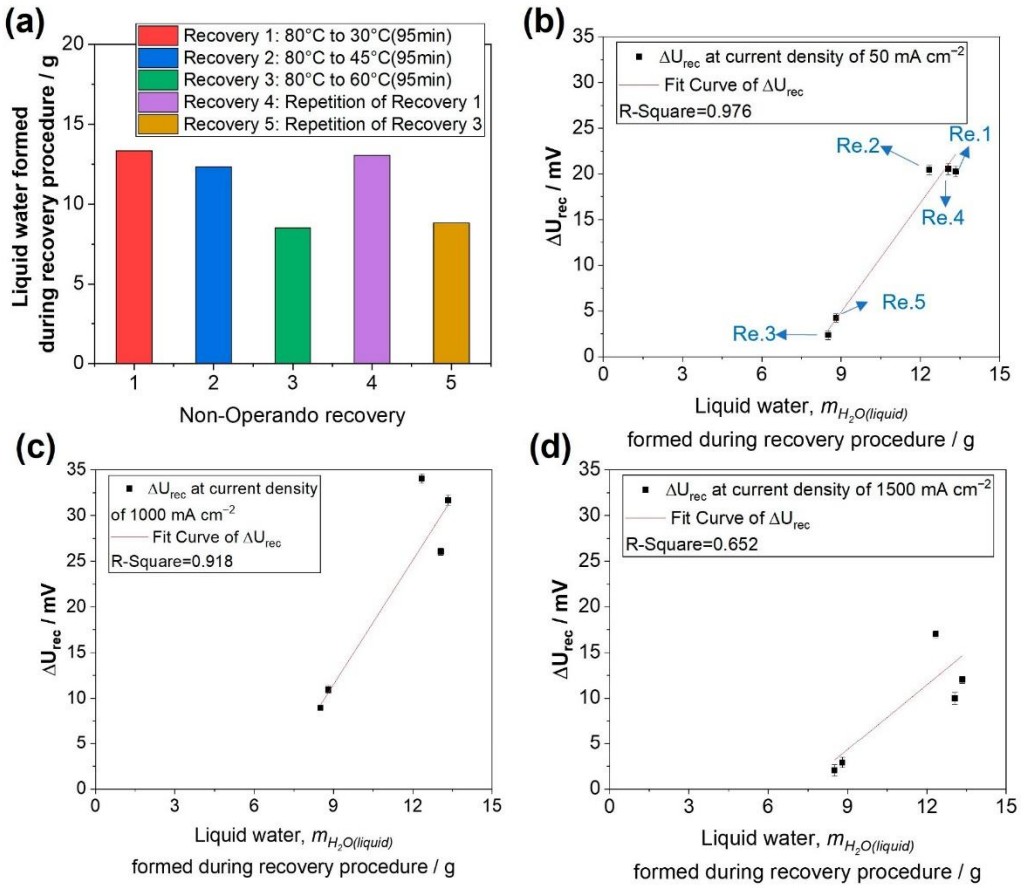

Figure 7. (**a**) Total amounts of liquid water $m_{H_2O(liquid)}$ (integrated signals of $\dot{m}_{H_2O(liquid),outlet}$) during different non-operando temperature reduction procedures. Absolute recovered voltage versus total amount of liquid water formed during non-operando recovery at (**b**) 0.05 A cm^{-2}, (**c**) 1 A cm^{-2}, and (**d**) 1.5 A cm^{-2}. The recovered voltage corresponds to the data from Figure 6b.

To elucidate the recovery mechanisms, the original data of EIS measurements at 0.8 A cm^{-2} conducted at the beginning of each test block, before and after each recovery procedure, are presented in Figure 8a. Directly assessing the influence of the recovery procedure from the recorded spectra of EIS measurements is challenging due to the small changes. This aligns with the subtle alterations observed in the polarization curves in Figure S6. Analyzing the EIS measurement data with other methods, such as model fitting, becomes necessary. The equivalent circuit in Figure 8b is selected and utilized, due to the acceptable fitting error (lower than 3%) and comparability with previous works [32,36]. The model consists of four components in series: (i) a resistor R_{Ohmic} describing the ohmic resistance of the MEA, including the contact resistances of the fuel cell components, (ii) the charge transfer circuit consisting of $R_{Charge\ transfer}$ in parallel with CPE_1 (constant phase element) describing the charge transfer resistance of the cathode catalyst layer, (iii) the mass transfer resistance circuit consisting of $R_{Masss\ transfer}$ in parallel with a constant phase element CPE_2, and (iv) an inductance element L regarding possible interferences due to wires or other sources of disturbance. According to the fitting results, the black columns in Figure 8c present the reduced resistance due to each recovery procedure in each test

block at 0.8 A cm^{-2}. The red columns with a shadow represent the reduced resistance by the JRC recovery protocol, which is performed at the end of each test block. In general, both the non-operando temperature reduction recovery procedures and the JRC recovery protocols predominantly reduced the charge transfer and mass transfer resistance, while the effect on the ohmic resistance is less prominent. Recovery 1 and 4 (80 °C to 30 °C) led to the highest reduction in $R_{Charge\ transfer}$ and $R_{Masss\ transfer}$, while Recovery 3 and 5 (80 °C to 60 °C) caused the lowest reduction, which is consistent with the observations from Figure 6. The reduction in the $R_{Charge\ transfer}$ due to Recovery 1 and 4 (80 °C to 30 °C) is about 55–66% of the one caused by the JRC recovery protocol, taking the error bar into consideration. The reduction in $R_{Masss\ transfer}$ corresponds to 49–56% of the value caused by the JRC protocol. Thus, it is concluded that the reduction in $R_{Charge\ transfer}$ mainly contributes to the recovery effect by the non-operando temperature reduction from 80 °C to 30 °C and 45 °C at 0.8 A cm^{-2}. In Figure 6c, the non-operando temperature reductions from 80 °C to 30 °C and 45 ° recover over 80% of the performance relative to the JRC protocol, which is supposed to be a combined result of the reduction in $R_{Charge\ transfer}$ and $R_{Masss\ transfer}$. There is a discrepancy in the relative recovery evaluated with the EIS data and the polarization curves, potentially arising from a deviation in the EIS measurements [37]. It has been reported that oxygen concentration oscillations along the cathode flow field exert a significant impact on the local and overall impedance response of the fuel cell in the frequency range lower than 10 Hz. This effect introduces a deviation from the stable fuel cell operation observed in polarization curves measurement [38].

For both operando and non-operando temperature reduction, the recovery effect increases with a longer cooling-down period and a lower cooling-down temperature from 60 °C to 45 or 30 °C. EIS results indicate that cell temperature reduction leads to a reduction in both $R_{Charge\ transfer}$ and $R_{Masss\ transfer}$. During the cell temperature reduction, liquid water condenses in the catalyst layers of the anode and cathode. As demonstrated earlier, there is a strong correlation between the amount of liquid water and the recovered voltage. According to Paul et al. [17], exposure to liquid water results in simultaneous reorganization/rearrangement of the ionomer film surface and bulk, which strongly influences the operando behavior of ionomer in the cathode catalyst layer of PEMFCs. Consequently, adjusting relative humidity or cooling down the cell can eliminate part of the performance loss caused by ionomer degradation, as it facilitates ionomer regeneration and redistribution in the catalyst layer [39,40].

It is widely acknowledged that the ion- and solvent-transport capabilities of PFSA ionomers are governed by their morphology, which, however, highly depend on the hydration of the hydrophilic ionic groups [41,42]. The ionic and mass transfer resistance reduces with increased humidity due to a varying ionomer morphology, which is minimized when the PFSA ionomer is immersed into water [43,44]. It has been observed that the fraction of conductive and hydrophilic area of PFSA ionomer increases due to a regeneration/redistribution effect along with increased humidity [45,46]. In particular, there is a change in water content and morphology depending on the phase of water (vapor or liquid), which further influences the ionic and water conductivity in the ionomer and between the membrane/electrode interface [47,48]. Therefore, it is observed in this work that the temperature reduction step (in both the operando/non-operando recovery procedures and JRC recovery protocol) results in reduced charge transfer resistance in the cathode catalyst layer and, accordingly, a recovery effect on the performance degradation. However, the time constant of the process strongly depends on factors such as water uptake, morphology, temperature, and relative humidity [49,50]. It can take a long time, from days to weeks, to complete the regeneration/redistribution of the ionomer and reach a quasi-equilibrium state [51,52]. Thus, as observed in this work, the duration of the temperature reduction, which refers to the time the ionomer is exposed to liquid water, has a significant impact on the recovery efficiency.

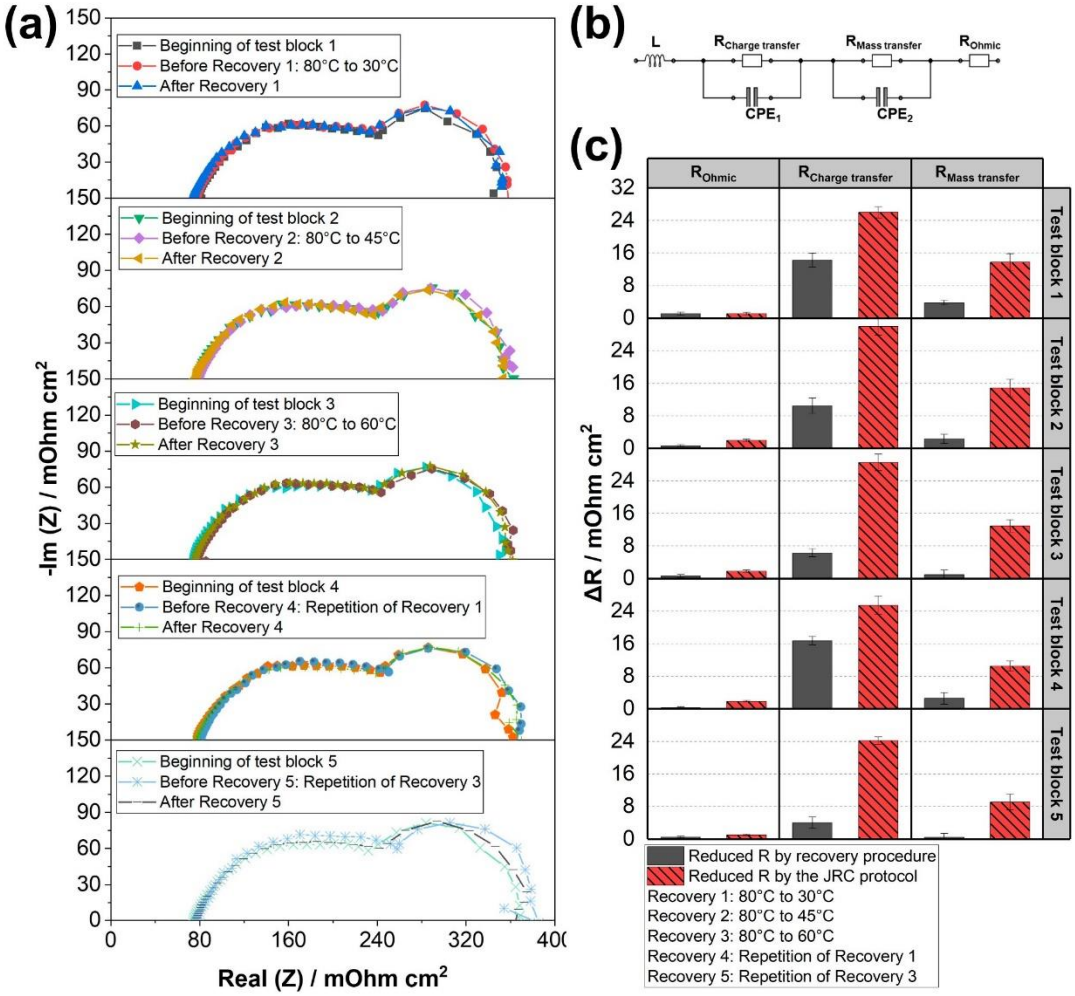

Figure 8. (**a**) EIS measurements at 0.8 A cm^{-2} conducted at the beginning of each test block, before and after each recovery procedure. Recorded frequency range was from 100 mHz to 10 kHz with a perturbation amplitude of ±5%. (**b**) Equivalent circuit model used for fitting EIS data recorded at the beginning and end of each test block, as well as after each recovery procedure. (**c**) Reduction in ohmic resistance, charge transfer resistance, and mass transfer resistance due to each performed recovery procedure (corresponding test block) and the following JRC recovery protocol.

Furthermore, both the temperature reduction and JRC recovery protocols result in increased water uptake due to the enhanced hydrophilicity of the ionomer. The pathway for water molecules to move is created within the nanostructure of the ionomer, which needs to accommodate the nanoswelling and growth of water domains [53,54]. Consequently, the water transfer coefficient increases in the ionomer as the water content increases, until reaching an equilibrium state [55,56]. In this study, the JRC recovery protocol requires a longer duration compared to the temperature reduction recovery protocol, bringing it closer to the equilibrium state and resulting in a more significant reduction in water transfer resistance.

Figure 6b,c indicate a decrease in both the absolute recovered voltage and the recovery relative to the JRC recovery protocol at a high current density range (>1.0 A cm^{-2}). This suggests that the JRC recovery protocol achieves a higher reduction in $R_{Masss\ transfer}$

compared to recovery procedures involving temperature reduction, leading to superior recovery of performance losses at high current density. The JRC recovery protocol in this work includes a shut-down step, which follows a similar recovery mechanism to non-operando temperature reduction recovery procedures but with a longer cooling-down time and lower temperature (80 °C to 25 °C for 8 h). Additionally, the JRC recovery protocol involves two steps with dry N_2 purging in the anode and cathode lasting 1 h in total, aimed at removing excess water and preventing flooding on the catalyst surface. Moreover, the H_2 soak step aids in removing Pt oxides on the cathode's catalyst surface. These additional steps contribute to the higher recovery effect of the JRC protocol, reducing $R_{Charge\ transfer}$ and $R_{Masss\ transfer}$, especially at high current density.

4. Conclusions

In this study, we assessed the effectiveness of time-efficient (operando) procedures for recovering reversible performance degradation in PEMFCs through temperature reduction. We compared these procedures with the more intricate JRC recovery protocol, which served as a reference. The following conclusions can be drawn:

- Temperature reduction (associated with water condensation) is often attributed to the recovery of voltage losses resulting from the regeneration/redistribution of the ionomer structure, representing a primary effect. Therefore, its efficacy is anticipated to be influenced by specific operation conditions, particularly the level of relative humidity (RH). To avoid overinterpretation of our study, it is crucial to emphasize that the conclusions drawn from our study are applicable to MEAs operated at 100% RH; variations in RH levels are expected to result in quantitative differences in the observed outcomes;
- The amount of liquid water generated in the cathode during the operando recovery procedure exhibits a positive linear correlation with the absolute recovered voltage, particularly within a current density range below 1 A cm^{-2}. This finding confirms the pivotal role of liquid water in the recovery of performance losses, likely associated with ionomer hydration and the resultant structure changes. Consequently, the observed results are anticipated to be applicable irrespective of the catalyst type, whether Pt/C (as in this study) or an alloyed catalyst (e.g., Pt-Co/C) is utilized;
- Operando temperature reduction during load cycling leads to 60–70% of the recovery of the JRC protocol at a much shorter duration (1.5 h versus 10.5 h). If the cell is kept at OCV during temperature reduction, the relative recovery is higher than 80%, likely due to avoiding flooding since no product water can be generated;
- The reduction in temperature from 80 °C to 45 °C is sufficient, and a further reduction to 30 °C does not lead to further recovery (at a similar duration). Longer durations of the cooling-down process have a slightly positive effect on the recovery of performance losses;
- Based on EIS data, the main contribution to recovery is the reduction in charge transfer resistance, followed by the reduction in mass transport resistance;
- It could be argued that the recovery due to water management, which was investigated using a specific flow field design, cannot be generalized because it strongly depends on the flow field design. Water management and the corresponding performances of PEMFCs have been shown to vary based on factors such as the flow field design (e.g., straight parallel channels, single or multiple serpentine channels, interdigitated channel or pin-type structures), channel geometry, and surface properties [57,58]. However, many studies have comparatively investigated, both experimentally and theoretically, the differences between flow field geometries, allowing variances for other configurations to be assessed [59,60].

Generally, temperature reduction during operation results in a partial recovery of the reversible performance degradation. In contrast to common recovery procedures, such as the protocol from JRC, the temperature reduction recovery is less time-demanding and easier to implement, since no additional equipment, such as a nitrogen gas supply, is needed.

Therefore, it is suitable for use during operation in transport applications. Moreover, it is expected that at the stack level the recovery procedure can be easily implemented, because the specific thermal mass is much lower (10–20 times) than in the lab-scale cell used in this study. On the other hand, it is noteworthy that a voltage drop occurs during the operando recovery procedure (up to 50 mV at 1 A cm^{-2}). In real-world applications, to prevent a significant cell voltage drop and potential global gas starvation, it is necessary to avoid high current density during the operando recovery procedure. In scenarios where there is a sudden demand for power, such as dynamic operations with fuel cell vehicles, the fuel cell stack can be supported by the battery pack during the implementation of an operando recovery procedure.

In this work, a global temperature reduction was applied, and no significant local recovery effects are expected. Thus, in a full-scale cell area without significant inhomogeneity of the current density distribution along the flow channels, the effect of the operando recovery procedure should be similar to the results obtained using a small-scale cell area. However, the scaling-up effect (from a small single cell to a full stack system) on recovery depends on the specific operation parameters and system configuration [61]. Therefore, operando temperature reduction with a full-scale fuel cell system needs to be investigated using dedicated experiments to determine the appropriate setpoint temperatures and durations for a given stack.

Supplementary Materials: The following supporting information can be downloaded at: https://www.mdpi.com/article/10.3390/en17040774/s1. Figure S1: Voltage changes during the operando temperature reduction: (a,e) correspond to Recovery 1, 80 °C to 45 °C (95 min); (b,f) correspond to Recovery 2, 80 °C to 60 °C (35 min); (c,g) correspond to Recovery 5, 80 °C to 60 °C (95 min); (d,h) correspond to Recovery 6, 80 °C to 45 °C (35 min). Recovery 3 and 4 are repetitions of Recovery 1 and 2, which show similar results and are not presented here. Figure S2: (a) Cell voltage recorded during the durability test for the investigation of recovery procedures based on operando temperature reduction. The red points are the cell voltage at the beginning of each test block at 1 A cm^{-2}. (b) Irreversible degradation rate at the current density range from 0 to 1 A cm^{-2}. Figure S3: Absolute recovered voltage versus total amount of liquid water formed during operando recovery at all the evaluated current densities, from 0 to 1 A cm^{-2}. Recovered voltage corresponds to data from Figure 3b. Figure S4: Slope and intercept of the linear fitting results between the absolute recovered voltage and the formed liquid water during each operando recovery procedure at different current densities. Figure S5: (a) Cell voltage recorded during the durability test for the investigation of recovery procedures based on non-operando temperature reduction. The red points are the cell voltage at the beginning of each test block at 1 A cm^{-2}. (b) Irreversible degradation rate at the current density range from 0 to 1 A cm^{-2}. Figure S6: Polarization curves measured during the durability test with non-operando temperature reduction. The error bars correspond to the standard deviation from the average of the last 30 s of the dwell time of each tested current density step. Figure S7: Absolute recovered voltage versus total amount of liquid water formed during non-operando recovery at all the evaluated current densities, from 0 to 1.5 A cm^{-2}. Recovered voltage corresponds to data from Figure 6b. Figure S8: Slope and intercept of the linear fitting results between the absolute recovered voltage and the formed liquid water during each non-operando recovery procedure at different current densities.

Author Contributions: Conceptualization, Q.Z., M.S., P.G. and K.A.F.; methodology, Q.Z., M.S., P.G. and K.A.F.; software, Q.Z.; validation, Q.Z.; formal analysis, Q.Z.; investigation, Q.Z.; writing—original draft preparation, Q.Z.; writing—review and editing, Q.Z., M.S., P.G. and K.A.F.; supervision, M.S., P.G. and K.A.F.; funding acquisition, Q.Z. All authors have read and agreed to the published version of the manuscript.

Funding: This research received funding from the China Scholarship Council.

Data Availability Statement: The data presented in this study are available on request from the corresponding author. The data are not publicly available due to privacy reasons.

Conflicts of Interest: The authors declare no conflicts of interest.

References

1. Jiang, S.; Wang, C.; Zhang, C.; Bai, H.; Xu, L. Adaptive estimation of road slope and vehicle mass of fuel cell vehicle. *eTransportation* **2019**, *2*, 100023. [CrossRef]
2. Greene, D.L.; Ogden, J.M.; Lin, Z. Challenges in the designing, planning and deployment of hydrogen refueling infrastructure for fuel cell electric vehicles. *eTransportation* **2020**, *6*, 100086. [CrossRef]
3. Tanaka, S.; Nagumo, K.; Yamamoto, M.; Chiba, H.; Yoshida, K.; Okano, R. Fuel cell system for Honda CLARITY fuel cell. *eTransportation* **2020**, *3*, 100046. [CrossRef]
4. Strategic Research and Innovation Agenda Clean Hydrogen Joint Undertaking 2021–2027. Available online: https://www.clean-hydrogen.europa.eu/about-us/key-documents/strategic-research-and-innovation-agenda_en (accessed on 1 October 2023).
5. Marcinkoski, J. Hydrogen Class 8 Long Haul Truck Targets 2019. Available online: https://www.hydrogen.energy.gov/docs/hydrogenprogramlibraries/pdfs/19006_hydrogen_class8_long_haul_truck_targets.pdf?Status=Master (accessed on 1 October 2023).
6. Zhao, J.; Li, X. Fuel cell durability under automotive driving cycles—Fundamentals and experiments. In *Fuel Cells for Transportation*; Elsevier: Amsterdam, The Netherlands, 2023; pp. 419–462. [CrossRef]
7. Lin, R.; Li, B.; Hou, Y.; Ma, J. Investigation of dynamic driving cycle effect on performance degradation and micro-structure change of PEM fuel cell. *Int. J. Hydrogen Energy* **2009**, *34*, 2369–2376. [CrossRef]
8. Garzon, F.H.; Lopes, T.; Rockward, T.; Sansinena, J.M.; Kienitz, B.; Mukundan, R.; Springer, T. The Impact of Impurities On Long Term PEMFC Performance. *ECS Trans.* **2009**, *25*, 1575–1583. [CrossRef]
9. Dhanushkodi, S.R.; Kundu, S.; Fowler, M.W.; Pritzker, M.D. Study of the effect of temperature on Pt dissolution in polymer electrolyte membrane fuel cells via accelerated stress tests. *J. Power Sources* **2014**, *245*, 1035–1045. [CrossRef]
10. Zago, M.; Baricci, A.; Bisello, A.; Jahnke, T.; Yu, H.; Maric, R.; Zelenay, P.; Casalegno, A. Experimental analysis of recoverable performance loss induced by platinum oxide formation at the polymer electrolyte membrane fuel cell cathode. *J. Power Sources* **2020**, *455*, 227990. [CrossRef]
11. Qi, Z.G.; Tang, H.; Guo, Q.H.; Du, B. Investigation on "saw-tooth" behavior of PEM fuel cell performance during shutdown and restart cycles. *J. Power Sources* **2006**, *161*, 864–871. [CrossRef]
12. Stumper, E.; Lohr, M.; Hamada, S. Diagnostic tools for liquid water in PEM fuel cells. *J. Power Sources* **2005**, *143*, 150–157. [CrossRef]
13. Mitzel, J.; Zhang, Q.; Gazdzicki, P.; Friedrich, K.A. Review on mechanisms and recovery procedures for reversible performance losses in polymer electrolyte membrane fuel cells. *J. Power Sources* **2021**, *488*, 229375. [CrossRef]
14. Shi, W.Y.; Yi, B.L.; Hou, M.; Jing, F.N.; Ming, P.W. Hydrogen sulfide poisoning and recovery of PEMFC Pt-anodes. *J. Power Sources* **2007**, *165*, 814–818. [CrossRef]
15. Du, F.M.; Dao, T.A.; Peitl, P.V.J.; Bauer, A.; Preuss, K.; Bonastre, A.M.; Sharman, J.; Spikes, G.; Perchthaler, M.; Schmidt, T.J.; et al. Effects of PEMFC Operational History under Dry/Wet Conditions on Additional Voltage Losses due to Ionomer Migration. *J. Electrochem. Soc.* **2020**, *167*, 144513–144527. [CrossRef]
16. Inaba, M.; Yamada, H.; Tokunaga, J.; Tasaka, A. Effect of agglomeration of Pt/C catalyst on hydrogen peroxide formation. *Electrochem. Solid. St.* **2004**, *7*, A474. [CrossRef]
17. Paul, D.K.; Karan, K. Conductivity and Wettability Changes of Ultrathin Nafion Films Subjected to Thermal Annealing and Liquid Water Exposure. *J. Phys. Chem. C* **2014**, *118*, 1828–1835. [CrossRef]
18. Ott, S.; Bauer, A.; Du, F.M.; Dao, T.A.; Klingenhof, M.; Orfanidi, A.; Strasser, P. Impact of Carbon Support Meso-Porosity on Mass Transport and Performance of PEMFC Cathode Catalyst Layers. *Chemcatchem* **2021**, *13*, 4759–4769. [CrossRef]
19. Langlois, D.A.; Lee, A.S.; Macauley, N.; Maurya, S.; Hawley, M.E.; Yim, S.D.; Kim, Y.S. A rejuvenation process to enhance the durability of low Pt loaded polymer electrolyte membrane fuel cells. *J. Power Sources* **2018**, *396*, 345–354. [CrossRef]
20. Cetinbas, F.C.; Ahluwalia, R.K.; Kariuki, N.N.; De Andrade, V.; Myers, D.J. Effects of Porous Carbon Morphology, Agglomerate Structure and Relative Humidity on Local Oxygen Transport Resistance. *J. Electrochem. Soc.* **2019**, *167*, 013508. [CrossRef]
21. Van Dine, L.L.; Steinbugler, M.M.; Reiser, C.A.; Scheffler, G.W. Procedure for Shutting Down A Fuel Cell System Having An Anode Exhaust Recycle Loop. U.S. Patent 6514635B2, 4 April 2004. Available online: https://patents.google.com/patent/US6514635B2/en (accessed on 1 October 2023).
22. Colombo, E.; Baricci, A.; Bisello, A.; Guetaz, L.; Casalegno, A. PEMFC performance decay during real-world automotive operation: Evincing degradation mechanisms and heterogeneity of ageing. *J. Power Sources* **2023**, *553*, 232246. [CrossRef]
23. Guétaz, L.; Escribano, S.; Sicardy, O. Study by electron microscopy of proton exchange membrane fuel cell membrane-electrode assembly degradation mechanisms: Influence of local conditions. *J. Power Sources* **2012**, *212*, 169–178. [CrossRef]
24. Steinbach, A.J.; Hamilton, C.V.; Debe, M.K. Impact of micromolar concentrations of externally-provided chloride and sulfide contaminants on PEMFC reversible stability. *ECS Trans.* **2007**, *11*, 889. [CrossRef]
25. Prass, S.; Friedrich, K.A.; Zamel, N. Tolerance and Recovery of Ultralow-Loaded Platinum Anode Electrodes upon Carbon Monoxide and Hydrogen Sulfide Exposure. *Molecules* **2019**, *24*, 3514. [CrossRef]
26. Pivac, I.; Barbir, F. Impact of Shutdown Procedures on Recovery Phenomena of Proton Exchange Membrane Fuel Cells. *Fuel Cells* **2020**, *20*, 185–195. [CrossRef]

27. Kabir, S.; Myers, D.J.; Kariuki, N.; Park, J.; Wang, G.X.; Baker, A.; Macauley, N.; Mukundan, R.; More, K.L.; Neyerlin, K.C. Elucidating the Dynamic Nature of Fuel Cell Electrodes as a Function of Conditioning: An ex Situ Material Characterization and in Situ Electrochemical Diagnostic Study. *ACS Appl. Mater. Interfaces* **2019**, *11*, 45016–45030. [CrossRef] [PubMed]
28. Zhang, J.X.; Litteer, B.A.; Coms, F.D.; Makharia, R. Recoverable Performance Loss Due to Membrane Chemical Degradation in PEM Fuel Cells. *J. Electrochem. Soc.* **2012**, *159*, F287. [CrossRef]
29. Robb, G.M.; Folmsbee, D.T. Procedure for Stack Voltage Recovery. U.S. Patent 9343760B2, 17 May 2014. Available online: https://patents.google.com/patent/US9343760B2/en (accessed on 1 October 2023).
30. Shokhen, V.; Strandberg, L.; Skoglundh, M.; Wickman, B. Impact of Accelerated Stress Tests on the Cathodic Catalytic Layer in a Proton Exchange Membrane (PEM) Fuel Cell Studied by Identical Location Scanning Electron Microscopy. *ACS Appl. Energy Mater.* **2022**, *5*, 11200–11212. [CrossRef]
31. Gazdzick, P.; Mitzel, J.; Sanchez, D.G.; Schulze, M.; Friedrich, K.A. Evaluation of reversible and irreversible degradation rates of polymer electrolyte membrane fuel cells tested in automotive conditions. *J. Power Sources* **2016**, *327*, 86–95. [CrossRef]
32. Talukdar, K.; Gazdzicki, P.; Friedrich, K.A. Comparative investigation into the performance and durability of long and short side chain ionomers in Polymer Electrolyte Membrane Fuel Cells. *J. Power Sources* **2019**, *439*, 227078. [CrossRef]
33. Sanchez, D.G.; Ortiz, A.; Friedrich, K.A. Oscillation of PEFC under low cathode humidification: Effect of gravitation and bipolar plate design. *J. Electrochem. Soc.* **2013**, *160*, F636. [CrossRef]
34. Zhang, Q.; Schulze, M.; Gazdzicki, P.; Friedrich, K.A. Comparison of different performance recovery procedures for polymer electrolyte membrane fuel cells. *Appl. Energy* **2021**, *302*, 117490. [CrossRef]
35. Tsotridis, G.; Pilenga, A.; De Marco, G.; Malkow, T. *EU Harmonised Test Protocols for PEMFC MEA Testing in Single Cell Configuration for Automotive Applications*; JRC Science for Policy report 2015; European Commission: Brussels, Belgium, 2015; Volume 27632. [CrossRef]
36. Schulze, M.; Wagner, N.; Kaz, T.; Friedrich, K.A. Combined electrochemical and surface analysis investigation of degradation processes in polymer electrolyte membrane fuel cells. *Electrochim. Acta* **2007**, *52*, 2328–2336. [CrossRef]
37. Tang, Z.P.; Huang, Q.A.; Wang, Y.J.; Zhang, F.Z.; Li, W.H.; Li, A.J.; Zhang, L.; Zhang, J.J. Recent progress in the use of electrochemical impedance spectroscopy for the measurement, monitoring, diagnosis and optimization of proton exchange membrane fuel cell performance. *J. Power Sources* **2020**, *468*, 228361. [CrossRef]
38. Schneider, I.A.; Kramer, D.; Wokaun, A.; Scherer, G.G. Oscillations in gas channels—II. Unraveling the characteristics of the low frequency loop in air-fed PEFC impedance spectra. *J. Electrochem. Soc.* **2007**, *154*, B770. [CrossRef]
39. Yin, Y.; Li, R.T.; Bai, F.Q.; Zhu, W.K.; Qin, Y.Z.; Chang, Y.F.; Zhang, J.F.; Guiver, M.D. Ionomer migration within PEMFC catalyst layers induced by humidity changes. *Electrochem. Commun.* **2019**, *109*, 106590. [CrossRef]
40. Morawietz, T.; Handl, M.; Oldani, C.; Friedrich, K.A.; Hiesgen, R. Quantitative in Situ Analysis of Ionomer Structure in Fuel Cell Catalytic Layers. *ACS Appl. Mater. Interfaces* **2016**, *8*, 27044–27054. [CrossRef]
41. Mauritz, K.A.; Moore, R.B. State of Understanding of Nafion. *Chem. Rev.* **2004**, *104*, 4535–4586. [CrossRef]
42. Kusoglu, A.; Weber, A.Z. New Insights into Perfluorinated Sulfonic-Acid Ionomers. *Chem. Rev.* **2017**, *117*, 987–1104. [CrossRef]
43. Ye, X.; LeVan, M.D. Water transport properties of Nafion membranes: Part I. Single-tube membrane module for air drying. *J. Membr. Sci.* **2003**, *221*, 147–161. [CrossRef]
44. Monroe, C.W.; Romero, T.; Mérida, W.; Eikerling, M. A vaporization-exchange model for water sorption and flux in Nafion. *J. Membr. Sci.* **2008**, *324*, 1–6. [CrossRef]
45. Aleksandrova, E.; Hiesgen, R.; Eberhard, D.; Friedrich, K.A.; Kaz, T.; Roduner, E. Proton Conductivity Study of a Fuel Cell Membrane with Nanoscale Resolution. *ChemPhysChem* **2007**, *8*, 519–522. [CrossRef] [PubMed]
46. He, Q.; Kusoglu, A.; Lucas, I.T.; Clark, K.; Weber, A.Z.; Kostecki, R. Correlating humidity-dependent ionically conductive surface area with transport phenomena in proton-exchange membranes. *J. Phys. Chem. B* **2011**, *115*, 11650–11657. [CrossRef]
47. Adachi, M.; Navessin, T.; Xie, Z.; Frisken, B.; Holdcroft, S. Correlation of in situ and ex situ measurements of water permeation through Nafion NRE211 proton exchange membranes. *J. Electrochem. Soc.* **2009**, *156*, B782. [CrossRef]
48. Adachi, M.; Navessin, T.; Xie, Z.; Li, F.H.; Tanaka, S.; Holdcroft, S. Thickness dependence of water permeation through proton exchange membranes. *J. Membr. Sci.* **2010**, *364*, 183–193. [CrossRef]
49. Alberti, G.; Narducci, R. Evolution of permanent deformations (or memory) in Nafion 117 membranes with changes in temperature, relative humidity and time, and its importance in the development of medium temperature PEMFCs. *Fuel Cells* **2009**, *9*, 410–420. [CrossRef]
50. Casciola, M.; Alberti, G.; Sganappa, M.; Narducci, R. On the decay of Nafion proton conductivity at high temperature and relative humidity. *J. Power Sources* **2006**, *162*, 141–145. [CrossRef]
51. Fumagalli, M.; Lyonnard, S.; Prajapati, G.; Berrod, Q.; Porcar, L.; Guillermo, A.; Gebel, G. Fast water diffusion and long-term polymer reorganization during Nafion membrane hydration evidenced by time-resolved small-angle neutron scattering. *J. Phys. Chem. B* **2015**, *119*, 7068–7076. [CrossRef] [PubMed]
52. Gebel, G.; Lyonnard, S.; Mendil-Jakani, H.; Morin, A. The kinetics of water sorption in Nafion membranes: A small-angle neutron scattering study. *J. Phys. Condens. Matter* **2011**, *23*, 234107. [CrossRef] [PubMed]
53. Gierke, T.D.; Munn, G.; Wilson, F. The morphology in nafion perfluorinated membrane products, as determined by wide-and small-angle x-ray studies. *J. Polym. Sci. Polym. Phys. Ed.* **1981**, *19*, 1687–1704. [CrossRef]

54. Safiollah, M.; Melchy, P.-E.A.; Berg, P.; Eikerling, M. Model of water sorption and swelling in polymer electrolyte membranes: Diagnostic applications. *J. Phys. Chem. B* **2015**, *119*, 8165–8175. [CrossRef]
55. Mittelsteadt, C.K.; Staser, J. Simultaneous water uptake, diffusivity and permeability measurement of perfluorinated sulfonic acid polymer electrolyte membranes. *ECS Trans.* **2011**, *41*, 101. [CrossRef]
56. Takamatsu, T.; Hashiyama, M.; Eisenberg, A. Sorption phenomena in Nafion membranes. *J. Appl. Polym. Sci.* **1979**, *24*, 2199–2220. [CrossRef]
57. Sauermoser, M.; Kizilova, N.; Pollet, B.G.; Kjelstrup, S. Flow Field Patterns for Proton Exchange Membrane Fuel Cells. *Front. Energy Res.* **2020**, *8*, 13. [CrossRef]
58. Lim, B.H.; Majlan, E.H.; Daud, W.R.W.; Husaini, T.; Rosli, M.I. Effects of flow field design on water management and reactant distribution in PEMFC: A review. *Ionics* **2016**, *22*, 301–316. [CrossRef]
59. Pan, W.T.; Wang, P.H.; Chen, X.L.; Wang, F.C.; Dai, G.C. Combined effects of flow channel configuration and operating conditions on PEM fuel cell performance. *Energy Convers. Manag.* **2020**, *220*, 113046. [CrossRef]
60. Arif, M.; Cheung, S.C.; Andrews, J. Numerical investigation of effects of different flow channel configurations on the 100 cm^2 PEM fuel cell performance under different operating conditions. *Catal. Today* **2022**, *397*, 449–462. [CrossRef]
61. Bonnet, C.; Didierjean, S.; Guillet, N.; Besse, S.; Colinart, T.; Carré, P. Design of an 80 kWe PEM fuel cell system: Scale up effect investigation. *J. Power Sources* **2008**, *182*, 441–448. [CrossRef]

Supporting Information for

Temperature Reduction as Operando Performance Recovery Procedure for Polymer Electrolyte Membrane Fuel Cells

Qian Zhang [1,2], Mathias Schulze [1], Pawel Gazdzicki [1,*] and Kaspar Andreas Friedrich [1,2]

[1] Electrochemical Energy Technology, Institute of Engineering Thermodynamics, German Aerospace Center (DLR), Pfaffenwaldring 38-40, 70569 Stuttgart, Germany
[2] Institute of Building Energetics, Thermal Engineering and Energy Storage (IGTE), University of Stuttgart, Pfaffenwaldring 31, 70569 Stuttgart, Germany
* Correspondence: pawel.gazdzicki@dlr.de; Tel.: +49-711-6862-8094

JRC recovery protocol:

Upon the load switching off, the air flow and cathode outlet are closed. The hydrogen flow on the anode side is maintained until the cell voltage drops below 0.1 V, which takes about 25 min. After that, dry N_2 purges both the anode and cathode for 30 min, followed by dry air purging for another 30 min. Subsequently, the gas supply to both anode and cathode is switched off while keeping the gas outlet valves closed. For the next 8 h, the cell heating is shut down, allowing the cell to cool to ambient temperature. Upon restarting of the cell, both the anode and cathode are purged with humified N_2 for 30 min while heating the cell to 80 °C. The entire procedure, including the restart, takes 10 h 25 min in our lab.

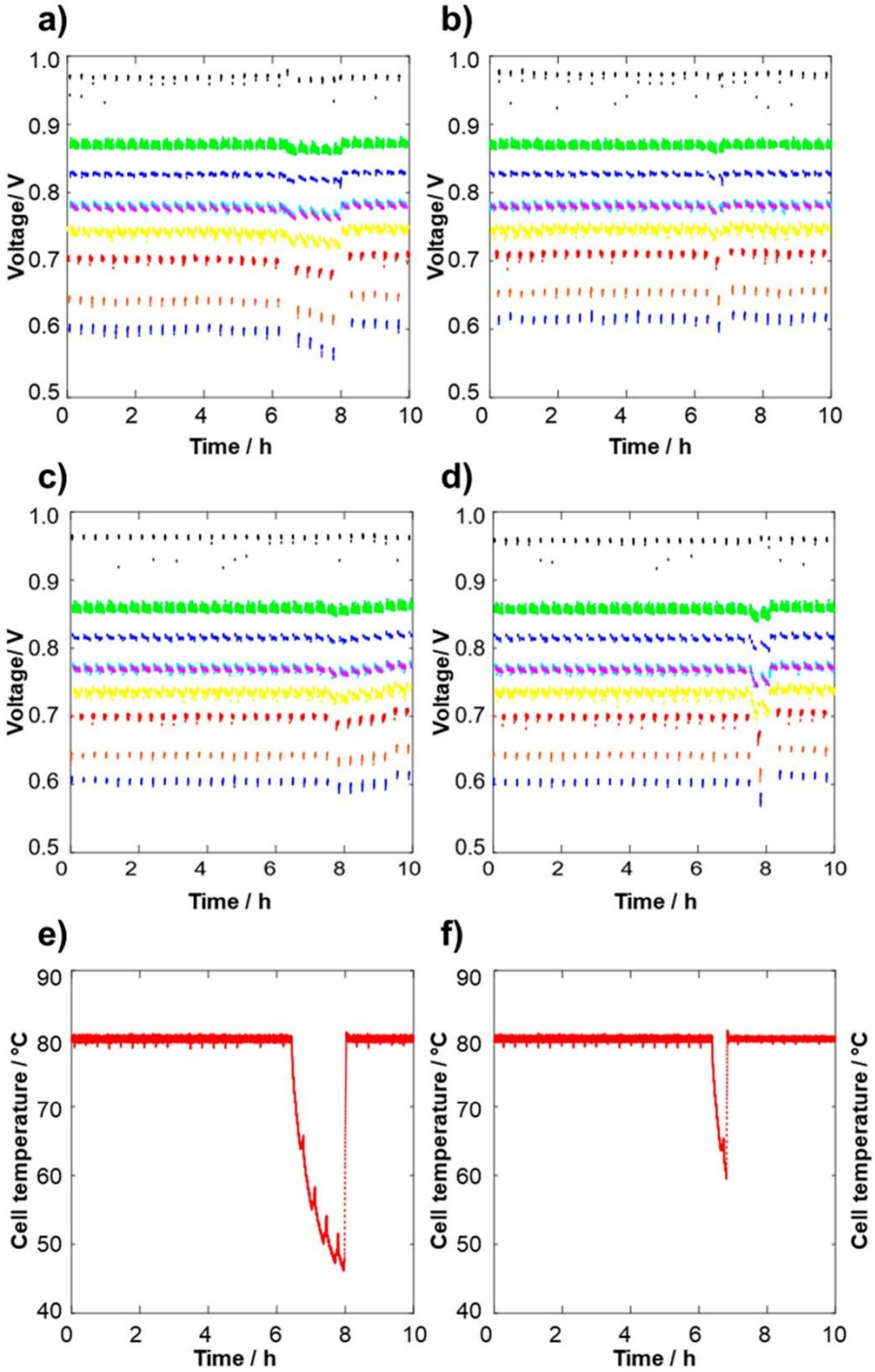
a)
b)
c)
d)
e)
f)
Voltage/ V
Time / h
Cell temperature / °C
1.0
0.9
0.8
0.7
0.6
0.5
90
80
70
60
50
40
0
2
4
6
8
10

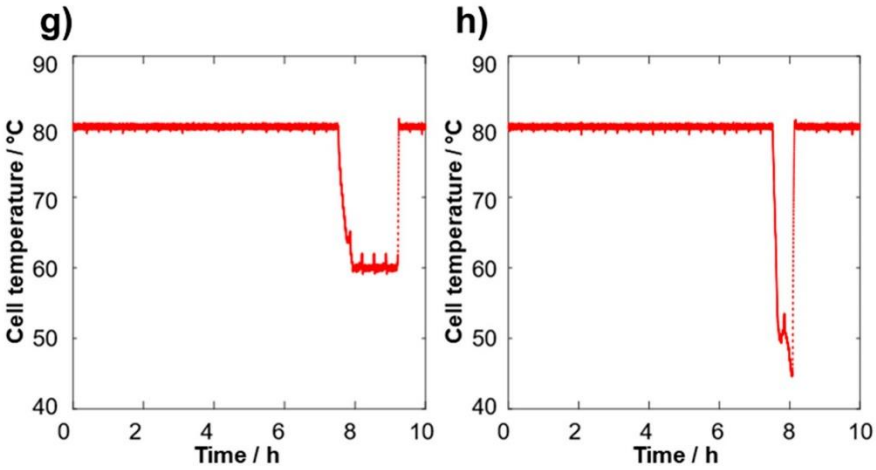

Figure S1. Voltage changes during the operando temperature reduction: (**a**,**e**) correspond to the Recovery 1, 80 °C to 45 °C (95 min); (**b**,**f**) correspond to the Recovery 2, 80 °C to 60 °C (35 min); (**c**,**g**) correspond to the Recovery 5, 80 °C to 60 °C (95min); (**d**,**h**) correspond to the Recovery 6, 80 °C to 45 °C (35 min). Recovery 3 and 4 are repetition of Recovery 1 and 2, which show similar results and are not presented here.

Irreversible degradation rate:

To calculate the irreversible performance degradation rate of the MEA during the durability test, voltage values (belonging to each current density level of the FC-DLC operation) at the beginning of each test block (i.e., after the JRC recovery protocol) were used to perform a linear regression. An example is provided in Figure S2a) for a current density of 1 A·cm^{-2}, represented by the red data points (voltage at the beginning of each test block) and the red dash line (linear fit). It is noted that the irreversible degradation defined by the slope of the linear fit refers to operation time (i.e., test time without all non-operando periods). The calculated irreversible degradation rates versus current density are provided in Figure S2b).

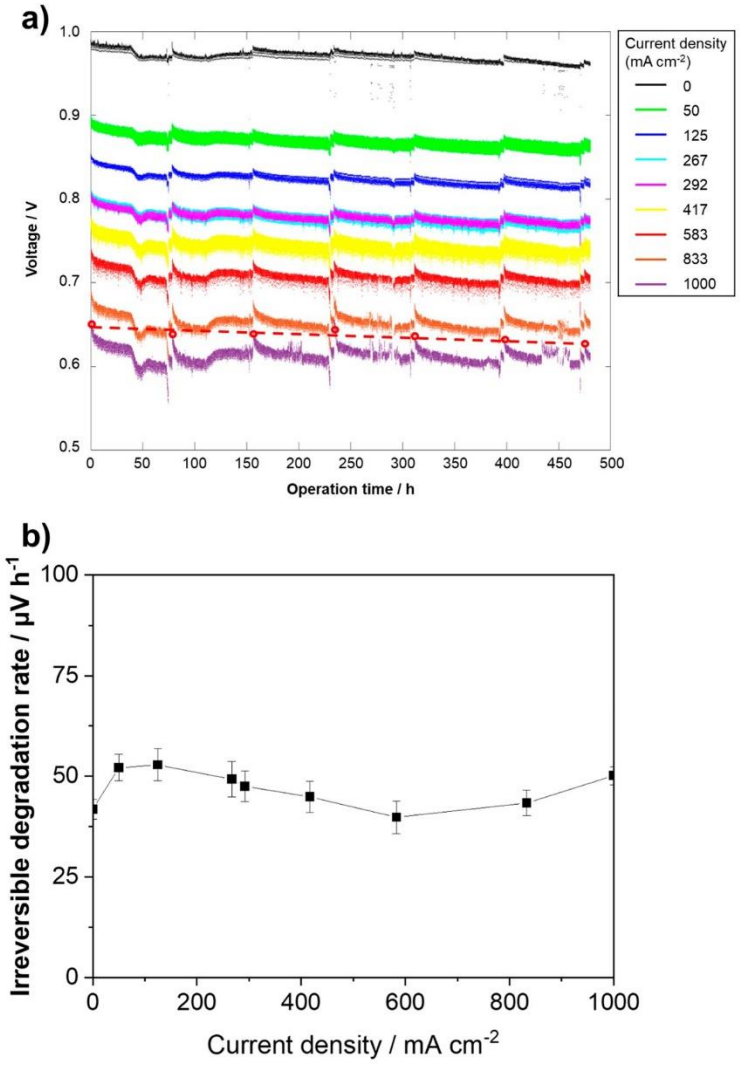

Figure S2. (**a**) Cell voltage recorded during the durability test for the investigation of recovery procedures based on operando temperature reduction. The red points are the cell voltage at the beginning of each test block at 1 A cm^{-2}. (**b**) Irreversible degradation rate at the current density range from 0 to 1 A cm^{-2}.

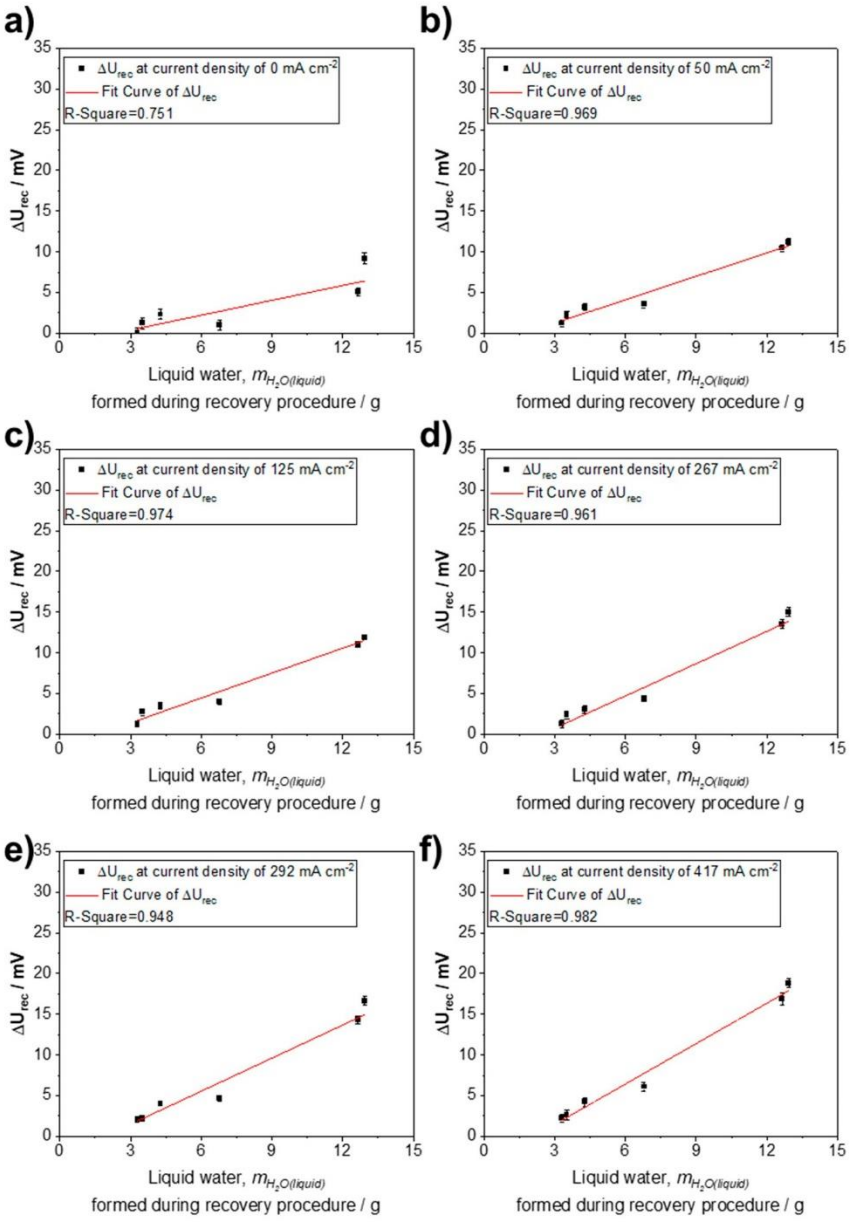
a)
ΔU_rec at current density of 0 mA cm-2
Fit Curve of ΔU_rec
R-Square=0.751
b)
ΔU_rec at current density of 50 mA cm-2
Fit Curve of ΔU_rec
R-Square=0.969
c)
ΔU_rec at current density of 125 mA cm-2
Fit Curve of ΔU_rec
R-Square=0.974
d)
ΔU_rec at current density of 267 mA cm-2
Fit Curve of ΔU_rec
R-Square=0.961
e)
ΔU_rec at current density of 292 mA cm-2
Fit Curve of ΔU_rec
R-Square=0.948
f)
ΔU_rec at current density of 417 mA cm-2
Fit Curve of ΔU_rec
R-Square=0.982
ΔU_rec / mV
Liquid water, m_H2O(liquid)
formed during recovery procedure / g

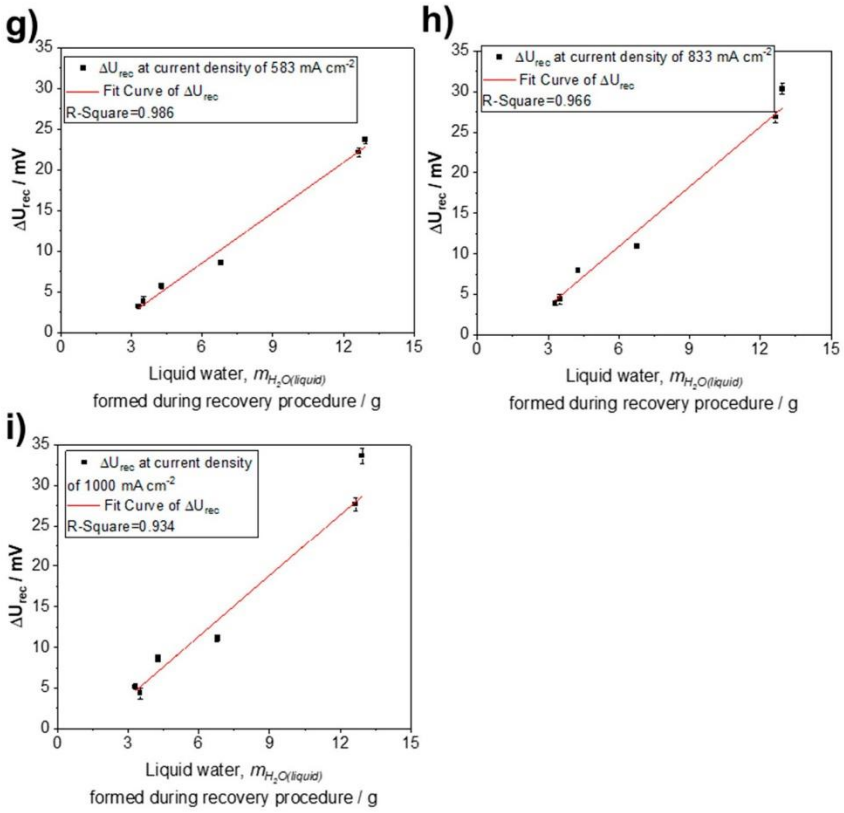

Figure S3. Absolute recovered voltage versus total amount of liquid water formed during operando recovery at all the evaluated current densities from 0 to 1 A cm^{-2}. Recovered voltage corresponds to data from Figure 3b.

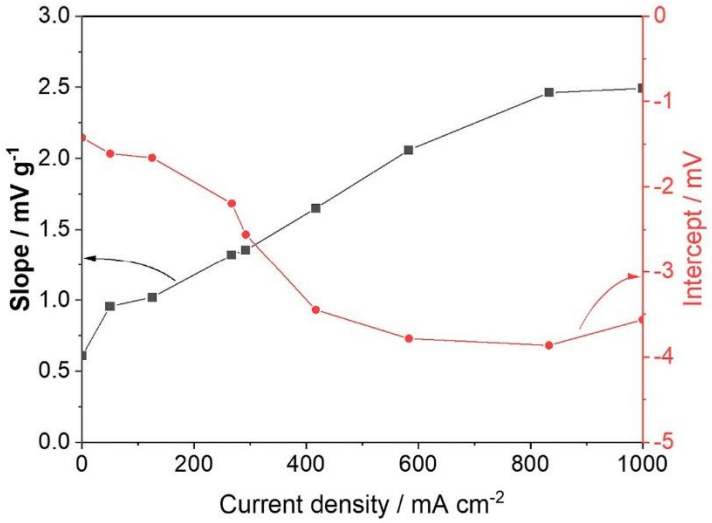

Figure S4. Slope and intercept of the linear fitting results between the absolute recovered voltage and the formed liquid water during each operando recovery procedure at different current densities.

Recovery effect of the non-operando performance recovery procedures with temperature reduction:

Figure S5 a) shows the cell voltages at various current density levels according to Figure 5, excluding all the recovery procedures and performance characterization measurements. Similar to Figure S2, the slope of the dashed red line presents the irreversible performance degradation rate of the fuel cell upon the 400-h FC-DLC operation. According to Figure 5 b), the irreversible performance degradation rate at the current density range from 0 to 1 A cm^{-2} varies between 75 and 125 $\mu V\,h^{-1}$. Additionally, the average reversible performance degradation rate of each test block, calculated using $\Delta U_{i=n}^{rev}$ from Figure 6, is 430 $\mu V\,h^{-1}$ at 1 A cm^{-2}. The similarity in average rates of reversible performance degradation in the two durability tests can be attributed to the same test hardware and operation parameters. On the other hand, the irreversible performance degradation rate in the durability test with the non-operando recovery procedure, although still much lower than the rates reported in the literature, is significantly higher than that observed with operando recovery procedures. This discrepancy is ascribed to the OCV periods during the recovery process.

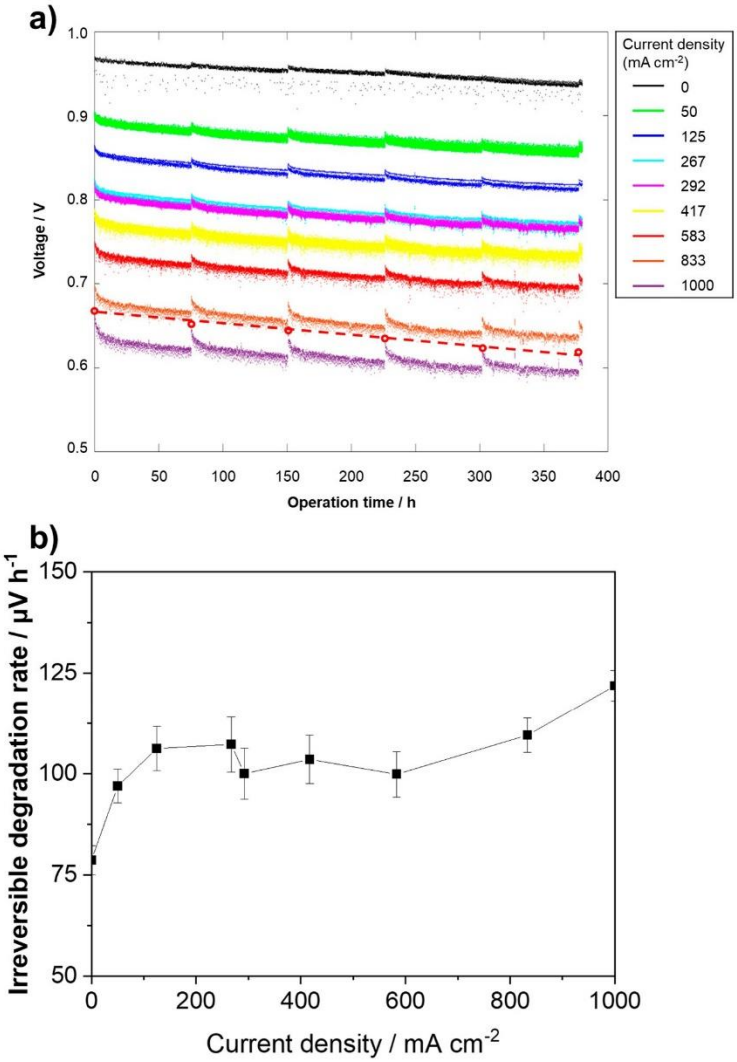

Figure S5. (**a**) Cell voltage recorded during the durability test for the investigation of recovery procedures based on non-operando temperature reduction. The red points are the cell voltage at the beginning of each test block at 1 A cm^{-2}. (**b**) Irreversible degradation rate at the current density range from 0 to 1 A cm^{-2}.

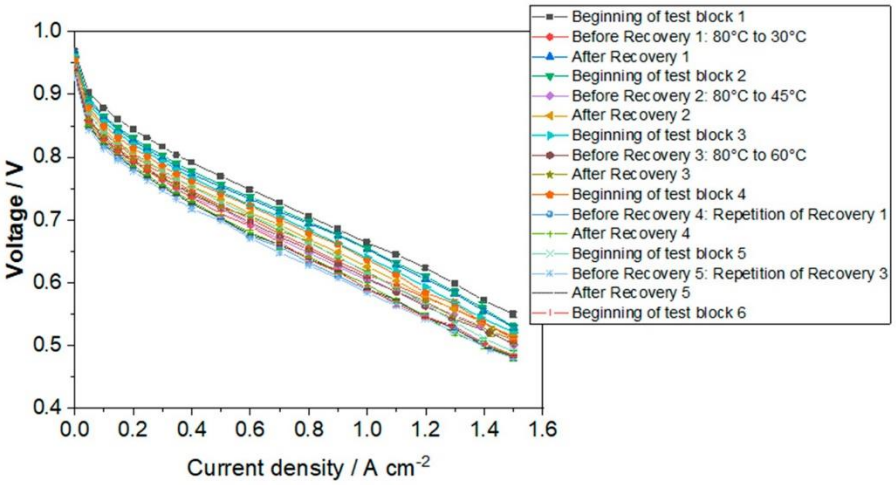

Figure S6. Polarization curves measured during the durability test with non-operando temperature reduction. The error bars correspond to the standard deviation from the average of the last 30 s of the dwell time of each tested current density step.

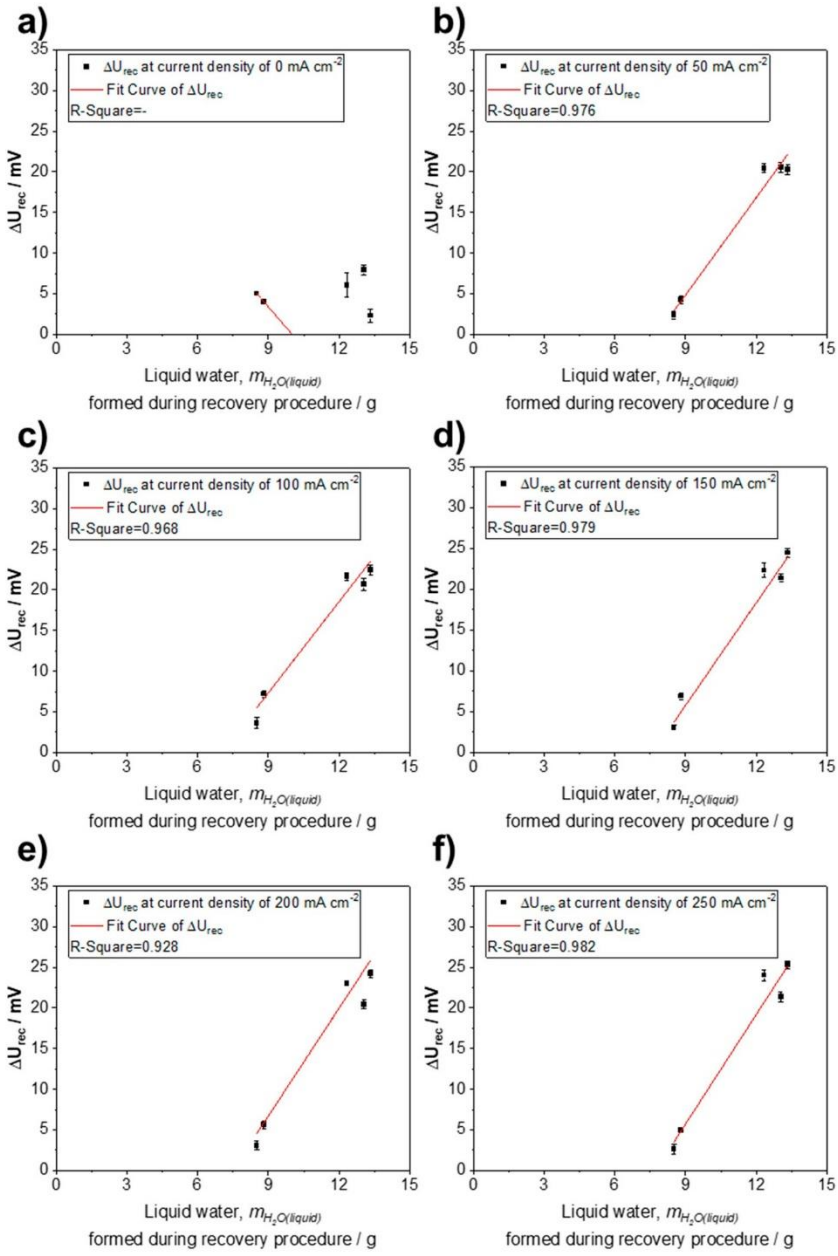
a)
ΔU_rec at current density of 0 mA cm^-2
Fit Curve of ΔU_rec
R-Square=-
b)
ΔU_rec at current density of 50 mA cm^-2
Fit Curve of ΔU_rec
R-Square=0.976
c)
ΔU_rec at current density of 100 mA cm^-2
Fit Curve of ΔU_rec
R-Square=0.968
d)
ΔU_rec at current density of 150 mA cm^-2
Fit Curve of ΔU_rec
R-Square=0.979
e)
ΔU_rec at current density of 200 mA cm^-2
Fit Curve of ΔU_rec
R-Square=0.928
f)
ΔU_rec at current density of 250 mA cm^-2
Fit Curve of ΔU_rec
R-Square=0.982
ΔU_rec / mV
Liquid water, m_H2O(liquid)
formed during recovery procedure / g

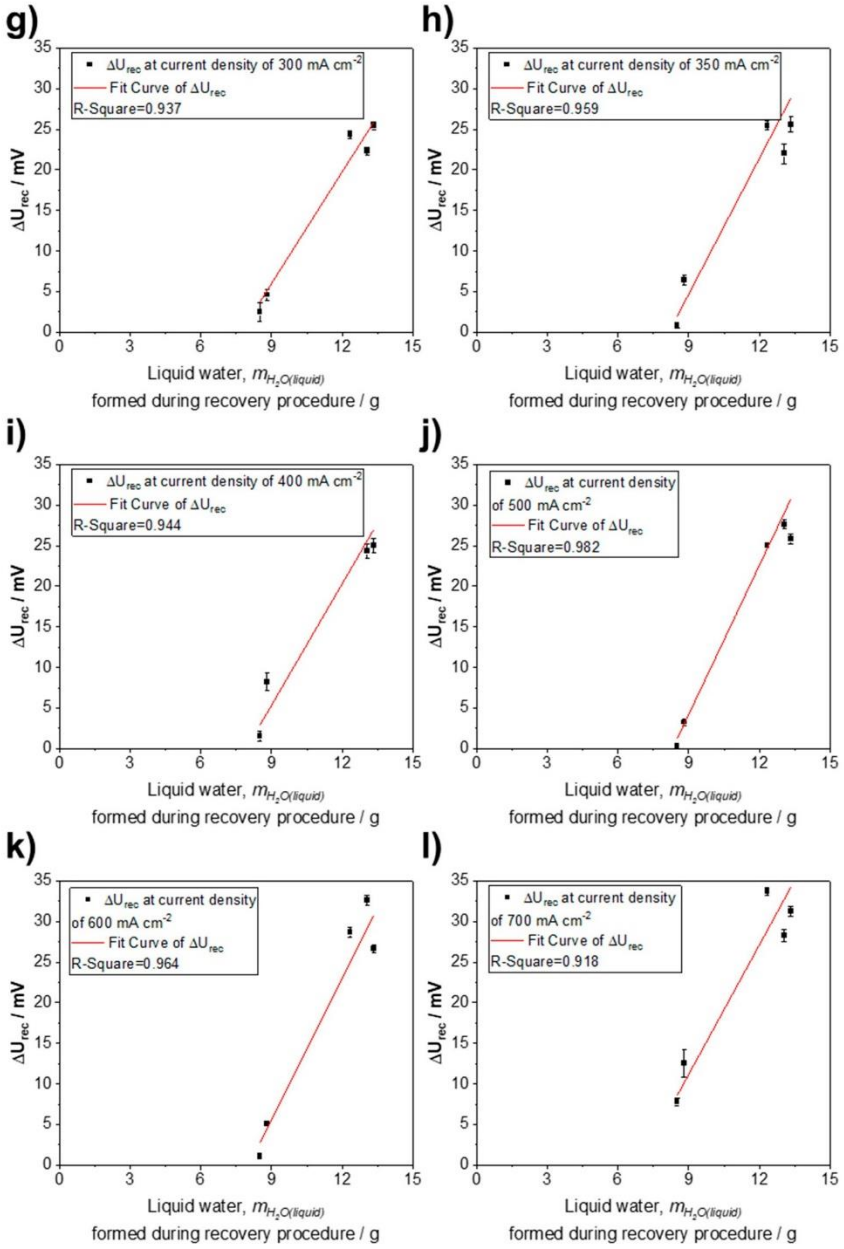
g)
ΔU_rec at current density of 300 mA cm^-2
Fit Curve of ΔU_rec
R-Square=0.937
h)
ΔU_rec at current density of 350 mA cm^-2
Fit Curve of ΔU_rec
R-Square=0.959
i)
ΔU_rec at current density of 400 mA cm^-2
Fit Curve of ΔU_rec
R-Square=0.944
j)
ΔU_rec at current density of 500 mA cm^-2
Fit Curve of ΔU_rec
R-Square=0.982
k)
ΔU_rec at current density of 600 mA cm^-2
Fit Curve of ΔU_rec
R-Square=0.964
l)
ΔU_rec at current density of 700 mA cm^-2
Fit Curve of ΔU_rec
R-Square=0.918
ΔU_rec / mV
Liquid water, m_H2O(liquid) formed during recovery procedure / g

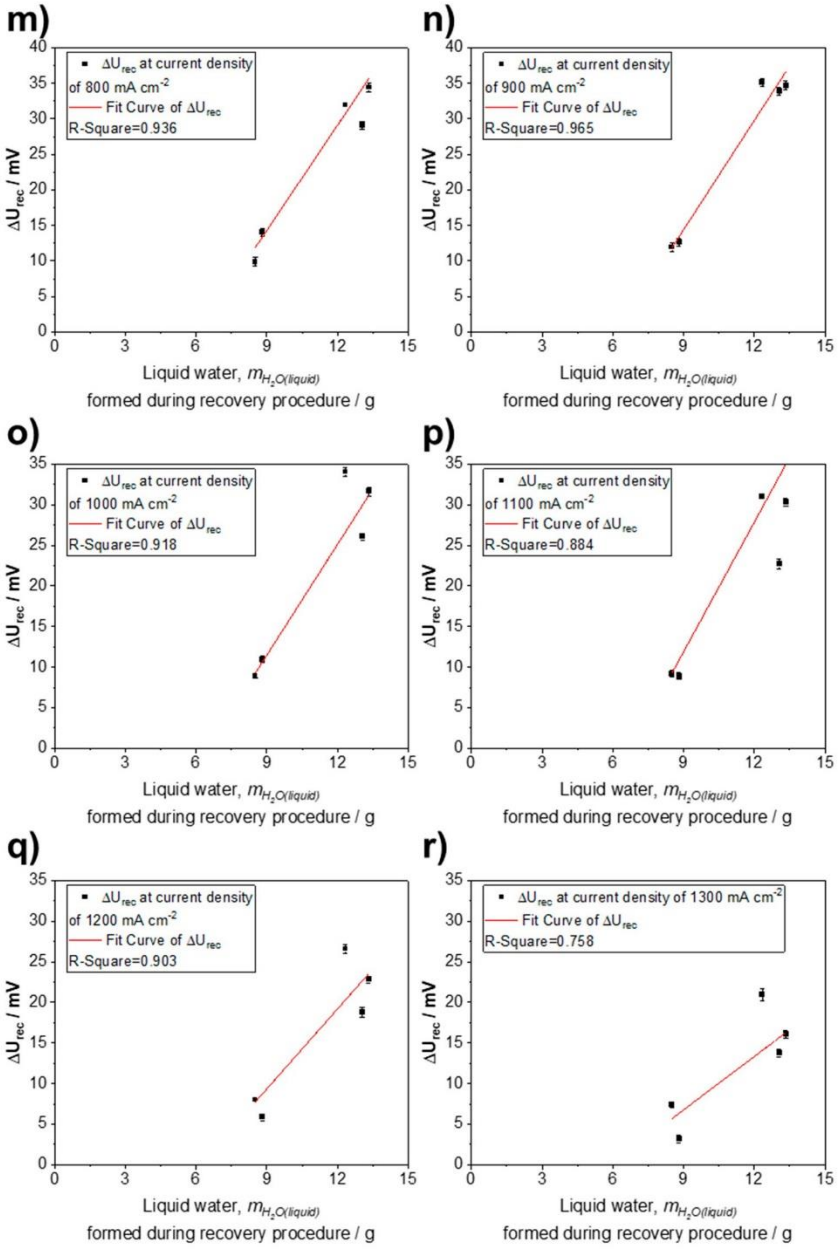
m)
ΔU_rec at current density of 800 mA cm-2
Fit Curve of ΔU_rec
R-Square=0.936
n)
ΔU_rec at current density of 900 mA cm-2
Fit Curve of ΔU_rec
R-Square=0.965
o)
ΔU_rec at current density of 1000 mA cm-2
Fit Curve of ΔU_rec
R-Square=0.918
p)
ΔU_rec at current density of 1100 mA cm-2
Fit Curve of ΔU_rec
R-Square=0.884
q)
ΔU_rec at current density of 1200 mA cm-2
Fit Curve of ΔU_rec
R-Square=0.903
r)
ΔU_rec at current density of 1300 mA cm-2
Fit Curve of ΔU_rec
R-Square=0.758
ΔU_rec / mV
Liquid water, m_H2O(liquid) formed during recovery procedure / g

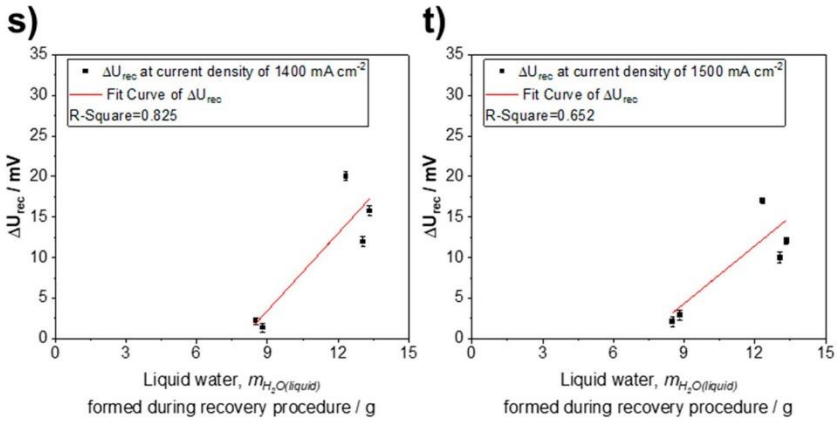

Figure S7. Absolute recovered voltage versus total amount of liquid water formed during non-operando recovery at all the evaluated current densities from 0 to 1.5 A cm^{-2}. Recovered voltage corresponds to data from Figure 6b.

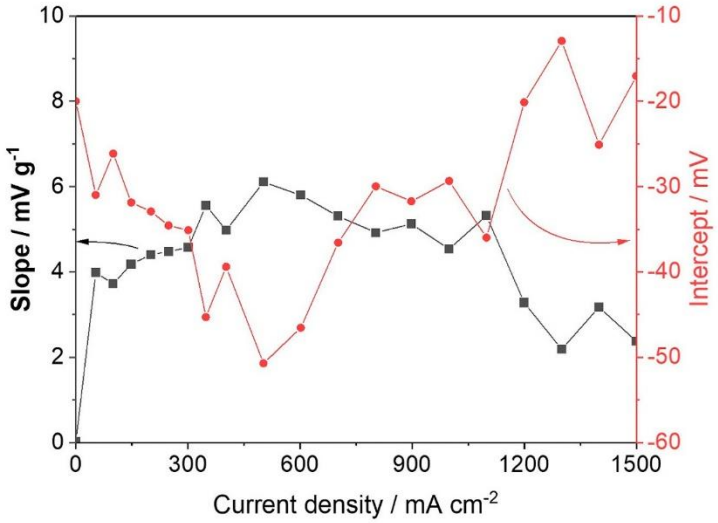

Figure S8. Slope and intercept of the linear fitting results between the absolute recovered voltage and the formed liquid water during each non-operando recovery procedure at different current densities.

9 Bibliography

[1] Mengel M, Nauels A, Rogelj J, Schleussner C-F. Committed sea-level rise under the Paris Agreement and the legacy of delayed mitigation action. Nature communications. 2018;9:1-10.

[2] Climate change, impacts and vulnerability in Europe 2016. https://www.eea.europa.eu/publications/climate-change-impacts-and-vulnerability-2016.

[3] Paris agreement. Report of the Conference of the Parties to the United Nations Framework Convention on Climate Change (21st Session, 2015: Paris) Retrived December.https://unfccc.int/process-and-meetings/the-paris-agreement.

[4] COP26 Presidency Outcomes The Climate Pact. https://ukcop26.org

[5] Fuel Cells and Hydrogen 2 Joint Undertaking, Hydrogen roadmap Europe : a sustainable pathway for the European energy transition, Publications Office, 2019, https://data.europa.eu/doi/10.2843/341510

[6] DOE National Clean Hydrogen Strategy and Roadmap (Draft). https://www.hydrogen.energy.gov/clean-hydrogen-strategy-roadmap.html

[7] Hart D, Jones S, Lewis J. The fuel cell industry review 2020. 2020.

[8] Strategic Research and Innovation Agenda 2021 – 2027, CLEAN HYDROGEN JOINT UNDERTAKING.

[9] Green Energy Oman. https://geo.om.

[10] HyDeal Ambition. https://www.hydeal.com/hydeal-ambition.

[11] Western Green Energy Hub. https://wgeh.com.au.

[12] Tsotridis G, Pilenga A, De Marco G, Malkow T. EU harmonised test protocols for PEMFC MEA testing in single cell configuration for automotive applications. JRC Science for Policy report. 2015;27632.

[13] The Fuel Cell Technologies Office Multi-Year Research, Development, and Demonstration Plan. Technical report: US Department of Energy; 2016.

[14] Qi Z, Tang H, Guo Q, Du B. Investigation on “saw-tooth” behavior of PEM fuel cell performance during shutdown and restart cycles. Journal of Power Sources. 2006;161:864-71.

[15] Gazdzick P, Mitzel J, Garcia Sanchez D, Schulze M, Friedrich KA. Evaluation of reversible and irreversible degradation rates of polymer electrolyte membrane fuel cells tested in automotive conditions. 2016;327:86-95.

[16] IEA (2019), The Future of Hydrogen, IEA, Paris https://www.iea.org/reports/the-future-of-hydrogen.

[17] KEY PERFORMANCE INDICATORS (KPIS) FOR FCH RESEARCH AND INNOVATION, HER and EERA Joint Reasearch Programme on Fuel Cells and Hydrogen technologies, 2020 - 2030.

[18] Fuel Cell Buses in U.S. Transit Fleets: Current Status 2020.

[19] Cullen DA, Neyerlin K, Ahluwalia RK, Mukundan R, More KL, Borup RL, et al. New roads and challenges for fuel cells in heavy-duty transportation. Nature energy. 2021;6:462-74.

[20] DOE U.S. Hydrogen Class 8 Long Haul Truck Targets. 2019.

[21] Fuel Cell Buses in U.S. Transit Fleets: Current Status 2018.

[22] Peng W, Wei Z, Huang C-G, Feng G, Li J. A Hybrid Health Prognostics Method For Proton Exchange Membrane Fuel Cells With Internal Health Recovery. IEEE Transactions on Transportation Electrification. 2023.

[23] Wang Y, Wang K, Wang B, Yin Y, Zhao H, Han L, et al. A data-driven approach to lifespan prediction for vehicle fuel cell systems. IEEE Transactions on Transportation Electrification. 2023.

[24] Kocha SS, Pollet BG. Advances in rapid and effective break-in/conditioning/recovery of automotive PEMFC stacks. Current Opinion in Electrochemistry. 2022;31:100843.

[25] Cheng X, Shi Z, Glass N, Zhang L, Zhang J, Song D, et al. A review of PEM hydrogen fuel cell contamination: Impacts, mechanisms, and mitigation. Journal of Power Sources. 2007;165:739-56.

[26] Detti A, Pahon E, Steiner NY, Jemei S, Bouillaut L, Same AB, et al. Remaining Useful Life Prediction for Proton Exchange Membrane Fuel Cells Including Reversible and Irreversible Losses. Power Engineering. 2022;11:39-46.

[27] Wang H, Lin R, Liu X, Liu S, Cai X, Ji W. Reducing Irreversible Performance Losses via a Graphene Oxide Buffer Layer for Proton-Exchange Membrane Fuel Cells. ACS Applied

Materials & Interfaces. 2022.

[28] Han J, Han J, Yu S. Experimental analysis of performance degradation of 3-cell PEMFC stack under dynamic load cycle. International Journal of Hydrogen Energy. 2020;45:13045-54.

[29] Gazdzick P, Mitzel J, Garcia Sanchez D, Schulze M, Friedrich KA. Evaluation of reversible and irreversible degradation rates of polymer electrolyte membrane fuel cells tested in automotive conditions. Journal of Power Sources. 2016;327:86-95.

[30] Du F, Dao TA, Peitl PVJ, Bauer A, Preuss K, Bonastre AM, et al. Effects of PEMFC Operational History under Dry/Wet Conditions on Additional Voltage Losses due to Ionomer Migration. Journal of The Electrochemical Society. 2020;167:144513-27.

[31] Jomori S, Komatsubara K, Nonoyama N, Kato M, Yoshida T. An Experimental Study of the Effects of Operational History on Activity Changes in a PEMFC. Journal of The Electrochemical Society. 2013;160:F1067-F73.

[32] Linse N, Scherer GG, Wokaun A, Gubler L. Quantitative analysis of carbon corrosion during fuel cell start-up and shut-down by anode purging. Journal of Power Sources. 2012;219:240-8.

[33] Choo H-S, Kinumoto T, Nose M, Miyazaki K, Abe T, Ogumi Z. Electrochemical oxidation of highly oriented pyrolytic graphite during potential cycling in sulfuric acid solution. Journal of Power Sources. 2008;185:740-6.

[34] Choo HS, Chun DK, Lee JH, Shin HS, Lee SK, Park YS, et al. Performance Recovery of Fuel Cell Stack for FCEV. SAE Technical Paper Series. 2015.

[35] Mitzel J, Zhang Q, Gazdzicki P, Friedrich KA. Review on mechanisms and recovery procedures for reversible performance losses in polymer electrolyte membrane fuel cells. Journal of Power Sources. 2021;488:229375.

[36] Rinaldo SG, Lee W, Stumper J, Eikerling M. Mechanistic Principles of Platinum Oxide Formation and Reduction. Electrocatalysis. 2014;5:262-72.

[37] Baturina OA, Swider-Lyons KE. Effect of SO2 on the Performance of the Cathode of a PEM Fuel Cell at 0.5–0.7 V. Journal of The Electrochemical Society. 2009;156:B1423.

[38] Jing F, Hou M, Shi W, Fu J, Yu H, Ming P, et al. The effect of ambient contamination on PEMFC performance. Journal of Power Sources. 2007;166:172-6.

[39] Baschuk J, Li X. Modelling CO poisoning and O2 bleeding in a PEM fuel cell anode. International Journal of Energy Research. 2003;27:1095-116.

[40] Camara G, Ticianelli EA, Mukerjee S, Lee S, McBreen J. The CO poisoning mechanism of the hydrogen oxidation reaction in proton exchange membrane fuel cells. Journal of The Electrochemical Society. 2002;149:A748.

[41] Guétaz L, Escribano S, Sicardy O. Study by electron microscopy of proton exchange membrane fuel cell membrane-electrode assembly degradation mechanisms: Influence of local conditions. Journal of Power Sources. 2012;212:169-78.

[42] Shao Y, Wang J, Kou R, Engelhard M, Liu J, Wang Y, et al. The corrosion of PEM fuel cell catalyst supports and its implications for developing durable catalysts. Electrochimica Acta. 2009;54:3109-14.

[43] Yuan X-Z, Nayoze-Coynel C, Shaigan N, Fisher D, Zhao N, Zamel N, et al. A review of functions, attributes, properties and measurements for the quality control of proton exchange membrane fuel cell components. Journal of Power Sources. 2021;491:229540.

[44] Yang Y, Zhou X, Li B, Zhang C. Recent progress of the gas diffusion layer in proton exchange membrane fuel cells: Material and structure designs of microporous layer. International Journal of Hydrogen Energy. 2021;46:4259-82.

[45] Kurnia JC, Sasmito AP. Hydrogen fuel cell in vehicle propulsion: Performance, efficiency, and challenge. Energy Efficiency in Mobility Systems. 2020:9-26.

[46] O'hayre R, Cha S-W, Colella W, Prinz FB. Fuel cell fundamentals. 2016.

[47] Tian G, Wasterlain S, Endichi I, Candusso D, Harel F, François X, et al. Diagnosis methods dedicated to the localisation of failed cells within PEMFC stacks. Journal of Power Sources. 2008;182:449-61.

[48] Zhang J, Tang Y, Song C, Zhang J, Wang H. PEM fuel cell open circuit voltage (OCV) in the temperature range of 23 C to 120 C. Journal of Power Sources. 2006;163:532-7.

[49] Rodatz P, Büchi F, Onder C, Guzzella L. Operational aspects of a large PEFC stack under practical conditions. Journal of Power Sources. 2004;128:208-17.

[50] Sammes N. Fuel cell technology: reaching towards commercialization. 2006.

[51] Yuan X-Z, Song C, Wang H, Zhang J. Electrochemical impedance spectroscopy in PEM

fuel cells: fundamentals and applications. 2010.

[52] Basu S. Fuel cell science and technology. 2007.

[53] Schmittinger W, Vahidi A. A review of the main parameters influencing long-term performance and durability of PEM fuel cells. Journal of Power Sources. 2008;180:1-14.

[54] Scholta J, Berg N, Wilde P, Jörissen L, Garche J. Development and performance of a 10 kW PEMFC stack. Journal of Power Sources. 2004;127:206-12.

[55] Li B, Wan K, Xie M, Chu T, Wang X, Li X, et al. Durability degradation mechanism and consistency analysis for proton exchange membrane fuel cell stack. Applied Energy. 2022;314:119020.

[56] Yousfi-Steiner N, Moçotéguy P, Candusso D, Hissel D, Hernandez A, Aslanides A. A review on PEM voltage degradation associated with water management: Impacts, influent factors and characterization. Journal of Power Sources. 2008;183:260-74.

[57] Okonkwo PC, Belgacem IB, Emori W, Uzoma PC. Nafion degradation mechanisms in proton exchange membrane fuel cell (PEMFC) system: A review. International Journal of Hydrogen Energy. 2021;46:27956-73.

[58] Prokop M, Drakselova M, Bouzek K. Review of the experimental study and prediction of Pt-based catalyst degradation during PEM fuel cell operation. Current Opinion in Electrochemistry. 2020;20:20-7.

[59] Moore JM, Adcock PL, Lakeman JB, Mepsted GO. The effects of battlefield contaminants on PEMFC performance. Journal of Power Sources. 2000;85:254-60.

[60] Pan Y, Wang H, Brandon NP. Gas diffusion layer degradation in proton exchange membrane fuel cells: Mechanisms, characterization techniques and modelling approaches. Journal of Power Sources. 2021;513:230560.

[61] Hinds G, Brightman E. Towards more representative test methods for corrosion resistance of PEMFC metallic bipolar plates. International Journal of Hydrogen Energy. 2015;40:2785-91.

[62] Yu X, Ye S. Recent advances in activity and durability enhancement of Pt/C catalytic cathode in PEMFC: Part II: Degradation mechanism and durability enhancement of carbon supported platinum catalyst. Journal of Power Sources. 2007;172:145-54.

[63] Gazdzicki P, Mitzel J, Dreizler AM, Schulze M, Friedrich KA. Impact of Platinum Loading on Performance and Degradation of Polymer Electrolyte Fuel Cell Electrodes Studied in a Rainbow Stack. Fuel Cells. 2018;18:270-8.

[64] Zhai Y, Bender G, Dorn S, Rocheleau R. The multiprocess degradation of PEMFC performance due to sulfur dioxide contamination and its recovery. Journal of The Electrochemical Society. 2009;157:B20.

[65] Teliska M, O'Grady W, Ramaker D. Determination of O and OH adsorption sites and coverage in situ on Pt electrodes from Pt L23 X-ray absorption spectroscopy. The Journal of Physical Chemistry B. 2005;109:8076-84.

[66] Xu H, Kunz R, Fenton JM. Investigation of platinum oxidation in PEM fuel cells at various relative humidities. Electrochemical and Solid-State Letters. 2006;10:B1.

[67] Shibata S, Sumino MP. Kinetics and mechanism of reduction of oxide film on smooth platinum electrodes with hydrogen. Electrochimica Acta. 1975;20:739-46.

[68] Paik C, Jarvi T, O'grady W. Extent of PEMFC cathode surface oxidation by oxygen and water measured by CV. Electrochemical and Solid-State Letters. 2004;7:A82.

[69] Zhang X, Guo L, Liu H. Recovery mechanisms in proton exchange membrane fuel cells after accelerated stress tests. Journal of Power Sources. 2015;296:327-34.

[70] Zago M, Baricci A, Bisello A, Jahnke T, Yu H, Maric R, et al. Experimental analysis of recoverable performance loss induced by platinum oxide formation at the polymer electrolyte membrane fuel cell cathode. Journal of Power Sources. 2020;455:227990.

[71] Gould BD, Bender G, Bethune K, Dorn S, Baturina OA, Rocheleau R, et al. Operational Performance Recovery of SO[sub 2]-Contaminated Proton Exchange Membrane Fuel Cells. Journal of The Electrochemical Society. 2010;157:B1569.

[72] Mathieu M-V, Primet M. Sulfurization and regeneration of platinum. Applied Catalysis. 1984;9:361-70.

[73] Najdeker E, Bishop E. The formation and behaviour of platinum sulphide on platinum electrodes. Journal of Electroanalytical Chemistry and Interfacial Electrochemistry. 1973;41:79-87.

[74] Contractor A, Lal H. The nature of species adsorbed on platinum from SO2 solutions. Journal of Electroanalytical Chemistry and Interfacial Electrochemistry. 1978;93:99-107.

[75] Argano E, Randhava S, Rehmat A. Effect of H2S poisoning on the i.-r.-spectrum of CO and COS adsorbed on alumina-supported platinum. Transactions of the Faraday Society. 1969;65:552-60.

[76] Shi W, Yi B, Hou M, Jing F, Ming P. Hydrogen sulfide poisoning and recovery of PEMFC Pt-anodes. Journal of Power Sources. 2007;165:814-8.

[77] Urdampilleta I, Uribe F, Rockward T, Brosha EL, Pivovar B, Garzon FH. PEMFC Poisoning with H2S: Dependence on Operating Conditions. ECS Transactions. 2019;11:831-42.

[78] Garzon F, Lopes T, Rockward T, Sansiñena J-M, Kienitz B, Mukundan R. The impact of impurities on long-term PEMFC performance. ECS Transactions. 2009;25:1575.

[79] Betournay MC, Bonnell G, Edwardson E, Paktunc D, Kaufman A, Lomma AT. The effects of mine conditions on the performance of a PEM fuel cell. Journal of Power Sources. 2004;134:80-7.

[80] Janssen GJM. Modelling study of CO2 poisoning on PEMFC anodes. Journal of Power Sources. 2004;136:45-54.

[81] Zhang J, Datta R. Online monitoring of anode outlet CO concentration in PEM fuel cells. Electrochemical and Solid-State Letters. 2002;6:A5.

[82] Pérez LC, Rajala T, Ihonen J, Koski P, Sousa JM, Mendes A. Development of a methodology to optimize the air bleed in PEMFC systems operating with low quality hydrogen. International Journal of Hydrogen Energy. 2013;38:16286-99.

[83] Adams W, Blair J, Bullock K, Gardner C. Enhancement of the performance and reliability of CO poisoned PEM fuel cells. Journal of Power Sources. 2005;145:55-61.

[84] Nam JH, Lee K-J, Hwang G-S, Kim C-J, Kaviany M. Microporous layer for water morphology control in PEMFC. International Journal of Heat and Mass Transfer. 2009;52:2779-91.

[85] Weber AZ, Newman J. Modeling Transport in Polymer-Electrolyte Fuel Cells. Chemical Reviews. 2004;104:4679-726.

[86] Dhanushkodi SR, Tam M, Kundu S, Fowler MW, Pritzker MD. Carbon corrosion fingerprint development and de-convolution of performance loss according to degradation mechanism in PEM fuel cells. Journal of Power Sources. 2013;240:114-21.

[87] Natarajan D, Van Nguyen T. Current distribution in PEM fuel cells. Part 1: Oxygen and fuel flow rate effects. AIChE Journal. 2005;51:2587-98.

[88] Ott S, Bauer A, Du F, Dao TA, Klingenhof M, Orfanidi A, et al. Impact of Carbon Support Meso-Porosity on Mass Transport and Performance of PEMFC Cathode Catalyst Layers. ChemCatChem. 2021.

[89] Cho J, Kim H-S, Min K. Transient response of a unit proton-exchange membrane fuel cell under various operating conditions. Journal of Power Sources. 2008;185:118-28.

[90] https://irdfuelcells.com

[91] Shi S, Weber AZ, Kusoglu A. Structure/property relationship of Nafion XL composite membranes. Journal of Membrane Science. 2016;516:123-34.

[92] https://www.balticfuelcells.de/htmdocs/en/testgeraete_qcf-12-high-amp.shtml

[93] https://fuelcellcomponents.freudenberg-pm.com/Products/fuel-cell-stack-seals

[94] Yuan X, Wang H, Sun JC, Zhang J. AC impedance technique in PEM fuel cell diagnosis—A review. International Journal of Hydrogen Energy. 2007;32:4365-80.

[95] Lefebvre MC. Characterization of Ionic Conductivity Profiles within Proton Exchange Membrane Fuel Cell Gas Diffusion Electrodes by Impedance Spectroscopy. Journal of The Electrochemical Society. 1999;2:259.

[96] Li G, Pickup PG. Ionic conductivity of PEMFC electrodes: effect of Nafion loading. Journal of The Electrochemical Society. 2003;150:C745.

[97] Mashio T, Ohma A, Yamamoto S, Shinohara K. Analysis of reactant gas transport in a catalyst layer. ECS Transactions. 2007;11:529.

[98] Baker DR, Caulk DA, Neyerlin KC, Murphy MW. Measurement of Oxygen Transport Resistance in PEM Fuel Cells by Limiting Current Methods. Journal of The Electrochemical Society. 2009;156.

[99] St-Pierre J, Wetton B, Kim GS, Promislow K. Limiting Current Operation of Proton Exchange Membrane Fuel Cells. Journal of The Electrochemical Society. 2007;154:B186.

[100] Greszler TA, Caulk D, Sinha P. The Impact of Platinum Loading on Oxygen Transport Resistance. Journal of The Electrochemical Society. 2012;159:F831-F40.

[101] Alberti G, Narducci R, Sganappa M. Effects of hydrothermal/thermal treatments on the

water-uptake of Nafion membranes and relations with changes of conformation, counter-elastic force and tensile modulus of the matrix. Journal of Power Sources. 2008;178:575-83.

[102] Fumagalli M, Lyonnard S, Prajapati G, Berrod Q, Porcar L, Guillermo A, et al. Fast water diffusion and long-term polymer reorganization during Nafion membrane hydration evidenced by time-resolved small-angle neutron scattering. The Journal of Physical Chemistry B. 2015;119:7068-76.

[103] Alberti G, Narducci R. Evolution of permanent deformations (or memory) in Nafion 117 membranes with changes in temperature, relative humidity and time, and its importance in the development of medium temperature PEMFCs. Fuel Cells. 2009;9:410-20.

[104] Casciola M, Alberti G, Sganappa M, Narducci R. On the decay of Nafion proton conductivity at high temperature and relative humidity. Journal of Power Sources. 2006;162:141-5.

[105] Owejan JP, Owejan JE, Gu W. Impact of Platinum Loading and Catalyst Layer Structure on PEMFC Performance. Journal of The Electrochemical Society. 2013;160:F824-F33.

[106] Yarlagadda V, Carpenter MK, Moylan TE, Kukreja RS, Koestner R, Gu W, et al. Boosting Fuel Cell Performance with Accessible Carbon Mesopores. ACS Energy Letters. 2018;3:618-21.

[107] Kriston A, Xie T, Popov BN. Impact of Ultra-low Platinum loading on Mass Activity and Mass Transport in H2-Oxygen and H2-Air PEM Fuel Cells. Electrochimica Acta. 2014;121:116-27.

[108] Cetinbas FC, Ahluwalia RK, Kariuki NN, De Andrade V, Myers DJ. Effects of Porous Carbon Morphology, Agglomerate Structure and Relative Humidity on Local Oxygen Transport Resistance. Journal of The Electrochemical Society. 2020;167:013508.

[109] Kongkanand A, Mathias MF. The Priority and Challenge of High-Power Performance of Low-Platinum Proton-Exchange Membrane Fuel Cells. Journal of Physical Chemistry Letters. 2016;7:1127-37.

[110] Cho J, Ko J, Park S. Comprehensive Analysis of Critical Factors Determining Limiting Current of PEMFC: O2 and H+ Transport Resistance without Cathode Humidification. Journal of The Electrochemical Society. 2020;167:084511.

[111] Weber AZ, Borup RL, Darling RM, Das PK, Dursch TJ, Gu W, et al. A Critical Review of

Modeling Transport Phenomena in Polymer-Electrolyte Fuel Cells. Journal of The Electrochemical Society. 2014;161:F1254-F99.

[112] Jinnouchi R, Kudo K, Kitano N, Morimoto Y. Molecular Dynamics Simulations on O2 Permeation through Nafion Ionomer on Platinum Surface. Electrochimica Acta. 2016;188:767-76.

[113] Muzaffar T, Kadyk T, Eikerling M. Tipping water balance and the Pt loading effect in polymer electrolyte fuel cells: a model-based analysis. Sustainable Energy & Fuels. 2018;2:1189-96.

[114] Chan K, Eikerling M. Impedance Model of Oxygen Reduction in Water-Flooded Pores of Ionomer-Free PEFC Catalyst Layers. Journal of The Electrochemical Society. 2011;159:B155-B64.

[115] Nonoyama N, Okazaki S, Weber AZ, Ikogi Y, Yoshida T. Analysis of Oxygen-Transport Diffusion Resistance in Proton-Exchange-Membrane Fuel Cells. Journal of The Electrochemical Society. 2011;158.

[116] Harzer GS, Orfanidi A, El-Sayed H, Madkikar P, Gasteiger HA. Tailoring Catalyst Morphology towards High Performance for Low Pt Loaded PEMFC Cathodes. Journal of The Electrochemical Society. 2018;165:F770-F9.

[117] Reshetenko TV, Ben BL. Exploration of operating conditions on oxygen mass transport resistance and performance of PEM fuel cells: Effects of inlet gas humidification. Electrochemical Science Advances. 2021:e2100134.

[118] Mauritz KA, Moore RB. State of understanding of Nafion. Chemical Reviews. 2004;104:4535-86.

[119] Kusoglu A, Weber AZ. New Insights into Perfluorinated Sulfonic-Acid Ionomers. Chemical Reviews. 2017;117:987-1104.

[120] Ye X, LeVan MD. Water transport properties of Nafion membranes: Part I. Single-tube membrane module for air drying. Journal of Membrane Science. 2003;221:147-61.

[121] Monroe CW, Romero T, Mérida W, Eikerling M. A vaporization-exchange model for water sorption and flux in Nafion. Journal of Membrane Science. 2008;324:1-6.

[122] Aleksandrova E, Hiesgen R, Eberhard D, Friedrich KA, Kaz T, Roduner E. Proton conductivity study of a fuel cell membrane with nanoscale resolution. ChemPhysChem.

2007;8:519-22.

[123] He Q, Kusoglu A, Lucas IT, Clark K, Weber AZ, Kostecki R. Correlating humidity-dependent ionically conductive surface area with transport phenomena in proton-exchange membranes. The Journal of Physical Chemistry B. 2011;115:11650-7.

[124] Adachi M, Navessin T, Xie Z, Frisken B, Holdcroft S. Correlation of in situ and ex situ measurements of water permeation through Nafion NRE211 proton exchange membranes. Journal of the Electrochemical Society. 2009;156:B782.

[125] Adachi M, Navessin T, Xie Z, Li FH, Tanaka S, Holdcroft S. Thickness dependence of water permeation through proton exchange membranes. Journal of Membrane Science. 2010;364:183-93.

[126] Gebel G, Lyonnard S, Mendil-Jakani H, Morin A. The kinetics of water sorption in Nafion membranes: a small-angle neutron scattering study. Journal of Physics: Condensed Matter. 2011;23:234107.

[127] Davis EM, Stafford CM, Page KA. Elucidating water transport mechanisms in Nafion thin films. ACS Macro Letters. 2014;3:1029-35.

[128] Kusoglu A, Dursch TJ, Weber AZ. Nanostructure/swelling relationships of bulk and thin-film PFSA ionomers. Advanced Functional Materials. 2016;26:4961-75.

[129] Kendrick I, Kumari D, Yakaboski A, Dimakis N, Smotkin ES. Elucidating the ionomer-electrified metal interface. Journal of the American Chemical Society. 2010;132:17611-6.

[130] Paul DK, Fraser A, Karan K. Towards the understanding of proton conduction mechanism in PEMFC catalyst layer: Conductivity of adsorbed Nafion films. Electrochemistry communications. 2011;13:774-7.

[131] Shim HK, Paul DK, Karan K. Resolving the contradiction between anomalously high water uptake and low conductivity of nanothin Nafion films on SiO2 substrate. Macromolecules. 2015;48:8394-7.

[132] Kim S, Dura JA, Page KA, Rowe BW, Yager KG, Lee H-J, et al. Surface-induced nanostructure and water transport of thin proton-conducting polymer films. Macromolecules. 2013;46:5630-7.

[133] Mashio T, Iden H, Ohma A, Tokumasu T. Modeling of local gas transport in catalyst layers of PEM fuel cells. Journal of Electroanalytical Chemistry. 2017;790:27-39.

[134] Gierke TD, Munn G, Wilson F. The morphology in nafion perfluorinated membrane products, as determined by wide-and small-angle x-ray studies. Journal of Polymer Science: Polymer Physics Edition. 1981;19:1687-704.

[135] Safiollah M, Melchy P-EA, Berg P, Eikerling M. Model of water sorption and swelling in polymer electrolyte membranes: Diagnostic applications. The Journal of Physical Chemistry B. 2015;119:8165-75.

[136] Mittelsteadt CK, Staser J. Simultaneous water uptake, diffusivity and permeability measurement of perfluorinated sulfonic acid polymer electrolyte membranes. ECS Transactions. 2011;41:101.

[137] Takamatsu T, Hashiyama M, Eisenberg A. Sorption phenomena in Nafion membranes. Journal of Applied Polymer Science. 1979;24:2199-220.

[138] James P, Elliott J, McMaster T, Newton J, Elliott A, Hanna S, et al. Hydration of Nafion® studied by AFM and X-ray scattering. Journal of Materials Science. 2000;35:5111-9.

[139] Van Nguyen T, Nguyen MV, Lin G, Rao N, Xie X, Zhu D-M. Characterization of surface ionic activity of proton conductive membranes by conductive atomic force microscopy. Electrochemical and solid-state letters. 2005;9:A88.

[140] Onishi LM, Prausnitz JM, Newman J. Water− Nafion equilibria. Absence of schroeder's paradox. The Journal of Physical Chemistry B. 2007;111:10166-73.

[141] Bass M, Freger V. An experimental study of Schroeder's paradox in Nafion and Dowex polymer electrolytes. Desalination. 2006;199:277-9.

10 Supporting information

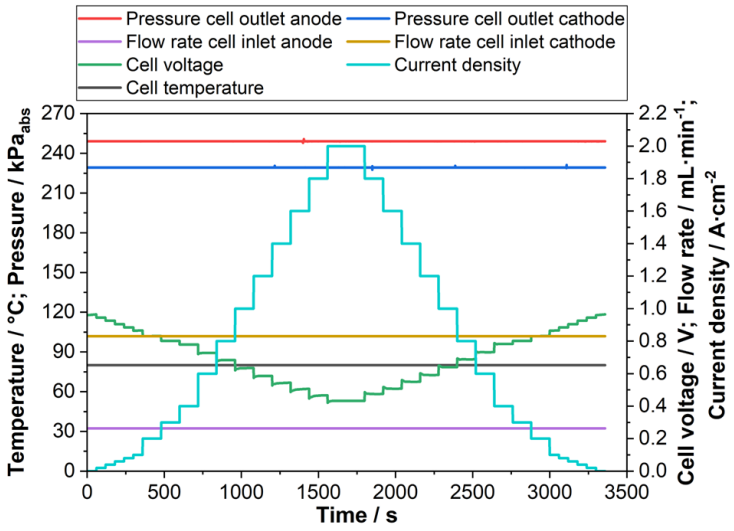

Figure S1: Testbench parameters during the polarization curves measurement.

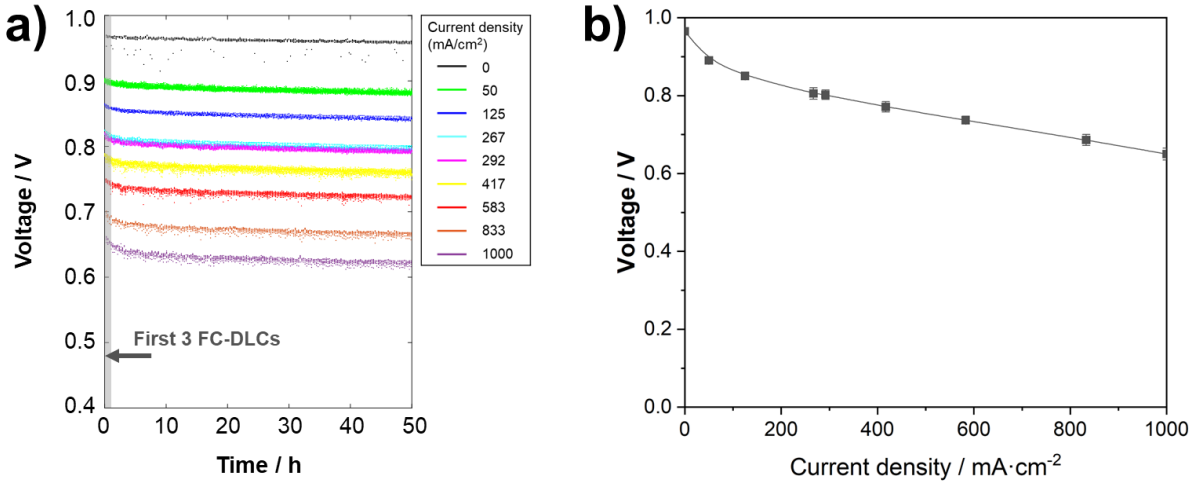

Figure S2: Schemes to convert a) FC-DLC data into a b) polarization curve. Both images are adapted from Section 5.1.

The shaded area of FC-DLCs data corresponds to the voltage data from the first 3 FC-DLCs as shown in Figure S2 a). According to the different current densities in the FC-DLC profile, Figure S2 b) is the converted polarization curve with the average and standard deviation of the voltage data from the first 3 FC-DLCs.

Table S1: The fitting results of the measured EIS data including errors from the Thales XT software. The equivalent model is described in Figure 10 in Section 4.3.3.

Time	R_{Ohmic} / mOhm	Error / %	$R_{Charge\ transfer}$ / mOhm	Error / %	$R_{Mass\ transport}$ / mOhm	Error / %
Test block 1 BoT	3.162	1.76	11.341	3.17	5.044	4.79
Test block 1 EoT	3.330	2.73	12.722	3.88	5.930	3.02
After the DOE protocol	3.264	1.78	12.324	4.86	5.330	4.26
Test block 2 BoT	3.230	1.12	11.601	3.54	5.115	4.29
Test block 2 EoT	3.466	1.52	13.562	4.17	6.479	3.95
After the modified protocol	3.387	1.67	12.713	2.49	5.679	3.90
Test block 3 BoT	3.390	2.95	12.271	3.61	5.524	4.15
Test block 3 EoT	3.691	1.21	14.451	2.03	6.773	3.77
After the DOE protocol	3.676	1.75	14.012	2.74	6.153	3.53
Test block 4 BoT	3.581	2.82	13.213	4.35	6.089	3.26
Test block 4 EoT	3.947	2.53	15.921	2.63	7.665	3.27
After the modified protocol	3.901	1.50	15.022	2.41	6.935	3.20
Test block 5 BoT	3.846	1.70	14.814	3.56	6.788	3.86

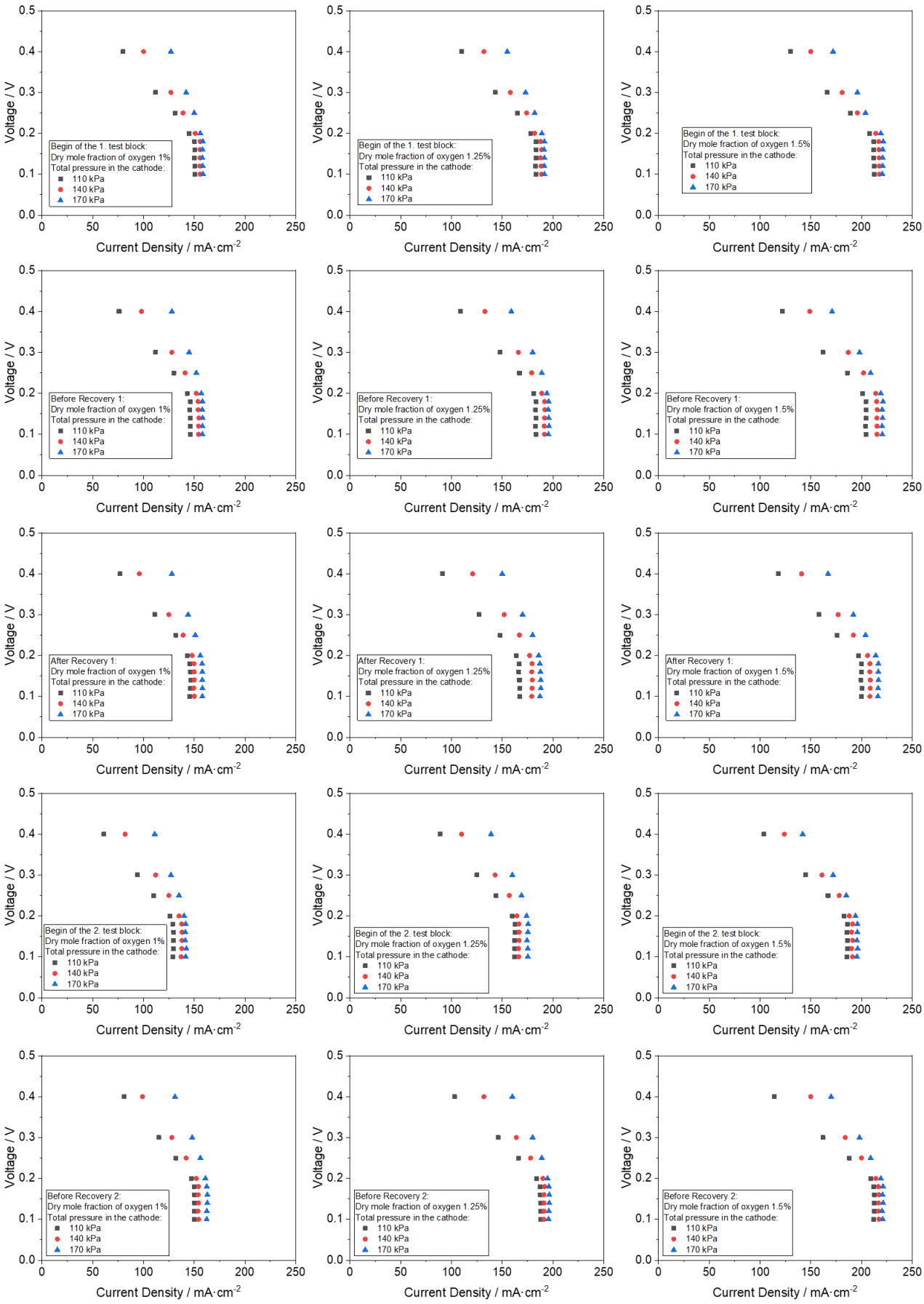
Voltage / V
Current Density / mA·cm-2
Begin of the 1. test block:
Dry mole fraction of oxygen 1%
Total pressure in the cathode:
110 kPa
140 kPa
170 kPa
Begin of the 1. test block:
Dry mole fraction of oxygen 1.25%
Total pressure in the cathode:
110 kPa
140 kPa
170 kPa
Begin of the 1. test block:
Dry mole fraction of oxygen 1.5%
Total pressure in the cathode:
110 kPa
140 kPa
170 kPa
Before Recovery 1:
Dry mole fraction of oxygen 1%
Total pressure in the cathode:
110 kPa
140 kPa
170 kPa
Before Recovery 1:
Dry mole fraction of oxygen 1.25%
Total pressure in the cathode:
110 kPa
140 kPa
170 kPa
Before Recovery 1:
Dry mole fraction of oxygen 1.5%
Total pressure in the cathode:
110 kPa
140 kPa
170 kPa
After Recovery 1:
Dry mole fraction of oxygen 1%
Total pressure in the cathode:
110 kPa
140 kPa
170 kPa
After Recovery 1:
Dry mole fraction of oxygen 1.25%
Total pressure in the cathode:
110 kPa
140 kPa
170 kPa
After Recovery 1:
Dry mole fraction of oxygen 1.5%
Total pressure in the cathode:
110 kPa
140 kPa
170 kPa
Begin of the 2. test block:
Dry mole fraction of oxygen 1%
Total pressure in the cathode:
110 kPa
140 kPa
170 kPa
Begin of the 2. test block:
Dry mole fraction of oxygen 1.25%
Total pressure in the cathode:
110 kPa
140 kPa
170 kPa
Begin of the 2. test block:
Dry mole fraction of oxygen 1.5%
Total pressure in the cathode:
110 kPa
140 kPa
170 kPa
Before Recovery 2:
Dry mole fraction of oxygen 1%
Total pressure in the cathode:
110 kPa
140 kPa
170 kPa
Before Recovery 2:
Dry mole fraction of oxygen 1.25%
Total pressure in the cathode:
110 kPa
140 kPa
170 kPa
Before Recovery 2:
Dry mole fraction of oxygen 1.5%
Total pressure in the cathode:
110 kPa
140 kPa
170 kPa

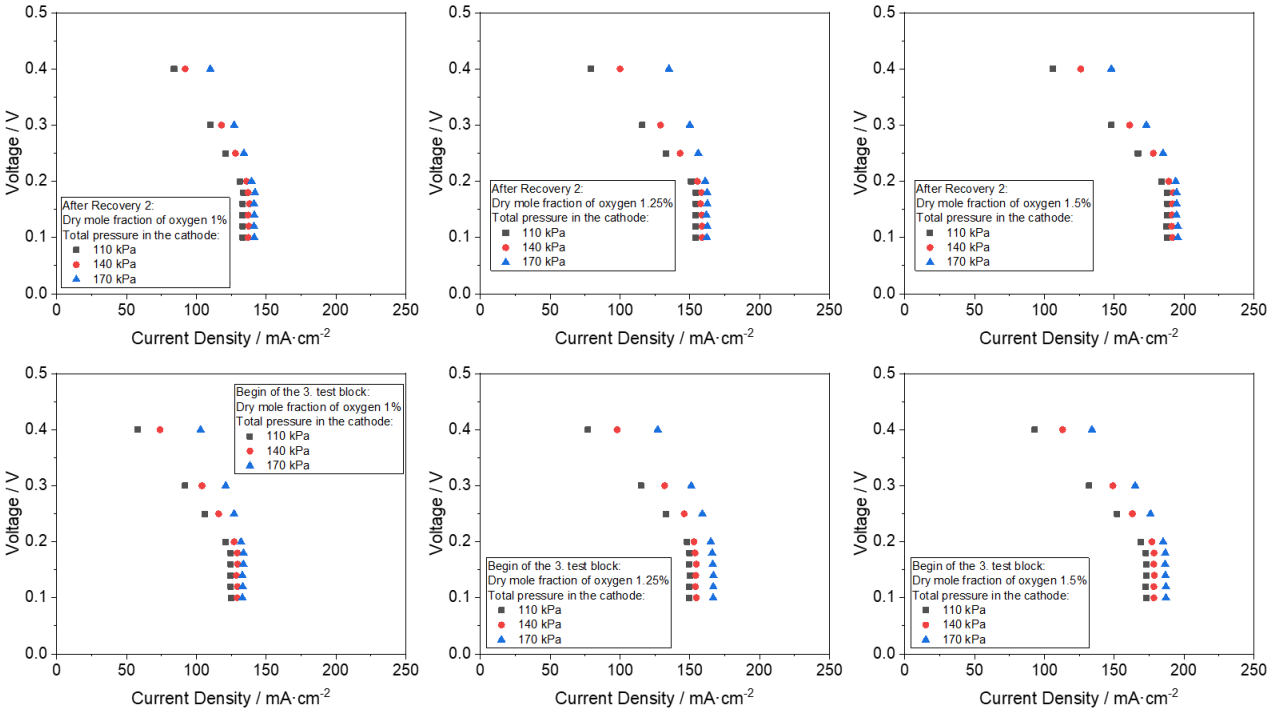

Figure S3: The results of the measured limiting current density of the fuel cell with dry mole fraction of oxygen of 1 %, 1.25 %, and 1.5 % with total pressure in the cathode of 110, 140 and 170 kPa at the beginning of each test block, before and after each recovery protocol during the durability test.

Table S2: Slope and intercept of the linear fitting results between the total pressure in the cathode and the total oxygen transfer resistance during the durability test according to the Figure 23.

Time	Slope	Intercept
Begin of the 1. test block	0.84	21.59
Before Recovery 1 (80°C -30°C)	0.74	20.72
After Recovery 1	0.72	26.99
Begin of the 2. test block	0.79	12.61
Before Recovery 2 (80°C -30°C) (repetition)	0.78	13.76
After Recovery 2 (repetition)	0.80	32.31
Begin of the 3. test block	0.87	25.97